

**TOWARDS REALISTIC NUMERICAL SIMULATIONS OF  
MAJORANA DEVICES**



# **TOWARDS REALISTIC NUMERICAL SIMULATIONS OF MAJORANA DEVICES**

## **Proefschrift**

ter verkrijging van de graad van doctor  
aan de Technische Universiteit Delft,  
op gezag van de Rector Magnificus prof. dr. ir. T.H.J.J. van der Hagen,  
voorzitter van het College voor Promoties,  
in het openbaar te verdedigen op  
maandag 11 mei 2020 om 15:00 uur

door

**Bas NIJHOLT**

Master of Science in Applied Physics,  
Technische Universiteit Delft, Delft, Nederland,  
geboren te Rotterdam, Nederland.

Dit proefschrift is goedgekeurd door de

promotor: Dr. A. R. Akhmerov

copromotor: Dr. M. T. Wimmer

Samenstelling promotiecommissie:

Rector Magnificus,	voorzitter
Dr. A. R. Akhmerov	Technische Universiteit Delft, promotor
Dr. M. T. Wimmer	Technische Universiteit Delft, copromotor

*Onafhankelijke leden:*

Prof. Dr. L. M. K. Vandersypen	Technische Universiteit Delft
Prof. Dr. C. W. J. Beenakker	Universiteit Leiden
Prof. Dr. A. P. Higginbotham	IST Austria, Oostenrijk
Prof. Dr. F. von Oppen	Vrije Universiteit Berlijn, Duitsland
Prof. Dr. E. Prada	Autonome Universiteit van Madrid, Spanje
Prof. Dr. A. F. Otto	Technische Universiteit Delft, reserve lid



*Printed by:* Proefschriftenprinten.nl

*Cover:* Each unique cover shows the conductance  $G$  (color intensity) through a different Majorana nanowire device as a function of  $V_{\text{bias}}$  and rotating magnetic field  $B$ , where the parameter space is adaptively sampled to minimize the computational time, and where the vertices of the triangles indicate the points at which  $G$  is sampled. Designed by Bas Nijholt and Stijn Balk.

Copyright © 2020 by B. Nijholt

Casimir PhD Series, Delft-Leiden 2020-11

ISBN 978-90-8593-438-7

An electronic version of this dissertation is available at  
<http://repository.tudelft.nl/>.

# CONTENTS

<b>Summary</b>	<b>ix</b>
<b>Samenvatting</b>	<b>xi</b>
<b>1 Introduction</b>	<b>1</b>
1.1 Preface . . . . .	1
1.2 Topological protection of Majoranas . . . . .	5
1.2.1 BCS theory and the mean-field approximation. . . . .	5
1.2.2 Topology and symmetry . . . . .	7
1.3 Non-Abelian statistics and braiding. . . . .	8
1.4 Majoranas in a minimal hybrid nanowire . . . . .	11
1.4.1 The Hamiltonian: term by term . . . . .	11
1.4.2 Wavefunction . . . . .	14
1.4.3 Phase diagram . . . . .	14
1.5 Majoranas in a more realistic 3D hybrid nanowire . . . . .	14
1.5.1 Multiple bands. . . . .	15
1.5.2 The orbital effect of the magnetic field . . . . .	16
1.5.3 Disorder . . . . .	17
1.5.4 Electrostatics. . . . .	17
1.5.5 Superconducting order parameter . . . . .	19
1.5.6 Spin-orbit coupling . . . . .	19
1.6 Numerical methods. . . . .	19
1.6.1 Band structure . . . . .	20
1.6.2 Discretization of the Hamiltonian . . . . .	20
1.6.3 Peierls substitution . . . . .	21
1.6.4 Topological phase boundaries . . . . .	22
1.6.5 Limits and complexity . . . . .	22
1.6.6 Adaptive sampling . . . . .	24
1.7 Structure of this thesis . . . . .	24
1.7.1 Chapter 2: Orbital effect of magnetic field on the Majorana phase diagram . . . . .	25
1.7.2 Chapter 3: Supercurrent Interference in Few-Mode Nanowire Josephson Junctions . . . . .	25
1.7.3 Chapter 4: Spin-Orbit Protection of Induced Superconductivity in Majorana Nanowires . . . . .	25
1.7.4 Chapter 5: Robustness of Majorana bound states in the short-junction limit . . . . .	26
1.7.5 Chapter 6: Enhanced proximity effect in zigzag-shaped Majorana Josephson junctions . . . . .	26

1.7.6	Chapter 7: <i>Adaptive</i> : parallel active learning of mathematical functions . . . . .	26
	References . . . . .	27
<b>2</b>	<b>Orbital effect of magnetic field on the Majorana phase diagram</b>	<b>33</b>
2.1	Introduction . . . . .	34
2.2	Model . . . . .	34
2.3	Symmetry analysis . . . . .	35
2.4	Calculating the topological phase diagram . . . . .	36
2.5	Results . . . . .	38
2.6	Discussion and Conclusions . . . . .	41
	References . . . . .	44
<b>3</b>	<b>Supercurrent interference in few-mode nanowire Josephson junctions</b>	<b>47</b>
3.1	Introduction . . . . .	48
3.2	Experimental setup . . . . .	48
3.3	Supercurrent measurements as a function of magnetic field . . . . .	49
3.4	Possible mechanisms causing supercurrent oscillations . . . . .	50
3.5	Supercurrent evolution with magnetic field and gate potential . . . . .	51
3.6	Theoretical model. . . . .	51
3.7	Discussion . . . . .	53
3.8	Conclusions. . . . .	54
3.9	Appendix . . . . .	55
3.9.1	Zero field gate dependence . . . . .	55
3.9.2	Shapiro step measurements . . . . .	56
3.9.3	Angle dependence of fluctuations . . . . .	58
3.9.4	Zero bias peaks due to supercurrent can onset at finite magnetic field . . . . .	59
3.9.5	Extracting switching current from experimental data . . . . .	61
3.9.6	Details of the modeling . . . . .	61
3.9.7	Detailed theoretical estimates . . . . .	61
3.9.8	Current phase relations and Josephson energies . . . . .	64
3.9.9	Effect of disorder. . . . .	66
3.9.10	Rotating magnetic field . . . . .	66
	References . . . . .	67
<b>4</b>	<b>Spin-orbit protection of induced SC in Majorana nanowires</b>	<b>73</b>
4.1	Introduction . . . . .	74
4.2	Device characterization. . . . .	74
4.3	Spin-orbit protection of superconductivity . . . . .	76
4.4	Interpretation of the anisotropy. . . . .	76
4.5	Orientation of the spin-orbit field. . . . .	80
4.6	Conclusions. . . . .	81
4.7	Appendix . . . . .	82
4.7.1	Supplemental Experimental Details . . . . .	82
4.7.2	Supplemental Theoretical Details . . . . .	82
4.7.3	Extraction of SOI strength . . . . .	83
4.7.4	Supplemental Experimental Data . . . . .	88

References . . . . .	88
<b>5 Robustness of Majorana bound states in the short-junction limit</b>	<b>97</b>
5.1 Introduction . . . . .	98
5.2 Scattering matrix formalism and the short-junction limit . . . . .	99
5.3 Scaling arguments for the MBS properties in the short-junction limit. . . . .	101
5.4 Model. . . . .	103
5.4.1 General solution . . . . .	103
5.4.2 Typical physical parameters of the heterostructure . . . . .	107
5.4.3 Modeling the NS interface . . . . .	107
5.4.4 Comparison with tight-binding dispersion simulations . . . . .	108
5.5 Analysis of the topological phase diagram . . . . .	109
5.5.1 Phases boundaries and the spectral gap . . . . .	109
5.5.2 Decay length of MBS. . . . .	111
5.6 Spectrum of finite length junctions . . . . .	113
5.7 Orbital field effect in thin shell approximation . . . . .	114
5.8 Numerical study of a three-dimensional nanowire . . . . .	117
5.9 Conclusions and outlook . . . . .	118
5.10 Appendix . . . . .	119
5.10.1 Interface transparency in a two-dimensional junction. . . . .	119
5.10.2 Independence of critical magnetic field on the superconducting gap	121
References . . . . .	121
<b>6 Enhanced proximity effect in zigzag-shaped Majorana JJ</b>	<b>127</b>
6.1 Introduction . . . . .	128
6.2 Setup . . . . .	128
6.3 Band structures . . . . .	130
6.4 Localization lengths and shape effects . . . . .	132
6.5 Topological phase diagram . . . . .	134
6.6 Discussion and Conclusions . . . . .	134
6.7 Appendix . . . . .	135
6.7.1 Zigzag device with a single superconductor . . . . .	135
6.7.2 Direction of the magnetic field. . . . .	135
6.7.3 Interface transparency vs. path length cut-off . . . . .	138
References . . . . .	138
<b>7 Adaptive: parallel active learning of mathematical functions</b>	<b>141</b>
7.1 Introduction . . . . .	142
7.2 Review of adaptive sampling . . . . .	145
7.3 Design constraints and the general algorithm. . . . .	146
7.4 Loss function design . . . . .	150
7.5 Examples . . . . .	150
7.5.1 Line simplification loss . . . . .	150
7.5.2 A parallelizable adaptive integration algorithm based on cquad . . . . .	151
7.5.3 Isoline and isosurface sampling . . . . .	152

---

7.6 Implementation and benchmarks. . . . .	152
7.7 Possible extensions . . . . .	155
References . . . . .	156
<b>Curriculum Vitæ</b>	<b>159</b>
<b>List of Publications</b>	<b>161</b>

# SUMMARY

By exploiting quantum mechanics, quantum computers are able to solve problems—for example in quantum chemistry—that are far out of reach of classical computers. Conventional approaches to quantum computers use qubits (quantum bits) that can either be made out of superconducting circuits (the currently leading approach used to demonstrate quantum supremacy), store quantum information in the state of single electrons, or in several other ways. However, all these designs share the same limitation: noise easily spoils the quantum states and therefore makes quantum error correction necessary. A fundamentally different approach is to use exotic particles: Majorana bound states, or simply Majoranas. These particles do not exist in nature but were predicted to exist in engineered devices. Majorana bound states offer the advantage of being resilient against small energy fluctuations or noise due to being protected by the system's fundamental symmetry.

There is an active search across many groups worldwide trying different pathways to experimentally create and detect these particles. One promising approach to create Majoranas relies on a theoretical prediction that a one-dimensional nanowire combining superconductivity, spin-orbit coupling, a tunable chemical potential, and a magnetic field should support Majoranas. Whenever the device parameters are in the right regime, the Majoranas should appear at the edges of the nanowire.

The experimental results diverge from the predictions made by the minimal theoretical model due to it missing several physical phenomena. To model the Majorana nanowires more realistically, we include previously neglected physical effects by considering the full three-dimensional geometry of the nanowire. These more complex models exceed the reach of analytical theories and require intensive numerical calculations instead. To cope with the increasing computational complexity, we develop adaptive parallel sampling algorithms (discussed in the Ch. 7), which in our research typically speeds up simulations by at least an order of magnitude. Our approach is illustrated on the cover of this thesis, which shows the conductance of a Majorana nanowire with the interesting regions sampled more accurately. The improved models and efficient sampling, allow us to unveil potential challenges that were not present in the simple model.

In Ch. 2, we study how the electrons are influenced by the magnetic field while moving across the nanowire—an effect completely neglected in the minimal model. We observe that this effect has a stronger impact on the Majoranas than what is included in the minimal model. Specifically, we observe that the protection of the Majoranas nearly vanishes when the electron density in the nanowire is high, and find that the magnetic field has to be precisely aligned with the nanowire to guarantee the presence of Majoranas.

Bringing two Majorana-carrying nanowires in contact and allowing a supercurrent flow between them is required for making a Majorana qubit. In Ch. 3, we apply our numerical model to analyze experimentally observed behavior of these nanowire junctions.

While our results agree with the experimental observations, we observe that the supercurrent decreases by an order of magnitude when Majoranas appear. This suppression poses a new challenge in creating a Majorana qubit.

Our findings may seem like bad news for the creation of Majoranas—unexpected pitfalls overlooked by the simplified models. The detailed simulations, however, bring new opportunities as well. Not being constrained to analyzing the devices that are easy to solve, we are able to design a new *zigzag* device geometry, that improves the robustness of Majoranas by an order of magnitude. In Ch. 6, we show that using a zigzag device geometry (instead of a straight nanowire) eliminates the long electron trajectories that are responsible for the degradation of the Majorana properties. In addition to the improved robustness of the Majoranas, this new zigzag geometry is insensitive to the geometric details and device tuning. This proposal is now the topic of active experimental investigations by several groups.

# SAMENVATTING

Door gebruik te maken van kwantummechanica, kunnen kwantumcomputers problemen oplossen—bijvoorbeeld in de kwantumchemie—die ver buiten het bereik van klassieke computers liggen. Conventioneel gebruiken kwantumcomputers qubits (quantumbits) die ofwel gemaakt kunnen worden van supergeleidende circuits (de momenteel leidende aanpak en gebruikt om kwantum suprematie aan te tonen), of van enkele elektronen waarin de kwantuminformatie in hun toestand wordt opgeslagen, of op diverse andere manieren. Al deze ontwerpen hebben echter dezelfde beperking: ruis kan de kwantumtoestanden gemakkelijk vernietigen en daardoor is kwantum error correctie noodzakelijk. Een fundamenteel andere aanpak is het gebruik van exotische deeltjes: gebonden Majoranatoestanden of gewoon Majorana's. Deze deeltjes bestaan niet in de natuur, maar het is voorspeld dat ze kunnen bestaan in artificieel gemaakte apparaten. Majorana's bieden het voordeel dat ze bestand zijn tegen kleine energiefluctuaties of ruis, omdat ze beschermd zijn door de fundamentele symmetrie van het systeem.

Wereldwijd wordt er in veel groepen actief gezocht naar verschillende manieren om deze deeltjes experimenteel te creëren en te detecteren. Een veelbelovende aanpak om Majorana's te creëren, is gebaseerd op een theoretische voorspelling dat een eendimensionale nanodraad die supergeleiding, spin-baankoppeling, een regelbare chemische potentiaal, en een magnetisch veld combineert, Majorana's zou moeten kunnen bevatten. Als de parameters in het juiste regime zijn, zouden de Majorana's aan de uiteinden van de nanodraad moeten verschijnen.

De experimentele resultaten wijken echter af van de voorspellingen van het minimale theoretische model omdat het verschillende fysische verschijnselen mist. Om de Majorana-nanodraden realistischer te modelleren, nemen we eerder verwaarloosde fysische effecten mee door de volledige driedimensionale geometrie van de nanodraad te beschouwen. Deze complexere modellen gaan het bereik van analytische theorieën te boven en vereisen in plaats daarvan intensieve numerieke berekeningen. Om met de toenemende computationele complexiteit om te gaan, ontwikkelen we adaptieve parallelle bemonsteringsalgoritmen (besproken in hoofdstuk 7), die in ons onderzoek de simulaties typisch versnellen met ten minste een orde van grootte. Onze aanpak wordt geïllustreerd op de cover van dit proefschrift. Dit laat de geleiding door een Majorana-nanodraad zien, waar de interessante regio's nauwkeuriger zijn bemonsterd. De verbeterde modellen en efficiëntere bemonstering, stellen ons in staat om potentiële uitdagingen te onthullen die niet aanwezig waren in het eenvoudige model.

In hoofdstuk 2 bestuderen we hoe de elektronen beïnvloed worden door het magnetisch veld als ze loodrecht op de nanodraad bewegen—een effect dat volledig verwaarloosd wordt in het minimale model. We zien dat dit effect een grotere impact heeft op de Majorana's dan dat wat er in het minimale model wordt beschouwd. Daarbij zien we dat de bescherming van de Majorana's vrijwel verdwijnt als de elektronendichtheid in de nanodraad hoog is en ontdekken we dat het magnetisch veld exact uitgelijnd moet worden

met de richting van de nanodraad, om de aanwezigheid van Majorana's te garanderen.

Het in contact brengen van twee Majorana-bevattende nanodraden en het toestaan van een superstroom daartussen, is een vereiste voor het maken van een Majorana-qubit. In hoofdstuk 3 passen we ons numerieke model toe om het experimenteel waargenomen gedrag van deze nanodraadjuncties te analyseren. Hoewel onze resultaten overeenkomen met de experimentele waarnemingen, zien we dat de superstroom met een orde van grootte afneemt wanneer Majorana's verschijnen. Deze onderdrukking van de superstroom vormt een nieuwe uitdaging voor het maken van een Majorana-qubit.

Onze bevindingen lijken misschien slecht nieuws voor de creatie van Majorana's—onverwachte valkuilen die niet voortkomen uit vereenvoudigde modellen. De gedetailleerde simulaties bieden echter ook nieuwe kansen. Omdat we ons niet beperken tot het analyseren van de apparaten die gemakkelijk te bestuderen zijn, zijn we in staat om een nieuwe *zigzag*-apparaatgeometrie te ontwerpen, die de robuustheid van Majorana's met een orde van grootte verbetert. In hoofdstuk 6 laten we zien dat het gebruik van een *zigzag*-apparaatgeometrie (in plaats van een rechte nanodraad) de lange elektrodenpaden elimineert, die verantwoordelijk zijn voor de verslechtering van de Majorana-eigenschappen. Naast de verbeterde robuustheid van de Majorana's, is deze nieuwe *zigzag*-geometrie ongevoelig voor de geometrische details en de precieze afstellingen van het apparaat. Ons voorstel wordt nu actief onderzocht door verschillende experimentele groepen wereldwijd.

# 1

## INTRODUCTION

### 1.1. PREFACE

All matter consists of atoms, yet it can appear in various forms and have various properties. Some familiar examples of these different forms are solids, gases, and liquids; however, more exotic forms exist, such as superfluids, magnets, plasmas, and Bose-Einstein condensates. These different forms of matter are called phases or states of matter. The various properties of a material depend on its phase (the way atoms structure itself in that material).

By studying the symmetries of the organization of atoms, we can understand how many of these different phases arise. Symmetry-breaking theory explains, that if the phase of a material changes (called a phase transition), such a symmetry changes. For example, in a liquid, the atoms are randomly distributed. A liquid remains a liquid when moving the atoms by any arbitrary distance. This property indicates that a liquid has a continuous translation symmetry. When a phase transition occurs, the liquid turns into a crystal (e.g. water to ice) and its atoms organize into a lattice. Only when moving the atoms by an integer number of the lattice constant (the distance between the smallest repeating pattern), the crystal stays the same. This property indicates that a crystal has a discrete translation symmetry. The reduction of the liquid's continuous translation symmetry to the crystal's discrete symmetry is an example of symmetry breaking. Another example is ferromagnets, where above a certain critical temperature  $T_c$  the spins of electrons are pointed in a random direction. This property indicates a continuous rotational symmetry. However, when  $T < T_c$  the spins align, which—like the previous example—reduces the continuous translation symmetry to a discrete rotational symmetry.

This symmetry-breaking theory was introduced by Lev Landau in 1937 [1]. It was long believed that it explains all phases in materials and all (continuous) phase transitions. In 1987, in an attempt to describe high  $T_c$  superconductors, the chiral spin state was introduced [2]. However, it was soon realized that the symmetry breaking description was not sufficient to explain its phase. A new kind of phase called a “topological phase” was introduced [3, 4]. It is a zero-temperature phase of matter (i.e. quantum matter)

that is described by a robust ground state degeneracy. This degenerate ground state has quantized non-Abelian geometric phases; we discuss what this means in Sec. 1.3.

The quantum Hall effect is an example of a state that cannot be described by its symmetries alone. Instead, it can be characterized by a distinct topology (see Fig. 1.1) [5]. Its signature—shown in Fig. 1.2—is robust and does not depend on the specific geometry and does not vanish upon smooth changes in the material’s parameters. Its signature is an exact quantization of the Hall conductance of an integer number of  $e^2/h$ , where  $e$  is the elementary charge, and  $h$  is the Planck constant, both fundamental constants. Because of its robustness—it is insensitive to specific experimental settings and purity of the material used—the quantum Hall effect is used to determine the standard for electrical resistance [6]. The effect appears upon applying a large perpendicular magnetic field  $B_{\perp}$  to a two-dimensional electron gas at low temperatures. This opens a gap between the energy bands and localizes the electrons in the bulk. Classically, we can visualize what happens (see Fig. 1.3), as electrons localizing in small cyclotron orbits; this leaves the electrons near the edges of the material to bounce along the edges [7]. These states that propagate along the edges are responsible for the conduction and are called “edge states.”

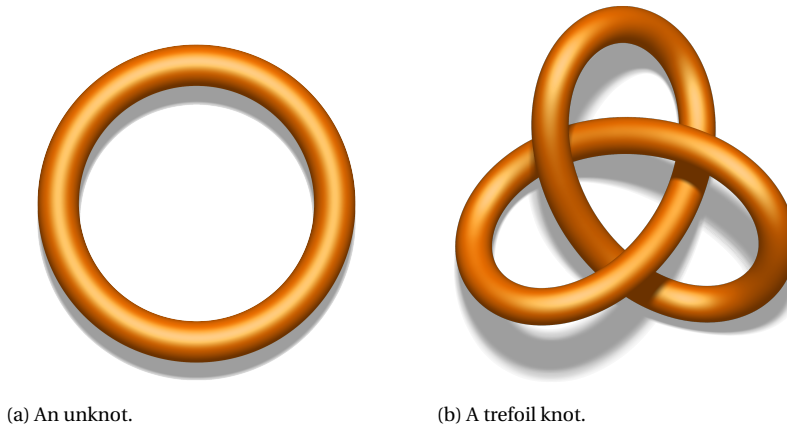


Figure 1.1: Topology in mathematics studies the properties of an object that are preserved under continuous deformations. For example, because an unknot (a) cannot be continuously transformed into a trefoil knot (b) without cutting it: they are not topologically equivalent. The object that is studied in condensed matter physics, is the Hamiltonian. Two Hamiltonians are topologically equivalent whenever an Hamiltonian can be continuously transformed into another Hamiltonian. Unlike a knot that can be visualized in space, the topology of the quantum Hall state manifests itself in momentum space. Images adapted from [8, 9].

The field of topology in condensed matter has substantially grown over the past decades. Recently, in 2016, the Nobel prize was awarded to Thouless, Haldane, and Kosterlitz for the theoretical findings of topological states. One of these new states are “topological insulators,” which also exhibit edge or surface states and have similarities to the quantum Hall effect, but do not require extreme conditions such as the large magnetic field [7, 10–13]. Here, spin-orbit coupling replaces the effect of the magnetic field (see Fig. 1.3). This is a coupling between the electron’s momentum and spin, effectively

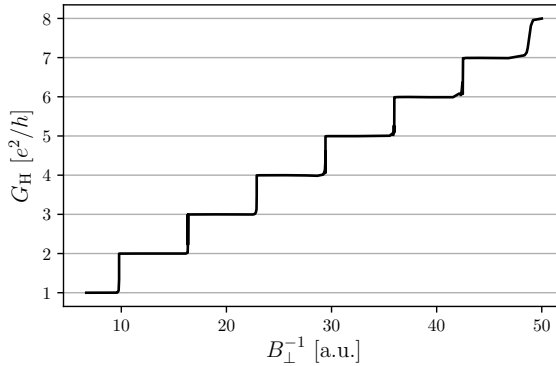


Figure 1.2: The integer quantum Hall effect. The Hall conductance  $G_H$  (reciprocal of the Hall resistance  $R_H$ ) of a simulated two-dimensional electron gas as a function of the perpendicular magnetic field  $B_\perp$  at 0 K. It displays a stairlike quantized sequence of Hall conductances equal to  $ne^2/h$ , where  $n$  is an integer characterizing each plateau.

causing a momentum dependent magnetic field for electrons that move through a crystal lattice. The spin-orbit coupling effect is discussed in more detail in Sec. 1.4.1. Due to the absence of a magnetic field (which breaks time-reversal symmetry in the quantum Hall effect), the edge states always come in counter-propagating pairs, shown in Fig. 1.3.

Besides the exciting new fundamental physical insights into topological materials, topological states might be used to design novel quantum devices. One of the most exciting applications of topological states, is to use them to build a topological quantum computer by exploiting their non-Abelian properties. It is predicted that a quantum computer is much faster than a classical systems computer in performing certain tasks. For example, the simulation of quantum systems [14] and prime factorization [15]. The fundamental building block of the quantum computer is the qubit (or quantum bit), which is the quantum equivalent of the classical transistor. Because these qubits store quantum information, they are extremely fragile, and even a small interaction with its environment can destroy its state, which results in computational errors. Physicists experiment with different approaches to create a qubit; for example, there are proposals (and some realizations of) qubits based on quantum optics [16], ultracold atoms [17], spin-based systems [18], and superconducting systems [19]. In general, one of the most significant problems is to limit and correct the computational errors, and therefore a large fraction of the research is focussed on error-correction [20]. Here, the advantage of using topological states becomes apparent because the topological qubit naturally protects its state against small perturbations in the environment [21].

The zero-energy Majorana bound state (MBS) is the simplest non-Abelian excitation. The MBS was first proposed to exist as quasiparticle excitations of the  $\nu = 5/2$  quantum Hall effect [22, 23], which requires a high material quality and very low temperatures. Other early proposals [24–26] rely on rare and exotic  $p$ -wave superconductors and are extremely challenging to realize experimentally. In 2008, Fu and Kane suggested a new approach to create MBSs by using a hybrid structure of an ordinary  $s$ -wave superconductor

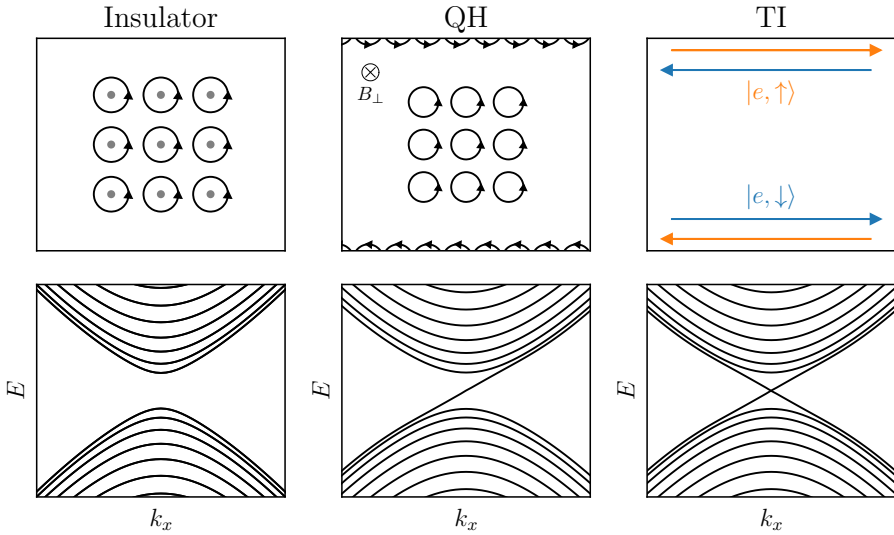


Figure 1.3: Comparison of schematic representations (top) and band structures (bottom) of a normal insulator (left), quantum Hall effect (middle), and a topological insulator (right). Classically, the electrons in an insulator (left) are localized around the cores of the ions and therefore cannot flow freely to create a current. From its band structure (bottom), we observe that at the Fermi level there are no electronic states available that can contribute to a current through the material. In the quantum Hall regime (middle), the strong perpendicular magnetic field localizes the electrons in the bulk in cyclotron orbits, while the states at the boundary scatter along the edges. The localized orbitals open an energy gap in the band structure, with the conducting gapless edge states remaining due to the unique topology of the system. The topological insulator (right) is similar to the quantum Hall state, however, it has two conducting edge channels of opposite spin.

coupled to a topological insulator to create a state that resembles a spinless  $p$ -wave superconductor [27]. Inspired by this hybrid approach, in 2010, two works [28, 29] suggested using a simpler one-dimensional nanowire system coupled to a  $s$ -wave superconductor. This simple model combines spin-orbit coupling, superconductivity, electrostatic tunability, and an applied magnetic field. When tuned into the right parameter regime, this system hosts MBSs at the edges of the nanowire. Since its introduction, many experiments have detected signatures of MBSs [30–35]; however, none have demonstrated the presence of MBSs with absolute certainty by showing its non-Abelian statistics. Because of the simplicity of the model, it can be solved analytically; however, it neglects many physical phenomena that are crucial for understanding the properties of the MBSs.

In this thesis, we study extensions to this model and go beyond the regime that can be studied analytically. The next sections introduce superconductivity and the topological protection of Majoranas (Sec. 1.2), non-Abelian statistics (Sec. 1.3), the minimal hybrid Majorana model (Sec. 1.4), and finally, a few extensions to this model (Sec. 1.5). At that point, it should be evident that solving this problem requires numerical methods, which is the topic of Sec. 1.6.

## 1.2. TOPOLOGICAL PROTECTION OF MAJORANAS

To understand the topological protection of Majorana bound states we first discuss superconductivity. This is a set of properties of certain materials that appear when they are cooled below a characteristic critical temperature  $T_c$ . Upon reaching this temperature, the material goes through a phase transition and it becomes superconducting. The characteristic properties of superconducting materials are their vanishing electrical resistance and expulsion of magnetic fluxes. While discovered in 1911, a good understanding of “conventional” superconductivity was only reached more than four decades later through the phenomenological Ginzburg-Landau theory and the microscopic BCS theory. A lot of today’s research focuses on exotic superconductors, high  $T_c$  superconductors, and hybrid structures that consist of a superconductor and another material. In this thesis, we study such hybrid structures.

### 1.2.1. BCS THEORY AND THE MEAN-FIELD APPROXIMATION

BCS theory describes superconductivity as a microscopic effect. It assumes that two electrons form a Cooper pair of two electrons, where the electrons effectively attract due to electron-phonon coupling [36–38]. It postulates that superconductivity is caused by a condensation of these Cooper pairs at the Fermi energy<sup>1</sup>  $E_F$  into a boson-like state, a Bose Einstein condensate. The model Hamiltonian in the language of second quantization [39] is

$$\mathcal{H}_{\text{BCS}} = \sum_{\mathbf{k}\sigma} \epsilon_{\mathbf{k}} c_{\mathbf{k}\sigma}^\dagger c_{\mathbf{k}\sigma} + \sum_{\mathbf{k}\mathbf{l}} V_{\mathbf{k}\mathbf{l}} c_{\mathbf{k}\uparrow}^\dagger c_{-\mathbf{k}\downarrow}^\dagger c_{-\mathbf{l}\downarrow} c_{\mathbf{l}\uparrow}, \quad (1.1)$$

where  $c$  is the annihilation operator,  $c^\dagger$  the creation operator,  $\mu$  the chemical potential,  $m$  the mass, and  $\epsilon_{\mathbf{k}} \equiv E_{\mathbf{k}} - \mu$ , where  $E_{\mathbf{k}}$  is the kinetic energy ( $\frac{\hbar^2 k^2}{2m}$ ). The  $s$ -wave symmetry interaction potential  $V_{\mathbf{k}\mathbf{l}}$  includes only the Cooper pairs consisting of two electrons with opposite spin and opposite momentum  $\mathbf{k}$ :  $\mathbf{k} \uparrow, -\mathbf{k} \downarrow$ . Finding the ground state of many interacting electrons is a major problem not only in condensed matter physics, but also in quantum chemistry, molecular biology, and many other fields. The BCS Hamiltonian approximates the Coulomb interaction in momentum space, however, it is still fundamentally difficult to solve; therefore, we have to make an approximation.

The mean-field approximation is a classic approximation scheme that describes the behavior of conventional superconductors remarkably well. To use it, we define the quantity

$$b_{\mathbf{k}} = \langle c_{\mathbf{k}\uparrow} c_{-\mathbf{k}\downarrow} \rangle, \quad (1.2)$$

which in turn we use to define the so-called gap energy

$$\Delta_{\mathbf{k}} = - \sum_{\mathbf{k}'} V_{\mathbf{k}\mathbf{k}'} b_{\mathbf{k}'}. \quad (1.3)$$

We write the last term in Eq. (1.1) as

$$c_{\mathbf{k}\uparrow}^\dagger c_{-\mathbf{k}\downarrow}^\dagger c_{-\mathbf{l}\downarrow} c_{\mathbf{l}\uparrow} = \left( c_{\mathbf{k}\uparrow}^\dagger c_{-\mathbf{k}\downarrow}^\dagger - b_{\mathbf{k}}^\dagger + b_{\mathbf{k}}^\dagger \right) (c_{-\mathbf{l}\downarrow} c_{\mathbf{l}\uparrow} - b_{\mathbf{l}} + b_{\mathbf{l}}), \quad (1.4)$$

<sup>1</sup>We assume zero temperature ( $T = 0$ ), so  $E_F = \mu$ , where  $\mu$  is the chemical potential.

and expand the products. We neglect the second-order fluctuation term

$$\left( c_{\mathbf{k}\uparrow}^\dagger c_{-\mathbf{k}\downarrow}^\dagger - b_{\mathbf{k}}^\dagger \right) (c_{-\mathbf{l}\downarrow} c_{\mathbf{l}\uparrow} - b_{\mathbf{k}}) \quad (1.5)$$

in Eq. (1.4) and rewrite Eq. (1.1) to

$$\mathcal{H}_{\text{BCSMF}} = \sum_{\mathbf{k}, \sigma} \epsilon_{\mathbf{k}} c_{\mathbf{k}\sigma}^\dagger c_{\mathbf{k}\sigma} - \sum_{\mathbf{k}} \left( \Delta_{\mathbf{k}} c_{\mathbf{k}\uparrow}^\dagger c_{-\mathbf{k}\downarrow}^\dagger + \Delta_{\mathbf{k}}^* c_{-\mathbf{k}\downarrow} c_{\mathbf{k}\uparrow} - \Delta_{\mathbf{k}} b_{\mathbf{k}}^* \right), \quad (1.6)$$

where the last term is a constant that can be neglected. We now introduce Nambu spinors

$$\Psi_{\mathbf{k}} = \begin{pmatrix} c_{\mathbf{k}\uparrow} \\ c_{-\mathbf{k}\downarrow}^\dagger \end{pmatrix}, \quad (1.7)$$

and write Eq. (1.6) matrix form

$$\mathcal{H}_{\text{BCSMF}} = \sum_{\mathbf{k}} \Psi_{\mathbf{k}}^\dagger \underbrace{\begin{pmatrix} \epsilon_{\mathbf{k}} & \Delta \\ \Delta_{\mathbf{k}}^* & -\epsilon_{\mathbf{k}} \end{pmatrix}}_{H_{\text{BdG}}} \Psi_{\mathbf{k}}. \quad (1.8)$$

To calculate the energy spectrum, we can diagonalize the Bogoliubov-de Gennes Hamiltonian  $H_{\text{BdG}}$ . Alternatively, we can square  $H_{\text{BdG}}$  which gives a diagonal matrix

$$H_{\text{BdG}}^2 = \begin{pmatrix} \epsilon_{\mathbf{k}}^2 + |\Delta|^2 & 0 \\ 0 & \epsilon_{\mathbf{k}}^2 + |\Delta|^2 \end{pmatrix}, \quad (1.9)$$

where the eigenvalues are the square root of the eigenvalues of  $H_{\text{BdG}}$ . This immediately result in the spectrum

$$E = \pm \sqrt{\epsilon_{\mathbf{k}}^2 + |\Delta|^2}. \quad (1.10)$$

The Bogoliubov-de Gennes Hamiltonian acts on the Nambu spinors [Eq. (1.7)]. These have annihilation operators of electrons (first half) and creations operators of the same electrons (second half). To go to a single-particle description (first quantization), we can view the latter creation operators as annihilation operators of an extra set of holes. In this way, we essentially double the number of degrees of freedom in the system. Besides the usual Pauli matrices that act on spin degree of freedom ( $\sigma_i$  where  $i \in x, y, z$ ), we introduce  $\tau_i$  to act on the electron-hole degree of freedom. The Hamiltonian becomes a  $4 \times 4$  matrix<sup>2</sup>

$$H_{\text{BdG}} = \epsilon_{\mathbf{k}} \tau_z \otimes \sigma_0 + \Delta \tau_x \otimes \sigma_0 = \begin{pmatrix} \epsilon_{\mathbf{k}} & 0 & \Delta & 0 \\ 0 & \epsilon_{\mathbf{k}} & 0 & \Delta \\ \Delta & 0 & -\epsilon_{\mathbf{k}} & 0 \\ 0 & \Delta & 0 & -\epsilon_{\mathbf{k}} \end{pmatrix}, \quad (1.11)$$

which acts on the wavefunction

$$\Psi = (\psi_{e\uparrow}, \psi_{e\downarrow}, \psi_{h\downarrow}, -\psi_{h\uparrow})^T, \quad (1.12)$$

where  $\psi_e, \psi_h$  are the electron and hole components of the wave function, and  $\psi_{\uparrow}, \psi_{\downarrow}$  are the spin-up and spin-down states. Due to the holes being related to the electrons, the Hamiltonian  $H_{\text{BdG}}$  has a particle-hole symmetry. A symmetry, or combination of symmetries, determines a material's specific topology. Symmetry and the topology that results from it, is the topic of the next section.

<sup>2</sup>Here  $\otimes$  denotes the Kronecker product and we usually omit  $\sigma_0$  and  $\tau_0$ .

### 1.2.2. TOPOLOGY AND SYMMETRY

Symmetry plays a fundamental part in physics. In condensed matter systems, only three discrete symmetries are important: time-reversal symmetry  $\mathcal{T}$ , particle-hole symmetry  $\mathcal{P}$ , and chiral symmetry  $\mathcal{C}$ . Wigner's theorem states that a symmetry must either be a unitary or an anti-unitary operator [40]. Both  $\mathcal{T}$  and  $\mathcal{P}$  have anti-unitary operators and may square either to  $+1$  or  $-1$  depending on the specifics of the system. Chiral symmetries have a unitary operator and always square to  $+1$ . The combination of these three symmetries form ten symmetry classes [41]. Each class is characterized by the absence or presence of these symmetries, and together with the dimensionality of a system determines the specific topological invariant it has. Topology studies whether objects can be continuously transformed into each other. The object that is studied in condensed matter physics is the Hamiltonian of a system. If two Hamiltonians can be continuously transformed<sup>3</sup> into each other without changing the topological invariant, the systems are "topologically equivalent." How a topological invariant changes, varies for the different symmetry classes.

We ended Sec. 1.2.1 by noting that  $H_{\text{BdG}}$  [Eq. (1.11)] has a particle-hole symmetry which is of the form  $\mathcal{P} = -i\sigma_y\tau_y\mathcal{K}$ , where  $\mathcal{K}$  is the complex conjugation operator. This Hamiltonian acts on a two-component (neglecting spin) wave function  $\psi_{\text{BdG}} = (\psi_e, \psi_h)^T$ . The symmetry of this Hamiltonian is most obvious in its dispersion relation, where each eigenstate  $\psi_E = (\psi_{e,0}, \psi_{h,0})^T$  has a particle-hole symmetric partner at  $\psi_{-E} = \mathcal{P}(\psi_{e,0}, \psi_{h,0})^T = (-\psi_{h,0}^*, \psi_{e,0}^*)^T$ . In constructing  $H_{\text{BdG}}$ , we artificially doubled the degrees of freedom by considering electrons and holes separately. Therefore, the creation operator  $c^\dagger$  of the quasiparticle in the  $\psi_E$  state is equal to the annihilation operator  $c$  of the quasiparticle in the  $\psi_{-E}$  state. From this, it is clear that  $\psi_E$  and  $\psi_{-E}$  correspond to the same quasiparticle. In a one or higher dimensional system, the operator  $\mathcal{P}$  will not only send  $E \rightarrow -E$  but will also send the momentum  $k \rightarrow -k$  as

$$\mathcal{P}^\dagger H(k) \mathcal{P} = -H^*(-k). \quad (1.13)$$

At zero energy, something curious happens: here we have a state  $\psi_0$  that upon applying  $\mathcal{P}$  is transforms into itself  $\mathcal{P}\psi_0 = \psi_0$ . This state has a creation operator  $\gamma^\dagger$  that is identical to the annihilation operator  $\gamma$  of itself, so  $\gamma^\dagger = \gamma$ . We call this property the Majorana condition. If we use the Majorana condition in the fermionic commutation relation

$$\gamma^\dagger\gamma + \gamma\gamma^\dagger = 1, \quad (1.14)$$

we get  $\gamma^\dagger\gamma = 1/2$  and see that the Majorana state is always half occupied. Removing a Majorana from zero energy is, therefore, only possible if it is paired with another Majorana to form a fermionic mode. Later, in Sec. 1.3 we make use of this property and show how these Majoranas exhibit non-Abelian statistics. Subsequently, in Sec. 1.4, we show that it is possible to create Majoranas at two opposite edges of a nanowire where they do not couple and are pinned to  $E = 0$ ; this provides the so-called topological protection. Here, the fermionic mode (which is occupied or unoccupied,) is the quantity that is protected.

<sup>3</sup>An example of a continuous transformation from  $H_1$  to  $H_2$ :  $H = \alpha H_1 + (1 - \alpha)H_2$  where  $\alpha = 0 \rightarrow 1$ .

The symmetry class of the one-dimensional system we study in this thesis has a particle-hole symmetry  $\mathcal{P}$ , and therefore belongs to class  $\mathcal{D}$ . This class has a  $\mathcal{Z}_2$  topological invariant  $Q$  that is the sign of the Pfaffian of the Hamiltonian:  $Q = \text{sgn Pf}(H)$ . This invariant can only assume two values (+1 or -1) and indicates the presence or absence of Majoranas.<sup>4</sup> This topological invariant is only defined for a system with an energy gap, which means the Hamiltonian of the system has no eigenvalues in a finite interval around zero energy, as in Eq. 1.11. If we can continuously transform a Hamiltonian  $H_1$  into another Hamiltonian  $H_2$  without ever closing the energy gap, we say  $H_1$  and  $H_2$  are topologically equivalent, and thus have the same topological invariant.

### 1.3. NON-ABELIAN STATISTICS AND BRAIDING

For many researchers, the ultimate motivation to study Majoranas is because of their fascinating property: non-Abelian quantum statistics. Quantum statistic studies what happens to wavefunctions describing identical particles when their positions are exchanged in space. In introductory quantum mechanics courses, we learn that particles are divided into two classes according to quantum statistics: bosons which stay the same under the exchange and fermions for which the wavefunction changes sign. However, Majorana bound states do not belong to either of these classes. Instead, they are non-Abelian anyons. The operation of exchanging two Majoranas (called braiding) can send the system into a different state with the same particle configuration. Explaining how to experimentally perform a braiding operation is beyond the scope of this thesis; therefore, we will focus on the mathematical operations that describe such a braiding process.

In one dimension, exchanging two Majoranas is ill-defined because it is impossible to swap them without colliding and consequently annihilating them. It is possible to construct a network of nanowires to form T-junctions (see Fig. 1.4), which allows to exchange the positions of Majoranas. Here, one can temporarily move a Majorana to the unoccupied wire section and perform the exchange without the Majoranas ever becoming too close to each other. The only thing distinguishing the Majoranas is their position. That means that after exchanging two Majoranas in space, the system looks identical to the way it looked before the exchange. We now assume the energy spectrum is gapped for  $|E| < \Delta$  with the Majorana ground state at  $E = 0$ . If this ground state contains several Majoranas, all at zero energy, they form a “ground state manifold.”

From now on, we only consider the states corresponding to the Majoranas and neglect the states that live in the bulk ( $E \geq \Delta$ ). As mentioned in Sec.1.2.2, a Majorana only has half a degree of freedom, and thus, they can only be assigned quantum states in pairs. In Fig. 1.4 we see six Majoranas (3 pairs), but for generality lets consider  $N$  pairs. By pairing two Majoranas (two times half a degree of freedom), we form fermionic modes that give two possible degenerate quantum states, either unoccupied  $|0\rangle$  or occupied  $|1\rangle$ . By pairing up neighboring Majoranas  $\gamma_{2n-1}$  and  $\gamma_{2n}$ , we get a creation operator that is its own complex conjugate  $c_n^\dagger = \frac{1}{2}(\gamma_{2n-1} + i\gamma_{2n})$ , where  $c$  is a fermionic creation operator. Each pair gives two possible quantum states, so  $N$  pairs will have  $2^N$  possible states. We can represent every state with a ket

$$|s_1, s_2, \dots, s_N\rangle, \tag{1.15}$$

<sup>4</sup>The Pfaffian for an anti-symmetric matrix is related to the determinant as  $\text{Pf}(A)^2 = \det(A)$ .

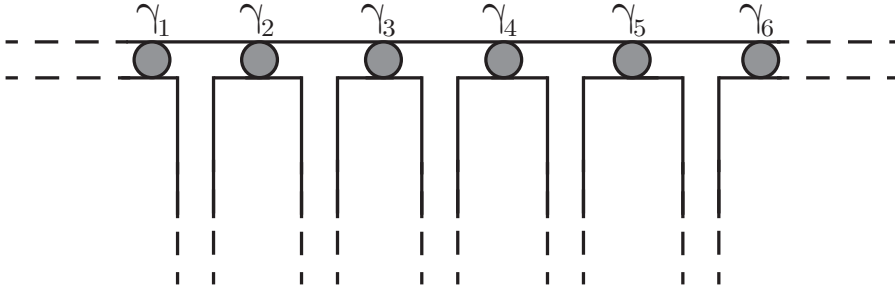


Figure 1.4: Majorana T-junction. The circles represent the Majoranas  $\gamma_1 \dots \gamma_6$ . This network of nanowires allows for the exchange of two Majoranas without having them collide. This is possible by temporarily bringing a Majorana to one of the vertical wires and then swapping the position of the other Majorana.

where  $s_n$  is either unoccupied 0 or occupied 1. These states form a complete basis of the Hilbert space.

We define the fermion parity operator

$$P_n \equiv 1 - 2c_n^\dagger c_n = i\gamma_{2n-1}\gamma_{2n}, \quad (1.16)$$

that acts on the states and where we recognize the  $c_n^\dagger c_n$  term as the number operator. All basis states in the Hilbert space of the Majoranas are eigenstates of  $P_n$ . For example, we have

$$P_1 |0, \dots\rangle = (1 - 2c_1^\dagger c_1) |0, \dots\rangle = +|0, \dots\rangle, \quad (1.17a)$$

$$P_1 |1, \dots\rangle = (1 - 2c_1^\dagger c_1) |1, \dots\rangle = -|1, \dots\rangle. \quad (1.17b)$$

Another important property of Majoranas is that a pair of Majorana operators all anti-commute with each other. So

$$(\gamma_1\gamma_2)(\gamma_3\gamma_4) = (\gamma_3\gamma_4)(\gamma_1\gamma_2), \quad (1.18)$$

however, if the pairs share a Majorana, they do not commute anymore, like

$$(\gamma_1\gamma_2)(\gamma_2\gamma_3) = -(\gamma_2\gamma_3)(\gamma_1\gamma_2). \quad (1.19)$$

Section 1.2 introduced the Hamiltonian Eq. (1.11), which does not conserve particle number; however, it conserves the parity. To calculate the total parity we multiply all parity operators

$$P_{\text{tot}} = P_1 \cdot P_2 \cdot \dots \cdot P_N = i^N \gamma_1 \gamma_2 \dots \gamma_{2N}, \quad (1.20)$$

where  $P_{\text{tot}}$  has eigenvalues  $\pm 1$ . Because the parity is Hermitian, it's observable and equivalently, can be measured experimentally.

We can now start to think about what happens when we exchange two Majoranas [42]. Our ground state manifold  $|\Psi\rangle$  never leaves the ground state if we perform the exchange slowly enough. The exchange of two Majoranas  $\gamma_n$  and  $\gamma_m$  changes the ground state

$|\Psi\rangle \rightarrow U|\Psi\rangle$  where  $U$  is a unitary operator. The exact form of  $U$  can be derived without a direct calculation. We do this by assuming that  $U$  only depends on the Majoranas involved in the exchange ( $\gamma_n$  and  $\gamma_m$ ) and by using that the slow exchange does not change the parity of the system because the system stays gapped at all times. Since the parity is conserved, we know that  $U$  commutes with the total fermion parity [ $U, P_{\text{tot}}] = 0$ , and that  $U$  can only depend on the product  $i\gamma_n\gamma_m$ . This product is Hermitian, so we can create a unitary operator by taking the exponential of  $i$  times this Hermitian operator as

$$U \equiv \exp(\beta\gamma_n\gamma_m) = \cos(\beta) + \gamma_n\gamma_m \sin(\beta), \quad (1.21)$$

where  $\beta$  is a real coefficient. In the last equality we used  $(\gamma_n\gamma_m)^2 = \gamma_n\gamma_m\gamma_n\gamma_m = -\underbrace{\gamma_n\gamma_m\gamma_m\gamma_n}_{=1} = -1$  in the Taylor expansion. We now move to the Heisenberg picture where we look at the evolution of the Majorana operators in time

$$\gamma_n \rightarrow U\gamma_nU^\dagger = (\cos\beta + \gamma_n\gamma_m \sin\beta)\gamma_n (\cos\beta + \gamma_m^\dagger\gamma_n^\dagger \sin\beta), \quad (1.22a)$$

$$= \gamma_n \cos^2\beta + (\gamma_n\gamma_m^\dagger\gamma_n^\dagger + \gamma_n\gamma_m\gamma_n) \sin\beta \cos\beta + \gamma_n\gamma_m\gamma_n\gamma_m^\dagger\gamma_n^\dagger \sin^2\beta, \quad (1.22b)$$

$$= \gamma_n \cos^2\beta - \gamma_n^\dagger \sin^2\beta - 2\gamma_m \sin\beta \cos\beta, \quad (1.22c)$$

$$= \gamma_n \cos 2\beta - \gamma_m \sin 2\beta. \quad (1.22d)$$

In a similar way, we get

$$\gamma_m \rightarrow U\gamma_mU^\dagger = \gamma_m \cos 2\beta + \gamma_n \sin 2\beta. \quad (1.23)$$

After the exchange happened we know that  $\gamma_m \rightarrow \gamma_n$  and  $\gamma_n \rightarrow \gamma_m$ , which means that  $\beta = \pm\pi/4$ . The two opposite signs distinguish the clockwise and the counterclockwise exchange of the Majoranas. We now found an operator that exchanges two Majoranas

$$U = \exp\left(\pm\frac{\pi}{4}\gamma_n\gamma_m\right) = \frac{1}{\sqrt{2}}(1 \pm \gamma_n\gamma_m). \quad (1.24)$$

As an example, we consider just four Majoranas  $\gamma_1, \gamma_2, \gamma_3,$  and  $\gamma_4$  and exchange their positions. The four basis states in the ground state manifold are

$$|00\rangle, |01\rangle, |10\rangle, |11\rangle, \quad (1.25)$$

where the first number is the occupation number of the fermionic mode  $c_1^\dagger = \frac{1}{2}(\gamma_1 + i\gamma_2)$  and the second number the occupation number of  $c_2^\dagger = \frac{1}{2}(\gamma_3 + i\gamma_4)$ . For instance, if we start from the state  $|00\rangle$  and we exchange  $\gamma_2$  and  $\gamma_3$  by applying  $U_{23} = \frac{1}{\sqrt{2}}(1 \pm \gamma_2\gamma_3)$ , we obtain

$$|00\rangle \rightarrow U_{23}|00\rangle = \frac{1}{\sqrt{2}}(|00\rangle + i|11\rangle). \quad (1.26)$$

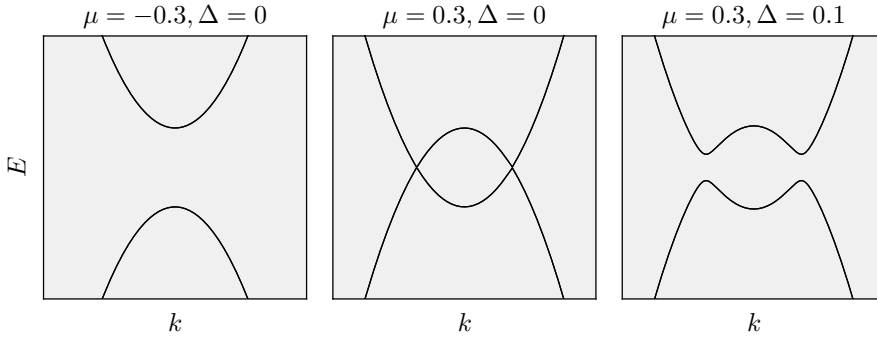


Figure 1.5: Band structures of Hamiltonians with chemical potential  $\mu = -0.3$  and superconducting gap  $\Delta = 0$  (left);  $\mu = 0.3$  and  $\Delta = 0$  (middle); and  $\mu = 0.3$  and  $\Delta = 0.1$  (right).

Here we see a superposition of states, which is not like bosons or fermions, where the exchange only changes the sign. Because of this property, Majoranas are non-Abelian anyons. As noted before, exchanging two non-Abelian anyons is called braiding. Using these braiding operations, it is possible to create a qubit that can perform a certain set (but not all) of rotations on the single-qubit Bloch sphere. This means that some of the qubit operations are topologically protected. This reduces the amount of error-correction needed in comparison with a non-topological qubit, and in turn, means that fewer physical qubits are required.

## 1.4. MAJORANAS IN A MINIMAL HYBRID NANOWIRE

The combined effect of superconductivity, spin-orbit coupling, and a Zeeman field can lead to the appearance of Majoranas near the edges of the wire [28, 29]. To understand how this happens, we study the effects of the various terms in the Hamiltonian. As discussed in Sec. 1.2.2, the appearance of Majoranas is a topological effect and is accompanied by the change of the topological invariant  $Q$  of symmetry class  $\mathcal{D}$ . This invariant can only assume  $Q = +1$  (no Majoranas) and  $Q = -1$  (Majoranas present) and changes when the band gap closes and reopens.

### 1.4.1. THE HAMILTONIAN: TERM BY TERM

The complete model Hamiltonian is rather complicated; therefore, we start with a one-dimensional single band Hamiltonian and study its band structure while adding the terms needed to make a topological band structure and “engineer” our way towards Majoranas. The Hamiltonian in its simplest form is quadratic in momentum and has an offset in chemical potential  $\mu$

$$H = \left( \frac{\mathbf{p}^2}{2m} - \mu \right) \tau_z, \quad (1.27)$$

where  $\tau_z$  is a Pauli matrix that acts on the electron-hole substructure. The band structure for this Hamiltonian with  $\mu = -0.3$  is shown in Fig. 1.5 (left). We assume that this band

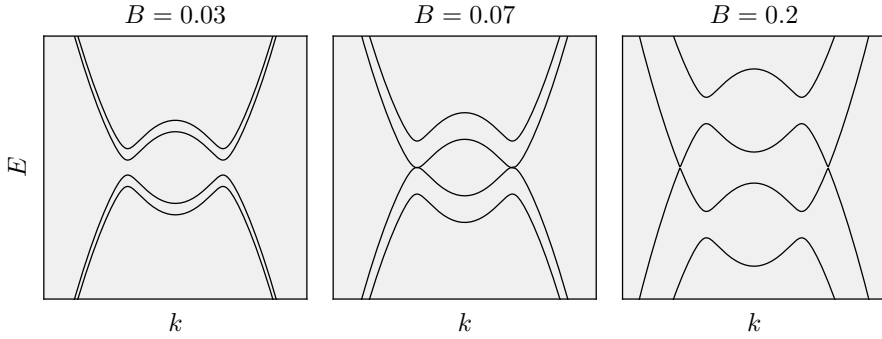


Figure 1.6: Band structures of Eq. (1.29) for different values of magnetic field and  $\Delta = 0.1$ ,  $\mu = 0.3$ .

structure is topologically trivial and has  $Q = +1$ . Because this Hamiltonian acts trivially in spin-space, the bands in Fig. 1.5 (left) are doubly degenerate. Finally, the electrons are at positive energy  $E$  and the holes on  $-E$ .

Next, we raise  $\mu$ , which shifts the bands [see Fig. 1.5 (middle)]. In Sec. 1.2.2, we explained that the topological invariant is only defined for a system with an energy gap. This band structure has no band gap, and therefore cannot be topological. Further, in Sec. 1.2 we observed that a BdG Hamiltonian has a gapped spectrum [Eq. (1.10)], so we add  $\Delta\tau_x$ , which results in

$$H_{\text{BdG}} = \left( \frac{\mathbf{p}^2}{2m} - \mu \right) \tau_z + \Delta\tau_x, \quad (1.28)$$

and opens a gap because  $\tau_x$  mixes the electron and holes [see Fig. 1.5 (right)].

We are left with a gapped spectrum; however, we closed the band gap twice because of the doubly degenerate spin bands both crossing zero energy simultaneously. The spin degeneracy (called a Kramers degeneracy<sup>5</sup>) is a result of a time-reversal symmetry and needs to be broken to create isolated Majoranas. To couple to spin we introduce the Zeeman field  $E_Z\sigma_x = \frac{1}{2}g\mu_B B\sigma_x$  in the Hamiltonian

$$H_{\text{BdG}} = \left( \frac{\mathbf{p}^2}{2m} - \mu \right) \tau_z + \Delta\tau_x + \frac{1}{2}g\mu_B B\sigma_x, \quad (1.29)$$

where  $g$  is the Landé factor,  $\mu_B$  the Bohr magneton, and  $B$  magnetic field along  $x$ , parallel to the wire direction. In Fig. 1.6 we plot the effect of a magnetic field on the band structure and observe that a magnetic field breaks the Kramers degeneracy. The bands moving towards each other have opposite spin (orthogonal states), and as we see in Fig. 1.6 (middle and left), these spins do not couple. The problem is that Zeeman conserves spin in  $x$ -direction, and therefore spin is still a good quantum number. We know that Majoranas must be spinless because they are their own complex conjugate.

<sup>5</sup>A Kramers degeneracy would result in two Majoranas per edge (just a fermion).

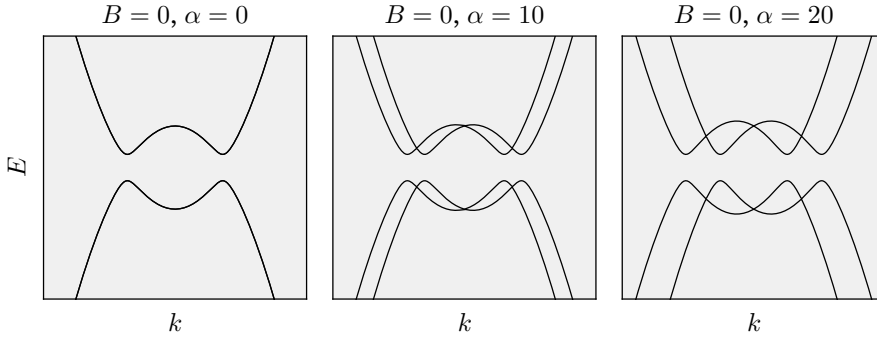


Figure 1.7: Band structures of Eq. (1.30) for different values of spin-orbit coupling  $\alpha$  and  $B = 0, \Delta = 0.1, \mu = 0.3$ .

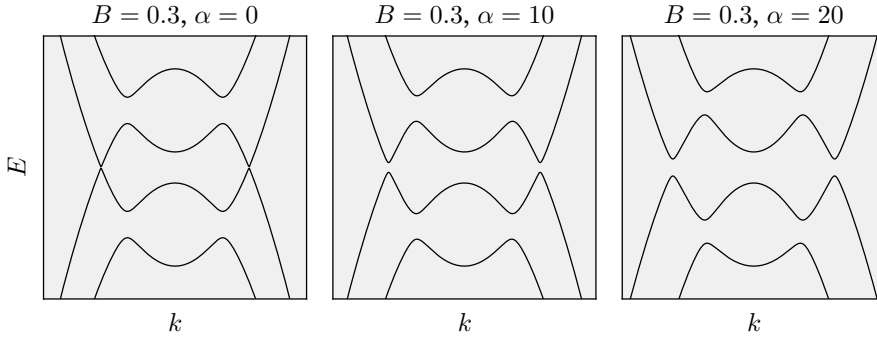


Figure 1.8: Band structures of Eq. (1.30) for different values of spin-orbit coupling  $\alpha$  and  $B = 0.3, \Delta = 0.1, \mu = 0.3$ .

The solution to this last problem is spin-orbit coupling, which in its simplest form is Rashba:  $H_{\text{Rashba}} = -\alpha p_x \sigma_y \tau_z$ . The Hamiltonian is now complete and equals

$$H_{\text{BdG}} = \left( \frac{\mathbf{p}^2}{2m} - \mu \right) \tau_z + \Delta \tau_x + \frac{1}{2} g \mu_B B \sigma_x - \alpha p_x \sigma_y \tau_z. \quad (1.30)$$

Spin-orbit by itself—even though it couples spin—is insufficient to break the Kramer degeneracy. In Fig. 1.7, we see that raising  $\alpha$  moves the different spin bands away in either  $+k$  or  $-k$  direction. However, a degeneracy remains at  $k = 0$ , revealing why a magnetic field is needed. Including a magnetic field opens the gap at  $k = 0$  (see Fig. 1.8) making the system topologically nontrivial. If the system is of a finite length, it will host Majoranas on its edges at  $E = 0$ .

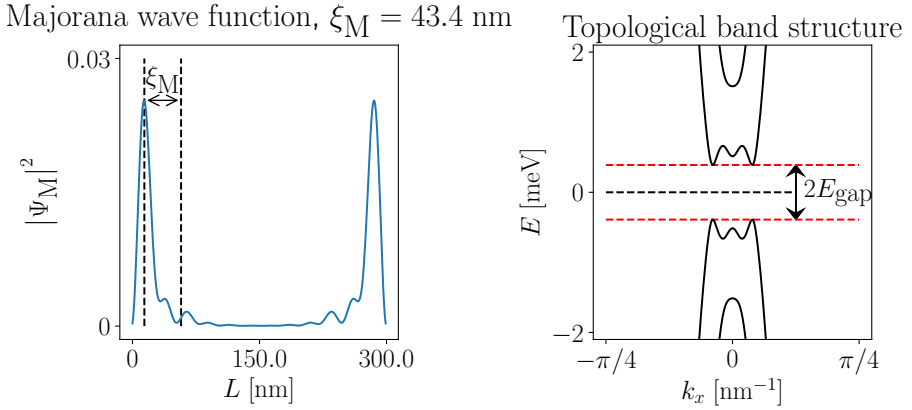


Figure 1.9: Probability density and band structure of a 1D system. The probability density of the lowest energy wavefunction (Majorana wavefunction) of a  $0.3 \mu\text{m}$  long nanowire (left) and a topological band structure (right) with the same parameter values, but for an infinite system. The Majorana length  $\xi$ —the decay length of the wavefunction—in the left plot is  $\xi_M = 43.4$  nm.

### 1.4.2. WAVEFUNCTION

We now have all the terms in the Hamiltonian to create a topological band structure, which we calculate for an infinite system (i.e., system with a translational symmetry). To observe Majoranas, we need to diagonalize the Hamiltonian of a finite system with the same parameters that resulted in the topological band structure and plot the wavefunction with the lowest energy: the Majorana wavefunction. In Fig. 1.9 (left), we plot the probability density of the Majorana wavefunction and observe that it is indeed localized near edges of the nanowire. This wavefunction decays exponentially from both sides with a decay length  $\xi_M$ .

### 1.4.3. PHASE DIAGRAM

The Hamiltonian [Eq. (1.30)] contains a few fundamental constants and constants that are material dependent; however, the chemical potential  $\mu$  and magnetic field  $B$  can be adjusted in an experiment. A good question is, for which values of  $B$  and  $\mu$  the system is topological. Due to its compactness, this model can be solved analytically, and it predicts that Majorana bound states appear when  $E_Z^2 > \mu^2 + \Delta^2$ , when the Zeeman energy becomes larger than the harmonic mean of the superconducting gap and the chemical potential. In Fig. 1.10 we plot a phase diagram, which indicates for which value of  $(B, \mu)$  the system is topological. In the next section, we will extend this model to three dimensions and study how it modifies the phase diagram.

## 1.5. MAJORANAS IN A MORE REALISTIC 3D HYBRID NANOWIRE

The simple one-dimensional model we introduced in the previous section is useful because it can be solved analytically and therefore, it gives us many insights. However, because of its simplicity, it also ignores multiple relevant physical effects. For example, the

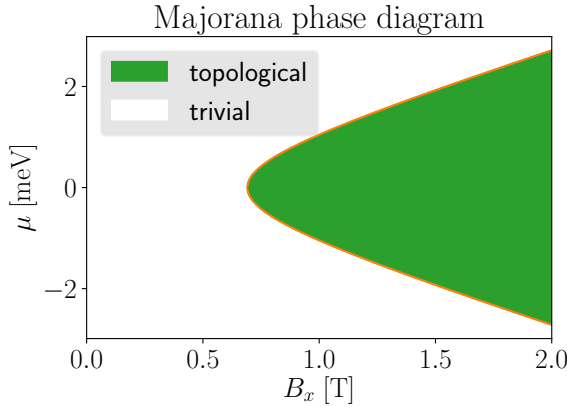


Figure 1.10: A phase diagram of a one-dimensional Majorana nanowire device as a function of magnetic field  $B$  and chemical potential  $\mu$ . The color indicates whether the system is in the topological or trivial phase. This system becomes topological whenever  $E_Z^2 > \mu^2 + \Delta^2$ .

model assumes a one-dimensional nanowire even though we live in a three-dimensional world, and so does the nanowire device when an experimentalist creates it. Besides the additional orbitals that are present in a three-dimensional system, the magnetic flux penetrating the nanowire cross-section modifies the Hamiltonian and changes the complex phases of the moving quasiparticles. Further, the simple model assumes a tunable but constant chemical potential  $\mu$  inside the nanowire. In an experiment, the nanowire is close to a metal gate at a certain voltage; its electric field changes the potential inside the nanowire non-homogeneously. In addition to these theoretical considerations, the experimental measurement results do not correspond to the predictions that the simple model makes. For example, for measuring the conductance from a nanowire hosting Majoranas to a normal lead, the model predicts a quantized conductance of  $2e^2/h$  at a bias voltage of  $V_B = 0$ , the so-called zero-bias peak. Nearly all experiments that measure this fail to reproduce this zero-bias peak where the conductance is quantized. Another effect that is not captured by the simple model is the superconducting density of states (DOS), which in theory predicts a vanishing DOS inside the gap ( $|E| < \Delta$ ) but in the experiment a non-zero DOS persists, this phenomenon is also called “soft gap.” Because of these limitations, we will improve the simple model by adding relevant physical effects.

### 1.5.1. MULTIPLE BANDS

In 3D, the model Hamiltonian [Eq. (1.30)] is modified to

$$H_{\text{BdG}} = \left( \frac{\mathbf{p}^2}{2m} - \mu \right) \tau_z + \Delta \tau_x + \frac{1}{2} g \mu_B B \sigma_x + \alpha (p_y \sigma_x - p_x \sigma_y) \tau_z, \quad (1.31)$$

such that it includes the transverse part of the Rashba spin-orbit. The two additional dimensions result in more orbitals and equivalently more bands; therefore, the condition  $E_Z^2 > \mu^2 + \Delta^2$  for a topological nanowire is no longer valid. Because there are more bands,

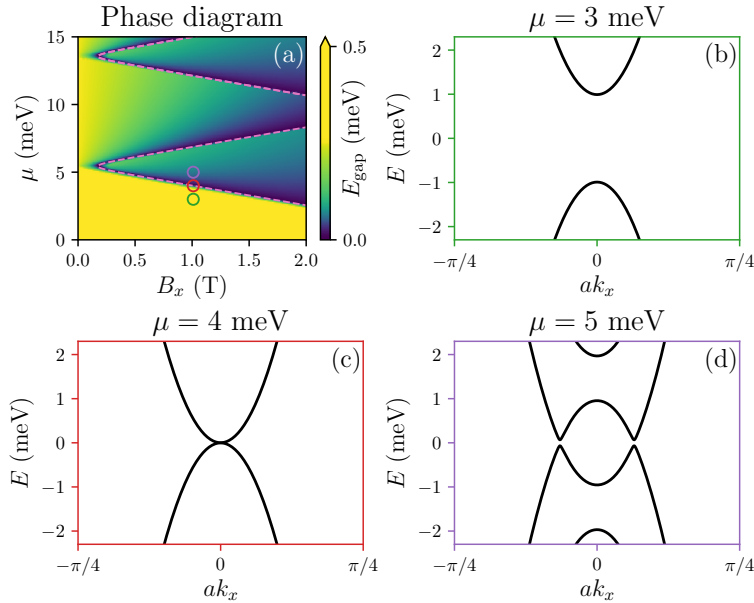


Figure 1.11: Topological phase diagram (a) of a 3D system where the dot indicate the parameter values of  $B$ ,  $\mu$  at which the surrounding band structures (b-d) are plotted. The color in the phase diagram (a) shows the size of the topological gap  $E_{\text{gap}} \equiv \min_k E(k)$  and the dashed lines are the topological phase boundaries. The band structure (b) is trivial but near a phase transition, (c) is at the phase transition, and (d) is inside of the topological regime.

multiple Majoranas can be created on both edges of the nanowire as  $\mu$  increases. However, these additional Majoranas are not topologically protected (without an additional symmetry), and a small perturbation can pair-wise annihilate all but  $N \bmod 2$  of them. The position of the phase boundaries now also depends on the cross-section's geometry. For example, Fig. 1.11 shows a phase diagram (and band structures at different combinations of  $B$  and  $\mu$ ) of a nanowire with a cylindrical cross-section.

### 1.5.2. THE ORBITAL EFFECT OF THE MAGNETIC FIELD

Whenever a magnetic flux can penetrate a surface of the nanowire, the canonical momentum operator in Eq. (1.31) is modified to include the vector potential

$$\mathbf{p} \rightarrow -i\hbar\nabla - q\mathbf{A}\tau_z, \quad (1.32)$$

where  $q$  is the elementary charge, which is different for electrons and holes. In the weak coupling regime—with a non transparent semiconductor/superconductor interface—and a wire that is symmetric with respect to the wire axis, the vector potential is  $\mathbf{A} = [B_y(z - z_0) - B_z(y - y_0), 0, B_x(y - y_0)]^T$ , which is chosen such that it does not depend on  $x$ . Here, we set the offsets  $y_0$  and  $z_0$  such that the average vector potential vanishes in the superconductor. Physically, this choice corresponds to a limit where the total supercurrent

$J_s$  is zero, appropriate for existing devices that use NbTiN as a superconducting shell. In this case, the superconductor can be considered as a perturbation that only provides the electron-hole coupling in the normal regime. However, devices that have a thin Al shell are in the strong coupling regime. Because of the high density inside the superconductor (compared to the semiconductor), the wire can no longer be considered as symmetric with respect to the wire axis. To get correct physical observables from both the vector potential and the superconducting phase difference  $\Phi$  [43], we have to ensure that the total supercurrent cancels out,

$$J_s = \frac{2en_s}{m} (2eA - \hbar\nabla\Phi) = 0, \quad (1.33)$$

where  $n_s$  is the density in the superconductor. At zero temperature, this can be archived by minimizing the kinetic energy, which is proportional to  $E_s \propto \int d\mathbf{x} J_s^2(\mathbf{x})$  [44]. This minimization results in the correct vector potential and the superconducting phase. The inclusion of the orbital effect modifies the phase diagram, which is discussed in Ch. 2 in the weakly coupled superconductor limit, while Ch. 5 discusses the strongly coupled superconductor limit.

### 1.5.3. DISORDER

Perfectly ordered crystalline solids are characterized by a faultlessly regular arrangement of their atoms in a crystal lattice, yet, these do not occur in nature [45]. Real solid-state systems are not perfectly smooth and have impurities: they are disordered. Disorder is always present and it has a strong impact on the physical properties of proximitized nanowires. Research has shown that both disorder in the semiconductor and at the semiconductor-superconductor interface is detrimental to the creation of Majoranas in proximitized nanowires [46–52]. However, semiconductor nanowire with epitaxially grown aluminum [53, 54] minimize the disorder effects and have high-quality semiconductors and semiconductor-superconductor interfaces; however, its outer surface is oxidized and therefore strongly disordered. Scattering of the disordered superconducting boundary randomizes the quasiparticle's motion inside the superconductor. Fortunately, because of the large difference in the effective masses and Fermi energies between the semiconductor and the superconductor, as argued by the authors of [47, 52, 55], disorder in the superconductor is not detrimental to the manipulation and observation of Majoranas, however, a more systematic numerical study is required. This problem is complex to study numerically because of the aforementioned high density differences, which means that the discretization in the superconductor has to be smaller than the Fermi wavelength of Al,  $\approx 0.1 \text{ \AA}$ . A full-scale three-dimensional simulation is therefore beyond what is currently feasible. Nevertheless, [56] simulates a slice of the proximitized nanowire, and finds that disorder strongly affects important quantities such as the induced gap  $\Delta_{\text{ind}}$ , the critical field  $B_C$ , and their dependence on the external gate voltage.

### 1.5.4. ELECTROSTATICS

The model Hamiltonian Eq. (1.31) has a constant chemical potential  $\mu$  in the nanowire. Experimentally,  $\mu$  is set by the external metal gates that, when applying a voltage, will change the electrostatic environment inside the device. Therefore, we replace the static

chemical potential by a spatially dependent electrostatic potential  $\mu \rightarrow -V(x, y, z)$  in the Hamiltonian. Recent proposals of scalable designs for topological quantum computing with Majoranas rely on a precise electrostatic control. A good understanding of how the metal gates influence the electrostatic potential is therefore required to interpret both existing Majorana experiments and future improved Majorana devices. One of the challenges is that the metal gates have band offsets in the 1-eV range, while a typical semiconductor's Fermi energy lies in the 1-meV range, three orders of magnitude difference [57]. Additionally, as mentioned in Sec. 1.3, the BCS mean-field approximation breaks charge conservation. We can formulate the quantum-electrostatic problem as a solution of three equations solved self-consistently. We have the Schrödinger equation

$$H_{\text{BdG}}\psi = E\psi, \quad (1.34)$$

the Poisson equation

$$\nabla^2\varphi = -\frac{\rho}{\varepsilon}, \quad (1.35)$$

where  $\varepsilon$  is the permittivity, and the density of states is

$$\rho = e \int dE \rho_i(E) f(E), \quad (1.36)$$

where  $f(E)$  is the Fermi distribution and  $\rho_i(E) \equiv \frac{1}{2\pi} \sum_{\alpha} |\psi_{\alpha E}(i)|^2$  the local density of states. Using these equations, one can iterate the following steps until convergence has been reached:

1. given the electronic density, solving the Poisson equation [Eq. (1.35)] results in the electrostatic potential,
2. given the electrostatic potential  $V(x, y, z)$ , solving the Schrödinger equation [Eq. (1.34)] results in the energy spectrum  $E$  and wave functions  $\psi$ ,
3. finally, using that the bands fill according to the Fermi distribution  $f(E)$ , we get the electronic density [Eq. (1.36)].

Several works have solved this problem, however, always using certain approximations. For example, [58] does this in the long junction or weakly coupled regime for a translationally invariant slice of the system. Other works try to solve this problem for the short junction or strongly coupled regime, also only simulating the cross-section of the nanowire [56], and/or by employing the Thomas-Fermi approximation [44, 59] (with which one can replace step 2. and 3. by using a scalar equation that returns the density  $\rho$ ), or by using other approximations [60–62]. These works find that applying a voltage on external metal gates renormalizes several important physical parameters, such as the induced superconducting gap  $\Delta_{\text{ind}}$  and the critical magnetic field  $B_c$ , and in turn, this means that the phase diagram changes. Due to the extreme computational complexity, no one has solved the full three-dimensional Schrödinger-Poisson problem, while treating the superconductor and semiconductor on equal footing.

### 1.5.5. SUPERCONDUCTING ORDER PARAMETER

In most studies [44, 56, 58, 63, 64], the superconducting order parameter  $\Delta$  is assumed to be constant inside the superconductor, even though an applied magnetic field might cause a spatial variation in both  $\Delta$ 's phase  $\phi$  and amplitude. One possible reason for this is the Meissner effect, where the superconductor (below its critical temperature  $T_c$ ) develops a supercurrent and expels the magnetic field. When the applied magnetic field  $B$  is large, vortices appear, which in the center have  $\Delta = 0$  and allow magnetic flux to penetrate the superconductor. In turn, this suppresses the induced superconducting gap  $\Delta_{\text{ind}}$  locally and creates unwanted subgap states in the superconductor. Ginzburg-Landau theory captures vortex formation. Section 4.7.2 investigates this for a NbTiN superconductor where the superconducting penetration depth  $\lambda$  is approximately three times smaller than the thickness of the superconductor and find that the vortices that appear do not have a substantial effect on the size of the induced gap. However, the epitaxially grown aluminum is much thinner (typically  $\approx 10$  nm). In this case,  $\lambda$  is much larger, resulting in a uniform magnetic field inside the superconductor. Here, the orbital effect of the magnetic field needs to be adequately treated, which is done by the authors of [43, 44], as discussed earlier. In principle, the amplitude  $|\Delta|$  is also spatially dependent, and can be solved self-consistently as it often done in ferromagnetic chains on superconductors [65, 66]. However, in the case of hybrid semiconductor-superconductor systems, it is shown that this effect is less significant [67].

### 1.5.6. SPIN-ORBIT COUPLING

Finally, the presence of strong spin-orbit coupling is crucial to create Majoranas. The Rashba spin-orbit term  $\alpha(p_y\sigma_x - p_x\sigma_y)$  in Eq. (1.31) can be derived in the framework of the k-p perturbation theory. Intuitively, it can be understood as an effective magnetic field that is the result of an inversion symmetry breaking electric field along the  $z$  axis  $H_E = -E_0z$ . An electron that moves through this electric field with velocity  $v$ , experiences an effective magnetic field  $\mathbf{B} = -(\mathbf{v} \times \mathbf{E})/c^2$  due to relativistic corrections. This effective magnetic field couples to the spin as  $H_{\text{SO}} = \frac{1}{2}g\mu_B\mathbf{B} \cdot \boldsymbol{\sigma} = -\frac{g\mu_B}{2c^2}(\mathbf{v} \times \mathbf{E}) \cdot \boldsymbol{\sigma}$ . Combining the constants into  $\alpha = g\mu_B E_0 \hbar / 2mc^2$  results in  $H_{\text{SO}}$  that appears in Eq. (1.31). Therefore, this term assumes a homogeneous electric field, which is the case for a wire with a constant chemical potential  $\mu$ . However, as discussed earlier, this is not the case. The k-p perturbation theory that includes multiple conduction and valance bands models the spin-orbit coupling more accurately. Here, the spin-orbit strength depends on the electric field resulting from the voltage that is applied to the external metal gates. In addition, k-p theory also provides a better model for the effective mass in a semiconductor. However, describing k-p theory is beyond the scope of this thesis. Finally, as Majorana device simulations become capable of correctly including the spatially varying electric field into their models (as discussed earlier), it enables researchers to understand how this affects the spin-orbit coupling by using the k-p theory.

## 1.6. NUMERICAL METHODS

Section 1.5 shows that realistically modeling Majorana devices is complex and that it is impossible to solve these problems analytically without making simplifications that still

capture all of the relevant physics. Therefore, to study Majorana devices, we must use numerical methods. Using the finite difference approximation, we can convert the linear ordinary differential equation, the continuous BdG Hamiltonian Eq. (1.31), into a system of equations described by a (potentially very large) sparse matrix. With readily available standard sparse linear algebra techniques, such as the shift-invert diagonalization method, we can efficiently find low energy wavefunctions of our system.

### 1.6.1. BAND STRUCTURE

In principle, to correctly predict device properties, one needs to simulate a large nanowire that includes the edges of the wire. However, because topology is robust and insensitive to details, we can simulate just the band structure in the bulk of the wire. From this, we understand whether the system is topological or topologically trivial. To calculate a band structure  $E(k)$ , we use Bloch's theorem, which states that the wave function in a crystal changes under translation only by a phase factor

$$\psi(\mathbf{r} + a) = e^{iak} \psi(\mathbf{r}), \quad (1.37)$$

where  $k$  is the wave vector of the wave function and  $a$  the size of the unit-cell. This implies that we only need to simulate a translationally invariant unit-cell to get  $E(k)$ . The Hamiltonian equals

$$H(k) = h + t \exp(ik) + t^\dagger \exp(-ik), \quad (1.38)$$

where  $h$  is the Hamiltonian of the cross section of the tight-binding system and  $t$  is the hopping matrix between the neighboring cross sections. Next section explains how to get the tight-binding model. Diagonalizing this Hamiltonian at  $k$  results in the spectrum  $E(k)$ . Finally, due to the discretization, the Brillouin zone is periodic. However, one should be careful to not simulate effects from its corners because the band structure only correctly represents the continuum model near the band bottom.

### 1.6.2. DISCRETIZATION OF THE HAMILTONIAN

To turn Eq. (1.31) into a discretized tight-binding model, we replace  $\mathbf{p} \rightarrow -i\hbar\nabla$ , where  $\nabla \equiv \left( \frac{\partial}{\partial x}, \frac{\partial}{\partial y}, \frac{\partial}{\partial z} \right) \equiv (\partial_x, \partial_y, \partial_z)$ , to get

$$H_{\text{BdG}} = \left( \frac{-\hbar^2 \nabla^2}{2m} - \mu \right) \tau_z + \Delta \tau_x + \frac{1}{2} g \mu_B B \sigma_x + i\hbar \alpha (\partial_x \sigma_y - \partial_y \sigma_x) \tau_z. \quad (1.39)$$

We discretize the differential operators in  $H_{\text{BdG}}$  on sites of a square lattice with lattice constant  $a$ . Every site is indexed by integer lattice coordinates  $(i, j, k)$ , which have real-space coordinates  $(x, y, z) = (ai, aj, ak) = \mathbf{r}$ . It is convenient to introduce creation  $c_r^\dagger$  and annihilation  $c_r$  operators that act on the sites, where

$$c_{\mathbf{r}} \equiv c_{ai, aj, ak} = c_{x, y, z}. \quad (1.40)$$

Using these, and assuming that  $a$  is sufficiently small, we express the first order differential operator as

$$\partial_x = \frac{1}{a} \sum_{i, j, k} \left( c_r^\dagger c_{r-a\hat{x}} - c_r^\dagger c_r \right), \quad (1.41)$$

and the second order differential operator as

$$\partial_x^2 = \frac{1}{a^2} \sum_{i,j,k} \left( c_r^\dagger c_{r+a\hat{x}} + c_{r+a\hat{x}}^\dagger c_r - 2c_r^\dagger c_r \right), \quad (1.42)$$

and similar expressions for  $\partial_y$ ,  $\partial_z$ ,  $\partial_y^2$ , and  $\partial_z^2$ . Substituting all of these into the Hamiltonian and using  $t = \frac{\hbar^2}{2ma^2}$  gives

$$H_{\text{BdG}} = \sum_{i,j,k} \mathbf{c}_r^\dagger H_{\text{onsite}} \mathbf{c}_r + \sum_{i,j,k} \left( \mathbf{c}_r^\dagger H_{\text{hop},x} \mathbf{c}_{r+a\hat{x}} + \mathbf{c}_r^\dagger H_{\text{hop},y} \mathbf{c}_{r+a\hat{y}} + \mathbf{c}_r^\dagger H_{\text{hop},z} \mathbf{c}_{r+a\hat{z}} + H.c. \right), \quad (1.43)$$

where  $\mathbf{c}$  is a vector of creation and annihilation operators that acts on the BdG degrees of freedom on the same site, and

$$H_{\text{onsite}} = \frac{B_x g \mu_B \sigma_x}{2} + \Delta \tau_x - \mu \tau_z + 6t \tau_z, \quad (1.44)$$

$$H_{\text{hop},x} = -t \tau_z + \frac{i \alpha \sigma_y \tau_z}{2a}, \quad (1.45)$$

$$H_{\text{hop},y} = -t \tau_z - \frac{i \alpha \sigma_x \tau_z}{2a}, \quad (1.46)$$

$$H_{\text{hop},z} = -t \tau_z. \quad (1.47)$$

These matrices can easily be implemented in a numerical model, for example, using the Kwant package [68].

### 1.6.3. PEIERLS SUBSTITUTION

In Sec. 1.5.2, we discussed the orbital effect of the magnetic field and included the vector potential as in Eq. (1.32). To include this into a discretized Hamiltonian, we use the Peierls substitution, which is the lattice version of the vector potential [69]. In the presence of an external magnetic vector potential  $\mathbf{A}$  (using the second quantization notation introduced in the previous subsection), we redefine translation operators  $\mathbf{c}_r^\dagger H_{\text{hop}} \mathbf{c}_{r+a\hat{x}}$  appearing in the kinetic and spin-orbit part of the Hamiltonian in the tight-binding model, as

$$\mathbf{T}_x = \mathbf{c}_{r+a\hat{x}}^\dagger H_{\text{hop}} \mathbf{c}_r e^{i\theta_r^x}, \quad (1.48a)$$

$$\mathbf{T}_y = \mathbf{c}_{r+a\hat{y}}^\dagger H_{\text{hop}} \mathbf{c}_r e^{i\theta_r^y}, \quad (1.48b)$$

$$\mathbf{T}_z = \mathbf{c}_{r+a\hat{z}}^\dagger H_{\text{hop}} \mathbf{c}_r e^{i\theta_r^z}, \quad (1.48c)$$

where the phases are defined as

$$\theta_r^x = \frac{q}{\hbar} \int_i^{i+1} A_x(x, j, k) dx, \quad (1.49a)$$

$$\theta_r^y = \frac{q}{\hbar} \int_j^{j+1} A_y(i, y, k) dy, \quad (1.49b)$$

$$\theta_r^z = \frac{q}{\hbar} \int_k^{k+1} A_z(i, j, z) dz. \quad (1.49c)$$

Here, the elementary charge  $q$ , is opposite for the electrons and the holes. Thus, adding a magnetic field  $\mathbf{B} = \nabla \times \mathbf{A}$ —including a choice for the vector potential  $\mathbf{A}$ —to the tight-binding model, thus amounts to adding the above phase terms to the hopping terms of the Hamiltonian.

#### 1.6.4. TOPOLOGICAL PHASE BOUNDARIES

There are many problem specific methods, for example, calculating the topological energy gap  $E_{\text{gap}} \equiv \min_k E(k)$  from the band structure, calculating the topological invariant  $\mathcal{Z}_2$ , or determining the position of the phase boundaries in parameter space. This section, explains the latter for a nanowire that has a constant chemical potential  $\mu$ . As discussed in Sec. 1.2.2, whenever the topological energy gap  $E_{\text{gap}}$  closes, the  $\mathcal{Z}_2$  topological invariant  $Q$  changes. Section 1.4.3 showed a phase diagram of a one-dimensional nanowire as a function of  $B_x$  and  $\mu$ , where the position of the topological phase boundaries are expressed through a simple analytical expression. In a three-dimensional nanowire this expression is no longer valid. Instead, we have to numerically find where the gap closes: we need to find when  $E_{\text{gap}}(B_x, \mu) = 0$ . This is computationally expensive because for each value of  $(B_x, \mu)$ , we have to solve a minimization problem. We can also use the property that the gap always closes at either  $k = 0$  (or  $k = \pi$ )<sup>6</sup>, however, we would still need to do many iterative solves of the eigenvalue problems to find where  $E(k = 0, B_x, \mu) = 0$ . Alternatively, we can use this property to define an optimized algorithm to simultaneously find all the values of  $\mu$  that correspond to the topological phase transition. We can reformulate the problem as an eigenvalue problem, and solve for the values of  $\mu$  and  $\psi$  in  $H_{\text{BdG}}(\mu, k = 0)\psi = 0$ . We rewrite this equation as a generalized eigenvalue problem by using that  $\mu$  enters  $H_{\text{BdG}}$  only as a prefactor of a linear operator. This results in

$$H_{\text{BdG}}(\mu = 0, k = 0)\psi = \mu\tau_z\psi. \quad (1.50)$$

Using standard generalized eigensolvers, we easily find its eigenvalues. The real eigenvalues are the values of  $\mu$  where the gap closes at  $k = 0$ . The difference between solving Eq. (1.50) and finding  $E(k = 0)$  is visualized in Fig. 1.12.

#### 1.6.5. LIMITS AND COMPLEXITY

Section 1.5 discussed many potential improvements to the Majorana nanowire model. Even when including all the proposed improvements, the model still has its limitations, of both a physical and computational nature. In some cases, alleviating the physical limitation of the discretized model may turn into a computational limitation. For example, we started with a model that is an approximation of the continuum Hamiltonian (Eq. (1.31)), which is only valid in the low-energy limit. As an example, Fig. 1.13 shows the band structure of both the discretized and continuum model for different lattice constants of the spin part of the one-dimensional Majorana Hamiltonian (Eq. (1.30)). Here, we observe that decreasing the lattice constant results in a better approximation to the continuum model at higher densities. The computational complexity arises when

<sup>6</sup>Gap closings at  $k = \pi$  do not occur in our model.

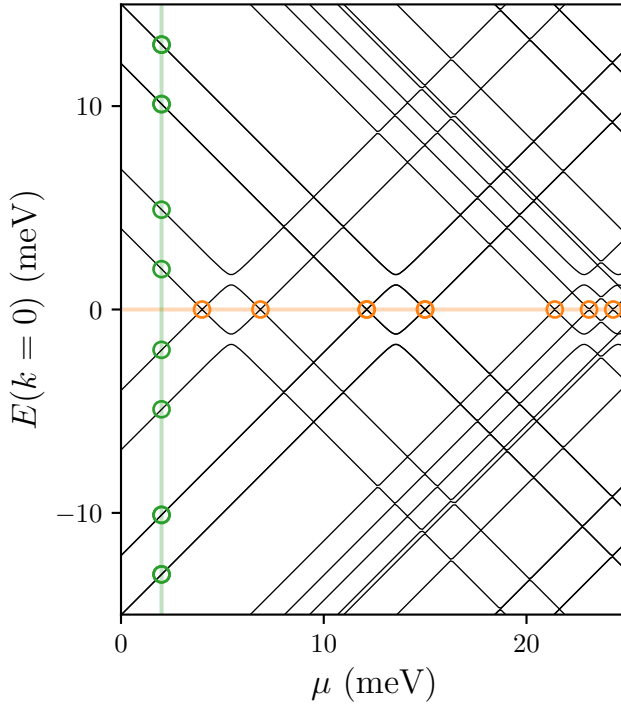


Figure 1.12: Energy spectrum at  $k = 0$  of as a function of chemical potential  $\mu$ . The orange circles are the real eigenvalues of Eq. (1.50) lying at  $E = 0$  (the orange line). The green circles are the solutions of  $H_{\text{BdG}}\psi = E\psi$  at fixed  $\mu$  marked by the green line. To find the phase transitions with the latter approach, one needs to sweep over  $\mu$  and find  $E(k = 0) < \epsilon$ , where  $\epsilon$  is the precision. Using the generalized eigenvalue problem, we find all phase transitions at once. The parameters used are the same as Fig. 1.11 at  $B_x = 1 \text{ T}$ .

simulating full three-dimensional nanowires. Here, the typical length of the physical nanowires is on the order of micrometers with a typical diameter of 100 nm. The Fermi wavelength  $\lambda_F$  sets a lower limit on the lattice constant  $a$ , which in the semiconductor is typically around  $a = 5 - 10 \text{ nm}$  for the low-density regime. This means that systems easily become larger than  $1e6$  sites, and including the spin and electron-hole degrees of freedom results in matrices of  $4e^6 \times 4e^6$ . To calculate a phase diagram  $E_{\text{gap}}(B_x, \mu)$  using this system, we need to diagonalize this large matrix—which is an expensive operation by itself—many times. In the case of strongly coupled superconductors, it becomes more problematic because the wavefunction has most of its weight in the superconductor, which means we have to simulate it on the level of its Fermi wavelength. Aluminum is typically used as the superconductor and has a Fermi energy of  $E_F \approx 11.7 \text{ eV}$ , which translates into  $\lambda_F \approx 0.36 \text{ nm}$ . So, to properly simulate even the thin layer of superconducting material on top of a nanowire, the lattice constant has to be smaller than an ångström, resulting in matrix sizes that go far beyond the current capabilities of even the largest computers.

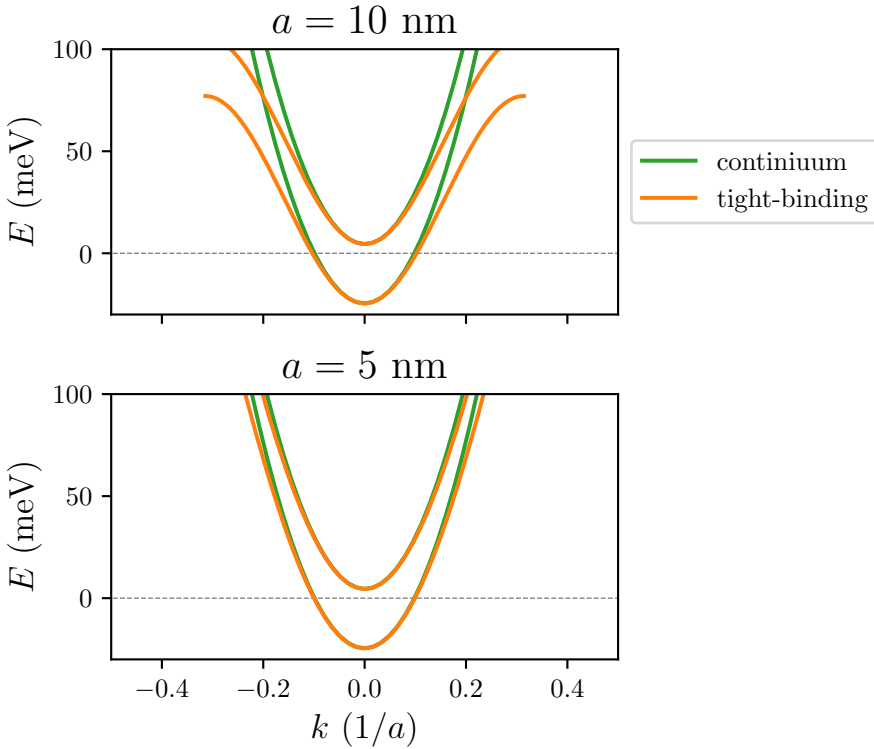


Figure 1.13: The band structure of Eq. (1.30) (without superconductivity) for a lattice constant  $a = 10$  nm (top) and  $a = 5$  nm (bottom), where we plot the continuum (green) and the discretized (orange) spectrum. The dotted line indicates the Fermi energy. The tight-binding approximation remains valid whenever the two models result in approximately the same spectrum below the Fermi energy.

### 1.6.6. ADAPTIVE SAMPLING

A partial solution to address the computational complexity, is to sample the parameter space of the function we are evaluating adaptively. In Ch. 7, we develop adaptive parallel sampling algorithms for low-dimensional ( $d \lesssim 4$ ) parameter sweeps, adaptive integration, and averaging stochastic functions. In our research, this typically sped up the simulations by at least an order of magnitude in comparison with sampling on a homogeneous grid.

## 1.7. STRUCTURE OF THIS THESIS

Here, we give a brief overview of the topics explored in the following chapters.

### 1.7.1. CHAPTER 2: ORBITAL EFFECT OF MAGNETIC FIELD ON THE MAJORANA PHASE DIAGRAM

Studies of Majorana bound states in semiconducting nanowires frequently neglect the orbital effect of a magnetic field. Systematically studying its role leads us to several conclusions for designing Majoranas in this system. Specifically, we show that for experimentally relevant parameter values the orbital effect of a magnetic field has a stronger impact on the dispersion relation than the Zeeman effect. While Majoranas do not require the presence of only one dispersion subband, we observe that the size of the Majoranas becomes unpractically large, and the band gap unpractically small when more than one subband is filled. Since the orbital effect of a magnetic field breaks several symmetries of the Hamiltonian, it leads to the appearance of large regions in parameter space with no band gap whenever the magnetic field is not aligned with the wire axis. The reflection symmetry of the Hamiltonian with respect to the plane perpendicular to the wire axis guarantees that the wire stays gapped in the topologically nontrivial region as long as the field is aligned with the wire.

### 1.7.2. CHAPTER 3: SUPERCURRENT INTERFERENCE IN FEW-MODE NANOWIRE JOSEPHSON JUNCTIONS

Junctions created by coupling two superconductors via a semiconductor nanowire in the presence of high magnetic fields are the basis for the potential detection, fusion and braiding of Majorana bound states. We study NbTiN/InSb nanowire/NbTiN Josephson junctions and find that the dependence of the critical current on the magnetic field exhibits gate-tunable nodes. This is in contrast with a well-known Fraunhofer effect, under which critical current nodes form a regular pattern with a period fixed by the junction area. Based on a realistic numerical model we conclude that the Zeeman effect induced by the magnetic field and the spin-orbit interaction in the nanowire are insufficient to explain the observed evolution of the Josephson effect. We find the interference between the few occupied one-dimensional modes in the nanowire to be the dominant mechanism responsible for the critical current behavior. We also report a strong suppression of critical currents at finite magnetic fields that should be taken into account when designing circuits based on Majorana bound states.

### 1.7.3. CHAPTER 4: SPIN-ORBIT PROTECTION OF INDUCED SUPERCONDUCTIVITY IN MAJORANA NANOWIRES

Spin-orbit interaction (SOI) plays a key role in creating Majorana zero modes in semiconductor nanowires proximity coupled to a superconductor. We track the evolution of the induced superconducting gap in InSb nanowires coupled to a NbTiN superconductor in a large range of magnetic field strengths and orientations. Based on realistic simulations of our devices, we reveal SOI with a strength of 0.15–0.35 eVÅ. Our approach identifies the direction of the spin-orbit field, which is strongly affected by the superconductor geometry and electrostatic gates.

#### 1.7.4. CHAPTER 5: ROBUSTNESS OF MAJORANA BOUND STATES IN THE SHORT-JUNCTION LIMIT

We study the effects of strong coupling between a superconductor and a semiconductor nanowire on the creation of the Majorana bound states, when the quasiparticle dwell time in the normal part of the nanowire is much shorter than the inverse superconducting gap. This “short-junction” limit is relevant for the recent experiments using the epitaxially grown aluminum characterized by a transparent interface with the semiconductor and a small superconducting gap. We find that the small superconducting gap does not have a strong detrimental effect on the Majorana properties. Specifically, both the critical magnetic field required for creating a topological phase and the size of the Majorana bound states are independent of the superconducting gap. The critical magnetic field scales with the wire cross-section, while the relative importance of the orbital and Zeeman effects of the magnetic field is controlled by the material parameters only:  $g$  factor, effective electron mass, and the semiconductor-superconductor interface transparency.

#### 1.7.5. CHAPTER 6: ENHANCED PROXIMITY EFFECT IN ZIGZAG-SHAPED MAJORANA JOSEPHSON JUNCTIONS

High density superconductor-semiconductor-superconductor junctions have a small induced superconducting gap due to the quasiparticle trajectories with a large momentum parallel to the junction having a very long flight time. Because a large induced gap protects Majorana modes, these long trajectories constrain Majorana devices to a low electron density. We show that a zigzag-shaped geometry eliminates these trajectories, allowing the robust creation of Majorana states with both the induced gap  $E_{\text{gap}}$  and the Majorana size  $\xi_{\text{M}}$  improved by more than an order of magnitude for realistic parameters. In addition to the improved robustness of Majoranas, this new zigzag geometry is insensitive to the geometric details and the device tuning.

#### 1.7.6. CHAPTER 7: *Adaptive*: PARALLEL ACTIVE LEARNING OF MATHEMATICAL FUNCTIONS

Large scale computer simulations are time-consuming to run and often require sweeps over input parameters to obtain a qualitative understanding of the simulation output. These sweeps of parameters can potentially make the simulations prohibitively expensive. Therefore, when evaluating a function numerically, it is advantageous to sample it more densely in the interesting regions (called adaptive sampling) instead of evaluating it on a manually-defined homogeneous grid. Such adaptive algorithms exist within the machine learning field. These methods can suggest a new point to calculate based on *all* existing data at that time; however, this is an expensive operation. An alternative is to use local algorithms—in contrast to the previously mentioned global algorithms—which can suggest a new point, based only on the data in the immediate vicinity of a new point. This approach works well, even when using hundreds of computers simultaneously because the point suggestion algorithm is cheap (fast) to evaluate. We provide a reference implementation in Python and show its performance.

## REFERENCES

- [1] L. D. Landau, *On the theory of phase transitions*, Ukr. J. Phys. **11**, 19 (1937).
- [2] V. Kalmeyer and R. B. Laughlin, *Equivalence of the resonating-valence-bond and fractional quantum Hall states*, Phys. Rev. Lett. **59**, 2095 (1987).
- [3] X. G. Wen, *Vacuum degeneracy of chiral spin states in compactified space*, Phys. Rev. B **40**, 7387 (1989).
- [4] X. G. Wen, *Topological orders in rigid states*, Int. J. Mod. Phys. B **04**, 239 (1990).
- [5] J. E. Avron, D. Osadchy, and R. Seiler, *A topological look at the quantum Hall effect*, Phys. Today **56**, 38 (2003).
- [6] B. Jeckelmann and B. Jeanneret, *The quantum Hall effect as an electrical resistance standard*, Rep. Prog. Phys. **64**, 1603 (2001).
- [7] M. Z. Hasan and C. L. Kane, *Colloquium: Topological insulators*, Rev. Mod. Phys. **82**, 3045 (2010).
- [8] Wikipedia contributors, *Blue trefoil knot — Wikipedia, the free encyclopedia*, (2010), [Online; accessed 31-March-2020].
- [9] Wikipedia contributors, *Blue unknot — Wikipedia, the free encyclopedia*, (2010), [Online; accessed 31-March-2020].
- [10] L. Fu and C. L. Kane, *Topological insulators with inversion symmetry*, Phys. Rev. B **76**, 045302 (2007).
- [11] L. Fu, C. L. Kane, and E. J. Mele, *Topological insulators in three dimensions*, Phys. Rev. Lett. **98**, 106803 (2007).
- [12] C. Kane and J. Moore, *Topological insulators*, Phys. World **24**, 32 (2011).
- [13] J. E. Moore and L. Balents, *Topological invariants of time-reversal-invariant band structures*, Phys. Rev. B **75**, 121306 (2007).
- [14] R. P. Feynman, *Simulating physics with computers*, Int J Theor Phys **21**, 467 (1982).
- [15] P. Shor, *Algorithms for quantum computation: discrete logarithms and factoring*, in *Proceedings 35th Annual Symposium on Foundations of Computer Science* (IEEE Comput. Soc. Press).
- [16] P. Kok, W. J. Munro, K. Nemoto, T. C. Ralph, J. P. Dowling, and G. J. Milburn, *Linear optical quantum computing with photonic qubits*, Rev. Mod. Phys. **79**, 135 (2007).
- [17] N. Friis, O. Marty, C. Maier, C. Hempel, M. Holzäpfel, P. Jurcevic, M. B. Plenio, M. Huber, C. Roos, R. Blatt, and B. Lanyon, *Observation of entangled states of a fully controlled 20-qubit system*, Phys. Rev. X **8**, 021012 (2018).

- [18] L. M. K. Vandersypen, H. Bluhm, J. S. Clarke, A. S. Dzurak, R. Ishihara, A. Morello, D. J. Reilly, L. R. Schreiber, and M. Veldhorst, *Interfacing spin qubits in quantum dots and donors—hot, dense, and coherent*, npj Quantum Inf **3**, 34 (2017).
- [19] F. Arute, K. Arya, R. Babbush, D. Bacon, J. C. Bardin, R. Barends, R. Biswas, S. Boixo, F. G. S. L. Brandao, D. A. Buell, B. Burkett, Y. Chen, Z. Chen, B. Chiaro, R. Collins, W. Courtney, A. Dunsworth, E. Farhi, B. Foxen, A. Fowler, C. Gidney, M. Giustina, R. Graff, K. Guerin, S. Habegger, M. P. Harrigan, M. J. Hartmann, A. Ho, M. Hoffmann, T. Huang, T. S. Humble, S. V. Isakov, E. Jeffrey, Z. Jiang, D. Kafri, K. Kechedzhi, J. Kelly, P. V. Klimov, S. Knysh, A. Korotkov, F. Kostritsa, D. Landhuis, M. Lindmark, E. Lucero, D. Lyakh, S. Mandrà, J. R. McClean, M. McEwen, A. Megrant, X. Mi, K. Michielsen, M. Mohseni, J. Mutus, O. Naaman, M. Neeley, C. Neill, M. Y. Niu, E. Ostby, A. Petukhov, J. C. Platt, C. Quintana, E. G. Rieffel, P. Roushan, N. C. Rubin, D. Sank, K. J. Satzinger, V. Smelyanskiy, K. J. Sung, M. D. Trevithick, A. Vainsencher, B. Villalonga, T. White, Z. J. Yao, P. Yeh, A. Zalcman, H. Neven, and J. M. Martinis, *Quantum supremacy using a programmable superconducting processor*, Nature **574**, 505 (2019).
- [20] D. A. Lidar, T. A. Brun, and T. Brun, eds., *Quantum Error Correction* (Cambridge University Press, 2009).
- [21] C. Nayak, S. H. Simon, A. Stern, M. Freedman, and S. D. Sarma, *Non-Abelian anyons and topological quantum computation*, Rev. Mod. Phys. **80**, 1083 (2008).
- [22] N. Read and D. Green, *Paired states of fermions in two dimensions with breaking of parity and time-reversal symmetries and the fractional quantum Hall effect*, Phys. Rev. B **61**, 10267 (2000).
- [23] G. Moore and N. Read, *Nonabelions in the fractional quantum hall effect*, Nuclear Physics B **360**, 362 (1991).
- [24] V. Gurarie, L. Radzihovsky, and A. V. Andreev, *Quantum phase transitions across a  $p$ -wave Feshbach resonance*, Phys. Rev. Lett. **94**, 230403 (2005).
- [25] S. D. Sarma, C. Nayak, and S. Tewari, *Proposal to stabilize and detect half-quantum vortices in strontium ruthenate thin films: Non-Abelian braiding statistics of vortices in a  $p_x + ip_y$  superconductor*, Phys. Rev. B **73**, 220502 (2006).
- [26] S. Tewari, S. D. Sarma, C. Nayak, C. Zhang, and P. Zoller, *Quantum computation using vortices and Majorana zero modes of  $p_x + ip_y$  superfluid of Fermionic cold atoms*, Phys. Rev. Lett. **98**, 010506 (2007).
- [27] L. Fu and C. L. Kane, *Superconducting proximity effect and Majorana Fermions at the surface of a topological insulator*, Phys. Rev. Lett. **100**, 096407 (2008).
- [28] R. M. Lutchyn, J. D. Sau, and S. D. Sarma, *Majorana Fermions and a topological phase transition in semiconductor-superconductor heterostructures*, Phys. Rev. Lett. **105**, 077001 (2010).
- [29] Y. Oreg, G. Refael, and F. von Oppen, *Helical liquids and Majorana bound states in quantum wires*, Phys. Rev. Lett. **105**, 177002 (2010).

- [30] V. Mourik, K. Zuo, S. M. Frolov, S. R. Plissard, E. P. A. M. Bakkers, and L. P. Kouwenhoven, *Signatures of Majorana Fermions in hybrid superconductor-semiconductor nanowire devices*, *Science* **336**, 1003 (2012).
- [31] A. Das, Y. Ronen, Y. Most, Y. Oreg, M. Heiblum, and H. Shtrikman, *Zero-bias peaks and splitting in an Al-InAs nanowire topological superconductor as a signature of Majorana fermions*, *Nat. Phys.* **8**, 887 (2012).
- [32] M. T. Deng, C. L. Yu, G. Y. Huang, M. Larsson, P. Caroff, and H. Q. Xu, *Anomalous zero-bias conductance peak in a Nb-InSb nanowire-Nb hybrid device*, *Nano Lett.* **12**, 6414 (2012).
- [33] M. T. Deng, S. Vaitiekėnas, E. B. Hansen, J. Danon, M. Leijnse, K. Flensberg, J. Nygård, P. Krogstrup, and C. M. Marcus, *Majorana bound state in a coupled quantum-dot hybrid-nanowire system*, *Science* **354**, 1557 (2016).
- [34] S. M. Albrecht, A. P. Higginbotham, M. Madsen, F. Kuemmeth, T. S. Jespersen, J. Nygård, P. Krogstrup, and C. M. Marcus, *Exponential protection of zero modes in Majorana islands*, *Nature* **531**, 206 (2016).
- [35] J. Chen, P. Yu, J. Stenger, M. Hocevar, D. Car, S. R. Plissard, E. P. A. M. Bakkers, T. D. Stanescu, and S. M. Frolov, *Experimental phase diagram of zero-bias conductance peaks in superconductor/semiconductor nanowire devices*, *Sci. Adv.* **3**, e1701476 (2017).
- [36] L. N. Cooper, *Bound electron pairs in a degenerate Fermi gas*, *Phys. Rev.* **104**, 1189 (1956).
- [37] J. Bardeen, L. N. Cooper, and J. R. Schrieffer, *Microscopic theory of superconductivity*, *Phys. Rev.* **106**, 162 (1957).
- [38] J. Bardeen, L. N. Cooper, and J. R. Schrieffer, *Theory of superconductivity*, *Phys. Rev.* **108**, 1175 (1957).
- [39] P. G. D. Gennes, *Superconductivity of Metals and Alloys* (CRC Press, 2018).
- [40] E. Wigner, *Gruppentheorie und ihre Anwendung auf die Quantenmechanik der Atom-spektren* (Vieweg+Teubner Verlag, 1931).
- [41] A. Altland and M. R. Zirnbauer, *Nonstandard symmetry classes in mesoscopic normal-superconducting hybrid structures*, *Phys. Rev. B* **55**, 1142 (1997).
- [42] D. A. Ivanov, *Non-Abelian statistics of half-quantum vortices in p-wave superconductors*, *Phys. Rev. Lett.* **86**, 268 (2001).
- [43] P. Wójcik and M. P. Nowak, *Durability of the superconducting gap in Majorana nanowires under orbital effects of a magnetic field*, *Phys. Rev. B* **97**, 235445 (2018).
- [44] G. W. Winkler, A. E. Antipov, B. van Heck, A. A. Soluyanov, L. I. Glazman, M. Wimmer, and R. M. Lutchyn, *Unified numerical approach to topological semiconductor-superconductor heterostructures*, *Phys. Rev. B* **99**, 245408 (2019).

- [45] J. Nölting, *Disorder in solids (ionic crystals and metals)*, Angew. Chem. Int. Ed. Engl. **9**, 489 (1970).
- [46] A. M. Lobos, R. M. Lutchyn, and S. D. Sarma, *Interplay of disorder and interaction in Majorana quantum wires*, Phys. Rev. Lett. **109**, 146403 (2012).
- [47] R. M. Lutchyn, T. D. Stanescu, and S. D. Sarma, *Momentum relaxation in a semiconductor proximity-coupled to a disordered-wave superconductor: Effect of scattering on topological superconductivity*, Phys. Rev. B **85**, 140513 (2012).
- [48] J. D. Sau, S. Tewari, and S. D. Sarma, *Experimental and materials considerations for the topological superconducting state in electron- and hole-doped semiconductors: Searching for non-Abelian Majorana modes in 1D nanowires and 2D heterostructures*, Phys. Rev. B **85**, 064512 (2012).
- [49] J. D. Sau and S. D. Sarma, *Density of states of disordered topological superconductor-semiconductor hybrid nanowires*, Phys. Rev. B **88**, 064506 (2013).
- [50] H.-Y. Hui, J. D. Sau, and S. D. Sarma, *Bulk disorder in the superconductor affects proximity-induced topological superconductivity*, Phys. Rev. B **92**, 174512 (2015).
- [51] W. S. Cole, J. D. Sau, and S. D. Sarma, *Proximity effect and Majorana bound states in clean semiconductor nanowires coupled to disordered superconductors*, Phys. Rev. B **94**, 140505 (2016).
- [52] D. E. Liu, E. Rossi, and R. M. Lutchyn, *Impurity-induced states in superconducting heterostructures*, Phys. Rev. B **97**, 161408 (2018).
- [53] R. M. Lutchyn, E. P. A. M. Bakkers, L. P. Kouwenhoven, P. Krogstrup, C. M. Marcus, and Y. Oreg, *Majorana zero modes in superconductor-semiconductor heterostructures*, Nat. Rev. Mater. **3**, 52 (2018).
- [54] P. Krogstrup, N. L. B. Ziino, W. Chang, S. M. Albrecht, M. H. Madsen, E. Johnson, J. Nygård, C. M. Marcus, and T. S. Jespersen, *Epitaxy of semiconductor-superconductor nanowires*, Nat. Mater. **14**, 400 (2015).
- [55] D. Sticlet, B. Nijholt, and A. Akhmerov, *Robustness of Majorana bound states in the short-junction limit*, Phys. Rev. B **95**, 115421 (2017).
- [56] A. E. Antipov, A. Bargerbos, G. W. Winkler, B. Bauer, E. Rossi, and R. M. Lutchyn, *Effects of gate-induced electric fields on semiconductor Majorana nanowires*, Phys. Rev. X **8**, 031041 (2018).
- [57] P. Armagnat, A. Lacerda-Santos, B. Rossignol, C. Groth, and X. Waintal, *The self-consistent quantum-electrostatic problem in strongly non-linear regime*, SciPost Phys. **7**, 031 (2019).
- [58] A. Vuik, D. Eeltink, A. R. Akhmerov, and M. Wimmer, *Effects of the electrostatic environment on the Majorana nanowire devices*, New J. Phys. **18**, 033013 (2016).

- [59] A. E. Mikkelsen, P. Kotetes, P. Krogstrup, and K. Flensberg, *Hybridization at superconductor-semiconductor interfaces*, Phys. Rev. X **8**, 031040 (2018).
- [60] S. D. Escribano, A. L. Yeyati, and E. Prada, *Interaction-induced zero-energy pinning and quantum dot formation in Majorana nanowires*, Beilstein J. Nanotechnol. **9**, 2171 (2018).
- [61] F. Domínguez, J. Cayao, P. San-Jose, R. Aguado, A. L. Yeyati, and E. Prada, *Zero-energy pinning from interactions in Majorana nanowires*, npj Quant Mater **2**, 13 (2017).
- [62] B. D. Woods, T. D. Stanescu, and S. D. Sarma, *Effective theory approach to the Schrödinger-Poisson problem in semiconductor Majorana devices*, Phys. Rev. B **98**, 035428 (2018).
- [63] B. Nijholt and A. R. Akhmerov, *Orbital effect of magnetic field on the Majorana phase diagram*, Phys. Rev. B **93**, 235434 (2016).
- [64] G. W. Winkler, D. Varjas, R. Skolasinski, A. A. Soluyanov, M. Troyer, and M. Wimmer, *Orbital contributions to the electron  $g$  factor in semiconductor nanowires*, Phys. Rev. Lett. **119**, 037701 (2017).
- [65] O. A. Awoga, K. Björnson, and A. M. Black-Schaffer, *Disorder robustness and protection of Majorana bound states in ferromagnetic chains on conventional superconductors*, Phys. Rev. B **95**, 184511 (2017).
- [66] P. D. Sacramento, V. K. Dugaev, and V. R. Vieira, *Magnetic impurities in a superconductor: Effect of domain walls and interference*, Phys. Rev. B **76**, 014512 (2007).
- [67] O. A. Awoga, J. Cayao, and A. M. Black-Schaffer, *Supercurrent detection of topologically trivial zero-energy states in nanowire junctions*, Phys. Rev. Lett. **123**, 117001 (2019).
- [68] C. W. Groth, M. Wimmer, A. R. Akhmerov, and X. Waintal, *Kwant: a software package for quantum transport*, New J. Phys. **16**, 063065 (2014).
- [69] R. Peierls, *Zur theorie des diamagnetismus von leitungselektronen*, Z. Physik **80**, 763 (1933).



# 2

## ORBITAL EFFECT OF MAGNETIC FIELD ON THE MAJORANA PHASE DIAGRAM

---

This chapter has been previously published as Bas Nijholt and Anton R. Akhmerov, *Orbital effect of magnetic field on the Majorana phase diagram*, Phys. Rev. B **93**, 235434, (2015)

My contribution to this work is the writing of the paper, implementing the numerical methods, and performing the numerical simulations.

## 2.1. INTRODUCTION

The search for Majorana bound states, the simplest non-Abelian particles, is fueled by their suitability for fault-tolerant quantum computation [1, 2]. A large fraction of the experimental effort [3–7] is focused on creating Majoranas in semiconducting nanowires with proximity superconductivity, spin-orbit coupling, and magnetic field. The theoretical foundation for this platform was initially developed for a single one-dimensional spinful band with intrinsic superconducting pairing [8, 9]. Due to its compactness this model can be solved analytically, and it predicts that Majorana bound states appear when  $E_Z^2 > \mu^2 + \Delta^2$ , when the Zeeman energy becomes larger than the harmonic mean of the superconducting gap and the chemical potential.

The single-mode model is minimalistic and neglects many physical phenomena that are crucial for understanding the properties of the Majorana bound states. The existing extensions of this model study multimode wires [10], better modeling of the induced gap [11, 12], the role of electrostatics [13], disorder [14–16], and the  $k \cdot p$ -model [17]. The orbital effect of a magnetic field was analyzed both in planar wires [18, 19] and on the surface of a cylinder [20].

We systematically study the influence of the orbital effect of a magnetic field on the symmetries of the Hamiltonian and the topological phase diagram for a three-dimensional (3D) nanowire. The orbital effect of a magnetic field perpendicular to the wire induces a skipping orbit motion of the electrons. The cyclotron radius becomes comparable to the typical wire diameters  $d \sim 100$  nm already at the field of 0.3 T, and at a chemical potential corresponding to the optimal topological band gap. In addition, a field parallel to the wire shifts the energies of each band due to the effect of magnetic flux. We expect the shift of the energies to be comparable to the level spacing when the flux through the wire diameter is of the order of a flux quantum. Our findings are very different from those of Refs. [18–20] because we do not limit our analysis to a Hamiltonian with an artificially high spatial symmetry, or low dimensionality.

## 2.2. MODEL

We consider a 3D semiconducting nanowire with Rashba spin-orbit coupling and proximity-induced s-wave superconductivity. The nanowire cross section is a regular hexagon, and the nanowire is translationally invariant in the  $x$ -direction. Its Bogoliubov-de Gennes Hamiltonian (BdG) is

$$H_{\text{BdG}} = \left( \frac{\mathbf{p}^2}{2m^*} - \mu \right) \tau_z + \alpha (p_y \sigma_x - p_x \sigma_y) \tau_z + \frac{1}{2} g \mu_B \mathbf{B} \cdot \boldsymbol{\sigma} + \Delta \tau_x, \quad (2.1)$$

and it acts on the spinor wave function  $\Psi = (\psi_{e\uparrow}, \psi_{e\downarrow}, \psi_{h\uparrow}, -\psi_{h\downarrow})^T$ , where  $\psi_e, \psi_h$  are its electron and hole components, and  $\psi_\uparrow, \psi_\downarrow$  are the spin-up and spin-down components. We introduced the Pauli matrices  $\sigma_i$  acting on the spin degree of freedom and  $\tau_i$  acting on the electron-hole degree of freedom. Further  $\mathbf{p} = -i\hbar\nabla + e\mathbf{A}\tau_z$  is the canonical momentum, with  $e$  the electron charge and the vector potential  $\mathbf{A} = [B_y(z - z_0) - B_z(y - y_0), 0, B_x(y - y_0)]^T$  chosen such that it does not depend on  $x$ . We set the offsets  $y_0$  and  $z_0$  to ensure that the average vector potential vanishes in the superconductor. This choice corresponds to a limit when the superconductor is thinner than

the screening length and its total supercurrent is zero, appropriate for existing devices. Finally,  $m^*$  is the effective electron mass,  $E_Z = \mu_B g \mathbf{B} \cdot \boldsymbol{\sigma} / 2$  the Zeeman energy,  $\Delta$  the superconducting pairing potential,  $\alpha$  the Rashba spin-orbit coupling strength, and  $\mu = \mu_0 + \mathcal{E}z$  the chemical potential created by a constant electric field  $\mathcal{E}$  in the sample parallel to the  $z$ -axis, such that the Rashba spin-orbit acts in the  $xy$ -plane.

First we consider a model with a constant superconducting gap  $\Delta$  inside the wire [see Fig. 2.1(a)] and then proceed to make a more realistic model of the superconductor. To do that we set the superconducting order parameter  $\Delta$  to zero in the wire and add a superconductor to the top which covers 3/8 of the circumference of the wire [see Fig. 2.1(b)]. We choose the thickness of the superconductor to be 20 nm and set  $\Delta$  in the superconductor such that the induced gap of the lowest band is  $\Delta_{\text{ind}} = 0.250$  meV. This is done by computing band energies at  $k = 0$  over a range of  $\mu$  and matching the minimum to  $\Delta_{\text{ind}}$ . We add a tunnel barrier between the two materials to change the transparency of the superconductor. In the setup of Fig. 2.1(c), we break the reflection symmetry with respect to the  $xz$ -plane by moving the superconductor to the side similar to the experimental setup of Mourik *et al* [3].

To perform the numerical simulations we discretize the Hamiltonian on a cubic lattice with lattice constant  $a = 10$  nm, much smaller than the minimal Fermi wavelength in the parameter range we consider. The discretization does not break or introduce any additional symmetries. The Hamiltonian at a lattice momentum  $k$  equals  $H(k) = h + t \exp(ik) + t^\dagger \exp(-ik)$  where  $h$  is the Hamiltonian of the cross section of the tight-binding system and  $t$  is the hopping matrix between the neighboring cross sections. We introduce the vector potential by Peierls substitution  $t_{nm} \rightarrow t_{nm} \exp(-ie \int \mathbf{A} d\mathbf{l})$  [21]. We perform the numerical simulations using the Kwant code [22]. The source code and the specific parameter values are available in the Supplemental Material of [23]. The resulting raw data are available in Ref. [24].

## 2.3. SYMMETRY ANALYSIS

The Majorana bound states are protected by the combination of the band gap and the particle-hole symmetry of the Hamiltonian  $\mathcal{P}H(k)\mathcal{P}^{-1} = -H(-k)$ . In the basis of Eq. (2.1) this symmetry has the form  $\mathcal{P} = \sigma_y \tau_y \mathcal{K}$ , with  $\mathcal{K}$  the complex conjugation. In general there are no additional symmetries and the Hamiltonian belongs to symmetry class D [25]. Particle-hole symmetry only requires that the energy  $E_n(k)$  of  $n$ -th band at momentum  $k$  is  $E_n(k) = -E_m(-k)$  of some other  $m$ -th band; at the same time  $\mathcal{P}$  puts no constraints on  $E_n$  itself. This means that whenever  $E_n$  changes sign at a certain momentum, the band structure becomes gapless. This tilting of the band structure [26] [shown in the middle panels in Fig. 2.2, where  $E_n(k) \neq -E_m(k)$ ] is a strong effect that does not vanish with superconducting gap or spin-orbit, and can easily become larger than the induced gap, rendering the creation of Majoranas impossible.

The tilting of the band structure is absent if the Hamiltonian has an extra chiral symmetry alongside  $\mathcal{P}$ . It has been shown that the Hamiltonian has an approximate chiral symmetry  $\mathcal{C}H(k)\mathcal{C}^{-1} = -H(k)$ ,  $\mathcal{C} = \sigma_y \tau_y$ , valid when the wire diameter  $d$  is smaller than the spin-orbit length  $l_{so} = \hbar^2 / m^* \alpha$  [27, 28], and  $B_y = 0$ . Then the  $p_y \sigma_x \tau_z$  term, associated with the transverse motion in Eq. (2.1), is negligible. Without the tilting, the system is gapped in every region of parameter space, except at the topological phase boundaries.

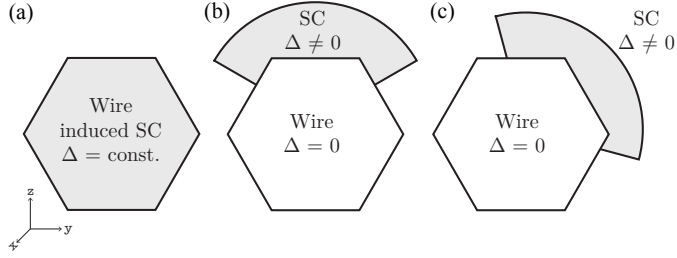


Figure 2.1: Three hexagonal nanowire devices we consider: (a) with an intrinsic pairing term and with a proximity-coupled superconductor (b) on the top and (c) on the side. The last two setups have tunnel barriers between the superconductor and the nanowire.

However, for relevant experimental parameters [3], the orbital terms break this symmetry more strongly than the spin-orbit term, bringing the system back to symmetry class D.

We perform a systematic search of symmetries that the Hamiltonian (2.1) may have. [29] We find the reflection symmetry with respect to the  $yz$ -plane  $\mathcal{R}_x H(k) \mathcal{R}_x^{-1} = H(-k)$ ,  $\mathcal{R}_x = \sigma_x \delta(x + x')$ . It is independent of the wire geometry and spin-orbit strength and guarantees the absence of tilting whenever the field is aligned with the  $x$ -axis. The combined symmetry  $\mathcal{P}' = \mathcal{R}_x \mathcal{P}$  is local in momentum space and ensures the absence of band structure tilting:  $\mathcal{P}' H(k) \mathcal{P}'^{-1} = -H(k)$ .

Additionally, we find a chiral symmetry  $\mathcal{C}' = \tau_y \mathcal{R}_y$ ,  $\mathcal{C}' H(k) \mathcal{C}'^{-1} = -H(k)$ , with  $\mathcal{R}_y = \sigma_y \delta(y + y')$  the reflection with respect to the  $y$ -axis. This chiral symmetry holds when the magnetic field lies in the  $xz$ -plane and none of the potentials in Eq. (2.1) break  $\mathcal{R}_y$ , like in the setups of Figs. 2.1(a) and 2.1(b). When present,  $\mathcal{C}'$  guarantees the absence of band structure tilting just like  $\mathcal{C}$ . This symmetry is present in most theoretical models, and in particular it is obeyed by the Hamiltonians used in Refs. [18–20]. A finite  $B_y$  breaks both  $\mathcal{R}_x$  and  $\mathcal{C}'$  therefore, the bands can tilt and close the topological gap. The band structures in Fig. 2.2 summarize the relation between the geometry of the setup of Figs 2.1(b) and Fig. 2.1(c), magnetic field orientation, and the symmetries of the Hamiltonian.

## 2.4. CALCULATING THE TOPOLOGICAL PHASE DIAGRAM

We use an optimized algorithm to quickly find all the  $\mu$  values corresponding to the topological phase transitions at once. The topological transitions in symmetry class D occur when  $\text{Pf}H_{\text{BdG}}(k=0)$  changes sign.<sup>1</sup> Since the sign change of  $\text{Pf}H_{\text{BdG}}$  is accompanied by the appearance of zero energy states, we need to find  $\mu$  and  $\psi$  such that  $H(\mu, k=0)\psi = 0$ . Using that  $\mu$  enters the Hamiltonian as a prefactor of a linear operator, we rewrite this equation as a generalized eigenproblem:

$$H_{\text{BdG}}(\mu=0, k=0)\psi = \mu \tau_z \psi. \quad (2.2)$$

The real eigenvalues of this eigenproblem are the values of  $\mu$  where the gap closes at  $k=0$  [see Fig. 2.3(a)], and they can be found using standard generalized eigensolvers. If the

<sup>1</sup>The band gap closings at  $k=\pi$  can be treated identically, but they never appear in our model Hamiltonian.

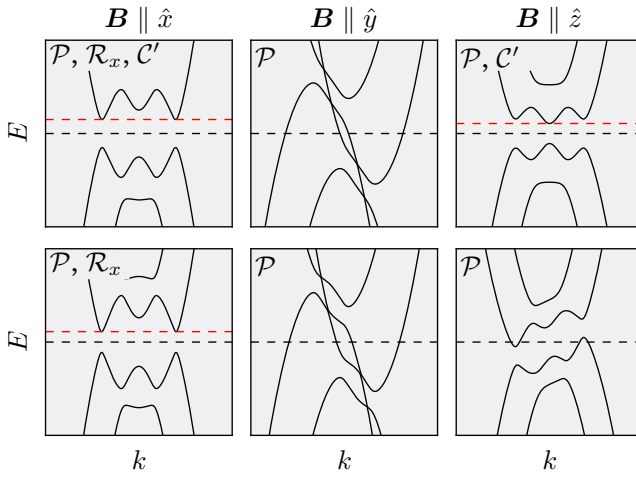


Figure 2.2: Band structures of the setup of Fig. 2.1(b) (top) and Fig. 2.1(c) (bottom). Each panel is labeled with the symmetries respected by the corresponding Hamiltonian. The dashed black line indicates the Fermi energy ( $E = 0$ ). The red dashed lines show the size of the band gap if it is present. In the top row, the reflection symmetry of the wire along the  $y$ -axis  $\mathcal{R}_y$  makes the Hamiltonian have a chiral symmetry  $\mathcal{C}'$  when the magnetic field lies in the  $xz$ -plane. The wire used for the calculation of the bottom row dispersions lacks  $\mathcal{R}_y$  and therefore has no  $\mathcal{C}'$ . Without  $\mathcal{C}'$  the bands are allowed to tilt and the gap may close whenever  $B_y \neq 0$  or  $B_z \neq 0$ . A magnetic field parallel to the  $x$ -axis preserves  $\mathcal{R}_x$ , which protects the band gap from closing.

dispersion relation is gapped also at any finite  $k$ , these gap closings are the boundaries of the topological phase.

Since the eigenvalues of  $H_{\text{BdG}}$  come in opposite sign pairs, the real eigenvalues of Eq. (2.2) always come in degenerate pairs, and each pair lies at a transition between a trivial and a nontrivial phase. We complete the calculation of the topological phase diagram by using as a reference point that  $H_{\text{BdG}}(\mu = -\infty)$  is topologically trivial.

The generalized eigenvalue algorithm for finding phase boundaries does not guarantee that  $H(k)$  is gapped for  $k \neq 0$ , and therefore we calculate the magnitude of the gap  $E_{\text{gap}}$  in the topologically nontrivial regime separately for each set of parameter values. We form a translation eigenvalue problem to calculate all the modes of  $H_{\text{BdG}}$  at a given energy  $E$  and check whether there are any propagating modes [22]. By using a binary search in  $E$  for the energy at which the propagating modes start to appear, we find  $E_{\text{gap}}$  [see Fig. 2.3(b)].

The real space size of the Majoranas  $\xi$  imposes a lower bound on the nanowire length required to create them. To calculate  $\xi$  we find the eigenvalue decomposition of the translation operator at zero energy. The eigenvalue  $\lambda_{\text{min}}$  closest to the unit circle corresponds to the slowest decaying part of the Majorana wave function. We calculate  $\xi$  using

$$\xi = |\log^{-1}|\lambda_{\text{min}}||. \quad (2.3)$$

## 2.5. RESULTS

We use realistic parameters of an InSb nanowire [3]:  $\alpha = 20 \text{ meV nm}$ ,  $m^* = 0.015 m_e$ ,  $\Delta = 0.250 \text{ meV}$ ,  $d = 100 \text{ nm}$ , and  $g = 50$ . At the high fields that are typically used in experiment ( $B \gtrsim 1 \text{ T}$ ), we find that the Zeeman effect of the magnetic field has a lower impact on the phase boundaries than the orbital effect of the magnetic field (see Fig. 2.4). We verify that the band gap is protected by  $\mathcal{C}'$  as long as  $B_y = 0$ , despite that the orbital effect of the magnetic field reduces  $E_{\text{gap}}$ .

In agreement with our expectations a finite  $B_y \lesssim 0.1 \text{ T}$  leads to the closing of the band gap (see Figs. 2.2 and 2.5). The maximum tolerable  $B_y$  becomes smaller with increasing  $\mu$ . The narrow regions with suppressed  $E_{\text{gap}}$  visible in Figs. 2.4(c) and 2.4(d) are the consequence of Dirac cones appearing in  $(k_x, B)$ -space and are protected by  $\mathcal{C}'$ . Breaking  $\mathcal{R}_y$  breaks  $\mathcal{C}'$  and removes these Dirac cones.

We now turn to study the system shown in Fig. 2.1(c) that has  $\mathcal{C}'$  strongly broken and only  $\mathcal{R}_x$  and  $\mathcal{P}$  remaining. Since the induced superconducting gap  $\Delta_{\text{ind}} \approx 250 \mu\text{eV}$  in Ref. [3] is much smaller than the NbTiN gap  $2 \text{ meV}$ , the system must be in the long junction limit, where  $E_{\text{Th}} \ll \Delta$ . In the long junction limit the induced gap equals  $\Delta_{\text{ind}} \approx \hbar T \nu_{\text{F}} / d$ , where  $T$  is the transparency of the tunnel barrier, and  $\nu_{\text{F}}$  the Fermi velocity. In the absence of the orbital effect of a magnetic field, this means that the Zeeman energy has to exceed  $\Delta_{\text{ind}}$  and therefore the critical value of the magnetic field at which the gap closes strongly depends on  $\mu$  as seen in Fig. 2.6(a). With the orbital effect of the magnetic field flux, penetration through the quasiparticle trajectory changes the interference phases, which suppresses the induced gap and causes the topological phase transitions to occur at a value of  $B$  corresponding to a single flux quantum penetrating the wire area [see Fig. 2.6(b)].

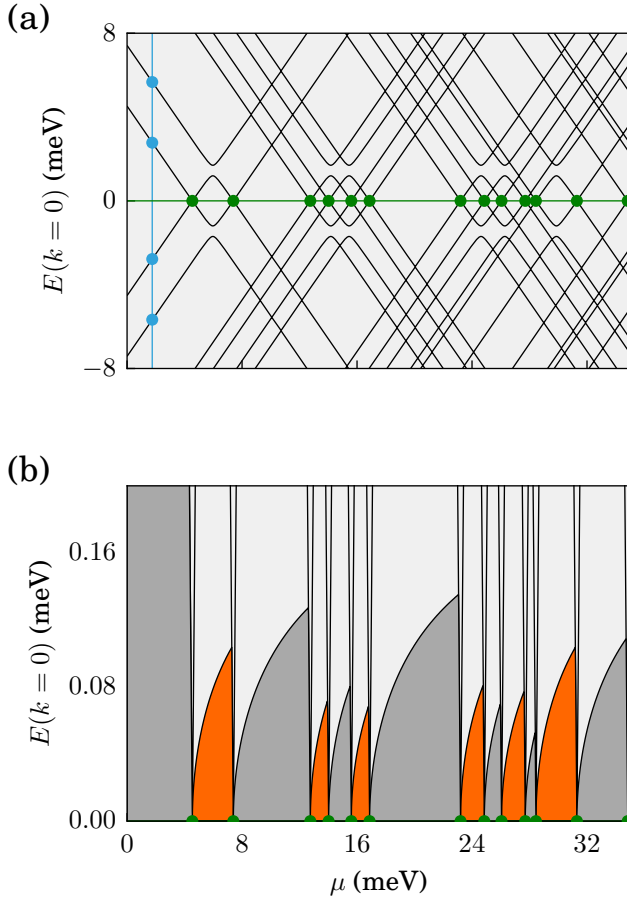


Figure 2.3: (a) Energy spectrum at  $k = 0$  of the setup of Fig.2.1(a) as a function of chemical potential  $\mu$ . The blue points are the solutions of  $H_{\text{BdG}}\Psi = E\Psi$  at fixed  $\mu$  marked by the blue line. The green points are the real eigenvalues of Eq. (2.2) lying at  $E = 0$  (the green line). (b) The gap size for the same setup and parameters, with dark gray regions trivial and the orange regions topological.

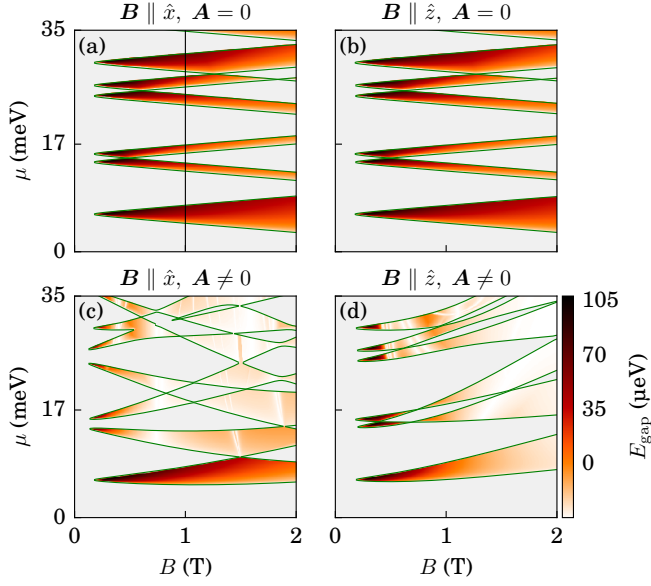


Figure 2.4: Phase diagrams of the setup of Fig. 2.1(a) (a), (b) without the orbital effect of a magnetic field and (c), (d) with it. The green lines depict the topological phase transitions. The colored regions are topologically nontrivial, with the color representing the size of the topological band gap  $E_{\text{gap}}$ . At  $B \gtrsim 1$  T the orbital effect of the magnetic field becomes stronger than the Zeeman effect and changes the sign of the slope of half of the phase boundaries. Furthermore, the orbital effect leads to a faster suppression of the band gaps with magnetic field. The narrow regions with suppressed  $E_{\text{gap}}$  originating from the crossings of the phase boundaries in (c) are due to Dirac cones appearing in  $(k_x, B)$ -space and are protected by  $C'$ . The vertical black line in (a) indicates the value of the magnetic field used in Fig. 2.3.

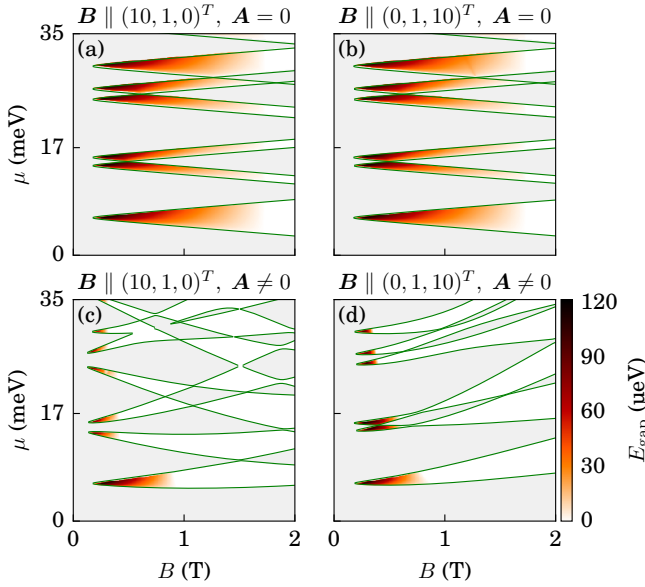


Figure 2.5: Same as Fig. 2.4, but with the magnetic field slightly misaligned. We observe that the band gaps close quickly upon changing the direction of the magnetic field towards the spin-orbit direction in  $y$ .

The Majorana decay lengths  $\xi$  significantly increase when including the orbital effect of the magnetic field in the Hamiltonian (see Fig. 2.7). Specifically, the mode of the distribution of  $\xi$  changes by a factor of  $\sim 4$  in the parameter range we consider (see histograms in Fig. 2.7). However, the minimum values of  $\xi$  without orbital effect and with it are both  $\approx 200$  nm. Therefore,  $\mu$  needs to be tuned with sub-meV precision within the lowest band in order to create Majorana bound states with practically relevant parameters.

To investigate the effect of the spin-orbit coupling on the Majorana properties in the presence of an orbital field, we have repeated the calculations shown in Figs. 2.6 and 2.7 using a fivefold larger spin-orbit strength reported in Ref. [30]. We find that the topological band gap increases overall and in particular the maximal gap grows from 0.14 meV to 0.21 meV, while the minimal decay length remains almost the same. Therefore, increasing spin-orbit strength has a positive but not very strong effect on the topological band gap.

## 2.6. DISCUSSION AND CONCLUSIONS

We have shown that the orbital effect of a magnetic field complicates the creation of Majoranas in nanowires. Orbital terms break the chiral symmetry  $\mathcal{C}$  and prevent the appearance of Majoranas whenever the magnetic field is not aligned with the wire axis. When the field does point along the  $x$ -axis, we find that the reflection symmetry  $\mathcal{R}_x$  in combination with particle-hole symmetry  $\mathcal{P}$  protects the band gap from closing everywhere in  $(B, \mu)$ -space, except at the topological phase boundaries. At experimentally relevant values of magnetic field, the orbital effect has a stronger impact on the dispersion

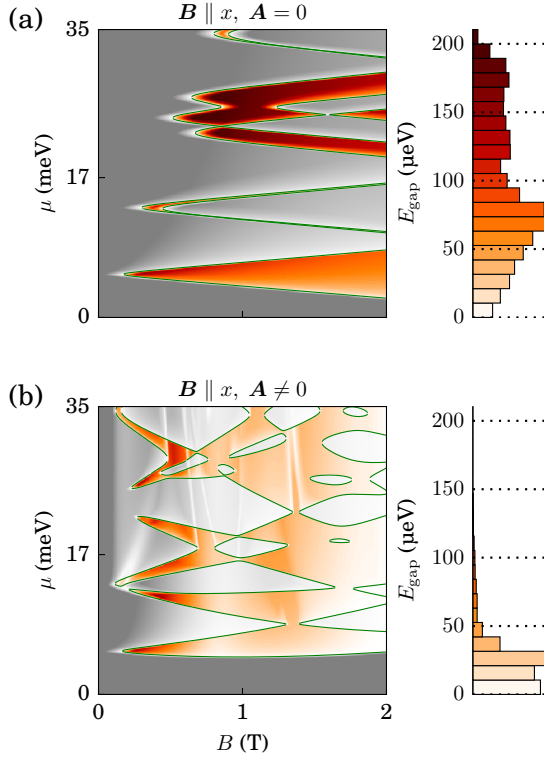


Figure 2.6: Phase diagrams of the setup of Fig. 2.1(c) (a) without the orbital effect of a magnetic field and (b) with it. Color scale corresponds to  $E_{\text{gap}}$ , with the topological regions colored and trivial regions in grayscale. The histograms in the right-hand panels show the distribution of the gap values sampled in the topological regime within the selected parameter range. Neglecting the orbital effect of the magnetic field incorrectly leads to a strong dependence of the critical field on  $\mu$ . With the orbital effect of magnetic field flux penetration through the quasiparticle trajectory changes the interference phases and can suppress the topological gap  $E_{\text{gap}}$ .

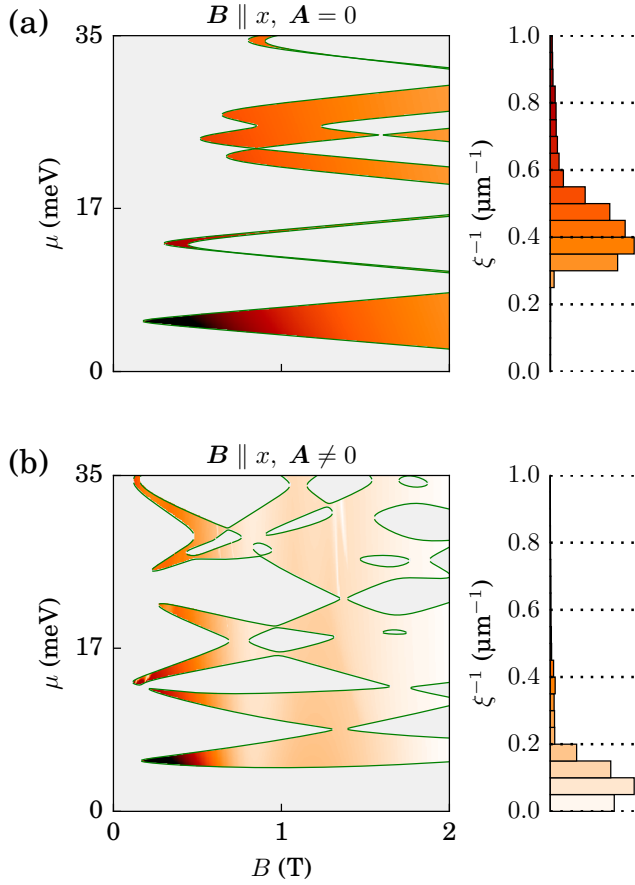


Figure 2.7: Same as Fig. 2.6, but with color representing inverse Majorana length  $\xi^{-1}$ . The histogram and color scales are truncated from above at  $1 \mu\text{m}^{-1}$ . The mode of the distribution of  $\xi^{-1}$  reduces from  $0.35 \mu\text{m}^{-1}$  to  $0.10 \mu\text{m}^{-1}$  upon taking the orbital effect into account. Although the Majorana lengths are overall much larger with the orbital effect of the magnetic field, the minimal length is close to 200 nm in both cases.

relation than the Zeeman effect. Furthermore, the orbital effect suppresses  $E_{\text{gap}}$  and increases  $\xi$ . However, the maximum value of the  $E_{\text{gap}}$  in the topologically nontrivial region does not change as drastically (from 0.21 meV to 0.14 meV) and the minimal decay length changes even less (from 201 nm to 210 nm). The reflection symmetry  $\mathcal{R}_x$  of the Hamiltonian that we consider is respected by any Rashba spin-orbit interaction. Dresselhaus spin-orbit coupling breaks  $\mathcal{R}_x$ ; however, it is expected to be weak in the nanowires.

Our simulations can be made more complete by complementing them with self-consistent electrostatics and magnetic field screening by the superconductor. An additional extension of our work is to go beyond the effective mass approximation and to use the  $k \cdot p$  model. A separate topic of study is the interplay between the orbital effect of the magnetic field and disorder. We expect that the sensitivity to disorder will increase by taking the orbital effect of the magnetic field into account.

Our results suggest that keeping the chemical potential low is required to obtain Majoranas with reasonable length and energy scales. Furthermore, our findings reveal a complication in realizing more sophisticated Majorana setups, such as a T-junction required for braiding. This is because of the requirement that the field should be aligned with the nanowire. A possible strategy to reduce the undesirable orbital effect of the magnetic field is to use nanowires with smaller diameters at a cost of reduced electric field effect and increased disorder sensitivity.

## REFERENCES

- [1] J. Alicea, *New directions in the pursuit of Majorana fermions in solid state systems*, Rep. Prog. Phys. **75**, 076501 (2012).
- [2] C. Beenakker, *Search for Majorana Fermions in superconductors*, Annu. Rev. Condens. Matter Phys. **4**, 113 (2013).
- [3] V. Mourik, K. Zuo, S. M. Frolov, S. R. Plissard, E. P. A. M. Bakkers, and L. P. Kouwenhoven, *Signatures of Majorana Fermions in hybrid superconductor-semiconductor nanowire devices*, Science **336**, 1003 (2012).
- [4] A. Das, Y. Ronen, Y. Most, Y. Oreg, M. Heiblum, and H. Shtrikman, *Zero-bias peaks and splitting in an Al-InAs nanowire topological superconductor as a signature of Majorana fermions*, Nat. Phys. **8**, 887 (2012).
- [5] M. T. Deng, C. L. Yu, G. Y. Huang, M. Larsson, P. Caroff, and H. Q. Xu, *Anomalous zero-bias conductance peak in a Nb-InSb nanowire-Nb hybrid device*, Nano Lett. **12**, 6414 (2012).
- [6] H. O. H. Churchill, V. Fatemi, K. Grove-Rasmussen, M. T. Deng, P. Caroff, H. Q. Xu, and C. M. Marcus, *Superconductor-nanowire devices from tunneling to the multichannel regime: Zero-bias oscillations and magnetoconductance crossover*, Phys. Rev. B **87**, 241401 (2013).
- [7] M. T. Deng, C. L. Yu, G. Y. Huang, M. Larsson, P. Caroff, and H. Q. Xu, *Parity independence of the zero-bias conductance peak in a nanowire based topological superconductor-quantum dot hybrid device*, Sci. Rep. **4**, 7261 (2014).

- [8] R. M. Lutchyn, J. D. Sau, and S. D. Sarma, *Majorana Fermions and a topological phase transition in semiconductor-superconductor heterostructures*, Phys. Rev. Lett. **105**, 077001 (2010).
- [9] Y. Oreg, G. Refael, and F. von Oppen, *Helical liquids and Majorana bound states in quantum wires*, Phys. Rev. Lett. **105**, 177002 (2010).
- [10] A. C. Potter and P. A. Lee, *Multichannel generalization of Kitaev's Majorana end states and a practical route to realize them in thin films*, Phys. Rev. Lett. **105**, 227003 (2010).
- [11] J. Liu, A. C. Potter, K. T. Law, and P. A. Lee, *Zero-bias peaks in the tunneling conductance of spin-orbit-coupled superconducting wires with and without Majorana end-states*, Phys. Rev. Lett. **109**, 267002 (2012).
- [12] T. D. Stanescu, R. M. Lutchyn, and S. D. Sarma, *Soft superconducting gap in semiconductor-based Majorana nanowires*, Phys. Rev. B **90**, 085302 (2014).
- [13] A. Vuik, D. Eeltink, A. R. Akhmerov, and M. Wimmer, *Effects of the electrostatic environment on the Majorana nanowire devices*, New J. Phys. **18**, 033013 (2016).
- [14] A. C. Potter and P. A. Lee, *Topological superconductivity and Majorana fermions in metallic surface states*, Phys. Rev. B **85**, 094516 (2012).
- [15] F. Pientka, G. Kells, A. Romito, P. W. Brouwer, and F. von Oppen, *Enhanced zero-bias Majorana peak in the differential tunneling conductance of disordered multisubband quantum-wire/superconductor junctions*, Phys. Rev. Lett. **109**, 227006 (2012).
- [16] Í. Adagideli, M. Wimmer, and A. Teker, *Effects of electron scattering on the topological properties of nanowires: Majorana fermions from disorder and superlattices*, Phys. Rev. B **89**, 144506 (2014).
- [17] T. D. Stanescu and S. Tewari, *Majorana fermions in semiconductor nanowires: fundamentals, modeling, and experiment*, J. Phys.: Condens. Matter **25**, 233201 (2013).
- [18] J. Osca and L. Serra, *Majorana states and magnetic orbital motion in planar hybrid nanowires*, Phys. Rev. B **91**, 235417 (2015).
- [19] J. S. Lim, L. Serra, R. López, and R. Aguado, *Magnetic-field instability of Majorana modes in multiband semiconductor wires*, Phys. Rev. B **86**, 121103 (2012).
- [20] J. S. Lim, R. Lopez, and L. Serra, *Emergence of Majorana modes in cylindrical nanowires*, EPL **103**, 37004 (2013).
- [21] D. R. Hofstadter, *Energy levels and wave functions of bloch electrons in rational and irrational magnetic fields*, Phys. Rev. B **14**, 2239 (1976).
- [22] C. W. Groth, M. Wimmer, A. R. Akhmerov, and X. Waintal, *Kwant: a software package for quantum transport*, New J. Phys. **16**, 063065 (2014).

- [23] B. Nijholt and A. R. Akhmerov, (2016), see Supplemental Material at <http://link.aps.org/supplemental/10.1103/PhysRevB.93.235434> for the source code that produces the data and figures.
- [24] Nijholt, B. (Bas) and Akhmerov, A.R. (Anton), *Orbital effect of magnetic field on Majorana phase diagram (theory)*, (2016).
- [25] A. Altland and M. R. Zirnbauer, *Nonstandard symmetry classes in mesoscopic normal-superconducting hybrid structures*, Phys. Rev. B **55**, 1142 (1997).
- [26] S. Rex and A. Sudbø, *Tilting of the magnetic field in Majorana nanowires: Critical angle and zero-energy differential conductance*, Phys. Rev. B **90**, 115429 (2014).
- [27] S. Tewari and J. D. Sau, *Topological invariants for spin-orbit coupled superconductor nanowires*, Phys. Rev. Lett. **109**, 150408 (2012).
- [28] M. Diez, J. P. Dahlhaus, M. Wimmer, and C. W. J. Beenakker, *Andreev reflection from a topological superconductor with chiral symmetry*, Phys. Rev. B **86**, 094501 (2012).
- [29] D. Varjas, T. O. Rosdahl, and A. R. Akhmerov, *Qsymm: algorithmic symmetry finding and symmetric hamiltonian generation*, New J. Phys. **20**, 093026 (2018).
- [30] I. van Weperen, B. Tarasinski, D. Eeltink, V. S. Pribiag, S. R. Plissard, E. P. A. M. Bakkers, L. P. Kouwenhoven, and M. Wimmer, *Spin-orbit interaction in InSb nanowires*, Phys. Rev. B **91**, 201413 (2015).

# 3

## SUPERCURRENT INTERFERENCE IN FEW-MODE NANOWIRE JOSEPHSON JUNCTIONS

---

This chapter has been previously published as Kun Zuo, Vincent Mourik, Daniel B. Szombati, Bas Nijholt, David J. Van Woerkom, Attila Geresdi, Jun Chen, Viacheslav P. Ostroukh, Anton R. Akhmerov, Sebasti en R. Plissard, Diana Car, Erik P. A. M. Bakkers, Dmitry I. Pikulin, Leo P. Kouwenhoven, and Sergey M. Frolov, *Supercurrent interference in few-mode nanowire Josephson junctions*, Phys. Rev. Lett. **119**, 187704, (2017)

My contributions to this work include writing parts of the paper, implementing the numerical methods to calculate supercurrents, and performing the numerical simulations.

### 3.1. INTRODUCTION

Semiconductor nanowires coupled to superconductors form a promising platform for generating and investigating Majorana bound states [1–7]. Josephson weak links based on nanowires may provide additional evidence for Majorana bound states, e.g. through the fractional Josephson effect [8–10]. These weak links can also become elements of Majorana-based topological quantum circuits [11–14]. Previous work on semiconductor nanowire Josephson junctions demonstrated supercurrent transistors [15], transport through few channels [16], a nonsinusoidal current-phase relationship [17], nanowire superconducting quantum interference devices (SQUIDs) [18, 19], and gate-tunable superconducting quantum bits [20, 21]. Recent works reported Josephson effects at high magnetic fields, sufficient to generate unpaired Majorana bound states [19, 22–24].

In this chapter we study the critical current as a function of the magnetic field and gate voltage in nanowire Josephson junctions tuned to the mesoscopic few-mode regime. The junctions consist of InSb weak links and NbTiN superconductor contacts. For magnetic fields parallel to the nanowire, we observe a strong suppression of the critical current at magnetic fields on the scale of 100 mT. When the magnetic field exceeds  $\sim 100$  mT, the critical current exhibits aperiodic local minima (nodes). In contrast with supercurrent diffraction in large multimode junctions, the magnetic field nodes of the critical current are strongly tunable by the voltages on local electrostatic gates, and are not uniquely determined by the junction geometry and supercurrent density distribution. To understand our data, we develop a numerical model of a quasiballistic few-mode nanowire of realistic geometry. Our model includes the intrinsic spin-orbit effect, as well as the vector-potential and Zeeman effects of the external magnetic fields. Based on the simulations, we conclude that quantum interference between supercurrents carried by different transverse modes is the dominant mechanism responsible for both the critical current suppression, and the gate-sensitive nodes in the critical current.

### 3.2. EXPERIMENTAL SETUP

Figure 3.1(a) presents a schematic of a few-mode nanowire Josephson junction. The inset of Fig. 3.1(b) shows a device similar to those used in this study and their fabrication process is described in Ref. [4]. The junction consists of an InSb nanowire with a diameter of  $100 \pm 10$  nm with 80 nm thick dc magnetron sputtered NbTiN contacts. The wire sits on top of an array of 50 or 200 nm wide gates isolated from the junction by a dielectric. We report data from devices 1 and 2 in the main text and show additional data from device 3 in the appendix. Device 1(2) has a contact spacing of  $\sim 1 \mu\text{m}$  ( $\sim 625$  nm) and the nanowire is at an angle of  $25^\circ \pm 5^\circ$  ( $0^\circ \pm 5^\circ$ ) with respect to  $B$ . Device 3 has a shorter contact spacing of  $\sim 150$  nm and shows similar behavior of gate-tunable nodes but the initial critical current decay is extended to 400 mT. The measurements were performed in a dilution refrigerator with a base temperature of  $\sim 60$  mK. All bias and measurement lines connected to the device are equipped with standard  $RC$  and copper powder filtering at the mixing chamber stage to ensure a low electrical noise environment. The voltage measurements are performed in the four-terminal geometry.

We set all the gates underneath the nanowire to positive voltages, in the few-mode transparent regime in which no quantum dots are formed between the superconducting

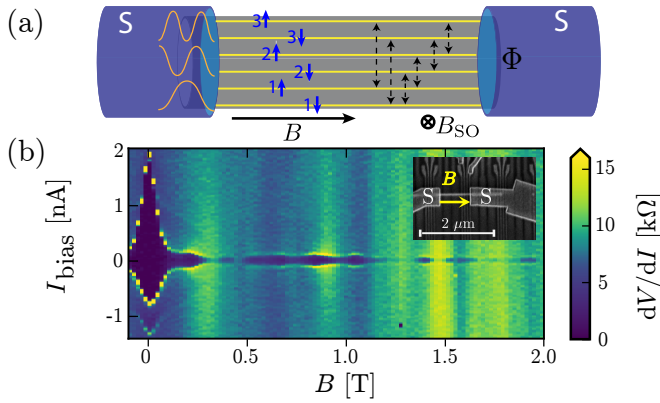


Figure 3.1: (a) Schematic superconductor (S)-nanowire-S Josephson junction. The cross section shows cartoon wave functions of  $n = 3$  transverse modes and the flux  $\Phi$  penetrating the area of the nanowire. The blue arrows indicate spin-resolved modes; the black dashed arrows are same-spin scattering events within the wire. All modes are coupled at the contacts. The directions of  $B$  and the spin-orbit effective field  $B_{SO}$  are indicated. (b) Differential resistance  $dV/dI$  versus  $B$  and  $I_{bias}$ . The current bias sweep direction is from negative to positive. Data from device 1. Inset: SEM image of a typical device similar to those studied here.  $S$  labels the superconducting contacts while  $B$  indicates the in-plane magnetic field for device 2.

contacts, and the normal state conductance exceeds  $2e^2/h$  (see the full gate trace of the supercurrent in the appendix).

### 3.3. SUPERCURRENT MEASUREMENTS AS A FUNCTION OF MAGNETIC FIELD

Figure 3.1(b) shows a typical example of the differential resistance  $dV/dI$  as a function of the magnitude of the magnetic field  $B$  and the current bias  $I_{bias}$  in this few-mode regime, with low resistance supercurrent regions in dark blue around zero current bias. Note that the data at low field are asymmetric with respect to current reversal. Only one sweep direction is plotted for the rest of the figures.

A strong decrease of the switching current is observed from  $B = 0$  T to  $B = 100$ – $200$  mT. Beyond the initial decrease, the critical current exhibits nonmonotonic behavior with multiple nodes and lobes. Despite the  $1 \mu\text{m}$  contact separation, the supercurrent can be resolved up to fields as high as  $B = 2$  T, which is comparable to the estimated strength of the effective spin-orbit field  $B_{SO}$ . At finite magnetic fields where the Josephson energy is suppressed the sharp switching behavior is replaced with a smooth transition to a higher resistance state. In voltage-biased measurements, this manifests as a zero-bias conductance peak (see appendix). This signal can mimic the onset of the topological phase since it is also associated with the zero-bias conductance peak that appears at a finite magnetic field.

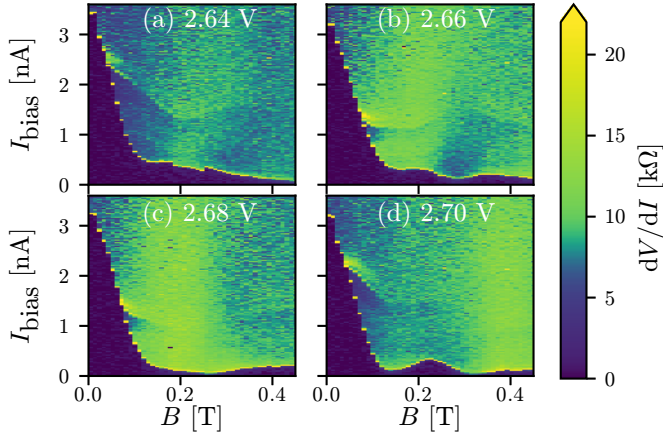


Figure 3.2: (a)–(d)  $dV/dI$  vs  $B$  and  $I_{\text{bias}}$  for different gate voltage settings  $V_g$  indicated above each panel. Data from device 2; see the appendix for the scanning electron micrograph of the device with the tuned gate marked.

### 3.4. POSSIBLE MECHANISMS CAUSING SUPERCURRENT OSCILLATIONS

We now qualitatively discuss the possible explanations for the behavior observed in Fig. 3.1(b). Zeeman splitting can induce  $0 - \pi$ -junction transitions which result in an oscillatory Josephson energy as a function of the magnetic field [25–27]. This alternating  $0 - \pi$  junction behavior is due to spin-up and spin-down channels acquiring different phases as they travel across the junction [Fig. 3.1(a)]. However, in our junctions a strong spin-orbit effective field, which has been reported to point perpendicular to the nanowire [28], reduces the relative phase shifts of spin-up and spin-down and lifts the nodes in the supercurrent [29–31]. For the spin-orbit strength previously reported in InSb nanowires [28, 32], we estimate an effective spin-orbit field  $B_{\text{SO}} \sim 1 - 2$  T for a chemical potential value in the middle of the subband. Therefore, we do not expect the occurrence of  $0 - \pi$ -transitions in ballistic nanowires for fields much lower than this typical value of  $B_{\text{SO}}$ , unless the chemical potential is close to a transverse mode edge (within  $1 - 2$  meV), where  $B_{\text{SO}}$  is suppressed. Given the typical mode spacing of  $10 - 20$  meV [33, 34], in combination with the occurrence of several nodes well below 1 T, the Zeeman  $\pi$ -junction effect is an unlikely explanation for all of the critical current nodes observed here for generic device settings.

Supercurrents carried by different transverse modes would also acquire different phase shifts and interfere due to mode mixing within the wire or at the contact between the nanowire and the superconductor lead [35]. Such an interference is analogous to the Fraunhofer effect in wide uniform junctions: it becomes relevant when a single superconducting flux quantum is threaded through the nanowire cross section, a regime that is reached for  $B \approx 0.25$  T, well within the range of the present study. A comparison of the experimental and numerical data in this chapter suggests that this is the effect that dominates the magnetic field dependence of the critical current.

Transitions in and out of the topological superconducting phase in the nanowire

segments covered by the superconductors were also predicted to induce reentrant critical current [36]. Although we used devices similar to those presented in recent Majorana experiments [4, 7, 37], here we did not gate tune the regions of the wire underneath the superconducting contacts into the topological regime. An accidental topological regime occurring on both sides of the junction in multiple devices is an unlikely explanation for the generic observations reported here.

### 3.5. SUPERCURRENT EVOLUTION WITH MAGNETIC FIELD AND GATE POTENTIAL

Figure 3.2 shows a typical sequence of magnetic field dependences of the critical current, obtained by adjusting one of the narrow local gates. The critical current exhibits multiple nodes [Fig. 3.2(d)], just a single node [Fig. 3.2(c)], or no node [Fig. 3.2(a)] in the same field range. At some nodes the critical current goes to zero, while a nonzero supercurrent is observed at other nodes. No periodic patterns such as those characteristic of a dc-SQUID or a uniform junction are observed. Note that slight changes in the gate voltage are sufficient to dramatically alter the magnetic field evolution curve; the corresponding change in chemical potential  $\Delta\mu$  is small ( $\Delta\mu < 1$  meV) compared with the typical intermode spacing ( $\sim 15$  meV). Furthermore, the gate used only tunes a 100 nm segment of the 650 nm long junction.

Typical gate sweeps of the supercurrent are presented in Fig. 3.3. The critical current is strongly reduced at fields above 100 mT irrespective of the gate voltage. At all fields, the supercurrent is strongly modulated by the gate voltage. However, gate voltages at which nodes in the critical current occur differ for each magnetic field. Thus, no straightforward connection can be made between the zero-field critical current and node positions at a finite field, see also Fig. 3.5(a).

### 3.6. THEORETICAL MODEL

In order to understand the magnetic field evolution of the Josephson effect, we develop an effective low-energy model of a spin-orbit and Zeeman-coupled few-mode nanowire, covered by superconductors at both ends. We define  $x$  as the direction along the wire,  $y$  perpendicular to the wire in the plane of the substrate, and  $z$  perpendicular to both wire and substrate. The corresponding Hamiltonian reads

$$H = \left( \frac{\mathbf{p}^2}{2m^*} - \mu + \delta U \right) \tau_z + \alpha (p_x \sigma_y - p_y \sigma_x) \tau_z + g \mu_B \mathbf{B} \cdot \boldsymbol{\sigma} + \Delta \tau_x. \quad (3.1)$$

Here  $\mathbf{p} = -i\hbar\nabla + e\mathbf{A}\tau_z$  is the canonical momentum, where  $e$  is the electron charge, and  $\mathbf{A} = [B_y z - B_z y, 0, B_x y]^T$  is the vector potential chosen such that it does not depend on  $x$ . Further,  $m^*$  is the effective mass,  $\mu$  is the chemical potential controlling the number of occupied subbands in the wire,  $\alpha$  is the strength of Rashba spin-orbit interaction,  $g$  is the Landé  $g$ -factor,  $\mu_B$  is the Bohr magneton, and  $\Delta$  is the superconducting pairing potential. The Pauli matrices  $\sigma_i$  and  $\tau_i$  act in spin and electron-hole spaces, respectively. We assume that the electric field generated by the substrate points along the  $z$  direction,

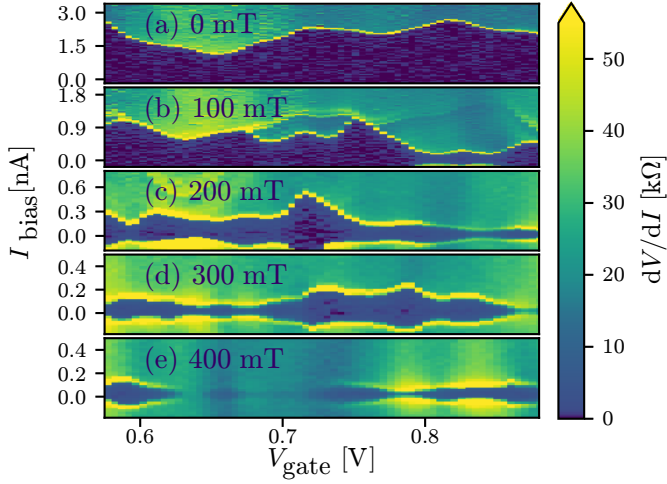


Figure 3.3: (a)-(e)  $dV/dI$  vs  $V_g$  and  $I_{\text{bias}}$  at different  $B$  (indicated within each panel). Data from device 2. The gate used for tuning is different from that used in Fig. 3.2, see the appendix.

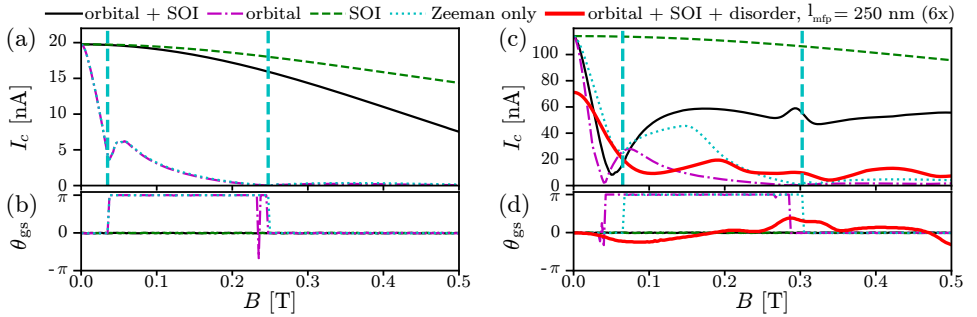


Figure 3.4: Critical current and corresponding ground state phase difference for different combinations of terms in the Hamiltonian. The Zeeman effect ( $g = 50$ ) is present in all of the curves. Only the system corresponding to the red curve labeled with  $l_{\text{mfp}} = 250$  nm includes disorder, for which the critical current is multiplied by a factor of 6. The simulation is performed at  $T = 100$  mK. The curves in panels (a) and (b) are for a single spinful transverse mode ( $\mu = 10$  meV). Panels (c) and (d) are for the multimode (three transverse or six spin-full modes) regime ( $\mu = 20$  meV). The vertical thick dashed light blue lines in (a) and (c) indicate the positions of  $0 - \pi$  transitions in the absence of disorder and with  $\alpha = 0$ ,  $\mathbf{A} = 0$ . Where not specified, the other constant simulation parameters are  $\alpha = 20$  nm meV,  $m_{\text{eff}} = 0.015 m_e$ ,  $\Delta_{\text{ind}} = 0.250$  meV; the lattice constant  $a = 8$  nm, the nanowire diameter  $d_1 = 104$  nm, the outer diameter (with superconductor)  $d_2 = 120$  nm, and the superconductor coverage angle  $\phi = 135^\circ$ . For plots of corresponding current-phase relationships, Josephson energies, and numerical geometry, see the Fig. 3.11, 3.12, and 3.13.

such that the Rashba spin orbit acts in the  $xy$ -plane, which is at low energies equivalent to an effective magnetic field  $\mathbf{B}_{\text{SO}} \parallel \hat{y}$ . We include the vector potential in the tight-binding system using the Peierls substitution [38]. Finally, we include an uncorrelated on-site disorder  $\delta U \in [-U, U]$ , with  $U$  the disorder strength, which we parametrize by a normal state mean free path  $l_{\text{mfp}}$  [39].<sup>1</sup>

We perform numerical simulations of the Hamiltonian (3.1) on a 3D lattice in a realistic nanowire Josephson junction geometry. The critical current is calculated using the algorithm described in Ref. [40] and the Kwant code [41]. We note that for moderately damped and overdamped Josephson junctions, such as those studied here, the theoretical  $I_c$  closely follows the experimentally measured switching current [42]. The source code and the specific parameter values are available in the appendix. The full set of materials, including computed raw data and experimental data, is available in Ref. [43].

### 3.7. DISCUSSION

Numerical results are presented in Figs. 3.4 and 3.5(b). First, we discuss the case of only a single transverse mode occupied [Figs. 3.4(a) and 3.4(b)], which is pedagogical but does not correspond to the experimental regime. When all field-related terms of Eq. (3.1) are included ( $\mathbf{A} \neq 0$ ,  $\alpha \neq 0$ ), we observe a monotonic decay of the critical current much more gradual than in the experiment, due to the absence of the intermode interference effect in the single-mode regime. The  $\pi$ -junction transitions do not appear up to fields of order 0.5T due to the strong spin-orbit effective field, which keeps spin-up and spin-down at the same energy so that they acquire the same phase shifts traversing the junction. The critical current eventually decays because the Zeeman term overtakes the spin-orbit term at fields greater than 0.5 T. When the spin-orbit term is turned off ( $\alpha = 0$ ), we see several  $0 - \pi$  transitions taking place within the studied field range, confirmed by the ground state phase switching between 0 and  $\pi$  at a series of magnetic fields [Fig. 3.4(b)].

The experimentally relevant regime is when several transverse modes are occupied. The measurements display three qualitative features: (i) the initial critical current at  $B = 0$ T is strongly suppressed within 100 – 200mT; (ii) the critical current then revives and continues to display nodes of variable depth and periodicity; (iii) this revival of the critical current after suppression is about 10% of its original value at  $B = 0$ T. Models that neglect the orbital effect display either a slow monotonic decay of the critical current (spin-orbit included,  $\alpha \neq 0$ ), or regular critical current nodes due to  $0 - \pi$  transitions (no spin-orbit,  $\alpha = 0$ ) [Fig. 3.4(d)], as in the single-mode case. When orbital effects are included,  $\mathbf{A} \neq 0$ , observations (i) and (ii) are reproduced but the revival of the critical current after initial suppression is still strong. Inclusion of a realistic amount of disorder, which creates additional interference paths and suppresses supercurrent further, reproduces all observations (i), (ii), and (iii). Thus, we conclude that the experiment is best reproduced when  $\mathbf{A} \neq 0$ ,  $\alpha \neq 0$  and weak disorder that induces intermode scattering is included within the junction model.

The inclusion of disorder in the multimode regime breaks mirror symmetry [30, 31] and generates a spin-orbit field along the external magnetic field  $B$ , which gives rise

<sup>1</sup>To determine  $l_{\text{mfp}}$  we calculate a disorder-averaged normal state conductance  $g$  and evaluate the mean free path  $l_{\text{mfp}}$  by fitting,  $g = g_0 N_{\text{ch}} / (1 + L/l_{\text{mfp}})$ , with  $N_{\text{ch}}$  the number of conduction channels, and  $g_0$  conductance quantum.

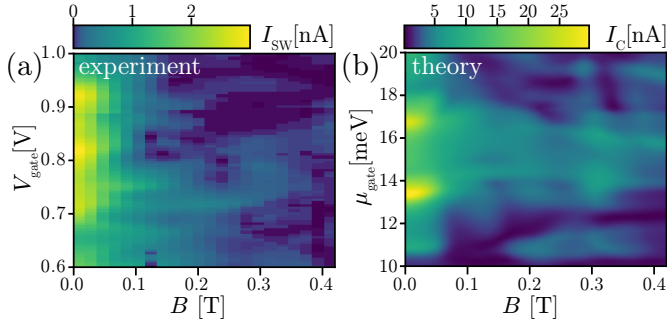


Figure 3.5: Comparison between experimental (a) and numerical (b) results. The parameters for the numerical simulations are the same as in Figs. 3.4(c) and 3.4(d), red curve. The range of the chemical potential in the gated region ( $\mu_{gate}$ ) is chosen using Ref. [44]. The experimental data are taken with device 2.

to a nonsymmetric current-phase relation, inducing a  $\varphi_0$  junction (see Sec. 3.9.8 for a detailed explanation). The ground state phase of the  $\varphi_0$  junction can continuously change between 0 and  $\pi$  [red trace in Fig. 3.4(d)]. Experimental verification of such phase-related effects is not possible in the two-terminal junction geometry used here, it requires phase-sensitive experiments in the SQUID geometry.

In Fig. 3.5 we compare side-by-side experiment and simulations via field-versus-gate maps of the supercurrent. In Fig. 3.5(a), the switching current from a set of  $dV/dI$  versus  $I_{bias}$  traces similar to those in Fig. 3.3 was extracted from device 2 (see the appendix for algorithm details). Beyond the decay of the switching current on the scale of 100 mT, the experimental data show a complex evolution of switching current maxima and minima in gate-field space. Characteristic features of this evolution are reproduced by our simulation shown in Fig. 3.5(b). In particular, the experimentally observed magnetic field scale of initial supercurrent decay is reproduced in the simulation. Furthermore, the gate-tunable maxima and minima of the critical current are recovered in our model; both in experiment and simulation these do not evolve in a regular fashion (a consequence of the complexly shaped interference trajectories). This qualitative agreement found additionally substantiates the applicability of our model to the experimental results.

### 3.8. CONCLUSIONS

Our results are instrumental for modeling Majorana setups. Specifically, the decrease of Josephson energy by an order of magnitude is observed at fields at which the onset of topological superconductivity is reported. This effect should, therefore, be taken into account in efforts to realize recent proposals for fusion and braiding of Majorana fermions [11–14], especially in those that rely on controlling the Josephson coupling [11, 12, 14]. Our findings are applicable not only to bottom-up grown nanowires and networks but also to scalable few-mode junctions fabricated out of two-dimensional electron gases [45, 46]. We suggest that in such devices narrow multimode nanowires should be used. At the magnetic field strengths required for braiding the many modes would facilitate strong Josephson coupling, whereas a small diameter prevents its suppression

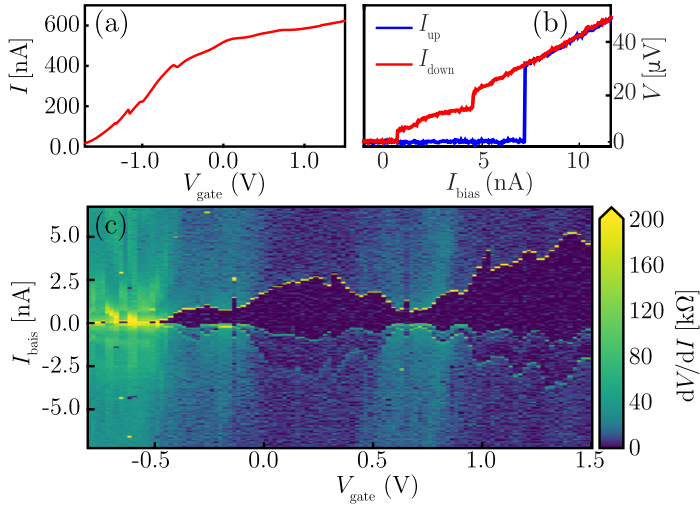


Figure 3.6: (a) Device current as a function of gate voltage,  $V_{\text{bias}} = 10$  mV. Except the gate that is varied in this scan, other gates are at +3 V. (b) Voltage-current characteristic for both upwards (blue) and downwards (red) sweeping direction of current bias. The supercurrent of 8 nA is the maximum supercurrent observed in this device and corresponds to all gates at +3V. (c) Numerical derivative  $dV/dI$  of  $V(I)$  as function of current and gate voltage. Current bias is swept from negative to positive.

due to supercurrent interference.

Phase-sensitive measurements in the SQUID loop geometry will reveal effects such as the Zeeman-induced  $\pi$  junction and the spin-orbit induced  $\varphi_0$  junction, which our study identifies numerically but does not access experimentally. Single quantum mode junctions are within reach thanks to the recent demonstration of quantum point contacts in InSb nanowires at a zero magnetic field [34]. In that regime phenomena such as induced  $p$ -wave superconductivity can be studied in a unique gate-tunable setup, when tuning down to a single spin-polarized mode in the weak link. The results are also applicable to other interesting material systems where spin-orbit, orbital, and Zeeman effects interplay - systems such as Ge/Si, PbS, InAs, and Bi nanowires and carbon nanotubes [47].

## 3.9. APPENDIX

### 3.9.1. ZERO FIELD GATE DEPENDENCE

Characterization of device 2 at  $B=0$  T is shown in Fig. 3.6, devices 1 and 3 behave similarly (data not shown). Current versus local gate voltage is measured at  $V_{\text{bias}} = 10$  mV (Figure 3.6(a)). Taking known series resistances into account, the device resistance of  $\sim 6$  k $\Omega$  is found, corresponding to the sum of the conduction channels and contact resistances.

As shown in Fig. 3.6(b), by optimizing the gate voltages a maximal supercurrent of 8 nA was found, with a corresponding voltage of 32  $\mu$ V, which developed upon switching to the normal state. The junction is hysteretic as shown by the low retrapping current, and has a sharp transition to the normal state, indicating that the junction is in the underdamped

regime. Note that self-heating may also contribute to the hysteresis [48].

### 3.9.2. SHAPIRO STEP MEASUREMENTS

Device 2 has been cooled down a second time with a microwave antenna near the sample. This enabled the study of Shapiro steps in the junction as a function of microwave power and frequency, see Fig. 3.7. The device is again tuned to a multi-mode regime, comparable to  $V_{\text{gate}} = 0.5$  V in Fig. 3.6(c). Due to an increased microwave background noise in the vicinity of the junction upon adding the antenna, an extra rounding of the  $V(I)$ -trace near the switching bias is present.

Figure 3.7(a) is a magnetic field  $B$  dependence of supercurrent in the absence of microwave drive. The supercurrent pattern as a function of  $B$  is similar to the one shown in Fig. 3.2. This indicates that thermally cycling the device did not change the qualitative behavior of the device, although the exact gate tunings are different.

We focus on the power dependence of Shapiro steps at different  $B$  strengths of 0mT, 100mT, 200mT and 300 mT corresponding to Fig. 3.7(c), (e), (f), (g) respectively. The microwave frequency is kept fixed at 2.0 GHz. Shapiro steps show up at voltages corresponding to  $V = n \cdot \frac{hf}{2e}$ , where  $n$  may be a fraction. At  $B = 0$  mT [Fig. 3.7(c)], half integer steps are only weakly present. At  $B = 100$  mT [Fig. 3.7(e)], not only  $n = 1/2$  steps but also weak  $n = 1/4$  steps are visible (not marked with circled number). This is clearly visible in Fig. 3.7(h), where the same data is plotted in a voltage histogram, with high voltage counts corresponding to the plateaus of the Shapiro steps.

The  $B = 200$  mT and  $B = 300$  mT cases [Fig. 3.7(f), (g)] correspond to low critical currents. Nevertheless, Shapiro steps can still be resolved. At  $B = 200$  mT, which is closest to the minimum of critical current, the width of the  $1/2$  step is more than half the width of the 1st step, and it is similarly large compared to the 1st step at 300 mT. Fig. 3.7(i), (j) are the histogram representations of Fig. 3.7(f), (g).

Shapiro steps at fractional frequencies, especially the half-integer steps, have been previously observed in Josephson junctions under various conditions [49–53]. For instance, they can arise due to Josephson coupling of higher orders accompanied by a non-sinusoidal current-phase relationship [54]. In quasi-ballistic few-mode Josephson junctions the current-phase relation is expected to be non-sinusoidal, consistent with half-integer Shapiro steps observed here even at zero magnetic field. The higher order  $1/4$ -steps are more exotic and deserve a deeper study in the future, though they may also originate from a non-sinusoidal current-phase relationship. Non-sinusoidal current-phase relationships are obtained within our model, see Fig. 3.13. However, Fourier analysis of the simulation suggests that Shapiro steps at  $1/3$  the Josephson voltage should dominate over  $1/4$  steps. This discrepancy remains not understood.

In a non-sinusoidal Josephson junction tuned to the  $0 - \pi$  transition the first order Josephson effect which is responsible for strong integer Shapiro steps vanishes, thus the current phase relationship is dominated by higher harmonics. In this case, Shapiro steps at half-integer and integer frequencies are expected to appear with the same step widths. The results presented here show that the ratio of step widths for half integer to integer steps indeed increases near a field-induced node in the critical current. However, the results are not conclusive as to whether this is due to a  $0 - \pi$  transition.

On the other hand, Majorana zero modes coupled across a junction barrier are pre-

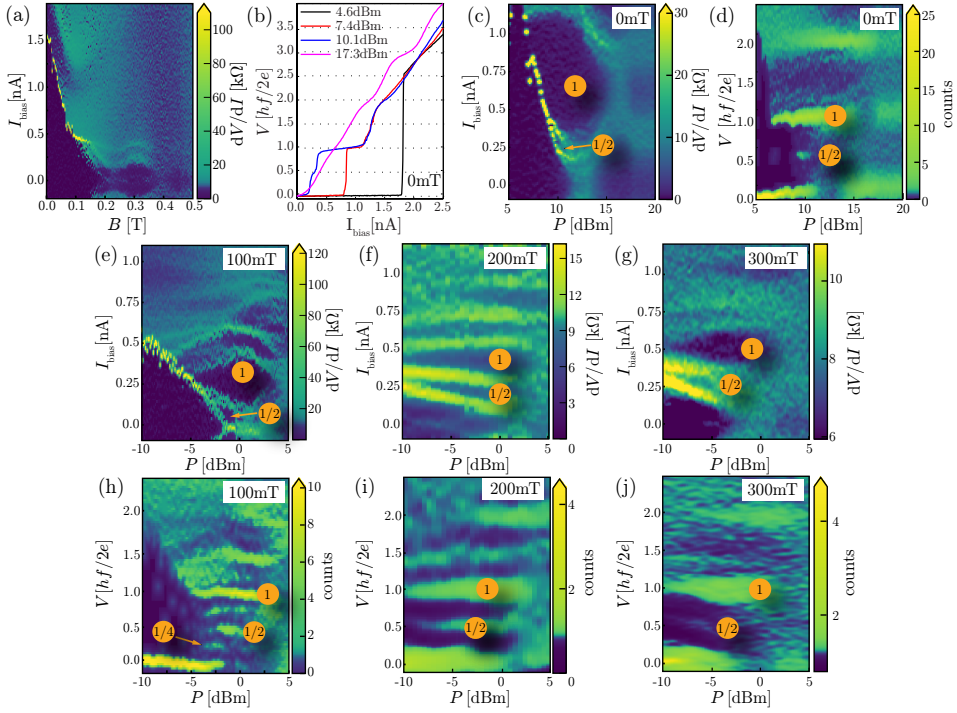


Figure 3.7: Shapiro steps in magnetic field. (a)  $B$  dependence of supercurrent without microwave radiation applied. Numerical derivative  $dV/dI$  of the original  $V(I)$  curves is shown. (b) Shapiro steps at  $B = 0$  T for different microwave powers. At the lowest RF power of 4.6 dBm (black line) no Shapiro steps are present. A half integer step is visible at 10.1 dBm (blue line). (c), (e)-(g) Microwave power dependence of Shapiro steps for different  $B$ . Numerical derivative  $dV/dI$  of the original  $V(I)$  curves is shown, in this representation the Shapiro step plateau corresponds to low differential resistance (blue color). (d), (h)-(j) are Shapiro steps for different  $B$  as a function of microwave power plotted in histogram. High voltage counts correspond to the plateaus in the Shapiro steps. At  $B = 0$  T [panel (c)], the power dependence is dominated by integer Shapiro steps and only a small contribution of half integer steps is visible. At  $B = 100$  mT [panel (e)] fractional steps are visible. Noticeably, not only half integer steps, but also quarter steps are weakly present in panel (h).  $B = 200$  mT [panel (f)] is closest to the minimum supercurrent at 250 mT. Here the half integer and integer steps are almost equal in width. Finally, beyond the minimum of supercurrent, at  $B = 300$  mT [panel (g)], the integer steps increase again in width relative to the half integer step. Curves in (b) are from the same dataset as shown in (c). Values given for the RF power in panels (b)-(j) are the output power of microwave source, 60 dB attenuation, of which 20 dB at low T, is applied. Data is from device 2, second cooldown.

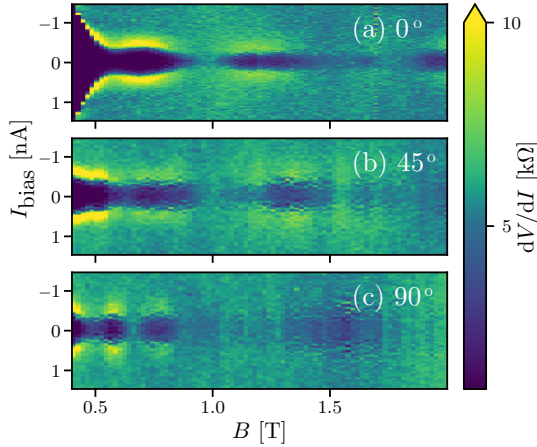


Figure 3.8: Differential resistance measured as a function of current bias and magnetic field strength of device 3. The angle indicated in each panel is the angle of the magnetic field relative to the wire axis, in the plane of the substrate.

dicted to result in disappearing odd-integer Shapiro steps [2, 3]. Thus the behavior observed here is opposite to that expected due to Majorana modes: extra fractional steps in addition to integer steps are observed.

### 3.9.3. ANGLE DEPENDENCE OF FLUCTUATIONS

In this section we present results from device 3 [Fig. 3.9(c)] with contact spacing of 150 nm on which we performed current bias measurements with similar conditions as reported in the main text. Device 3 is fabricated with similar methods as device 1 and 2, with the exception that  $\text{HfO}_x$  is used as the dielectric material instead of  $\text{SiN}_x$ .

The device shows a monotonic decrease of the critical current for magnetic field values up to 400 mT (not shown in the figure). This extended initial decay is attributed to the shorter contact separation, and hence reduced influence of disorder on intermode interference.

Beyond 400 mT, the critical current fluctuates at a period depending on the direction of the magnetic field. Figure 3.8 shows the differential resistance of the device for three different field directions. The top panel shows data where the field is pointed along the nanowire. The critical current decays until the field reaches 600 mT, beyond which it exhibits a weakly pronounced maximum and disappears at 900 mT after which it reappears again. As the field angle is rotated in the plane of the substrate [Figs. 3.8(b),(c)], the critical current decays faster as a function of the field strength, and the subsequent nodes of the critical current are closer spaced in field. We associate this behavior with increased flux through the nanowire at finite angles between the field and the wire.

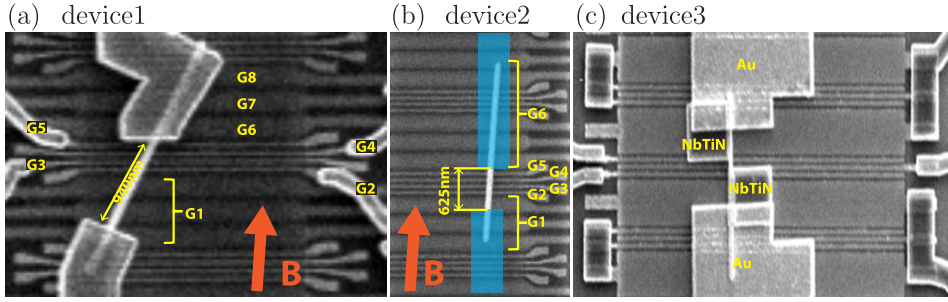


Figure 3.9: Schematics based on SEM picture of device 1, device 2 and device 3. (a) Device 1, with an angle of  $25^\circ \pm 5^\circ$  with the magnetic field. In all devices, not all local gates are operated independently: as indicated in the figures, larger gates are formed by shorting some of the local gates together, e.g. G1. (b) Device 2, shown with the superconducting electrode design superimposed on top of the SEM image, as this device has not been imaged after the final fabrication step. The device has a contact spacing of  $\sim 625$  nm, with the wire at an angle of  $0^\circ \pm 5^\circ$  with respect to magnetic field. (c) Device 3, incorporating two quasi-particles traps (Au) next to the superconducting contacts. The length of the Josephson junction is  $\sim 150$  nm. Device 3 is cooled down in a setup where the magnetic field could be rotated using a 3D vector magnet.

### 3.9.4. ZERO BIAS PEAKS DUE TO SUPERCURRENT CAN ONSET AT FINITE MAGNETIC FIELD

If the Josephson junctions are tuned into the topological regime, devices used in this study can also support Majorana fermions. As a matter of fact, such a design is employed by several groups for the purpose of searching for Majorana zero modes. Here we show that such Josephson junction based devices, even if the contacts are almost  $1 \mu\text{m}$  apart, cannot be used for unambiguous detection of Majorana zero modes [55–57]. Specifically, we observe that, in a voltage-biased measurement, supercurrent can appear as a zero-bias peak that onsets at a finite magnetic field, in the same range of parameters as those used in Majorana experiments, thus mimicking a key Majorana signature.

Figure 3.10 shows the results. By applying a negative voltage to one of the local gates in between the superconducting contacts, a tunneling regime comparable to  $V_{\text{gate}} < -0.5$  V shown in Fig. 3.6(a) for device 2 is achieved. The result of a current biased measurement in this regime is shown in Fig. 3.10(a), a very small (down to 1 pA) supercurrent could be resolved. Interestingly, for gate regimes with lower resistance the supercurrent initially grows as expected, but then the  $dV/dI$  peak related to the switching current broadens and is no longer visible. Here, we focus on the  $B$  dependent behavior as shown in Fig. 3.10(b),(c),(d) at a gate voltage indicated by the yellow line in Fig. 3.10(a). At  $B = 0$  T, no supercurrent was resolved in a current biased measurement, but upon increase of magnetic field, at around 200 mT, a small supercurrent shows up in a slightly more resistive regime. Such a small supercurrent may show up in a differential conductance measurement as a small zero bias peak (ZBP). Indeed, upon switching to a voltage biased differential conductance measurement, a small ZBP with height  $\sim 0.01 \frac{2e^2}{h}$  is found. Note that the ranges in which the supercurrent is visible in a current biased measurement and in which the ZBP is visible in a voltage biased measurement are not identical due to a minor gate switch between the two measurements.

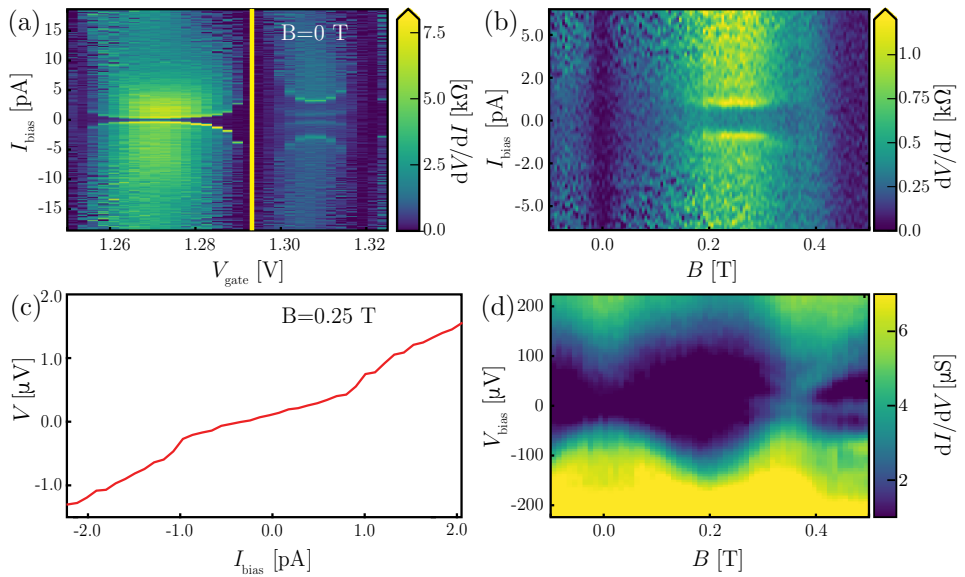


Figure 3.10: Supercurrents and zero bias peaks at finite  $B$ . (a) Differential resistance vs gate. In this scan, one of the local gates is set at -0.45 V and all other gates are at +1.5 V. (b) Differential resistance vs  $B$  at the indicated gate position in (a). (c) Linecut from (b) at  $B = 0.25$  T. (d) Differential conductance vs  $B$  corresponding to (b). Numerical derivative of original  $V(I)$  curves is shown in (a) and (b). Data from device 1.

### 3.9.5. EXTRACTING SWITCHING CURRENT FROM EXPERIMENTAL DATA

To obtain Fig. 3.5(a), switching currents are extracted from a large set of voltage-current characteristics by numerically detecting the voltage step upon switching from the superconducting to the resistive regime. First, an initial low-pass filter is applied to the data reducing spurious fast fluctuations. Next, a numerical derivative of the  $V(I)$ -curve is taken. This first derivative has a clear maximum for an  $V(I)$ -curve with a sharp transition, allowing for straightforward identification of the switching current. However, the finite  $B$ -field  $V(I)$ -curves typically display smooth transitions from the superconducting to the resistive state, resulting in unclear or even absent maximums in the first derivative. A smooth transition still generates a maximum of the second derivative, allowing for identification of the switching current. We, therefore, introduced a threshold for a first derivative maximum, below which a second derivative is taken of the  $V(I)$ -curve with its maximum identified as the switching current. A second threshold is introduced for the maximum of the second derivative, below which the switching current is considered to be zero. Algorithm parameters are optimized to both correctly identify the sharp transitions of large switching currents and to avoid false positives of small switching current.

### 3.9.6. DETAILS OF THE MODELING

We discretize the Hamiltonian Eq. (3.1) on a cubic lattice with a lattice constant of  $a = 8$  nm. The nanowire cross section has a diameter of 104 nm and the superconductor on top of the semiconductor nanowire adds two more layers of unit cells partially covering the nanowire ( $135^\circ$  of the wire's circumference). There are 3 free parameters in the simulation for obtaining the correct induced gap in the nanowires, namely the coverage angle of the superconductor, the tunnel barrier between the SC and the SM, and the superconducting gap. The coverage angle is fixed at  $135^\circ$  in order to save computational time. Since the Meissner effect is not included in the simulation, the exact value of the angle does not play a critical role. The superconducting order parameter  $\Delta$  is set such that the induced gap inside the nanowire at zero field is  $\Delta_{\text{ind}} = 0.250$  meV.

The superconductor has the same lattice constant and effective mass as the nanowire, justified by the long-junction limit. This means that the wave function has most of its weight in the nanowire and that the superconducting shell merely serves as an effective boundary condition that ensures that all particles are Andreev-reflected. Further, the superconductor lacks the Zeeman effect and spin-orbit interaction. Zeeman effect in the superconductor is neglected because the  $g$ -factor in NbTiN is 2, much smaller than the  $g$ -factor in InSb (which is 50). We use realistic parameters of an InSb nanowire [4]:  $\alpha = 20$  meV · nm,  $m^* = 0.015 m_e$ , and  $g = 50$ .

The geometry of the modeled system is shown in Fig. 3.11.

### 3.9.7. DETAILED THEORETICAL ESTIMATES

In this section we estimate the strength of different possible mechanisms that can cause supercurrent fluctuations in the nanowire Josephson junction.

*Interference between orbital channels.* The area of the cross section of the nanowire is  $\sim \pi \times (50 \text{ nm})^2$ . This means that the magnetic field value of  $B \approx 0.26$  T corresponds to one flux quantum penetrating the cross section of the nanowire. At this value of the magnetic field we expect the phase shifts between different bands propagating between the two

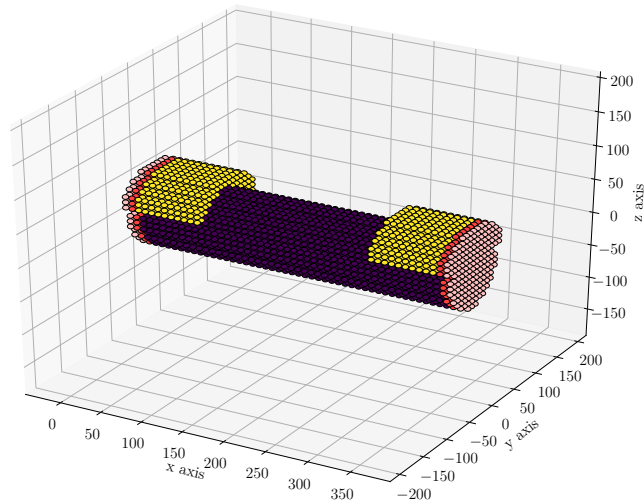


Figure 3.11: The modeled tight-binding system. The purple sites indicate the semi-conductor and the yellow sites show the superconductor. The red and light red colored cross sections indicate that the wire extends infinitely in that direction. We defined the length of the wire  $L$  as the part that is not covered with the superconductor. In this figure for clarity we plot a shorter wire ( $L = 200$  nm), while in the simulations we chose  $L = 640$  nm. The other dimensions used in the simulations are as depicted. Specifically, the wire diameter is 104 nm, the thickness of the superconductor is 16 – 24 nm, and the coverage angle of the superconductor is  $135^\circ$ .

superconductors to be comparable to  $\pi$ . This sets the typical  $B$  scale for the interference of different orbital modes carrying current, which is well within the experimentally observed typical difference in  $B$  of consecutive critical current minimums. This simple estimate neglects the magnetic field expulsion of the superconductor, which may create a higher flux in the nanowire near the superconducting contacts, thus lowering the effective field scale.

These estimates are similar to the analysis for the Fraunhofer-like interference in diffusive many-channel junctions [58]. The novelty is, however, in the small number of channels in our junction, which causes irregular interference instead of the regular Fraunhofer pattern in the former case. Another important observation in our case is that even though the magnetic field is along the junction, it can still cause the interference due to different transverse profiles of the propagating modes.

*Interference between spin channels.* Supercurrent fluctuations can be produced by  $0-\pi$  transitions due to the Zeeman splitting of the Andreev bound states inside the Josephson junction. The characteristic  $B$  scale of such supercurrent fluctuations is determined by the ratio of Zeeman energy to the Thouless energy. This sets the relative phase  $\theta_B$  of the Andreev bound states,  $\theta_B = E_Z L / \hbar v_F$ . Here  $E_Z$  is the Zeeman energy,  $L$  the length of the nanowire junction, and  $v_F$  the Fermi velocity in the nanowire. The junction undergoes a  $0-\pi$  transition when the relative phase difference of the ABS  $\theta_B$  reaches the value  $\pi/2$ . Such a transition is marked by a minimum in the junction critical current as a function of  $B$ . Since  $v_F \approx \sqrt{2\mu/m^*}$ , the field value at which  $\theta_B = \pi/2$  depends on the chemical potential  $\mu$ . We thus estimate the upper bound of the magnetic field at which the first  $0-\pi$  transition occurs by assuming a maximal value of  $\mu \sim 15$  meV corresponding to the intermode spacing [32, 34]. Assuming a junction length of  $L = 1 \mu\text{m}$ , the upper bound of the transition occurs at  $B \sim 0.5$  T. Generally, for smaller  $\mu$ , this value is significantly lower, therefore purely Zeeman induced supercurrent fluctuations are well within the range of our experiment. These estimates are confirmed in our numerical simulations, see  $\alpha = 0$  lines of Fig. 3.12.

*Interference between spin, Zeeman and spin-orbit.*

The previous discussion on spin related interference considered the Zeeman effect only. However, the strong spin-orbit interaction in the nanowire fixes the spin direction to the propagation direction and thus counteracts the effect of the Zeeman splitting. Following Ref. [30], the characteristic parameter for spin-orbit is  $\theta_{SO} = \frac{\alpha k_F L}{\hbar v_F} = \frac{\alpha m^* L}{\hbar^2} = L/L_{SO}$ . Here  $L_{SO}$  is the spin-orbit length, which is expected to be in the 50 – 250 nm range, much shorter than  $L$ . For the Zeeman effect to cause a  $0-\pi$  transition it needs to overcome the spin-orbit spin quantization. This means that the spin-orbit term increases the field at which the first  $0-\pi$  transition happens, and this increase is stronger as the chemical potential is further away from the band bottom. This interplay between Zeeman and spin-orbit interaction is expected to be highly anisotropic [30] in the direction of  $B$ ; the scenario described above assumes the external  $B$  field and effective spin-orbit field to be perpendicular, as is expected for applying  $B$  along the nanowire axis. To substantiate our estimates we have used a nanowire toy model [2, 3] to obtain critical current as a function of gate voltage, magnetic field, and spin-orbit coupling in Fig. 3.12. The model indeed illustrates that the further the chemical potential is from the bottom of the band

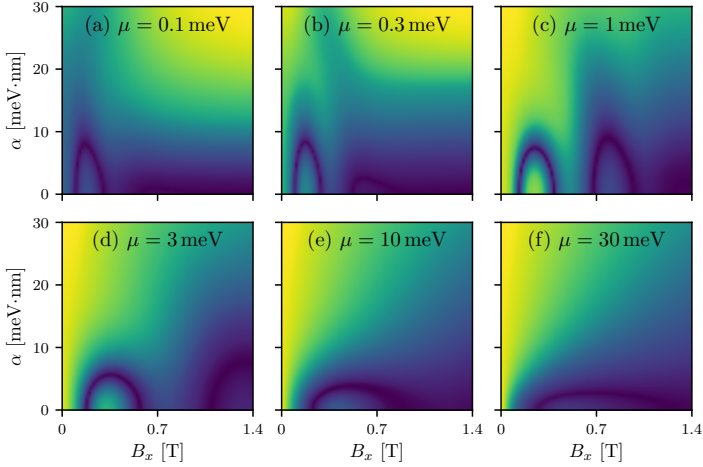


Figure 3.12: Critical currents in a simple one-channel toy nanowire model [2, 3] as a function of spin-orbit coupling strength  $\alpha$  and magnetic field along the wire  $B_x$ . The different panels (a)-(f) are taken at different chemical potentials, 0.1, 0.3, 1, 3, 10, 30 meV respectively. The color scales are not normalized across the different panels, but are all separately scaled to optimally show all features in every plot. We observe how the  $0 - \pi$  transitions at finite  $B_x$  get mutually annihilated upon increasing  $\alpha$ .

the higher is the value of the magnetic field at which the  $0 - \pi$  transition occurs.

In summary, the above estimates suggest that orbital interference is present regardless of the exact value of  $\mu$ , whereas spin related interference is highly restricted in  $\mu$  range. This favors an orbital interference interpretation of the experimental observations, since the supercurrent variations in the experiment are always present in a similar field range no matter the exact gate potential.

To illustrate this reasoning we produced Fig. 3.12, which shows supercurrent fluctuations as a function of the distance to the bottom of the band in a single-band wire. With increasing the distance to the bottom of the bands  $0 - \pi$  transitions happen at higher fields. Upon ramping up spin-orbit strength the  $0 - \pi$  transitions disappear.

### 3.9.8. CURRENT PHASE RELATIONS AND JOSEPHSON ENERGIES

To further support the claims of the previous section and to discuss the role of the ground state phase, we plot the evolution of the critical current and the ground state phase difference with magnetic field, and show the current-phase relations and Josephson energies characteristic for each junction state in Fig. 3.13.  $0 - \pi$  transitions happen in the absence of spin-orbit interaction (Fig. 3.13(a)-(e)). In the presence of spin-orbit and disorder, due to breaking of the spatial symmetry the ground state phase can obtain any single value  $\varphi_0$  (a so-called  $\varphi_0$ -junction) near the crossover between 0 and  $\pi$  states of the junction ((Fig. 3.13(f)-(g)). Note that without disorder, the spatial mirror symmetry with respect to the middle of the system forces all CPRs  $I(\phi)$  to be odd functions and all  $E_J(\phi)$  to be even functions of  $\phi$ . When spatial mirror symmetry holds, the junction's Josephson

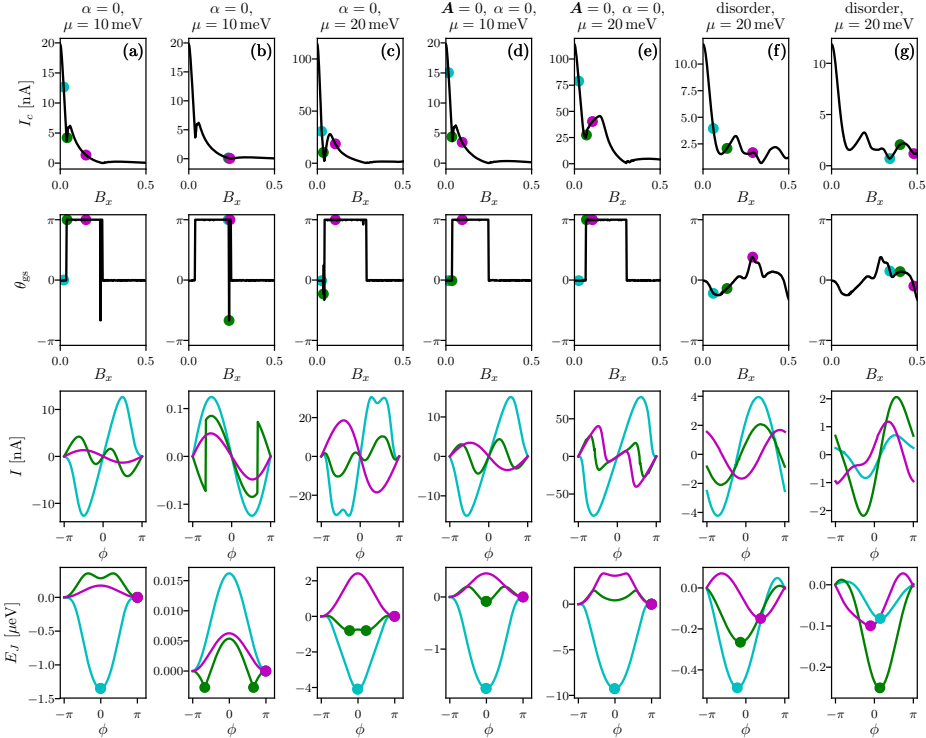


Figure 3.13: (a)-(g) The critical current and ground state phase difference as function of magnetic field, and current phase relations (CPRs) and Josephson energies as functions of phase difference between the superconductors, for different parameters used in the model as labeled. From top to bottom:  $I_c(B_x)$  and  $\theta_{gs}$  with the three points indicating the magnetic field values for which the CPR and  $E_J(\phi)$  are plotted; CPRs for the three values of magnetic fields; Josephson energies as functions of the phase difference. The dot in the bottom row  $E_J$  indicates the energy minimum and the ground state phase difference. Note that identical model parameters are used in columns (a),(b) and (f),(g) respectively, but different consecutive junctions states of interest are highlighted in the individual columns.

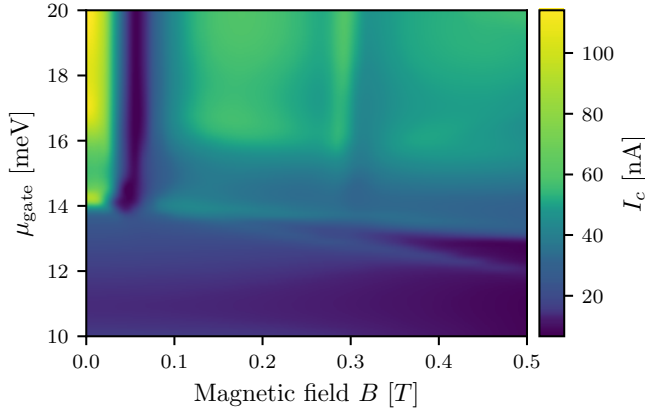


Figure 3.14: Critical current as a function of the magnetic field and the gate voltage. The simulation parameters are identical to the ones used in Fig. 3.5, but we set disorder to zero.

energy can still have a double minimum at  $\pm\varphi$  (a so called  $\varphi$ -junction), thus  $E_J(\varphi)$  taking a Mexican hat type shape (green curves in (Fig. 3.13(b)-(c))). However, because of this restriction imposed by spatial mirror symmetry,  $\varphi$ -junctions are rare and most junctions are either 0 or  $\pi$ -junctions. Contrarily, including disorder breaks this symmetry leading to commonly occurring  $\varphi_0$ -junctions.

### 3.9.9. EFFECT OF DISORDER

Here we prove the essential effect of disorder on the supercurrent dependence on gate voltage. We see the effect of disorder on  $I_c(V_{\text{gate}})$  by comparing Fig. 3.5(b) and Fig. 3.14, where we have switched off disorder. In the clean case, where the main effect of the gate voltage on the supercurrent is via the gradual suppression of transmission through the nanowire, we observe that varying the gate voltage barely causes fluctuations of the supercurrent, even at finite magnetic field. In the disordered case, changing the gate voltage effectively changes the realization of disorder in the region of the wire above the gate, thus causing supercurrent fluctuations. With the increased disorder, the dwell time in the gated region of the nanowire is increased, so the gate voltage dependence increases with reduced mean free path. We found that no disorder and disorder with mean free path greater than the system size cannot explain the observed dependence of the critical current on magnetic field and gate voltage.

### 3.9.10. ROTATING MAGNETIC FIELD

Here we model the supercurrent fluctuations for different directions of the magnetic field, from parallel to the wire to perpendicular to it. The results of the modeling are in Fig. 3.15. We see that for all directions of the field, besides one parallel to the wire, the fluctuation pattern is basically the same. This is in accordance with the experimental observations of Fig. 3.8.

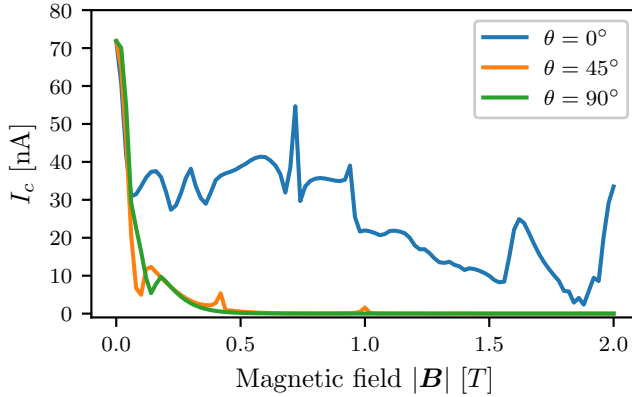


Figure 3.15: Supercurrent as a function of magnetic field for different directions of the applied field. The angle is measured with respect to the wire axis and is rotated in the plane  $\hat{x}$  parallel to the wire and  $\hat{y}$  perpendicular to the wire and parallel to the substrate. We use the same parameters as in Fig. 3.5. Besides the field purely along  $\hat{y}$  the fluctuations pattern is qualitatively similar in all the directions.

## REFERENCES

- [1] A. Y. Kitaev, *Unpaired Majorana fermions in quantum wires*, Phys. Usp. **44**, 131 (2001).
- [2] Y. Oreg, G. Refael, and F. von Oppen, *Helical liquids and Majorana bound states in quantum wires*, Phys. Rev. Lett. **105**, 177002 (2010).
- [3] R. M. Lutchyn, J. D. Sau, and S. D. Sarma, *Majorana Fermions and a topological phase transition in semiconductor-superconductor heterostructures*, Phys. Rev. Lett. **105**, 077001 (2010).
- [4] V. Mourik, K. Zuo, S. M. Frolov, S. R. Plissard, E. P. A. M. Bakkers, and L. P. Kouwenhoven, *Signatures of Majorana Fermions in hybrid superconductor-semiconductor nanowire devices*, Science **336**, 1003 (2012).
- [5] M. T. Deng, S. Vaitiekėnas, E. B. Hansen, J. Danon, M. Leijnse, K. Flensberg, J. Nygård, P. Krogstrup, and C. M. Marcus, *Majorana bound state in a coupled quantum-dot hybrid-nanowire system*, Science **354**, 1557 (2016).
- [6] S. M. Albrecht, A. P. Higginbotham, M. Madsen, F. Kuemmeth, T. S. Jespersen, J. Nygård, P. Krogstrup, and C. M. Marcus, *Exponential protection of zero modes in Majorana islands*, Nature **531**, 206 (2016).
- [7] J. Chen, P. Yu, J. Stenger, M. Hocevar, D. Car, S. R. Plissard, E. P. A. M. Bakkers, T. D. Stanescu, and S. M. Frolov, *Experimental phase diagram of zero-bias conductance peaks in superconductor/semiconductor nanowire devices*, Sci. Adv. **3**, e1701476 (2017).

- [8] J. Wiedenmann, E. Bocquillon, R. S. Deacon, S. Hartinger, O. Herrmann, T. M. Klapwijk, L. Maier, C. Ames, C. Brüne, C. Gould, A. Oiwa, K. Ishibashi, S. Tarucha, H. Buhmann, and L. W. Molenkamp, *4 $\pi$ -periodic Josephson supercurrent in HgTe-based topological Josephson junctions*, Nat. Commun. **7**, 10303 (2016).
- [9] E. Bocquillon, R. S. Deacon, J. Wiedenmann, P. Leubner, T. M. Klapwijk, C. Brüne, K. Ishibashi, H. Buhmann, and L. W. Molenkamp, *Gapless Andreev bound states in the quantum spin Hall insulator HgTe*, Nat. Nanotechnol. **12**, 137 (2016).
- [10] R. Deacon, J. Wiedenmann, E. Bocquillon, F. Domínguez, T. Klapwijk, P. Leubner, C. Brüne, E. Hankiewicz, S. Tarucha, K. Ishibashi, H. Buhmann, and L. Molenkamp, *Josephson radiation from gapless Andreev bound states in HgTe-based topological junctions*, Phys. Rev. X **7**, 021011 (2017).
- [11] T. Hyart, B. van Heck, I. C. Fulga, M. Burrello, A. R. Akhmerov, and C. W. J. Beenakker, *Flux-controlled quantum computation with Majorana fermions*, Phys. Rev. B **88**, 035121 (2013).
- [12] D. Aasen, M. Hell, R. V. Mishmash, A. Higginbotham, J. Danon, M. Leijnse, T. S. Jespersen, J. A. Folk, C. M. Marcus, K. Flensberg, and J. Alicea, *Milestones toward Majorana-based quantum computing*, Phys. Rev. X **6**, 031016 (2016).
- [13] T. Karzig, C. Knapp, R. M. Lutchyn, P. Bonderson, M. B. Hastings, C. Nayak, J. Alicea, K. Flensberg, S. Plugge, Y. Oreg, C. M. Marcus, and M. H. Freedman, *Scalable designs for quasiparticle-poisoning-protected topological quantum computation with Majorana zero modes*, Phys. Rev. B **95**, 235305 (2017).
- [14] S. Plugge, A. Rasmussen, R. Egger, and K. Flensberg, *Majorana box qubits*, New J. Phys. **19**, 012001 (2017).
- [15] Y.-J. Doh, *Tunable supercurrent through semiconductor nanowires*, Science **309**, 272 (2005).
- [16] M. F. Goffman, C. Urbina, H. Pothier, J. Nygård, C. M. Marcus, and P. Krogstrup, *Conduction channels of an InAs-Al nanowire Josephson weak link*, New J. Phys. **19**, 092002 (2017).
- [17] E. M. Spanton, M. Deng, S. Vaitiekėnas, P. Krogstrup, J. Nygård, C. M. Marcus, and K. A. Moler, *Current-phase relations of few-mode InAs nanowire Josephson junctions*, Nat. Phys. **13**, 1177 (2017).
- [18] J. A. van Dam, Y. V. Nazarov, E. P. A. M. Bakkers, S. D. Franceschi, and L. P. Kouwenhoven, *Supercurrent reversal in quantum dots*, Nature **442**, 667 (2006).
- [19] D. B. Szombati, S. Nadj-Perge, D. Car, S. R. Plissard, E. P. A. M. Bakkers, and L. P. Kouwenhoven, *Josephson  $\phi_0$ -junction in nanowire quantum dots*, Nat. Phys. **12**, 568 (2016).

- [20] G. de Lange, B. van Heck, A. Bruno, D. van Woerkom, A. Geresdi, S. Plissard, E. Bakkers, A. Akhmerov, and L. DiCarlo, *Realization of microwave quantum circuits using hybrid superconducting-semiconducting nanowire Josephson elements*, Phys. Rev. Lett. **115**, 127002 (2015).
- [21] T. Larsen, K. Petersson, F. Kuemmeth, T. Jespersen, P. Krogstrup, J. Nygård, and C. Marcus, *Semiconductor-nanowire-based superconducting qubit*, Phys. Rev. Lett. **115**, 127001 (2015).
- [22] J. Paauste, M. Amado, S. Roddaro, F. S. Bergeret, D. Ercolani, L. Sorba, and F. Giazotto, *Pb/InAs nanowire Josephson junction with high critical current and magnetic flux focusing*, Nano Lett. **15**, 1803 (2015).
- [23] J. Tiira, E. Strambini, M. Amado, S. Roddaro, P. San-Jose, R. Aguado, F. S. Bergeret, D. Ercolani, L. Sorba, and F. Giazotto, *Magnetically-driven colossal supercurrent enhancement in InAs nanowire Josephson junctions*, Nat. Commun. **8**, 14984 (2017).
- [24] K. Gharavi, G. W. Holloway, R. R. LaPierre, and J. Baugh, *Nb/InAs nanowire proximity junctions from Josephson to quantum dot regimes*, Nanotechnology **28**, 085202 (2017).
- [25] L. N. Bulaevskii, V. V. Kuzii, and A. A. Sobyenin, *Superconducting system with weak coupling to the current in the ground state*, JETP Lett **25**, 290 (1977).
- [26] A. I. Buzdin, L. N. Bulaevskii, and S. V. Panyukov, *Critical-current oscillations as a function of the exchange field and thickness of the ferromagnetic metal (F) in an SFS Josephson junction*, JETP Lett **35**, 103 (1982).
- [27] E. A. Demler, G. B. Arnold, and M. R. Beasley, *Superconducting proximity effects in magnetic metals*, Phys. Rev. B **55**, 15174 (1997).
- [28] S. Nadj-Perge, V. S. Pribiag, J. W. G. van den Berg, K. Zuo, S. R. Plissard, E. P. A. M. Bakkers, S. M. Frolov, and L. P. Kouwenhoven, *Spectroscopy of spin-orbit quantum bits in indium antimonide nanowires*, Phys. Rev. Lett. **108**, 166801 (2012).
- [29] J. Michelsen, V. S. Shumeiko, and G. Wendin, *Manipulation with Andreev states in spin active mesoscopic Josephson junctions*, Phys. Rev. B **77**, 184506 (2008).
- [30] T. Yokoyama, M. Eto, and Y. V. Nazarov, *Anomalous Josephson effect induced by spin-orbit interaction and Zeeman effect in semiconductor nanowires*, Phys. Rev. B **89**, 195407 (2014).
- [31] T. Yokoyama and Y. V. Nazarov, *Magnetic anisotropy of critical current in nanowire Josephson junction with spin-orbit interaction*, EPL **108**, 47009 (2014).
- [32] I. van Weperen, B. Tarasinski, D. Eeltink, V. S. Pribiag, S. R. Plissard, E. P. A. M. Bakkers, L. P. Kouwenhoven, and M. Wimmer, *Spin-orbit interaction in InSb nanowires*, Phys. Rev. B **91**, 201413 (2015).

- [33] I. van Weperen, S. R. Plissard, E. P. A. M. Bakkers, S. M. Frolov, and L. P. Kouwenhoven, *Quantized conductance in an InSb nanowire*, Nano Lett. **13**, 387 (2012).
- [34] J. Kammhuber, M. C. Cassidy, H. Zhang, Önder Gül, F. Pei, M. W. A. de Moor, B. Nijholt, K. Watanabe, T. Taniguchi, D. Car, S. R. Plissard, E. P. A. M. Bakkers, and L. P. Kouwenhoven, *Conductance quantization at zero magnetic field in InSb nanowires*, Nano Lett. **16**, 3482 (2016).
- [35] K. Gharavi and J. Baugh, *Orbital Josephson interference in a nanowire proximity-effect junction*, Phys. Rev. B **91**, 245436 (2015).
- [36] P. San-Jose, E. Prada, and R. Aguado, *Mapping the topological phase diagram of multiband semiconductors with supercurrents*, Phys. Rev. Lett. **112**, 137001 (2014).
- [37] Önder Gül, H. Zhang, J. D. S. Bommer, M. W. A. de Moor, D. Car, S. R. Plissard, E. P. A. M. Bakkers, A. Geresdi, K. Watanabe, T. Taniguchi, and L. P. Kouwenhoven, *Ballistic Majorana nanowire devices*, Nat. Nanotechnol. **13**, 192 (2018).
- [38] D. R. Hofstadter, *Energy levels and wave functions of bloch electrons in rational and irrational magnetic fields*, Phys. Rev. B **14**, 2239 (1976).
- [39] C. W. J. Beenakker, *Random-matrix theory of quantum transport*, Rev. Mod. Phys. **69**, 731 (1997).
- [40] V. P. Ostroukh, B. Baxevanis, A. R. Akhmerov, and C. W. J. Beenakker, *Two-dimensional Josephson vortex lattice and anomalously slow decay of the Fraunhofer oscillations in a ballistic SNS junction with a warped Fermi surface*, Phys. Rev. B **94**, 094514 (2016).
- [41] C. W. Groth, M. Wimmer, A. R. Akhmerov, and X. Waintal, *Kwant: a software package for quantum transport*, New J. Phys. **16**, 063065 (2014).
- [42] R. L. Kautz and J. M. Martinis, *Noise-affected  $I$ - $v$  curves in small hysteretic Josephson junctions*, Phys. Rev. B **42**, 9903 (1990).
- [43] Zuo, K. (Kun), Mourik, V. (Vincent), Szombati, D.B. (Daniel), Nijholt, B. (Bas), Van Woerkom, D.J. (David), Geresdi, A. (Attila), Chen, J. (Jun), Ostroukh, V.P. (Viacheslav), Akhmerov, A.R. (Anton), Plissard, S.R. (Sébastien), Car, D. (Diana), Bakkers, E.P.A.M. (Erik), Pikulin, D.I. (Dmitry), Kouwenhoven, L.P. (Leo), and Frolov, S.M. (Sergey), *Data and code: Supercurrent interference in few-mode nanowire Josephson junctions*, (2017).
- [44] A. Vuik, D. Eeltink, A. R. Akhmerov, and M. Wimmer, *Effects of the electrostatic environment on the Majorana nanowire devices*, New J. Phys. **18**, 033013 (2016).
- [45] F. Nichele, A. C. Drachmann, A. M. Whiticar, E. C. O'Farrell, H. J. Suominen, A. Fornieri, T. Wang, G. C. Gardner, C. Thomas, A. T. Hatke, P. Krogstrup, M. J. Manfra, K. Flensberg, and C. M. Marcus, *Scaling of Majorana zero-bias conductance peaks*, Phys. Rev. Lett. **119**, 136803 (2017).

- [46] J. S. Lee, B. Shojaei, M. Pendharkar, A. P. McFadden, Y. Kim, H. J. Suominen, M. Kjaergaard, F. Nichele, H. Zhang, C. M. Marcus, and C. J. Palmström, *Transport studies of epi-Al/InAs two-dimensional electron gas systems for required building-blocks in topological superconductor networks*, Nano Lett. **19**, 3083 (2019).
- [47] J.-P. Cleuziou, W. Wernsdorfer, V. Bouchiat, T. Ondarçuhu, and M. Monthieux, *Carbon nanotube superconducting quantum interference device*, Nat. Nanotechnol. **1**, 53 (2006).
- [48] H. Courtois, M. Meschke, J. T. Peltonen, and J. P. Pekola, *Origin of hysteresis in a proximity Josephson junction*, Phys. Rev. Lett. **101**, 067002 (2008).
- [49] K. W. Lehnert, N. Argaman, H.-R. Blank, K. C. Wong, S. J. Allen, E. L. Hu, and H. Kroemer, *Nonequilibrium ac Josephson effect in mesoscopic Nb-InAs-Nb junctions*, Phys. Rev. Lett. **82**, 1265 (1999).
- [50] P. Dubos, H. Courtois, O. Buisson, and B. Pannetier, *Coherent low-energy charge transport in a diffusive S-N-S junction*, Phys. Rev. Lett. **87**, 206801 (2001).
- [51] R. C. Dinsmore, M.-H. Bae, and A. Bezryadin, *Fractional order shapiro steps in superconducting nanowires*, Appl. Phys. Lett. **93**, 192505 (2008).
- [52] H. Sellier, C. Baraduc, F. Lefloch, and R. Calemczuk, *Half-integer shapiro steps at the  $0 - \pi$  crossover of a ferromagnetic Josephson junction*, Phys. Rev. Lett. **92**, 257005 (2004).
- [53] M. Chauvin, P. vom Stein, H. Pothier, P. Joyez, M. E. Huber, D. Esteve, and C. Urbina, *Superconducting atomic contacts under microwave irradiation*, Phys. Rev. Lett. **97**, 067006 (2006).
- [54] Z. Radović, L. Dobrosavljević-Grujić, and B. Vujčić, *Coexistence of stable and metastable  $0$  and  $\pi$  states in Josephson junctions*, Phys. Rev. B **63**, 214512 (2001).
- [55] M. T. Deng, C. L. Yu, G. Y. Huang, M. Larsson, P. Caroff, and H. Q. Xu, *Anomalous zero-bias conductance peak in a Nb-InSb nanowire-Nb hybrid device*, Nano Lett. **12**, 6414 (2012).
- [56] M. T. Deng, C. L. Yu, G. Y. Huang, M. Larsson, P. Caroff, and H. Q. Xu, *Parity independence of the zero-bias conductance peak in a nanowire based topological superconductor-quantum dot hybrid device*, Sci. Rep. **4**, 7261 (2014).
- [57] A. D. K. Finck, D. J. V. Harlingen, P. K. Mohseni, K. Jung, and X. Li, *Anomalous modulation of a zero-bias peak in a hybrid nanowire-superconductor device*, Phys. Rev. Lett. **110**, 126406 (2013).
- [58] J. C. Cuevas and F. S. Bergeret, *Magnetic interference patterns and vortices in diffusive SNS junctions*, Phys. Rev. Lett. **99**, 217002 (2007).



# 4

## SPIN-ORBIT PROTECTION OF INDUCED SUPERCONDUCTIVITY IN MAJORANA NANOWIRES

---

This chapter has been previously published as Jouri D. S. Bommer, Hao Zhang, Önder Gül, Bas Nijholt, Michael Wimmer, Filipp N. Rybakov, Julien Garaud, Donjan Rodic, Egor Babaev, Matthias Troyer, Diana Car, Sébastien R. Plissard, Erik P. A. M. Bakkers, Kenji Watanabe, Takashi Taniguchi, Leo P. Kouwenhoven, *Spin-orbit protection of induced superconductivity in Majorana nanowires*, Phys. Rev. Lett. **122**, 187702, (2019)

My contributions to this work are developing and implementing the numerical methods used in the tight-binding calculations, performing the simulations that calculate the conductance, as well as writing about them.

## 4.1. INTRODUCTION

Spin-orbit interaction (SOI) is a relativistic effect that results from electrons moving (orbit) in an electric field ( $E$ ) experiencing a magnetic field ( $B_{SO}$ ) in their moving reference frame that couples to the electron's magnetic moment (spin). SOI is an essential ingredient of various realizations of topological superconductors, which host Majorana zero modes, the building blocks of topological quantum computation [1–3]. The prime platform for topological quantum computation is based on a semiconductor nanowire coupled to a superconductor, where the proximity effect opens a superconducting energy gap in the density of states of the nanowire [4, 5]. In general, a magnetic field suppresses superconductivity by closing the superconducting gap due to Zeeman and orbital effects [6]. If the nanowire has strong SOI, suppression of the superconducting gap is counteracted and a sufficiently large Zeeman energy drives the system into a topological superconducting phase, with Majorana zero modes localized at the wire ends [4, 5]. The main experimental effort in the last few years has focused on detecting these Majorana zero modes as a zero-bias peak in the tunneling conductance [7–13]. However, SOI, the mechanism providing the topological protection, has been challenging to detect directly in Majorana nanowires.

The electric field that gives rise to SOI in our system mainly results from structural inversion asymmetry of the confinement potential (Rashba SOI), which depends on the work function difference at the interface between the nanowire and the superconductor and on voltages applied to nearby electrostatic gates [14–17]. The Rashba SOI in nanowires has been investigated extensively by measuring spin-orbit related quantum effects: level repulsion of quantum dot levels [18, 19], and of Andreev states [9, 20], weak anti-localization in long diffusive wires [21, 22], and a helical liquid signature in short quasiballistic wire [23]. However, the SOI strength relevant to the topological protection is affected by the presence of the superconductor, necessitating direct observation of SOI in Majorana nanowires. Here, we reveal SOI in an InSb nanowire coupled to a NbTiN superconductor through the dependence of the superconducting gap on the magnetic field, both strength and orientation. We find that the geometry of the superconductor on the nanowire strongly modifies the direction of the spin-orbit field, which is further tunable by electrostatic gating, in line with the expected modifications of the electric field due to work function difference and electrostatic screening at the nanowire-superconductor interface.

## 4.2. DEVICE CHARACTERIZATION

Figure 4.1(a) shows the device image. An InSb nanowire (blue) is covered by a NbTi/NbTiN superconducting contact (purple) and a Cr/Au normal metal contact (yellow). The barrier gate underneath the uncovered wire (red) can deplete the nanowire, locally creating a tunnel barrier. The tunneling differential conductance ( $dI/dV$ ) resolves the induced superconducting gap, by sweeping the bias voltage ( $V$ ) across the tunnel barrier [Fig. 4.1(b)]. The dashed arrow indicates the induced gap of 0.65 meV. In this device, we have recently shown ballistic transport and Majorana signatures [10].

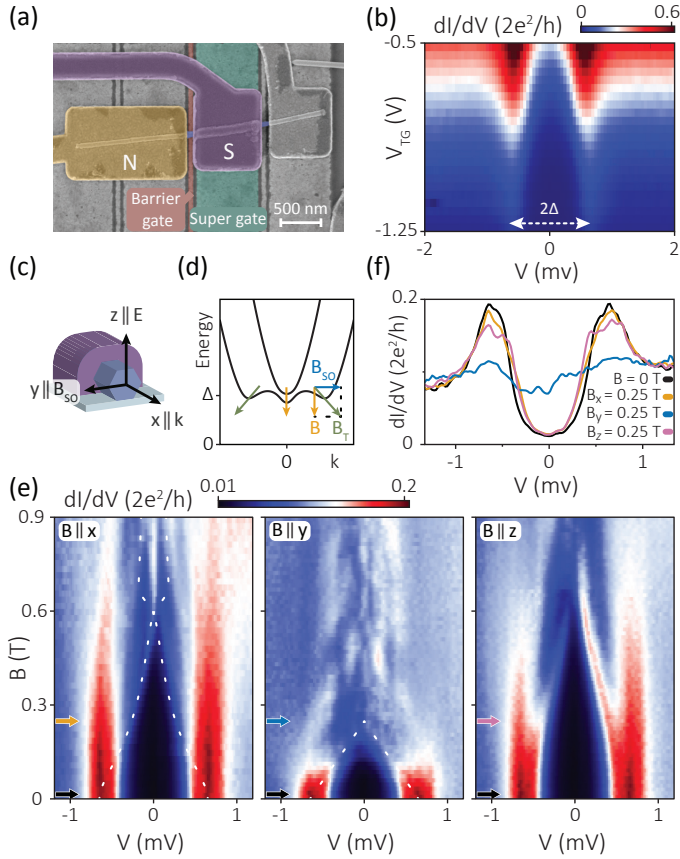


Figure 4.1: (a) False-color scanning electron micrograph of Majorana nanowire device *A*. An InSb nanowire (blue) is contacted by a normal metal contact (*N*, yellow) and a NbTiN superconducting contact (*S*, purple). The additional contact (gray) is kept floating. The nanowire is isolated from the barrier gate (red) and the super gate (green) by  $\sim 30$  nm thick boron nitride. (b) Differential conductance  $dI/dV$  as a function of bias voltage  $V$  and barrier gate voltage  $V_{\text{barrier}}$  at  $B = 0$  T. (c) Schematic of the nanowire device and definition of the axes. (d) Band diagram of a Majorana nanowire at an externally applied magnetic field  $B$  perpendicular to the spin-orbit field  $B_{\text{SO}}$ . The arrows indicate the total magnetic field  $B_T = B + B_{\text{SO}}$  along which the spin eigenstates are directed. At  $k = 0$  the spin always aligns with  $B$ . At increasing  $k$ ,  $B_{\text{SO}}$  increases, tilting the spin more towards  $B_{\text{SO}}$ . (e)  $dI/dV$  as a function of  $V$  at  $B$  along  $x$ ,  $y$ ,  $z$  (left, middle, right) for super gate voltage  $V_{\text{SG}} = 0$  V. The white dashed lines indicate a fit to the gap closing corresponding to  $\alpha = 0.15 \pm 0.05$  eVÅ. (f) Horizontal line cuts of (e) at  $B$  indicated by the colored arrows in (e).

### 4.3. SPIN-ORBIT PROTECTION OF SUPERCONDUCTIVITY

The magnetic field ( $B$ ) dependence of the induced gap of device  $A$ , with  $B$  along three different directions, is shown in Fig. 4.1(e). The coordinate system is illustrated in Fig. 4.1(c). The  $x$  axis is along the nanowire, parallel to the electron momentum ( $k$ ). The  $z$  axis is perpendicular to the substrate and coincides with the electric field ( $E$ ) direction due to the spatial symmetry of the device and the bottom gate. Since the Rashba spin-orbit field ( $B_{\text{SO}} \propto E \times k$ ) is perpendicular to both  $k$  and  $E$ , it points along the  $y$  axis. When  $B$  is aligned with  $x$  or  $z$  [left and right panels in Fig. 4.1(e)], both perpendicular to  $B_{\text{SO}}$ , the gap closes slowly (at around 0.6 T), followed by the emergence of a zero-bias peak possibly characteristic of a Majorana zero mode when  $B$  is along the nanowire, although we emphasize that a conjecture of Majorana zero modes is not essential for the purposes of this chapter. On the contrary, when  $B$  is aligned with the  $y$  axis (middle panel), parallel to  $B_{\text{SO}}$ , the gap closes much faster (at around 0.25 T). Figure 4.1(f) shows the line cuts at  $|B| = 0.25$  T along the three axes: for  $B \perp B_{\text{SO}}$ , the gap is almost the same as when  $B = 0$  T, while the gap is closed for  $B \parallel B_{\text{SO}}$ . This observation matches the predictions of the Majorana nanowire model, as illustrated in Fig. 4.1(d): when  $B \perp B_{\text{SO}}$ , SOI counteracts the Zeeman-induced gap closing by rotating the spin eigenstate towards  $B_{\text{SO}}$ , which reduces the component of the Zeeman field along the direction of the spin eigenstate. In contrast, when  $B \parallel B_{\text{SO}}$ , the spin eigenstate is always parallel to  $B$ , which prevents spin-orbit protection and results in a fast gap closing [24, 25]. This pronounced anisotropy of the gap closing with respect to different  $B$  directions is universally observed in over ten devices (four shown in this chapter) for all gate settings (see Fig. 4.8), which is a direct consequence of SOI in Majorana nanowires.

### 4.4. INTERPRETATION OF THE ANISOTROPY

Before we discuss the SOI in more detail, we rule out alternative mechanisms for the anisotropy which can originate in the bulk superconductor, or the InSb nanowire. First, an anisotropic magnetic field-induced closing of the bulk superconducting gap is excluded for the fields we apply, which are far below the critical field of NbTiN ( $>9$  T [26]). We note that this is different from aluminum films [9, 11, 27, 28], where a small magnetic field ( $<0.3$  T) perpendicular to the film completely suppresses superconductivity, making them unsuitable to reveal SOI from an anisotropic gap closing. Next, we consider Meissner screening currents in NbTiN that can cause deviations in the magnetic field in the nanowire. Our Ginzburg-Landau simulations show that the field corrections due to Meissner screening are negligible (see Fig. 4.5), since the dimensions of the NbTiN film ( $<1 \mu\text{m}$ ) are comparable to the penetration depth ( $\sim 290$  nm). The simulations also show that vortex formation is most favorable along the  $z$  axis, which implies that the observed anisotropic gap closing is not caused by gap suppression due to vortices near the nanowire [29], since we do not observe the fastest gap closing along  $z$  [Fig. 4.1(f)]. Finally, in the InSb nanowire, the Zeeman  $g$  factor can become anisotropic due to quantum confinement [19, 30, 31]. However, our nanowire geometry leads to confinement in both the  $y$  and  $z$  directions, implying similar gap closing along  $y$  and  $z$ , inconsistent with our observations [Fig. 4.1(e)].

Having excluded the above mechanisms, we are now left with three effects: spin

splitting of the electron states in magnetic fields with the Landé  $g$  factor (Zeeman effect), the orbital effect of the magnetic field representing the Lorentz force acting on traveling electrons, and SOI. To investigate the role of these effects, we use a theoretical three-dimensional Majorana nanowire model defined by the Hamiltonian [4–6]:

$$H = \left( \frac{\mathbf{p}^2}{2m^*} - \mu + V(y, z) \right) \tau_z + \frac{\alpha}{\hbar} \boldsymbol{\sigma} \cdot (\hat{\mathbf{E}} \times \mathbf{p}) \tau_z + \frac{1}{2} g \mu_B \mathbf{B} \cdot \boldsymbol{\sigma} + \Delta_0 \tau_x$$

Here, the first term represents the kinetic and potential energy, with  $\mu$  the chemical potential measured from the middle of the helical gap and  $V(y, z) = \frac{\Delta V_G}{R} [0, y, z] \cdot \hat{\mathbf{E}}$  is the electrostatic potential in the wire, whose magnitude is parametrized by  $\Delta V_G$ , with  $\hat{\mathbf{E}}$  the direction of the electric field and  $R$  the wire radius. The orbital effect enters the Hamiltonian via the vector potential  $\mathbf{A}$  in the canonical momentum:  $\mathbf{p} = -i\hbar\nabla + e\mathbf{A}$ . Here,  $e$  is the electron charge,  $\hbar$  is Planck's constant, and  $m^* = 0.015 m_e$  is the effective mass with  $m_e$  the electron mass. The second term represents Rashba SOI characterized by a SOI strength  $\alpha$ , which we set to  $0.2 \text{ eV}\text{\AA}$  to find qualitative agreement with the measurements. The third term is the Zeeman term, with an isotropic  $g$  factor set to 50 and  $\mu_B$  is the Bohr magneton. The last term accounts for the superconducting proximity effect, which we implement in the weak coupling approximation [6]. The Pauli matrices  $\tau$  and  $\sigma$  act in the particle-hole and spin space respectively. We perform numerical simulations of this Hamiltonian on a 3D lattice in a realistic nanowire geometry using the KWANT code [32]. We note that a recent theory work shows that the anisotropy is unaffected by additional factors such as the wire length, temperature, and strong coupling to the superconductor [33]. Additional details are provided in the Appendix 4.7.

We identify which effects explain the observed anisotropic gap closing behavior by including them separately in our simulations. Figure 4.2(a) shows the magnetic field dependence of the gap without SOI (setting  $\alpha = 0$  in the Hamiltonian). In contrast to Fig. 4.1(e) the gap closes around 0.3 T for all three directions, reflecting the dominant contribution of the Zeeman effect. In Fig. 4.2(b), we turn on the SOI, and turn off the orbital effect by setting the magnetic vector potential  $\mathbf{A} = 0$ , which qualitatively reproduces the anisotropic behavior between the  $y$  axis and the  $x$  and  $z$ -axes. We have explored other combinations of parameters and find that the experimental results of Fig. 4.1(e) can only be reproduced by including SOI. We note that adding the orbital effect in Fig. 4.2(c) shifts the gap closing to a field almost twice as small for  $B \parallel y$ , which explains why we observe a gap closing for  $B \parallel y$  at around 0.25 T, far below 0.45 T, the critical field expected when only the Zeeman effect with  $g = 50$  suppresses the gap. By fitting the curvature of the gap closing [34, 35] along  $x$  [white dashed line in Fig. 4.1(e)] we estimate a range of the SOI strength  $\alpha$  of  $0.15 - 0.35 \text{ eV}\text{\AA}$  from devices *A-D* (for fitting details and fits to additional devices, see Sec. 4.7.3). This SOI strength is in agreement with the values extracted from level repulsion of Andreev states [20, 36] in an additional device *E*, see Sec. 4.7.3 for more details. Since  $\alpha$  depends on the electric field in the wire, we expect the observed variation in the SOI strength of devices to be caused by differences in the applied gate voltages and wire diameter. Recently, the level repulsion of Andreev states in InSb nanowires covered with epitaxial aluminum has shown a SOI strength of approximately  $0.1 \text{ eV}\text{\AA}$  [20], slightly lower than we find for NbTiN covered nanowires, most likely due to strong coupling to the aluminum superconductor, leading to stronger renormalization of the InSb material

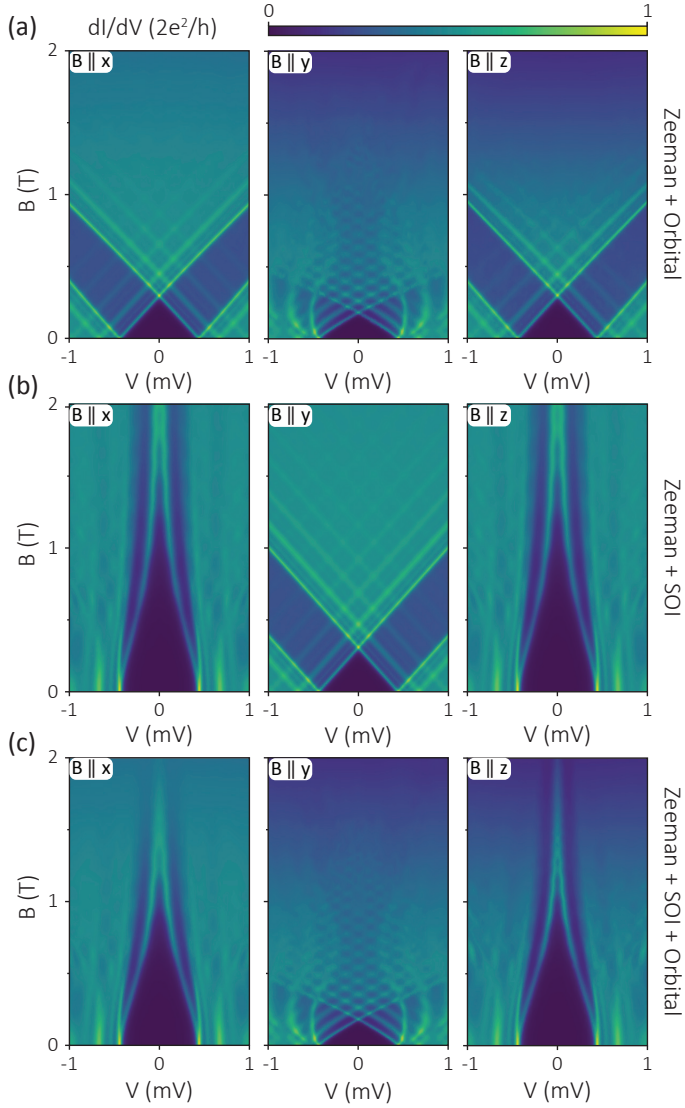


Figure 4.2: (a) Numerical simulations of  $dI/dV$  as a function of  $V$  and  $B$ , including the Zeeman and the orbital (Lorentz) effect of the magnetic field. (b) Same as (a), but including Zeeman and SOI instead of the orbital effect, reproducing the anisotropy in Fig. 4.1(e). (c) Same as (b), but including the Zeeman, SOI and orbital effect. The parameters used in (a)-(c) are  $\mu = 5.6$  meV and  $\Delta V_G = -8$  meV.

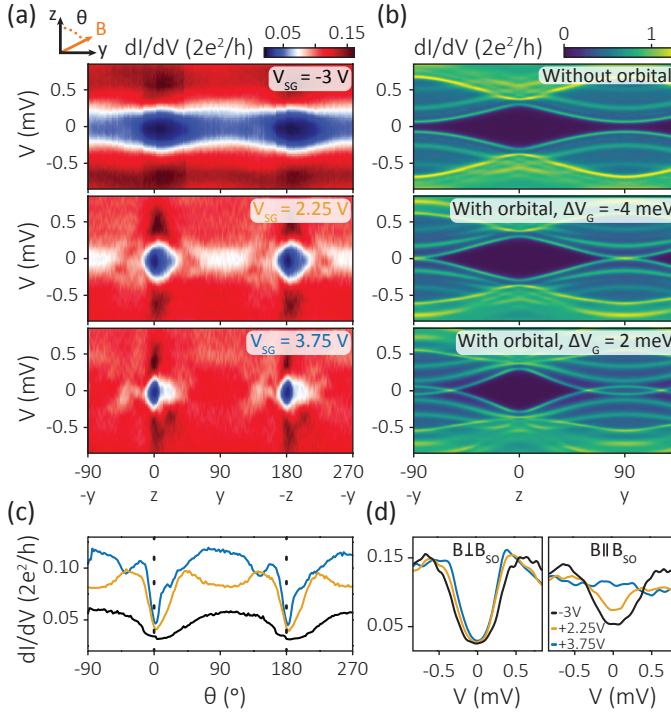


Figure 4.3: (a) Measured  $dI/dV$  as a function of  $V$  upon rotation of  $B$  at 0.3 T over angles  $\Theta$  between  $z$  and  $y$  in device  $B$  (see Fig. 4.9 for the same behavior in device  $A$ ). The voltage  $V_{SG}$  on the super gate (see insets) is varied in the three panels. (b) Simulated  $dI/dV$  as a function of  $\Theta$  and  $V$  at 0.25 T. The top panel includes the Zeeman effect and SOI. The middle and bottom panels additionally include the orbital effect at two values of the potential difference  $\Delta V_G$  between the top and middle of the wire. (c) Horizontal line cuts of (a) averaged over  $|V| < 0.2$  V at  $V_{SG} = -3, 2.25,$  and  $3.75$  V (black, orange, blue). Dashed lines indicate the  $z$  axis ( $\Theta = 0^\circ$ ). (d) Vertical line cuts of (a) at  $\Theta = 0^\circ$  (left) and  $\Theta = 90^\circ$  (right).

parameters [15–17, 37–39].

## 4.5. ORIENTATION OF THE SPIN-ORBIT FIELD

To resolve the direction of the spin-orbit field, we fix the  $B$  amplitude and continuously rotate the  $B$  direction, parametrized by the angle  $\Theta$  in the  $zy$  plane [inset Fig. 4.3(a)]. Figure 4.3(a) shows the dependence of the gap on  $\Theta$ , where we adjust the electric field strength in the nanowire with a voltage  $V_{SG}$  on the super gate (SG) underneath the superconductor [green in Fig. 4.1(a)]. We define the angle at which the gap is hardest as  $\Theta_{\max}$  and find  $\Theta_{\max} = 3 \pm 2^\circ$  ( $z$  axis) for all  $V_{SG}$  and in multiple devices (Fig. 4.3 and Fig. 4.9) (error due to uncertainty in the extraction procedure). This is illustrated in Fig. 4.3(c), which shows horizontal line cuts for subgap bias. The largest gap for a given  $B$  amplitude is expected for  $B \perp B_{SO}$ , indicating that  $B_{SO} \parallel y$ , in agreement with the  $E$ -field direction dictated by the device geometry.

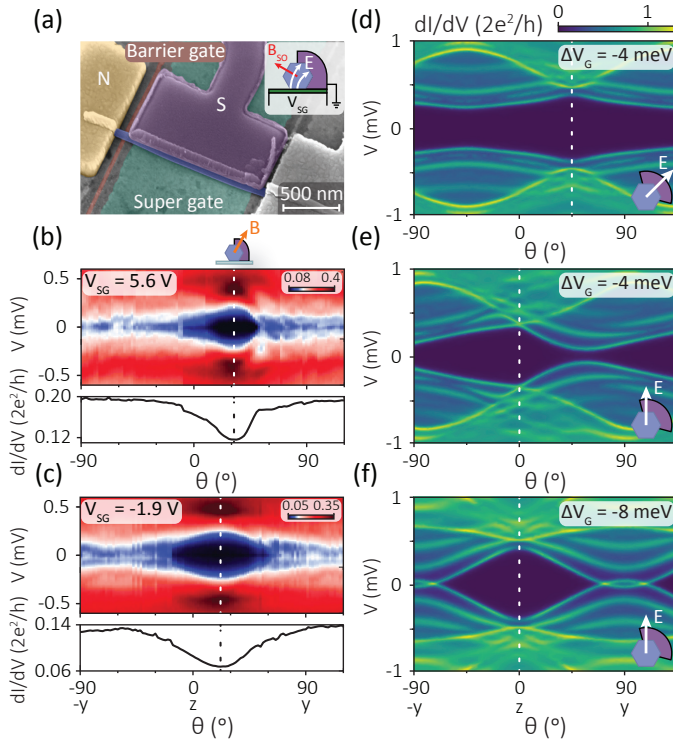


Figure 4.4: (a) Tilted view electron micrograph of Majorana nanowire device  $E$ , which is partially covered with NbTiN. In this device, the electric field  $E$  (and the associated spin-orbit field  $B_{SO}$ ) can rotate away from the  $z$  axis ( $y$  axis), as illustrated in the inset. (b) Measured  $dI/dV$  as a function of  $V$  and angle  $\theta$  in the  $zy$  plane at  $|B| = 75$  mT and  $V_{SG} = 5.6$  V, with a horizontal line cut averaged over  $|V| < 0.25$  mV in the lower panel. The gap is maximum at  $\theta_{max} = 32^\circ$  as indicated by the dashed line. (c) Same as (b), but at  $V_{SG} = -1.9$  V and  $|B| = 0.15$  T.  $\theta_{max}$  is gate tuned to  $22^\circ$ . (d)-(f) Simulated  $dI/dV$  at  $0.25$  T at various  $\Delta V_G$  (see inset) with the superconductor rotated to the side by  $45^\circ$  and including the Zeeman effect, SOI, and the orbital effect. The illustrations in the insets indicate the direction of  $E$ , which is rotated by  $45^\circ$  from  $z$  in (d).

Now, we check whether the orbital effect changes  $\Theta_{\max}$ . The simulations in Fig. 4.3(b) show the effect of magnetic field rotation on the gap with  $B_{\text{SO}} \parallel y$ , confirming that  $\Theta_{\max}$  is, indeed, always given by the direction perpendicular to  $B_{\text{SO}}$ , i.e.  $\Theta_{\max} = 0^\circ$ . Comparing the top panel (without the orbital effect) with the middle panel (with the orbital effect), we conclude that the orbital effect does not affect  $\Theta_{\max}$ . This conclusion also holds when we vary the potential difference  $\Delta V_G$  between the middle and outer of the wire (corresponding to  $V_{\text{SG}}$ ) in the middle panel and bottom panel. We note that, at  $\Delta V_G = 2$  meV (bottom panel) the wave function is moved towards the bottom of the nanowire, which increases the strength of the orbital effect by breaking the reflection symmetry about the  $z$  axis, as evidenced by the longer angle range over which the gap is closed compared to  $\Delta V_G = -4$  meV (middle panel). Experimentally, we also observe this in Fig. 4.3(a), with line cuts in Fig. 4.3(c), where the gap is closed over a significantly longer angle range with increasing  $V_{\text{SG}}$ . We note that we use small values of  $\Delta V_G$  in the simulations, because we expect a weak gate response due to effective electrostatic screening by the superconductor, which covers five of the six nanowire facets [40].

Finally, we turn to a second type of device in which the superconducting film only partially covers the nanowire facets [Fig. 4.4(a)]. This partial superconductor coverage can modify the orientation of  $B_{\text{SO}}$  by changing the associated electric field direction [14], as sketched in the inset of Fig. 4.4(a). The electric field in the wire has two main origins. The first one originates from the work function difference between the superconductor and nanowire, which leads to charge redistribution. The resulting electric field is expected to rotate away from the  $z$  axis due to the partial superconductor coverage which breaks the spatial symmetry. In Fig. 4.4(b), we rotate  $B$  in the  $zy$  plane, perpendicular to the nanowire axis, and find that  $\Theta_{\max}$  is, indeed, no longer at zero, but at  $32 \pm 2^\circ$ . The second contribution to the electric field arises from the applied  $V_{\text{SG}}$  and the electrostatic screening due to the grounded superconductor. Changing  $V_{\text{SG}}$  should, therefore, rotate the electric field for partial coverage. Indeed, we find that  $\Theta_{\max}$  shifts by  $10^\circ$  by adjusting  $V_{\text{SG}}$  by 7.5 V [Fig. 4.4(c)]. Field rotation at intermediate  $V_{\text{SG}}$  and magnetic field sweeps confirming the change of  $\Theta_{\max}$  are shown in Fig. 4.10. Our theory simulations confirm that  $\Theta_{\max}$  is still given by the direction orthogonal to  $B_{\text{SO}}$  when the electric field is not necessarily along a spatial symmetry axis of the partially covered device [Fig. 4.4(d) and 4.4(e)]. While the orbital effect does not change  $\Theta_{\max}$  [Fig. 4.4(e) and 4.4(f)], it can induce asymmetry in the energy spectrum around  $\Theta_{\max}$  resulting from wave function asymmetry when the electric field is not along the mirror plane of the device [Fig. 4.4(b) and 4.4(e)]. The significance of the orbital effect in our devices underlines the importance of including it in realistic simulations of Majorana nanowires.

## 4.6. CONCLUSIONS

In conclusion, the observed gap closing anisotropy for different magnetic field orientations demonstrates SOI in our Majorana nanowires, a necessary condition to create Majorana zero modes. Our experiments reveal that SOI is strongly affected by the work function difference at the nanowire-superconductor interface and the geometry of the superconductor, while electrostatic gating provides tunability of SOI.

## 4.7. APPENDIX

### 4.7.1. SUPPLEMENTAL EXPERIMENTAL DETAILS

#### NANOWIRE GROWTH AND DEVICE FABRICATION

The InSb nanowires used here were grown using a Au-catalyzed vapor-liquid-solid mechanism in a metal organic vapor phase epitaxy reactor, resulting in zinc blende nanowires grown along the [111] crystal orientation, which are free of stacking faults and dislocations [41]. Local gates, covered by a h-BN dielectric flake, were fabricated on a silicon substrate. The nanowires were individually placed over the gates using a micromanipulator [42]. The contacts are fabricated by exposing the chip to a mild oxygen plasma cleaning after resist development, followed by immersion in a saturated ammonium polysulphide solution diluted by water to a 1:200 ratio for 30 minutes at 60°C [43]. For the normal contacts, the wires are exposed to 30 seconds of in-situ helium ion milling, before evaporating 10 nm Cr and 110 nm Au. The NbTiN contacts are fabricated by exposing the nanowire to 5 seconds of Ar plasma etching at 25 W, followed by sputtering of 5 nm NbTi and 85 nm NbTiN [40, 44].

#### MEASUREMENT DETAILS

The measurements were performed in a dilution refrigerator at an electron temperature of  $\sim 50$  mK using a three-axis vector magnet and standard lockin techniques.

### 4.7.2. SUPPLEMENTAL THEORETICAL DETAILS

#### DETAILS OF THE TIGHT BINDING SIMULATIONS

The Hamiltonian defined in the main text is discretized on a lattice of a realistic nanowire geometry with a diameter of 70 nm and a length of  $2 \mu\text{m}$  using a lattice spacing of 10 nm. The nanowire is covered by a 35 nm thick superconducting shell covering  $3/8$  of the circumference of the wire, positioned on top of the wire [Fig. 4.2, 4.3(b)] or rotated from the top to the side by  $45^\circ$  [Fig. 4.4(b)]. Transport calculations are performed by connecting the nanowire to semi-infinite normal leads, separated by a tunnel barrier on one side. The normal leads provide broadening of the peaks in the simulations [45, 46]. The superconducting proximity effect is implemented using the weak coupling approximation [6], in which the pairing gap  $\Delta_0 = 0$  in the nanowire, which is tunnel coupled to a superconductor with  $\Delta_0 > 0$  providing an induced gap of 0.45 meV at  $B = 0$  T. The potential in the wire is given by  $V(y, z) = \frac{\Delta V_G}{R} (z \cos(\Phi) + y \sin(\Phi))$ , where  $\Delta V_G$  is the potential difference between the middle and outer points of the wire,  $R$  is the radius of the nanowire, and  $\Phi$  parametrizes the direction of the electric field  $\hat{\mathbf{E}}$ , which is set to  $\Phi = 0^\circ$  in all simulations, except for Fig. 4.4(d), where  $\Phi = 45^\circ$ . The vector potential  $\mathbf{A} = [B_y(z - z_0) - B_z(y - y_0), 0, B_x(y - y_0)]^T$  is chosen such that it does not depend on  $x$  and the offsets  $x_0, y_0, z_0$  are chosen such that the vector potential averages to zero inside the superconductor, implying a total supercurrent of zero in the superconductor. This choice is supported by the negligible screening currents we observe in our Ginzburg-Landau simulations [Fig. 4.5].  $\mathbf{A}$  is implemented in the tight-binding model using Peierls substitution in the hopping amplitudes [47].

#### DETAILS OF THE GINZBURG-LANDAU SIMULATIONS

To calculate the stray fields in the nanowire due to Meissner screening and vortex entry in the superconducting contact (results shown in Fig. 4.5), we have performed simulations on the Ginzburg-Landau model [48] in a realistic three-dimensional geometry using the dimensions of device A. We used a penetration depth  $\lambda = 290$  nm and a Ginzburg-Landau parameter  $\kappa = \lambda/\xi = 50$ , in line with the values expected for our NbTiN film, which has a room temperature resistivity of  $95 \mu\Omega\text{cm}$  and a critical temperature of 15 K. The Ginzburg-Landau functional is discretized both inside the superconducting contact as well as in its surrounding space [49] using a second-order finite difference scheme at a maximum internode distance of  $0.01\lambda$ . The resulting energy functional is minimized using the nonlinear conjugate gradient method and the code is implemented on a NVidia CUDA architecture with high parallelization. We obtain the energy of states with vortices at finite magnetic fields by first introducing artificial perturbations near the sample boundary, followed by energy minimization to find the local minimum corresponding to a specific number of vortices. The optimal number of vortices at a certain magnetic field is then determined by finding the state with the lowest energy globally. We note that non-optimal amounts of vortices can be metastable due to significant Bean-Livingston barriers for vortex entry, so the actual number of vortices is hysteretic and depends on the dynamics of the magnetic field.

#### 4.7.3. EXTRACTION OF SOI STRENGTH

##### DETERMINATION OF SOI STRENGTH $\alpha$ FROM GAP CLOSING

In a Majorana nanowire the SOI strength  $\alpha$  determines the shape of the gap closing along  $B$ -directions perpendicular to the spin-orbit field  $B_{\text{SO}}$  [34, 35] [see Fig. 4.6(a)]. To find an analytical expression for the dependence of the gap closing on  $\alpha$ , we start from the conventional one-dimensional Majorana nanowire Hamiltonian [4, 5], in which the gap size is given by the lowest energy eigenstate:

$$\Delta(B) = \min \left( \epsilon^2 + \epsilon_{\text{SO}}^2 + \epsilon_Z^2 + \Delta(0)^2 \pm 2\sqrt{\epsilon^2(\epsilon_{\text{SO}}^2 + \epsilon_Z^2) + \epsilon_Z^2\Delta(0)^2} \right)^{\frac{1}{2}} \quad (4.1)$$

Here,  $\epsilon = \hbar^2 k^2/2m^* - \mu$  represents the kinetic energy, with  $k$  the electron wave vector and  $m^* = 0.015m_e$  the effective mass.  $\epsilon_{\text{SO}} = \alpha k$  is the SOI term with  $\alpha$  the SOI strength.  $\epsilon_Z = \frac{1}{2}g\mu_B B$  is the Zeeman energy, with  $g$  the Landé  $g$ -factor and  $\mu_B$  the Bohr magneton.  $\Delta(0)$  is the induced superconducting gap at  $B = 0$  T, which we measure in the experiments (as indicated in Fig. 4.1(b)).

For  $B \parallel B_{\text{SO}}$  ( $y$ -axis) and neglecting the orbital effect the gap closes linearly with the Zeeman energy due to tilting of the bands [24, 25]:

$$\Delta(B) = \Delta(0) - \frac{1}{2}g\mu_B B \quad (4.2)$$

The orbital effect significantly enhances the gap closing in our devices [cf. Fig. 4.1, 4.2], with a strong dependence on the potential difference  $\Delta V_G$  in the three-dimensional model. Although the value of  $\Delta V_G$  in our devices is unknown, we find that the orbital effect can be effectively taken into account in the one-dimensional model by adjusting the  $g$ -factor to match the gap closing along  $B_{\text{SO}}$ , where SOI disappears and only the Zeeman and orbital

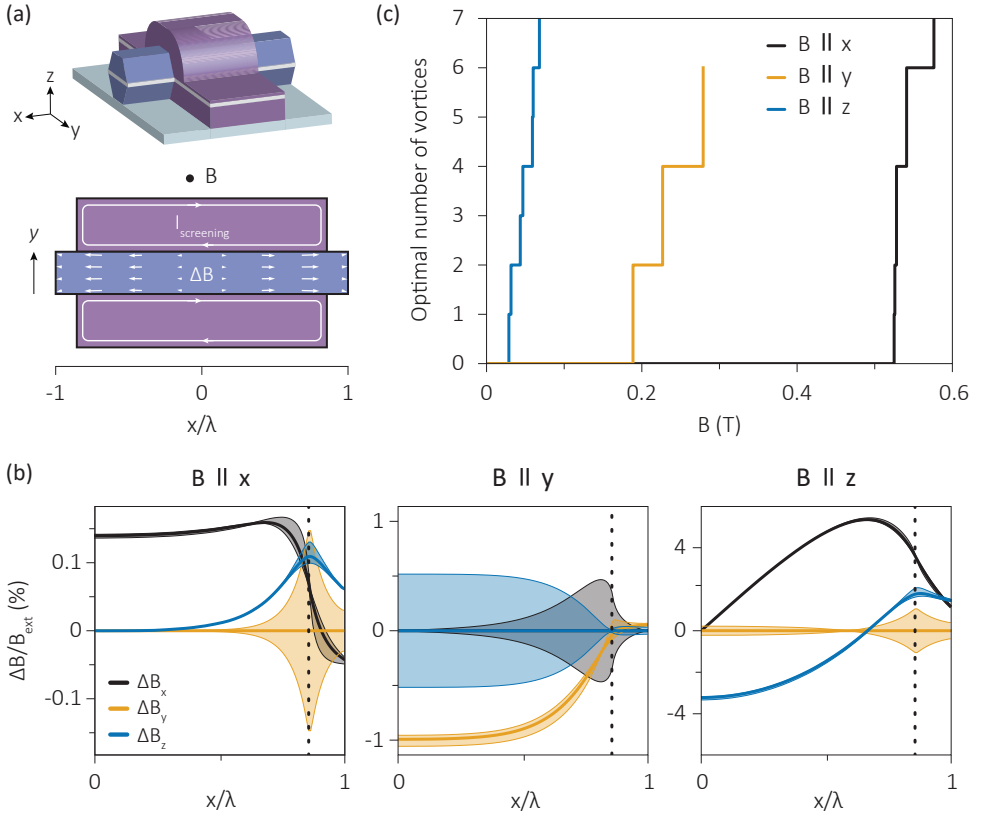


Figure 4.5: Ginzburg-Landau simulations. (a) The top panel shows the schematic of the geometry used for Ginzburg-Landau simulations: a superconducting film covering a hexagonal nanowire. In a superconductor exposed to an external magnetic field  $B$  we calculate the screening currents  $I_{\text{screening}}$ , which induce stray magnetic fields  $\Delta B$  in the nanowire. In (b) we show  $\Delta B$  in the  $xy$ -plane in the middle of the nanowire, as indicated by the white line in (a). The bottom panel shows a top view of this  $xy$ -plane, where the arrows indicate the  $x$  and  $y$  components of  $\Delta B$  in the nanowire for  $B \parallel z$ . (b) The  $x$ ,  $y$  and  $z$ -components (black, yellow, blue) of  $\Delta B$  relative to the external field  $B$  as a function of the position  $x$  along the nanowire axis, where  $x = 0$  corresponds to the middle of the superconducting contact. The lines show the mean stray field and the shaded regions are bounded by the minimum and maximum stray field found along the nanowire width at a particular  $x$ . The end of the superconducting film is indicated by the dashed line.  $B$  is along  $x$ ,  $y$  and  $z$  (left, middle and right panel). Since the device dimensions are comparable to the penetration depth  $\lambda = 290$  nm, the magnetic screening in the superconductor is incomplete, leading to small screening currents and stray fields of at most 4% of  $B$ . These modifications are much smaller and do not match the anisotropy we observe in the measurements, which excludes Meissner screening as the origin of the observed anisotropic gap closing. We note that we have also evaluated  $\Delta B$  at several different magnitudes of  $B$  as well as in the presence of vortices and find relative stray fields of very comparable magnitude. (c) Energetically most favorable number of vortices as a function of  $B$  along  $x$ ,  $y$  and  $z$  (black, yellow, blue). Vortices form far more easily for  $B \parallel z$ . An anisotropic gap closing due to vortices near the nanowire would therefore cause the fastest gap closing along  $z$ , contrary to the anisotropic gap closing we observe, where the gap closes fastest for  $B \parallel y$  [see e.g. Fig. 4.1(e)]. Furthermore, for  $B \parallel y$  vortices only start to appear at  $B > 0.2$  T, while the gap is already strongly suppressed at 0.2 T [see e.g. Fig. 4.1(e)], which excludes vortex formation as the origin of the gap closing for  $B \parallel y$  and indicates that vortices do not have a strong effect on the size of the induced gap.

effect contribute to the gap closing. We emphasize that the  $g$ -factor extracted from the fits therefore does not correspond to the pure Zeeman  $g$ -factor used in our tight-binding calculations. The validity of this approximation is demonstrated in Fig. 4.6(b), where the color map shows the gap closing resulting from our numerical calculations on the three-dimensional tight-binding model (taking the orbital effect into account and using  $g = 50$ ) and the dashed white lines show the gap given by Eq. (4.1) for  $B \parallel x$  and by Eq. (4.2) for  $B \parallel y$  using  $g = 65$ .

To extract  $\alpha$  from our measurements, we fit the model given by Eq. (4.1) and (4.2) to the measured gap closing both along the wire and along  $B_{\text{SO}}$  simultaneously. We prevent overfitting by independently constraining the free parameters. First,  $g$  is determined by the gap closing along  $B_{\text{SO}}$ , which only depends on the Zeeman effect. Then,  $\mu$  follows from the critical field  $B_C$  along  $x$ , where  $\frac{1}{2}g\mu_B B_C = \sqrt{\Delta(0)^2 + \mu^2}$  [4, 5] (note that  $B_C$  does not depend on  $\alpha$ ). The SOI strength  $\alpha$  is now the only free parameter left to fit the curvature of the gap closing along  $x$ . This procedure is applied to four devices [see Fig. 4.1(f), Fig. 4.8(b),(c), and Fig. 4.11], resulting in a SOI strength of 0.15 – 0.35 eVÅ, corresponding to a spin-orbit energy  $E_{\text{SO}} = m^* \alpha^2 / 2\hbar^2$  of 20 – 120  $\mu\text{eV}$ . The remaining parameters used for the fit of device A shown in Fig. 4.1(e) are  $g = 90$ ,  $\mu = 1.4$  meV. The values of  $g$  and  $\mu$  found for the remaining devices are given in Fig. 4.8. Table I shows the range of values of the fitting parameters for which good fits can be obtained. Since  $\alpha$  depends on the electric field in the wire, we expect the observed variation in the SOI strength of devices to be caused by differences in the applied gate voltages and wire diameter.

Table 4.1: Results of gap closing fitting procedure

	Device A	Device B	Device C	Device D
$g$	$90 \pm 10$	$60 \pm 20$	$85 \pm 5$	$160 \pm 20$
$\mu$ (meV)	$1.5 \pm 0.4$	$1.8 \pm 0.8$	$2.75 \pm 0.25$	$2.8 \pm 0.6$
$\alpha$ (eVÅ)	$0.15 \pm 0.05$	$0.3 \pm 0.1$	$0.35 \pm 0.05$	$0.35 \pm 0.05$

#### ESTIMATION OF SOI STRENGTH BASED ON LEVEL REPULSION

SOI induces coupling between states of different momentum and spin in finite length Majorana nanowires, which leads to level repulsion when energy levels are nearly degenerate [36]. Recently this level repulsion between longitudinal states within the same subband was used to estimate a SOI strength in epitaxial Al-InSb nanowires [20]. Here, we follow the same procedure to estimate the SOI strength in a separate device with a NbTiN superconductor that exhibits such level repulsion. We consider a low energy model of two levels dispersing in the magnetic field due to the Zeeman effect, coupled to each other by SOI with the matrix element  $\delta_{\text{SO}}$ :

$$H = \begin{bmatrix} E_0 + \frac{1}{2}g_0\mu_B B & \delta_{\text{SO}} \\ \delta_{\text{SO}} & E_1 - \frac{1}{2}g_1\mu_B B \end{bmatrix} \quad (4.3)$$

We fit the eigenenergies of  $H$  to our experimental data [Fig. 4.7a] to extract  $\delta_{\text{SO}}$ . The precise value of the coupling parameter  $\delta_{\text{SO}}$  depends not only on  $\alpha$ , but also on the details of the confinement and on the coupling strength to the superconductor [20]. A rough estimate, with reasonable agreement to numerical simulations, was proposed to be:  $2\delta_{\text{SO}}$

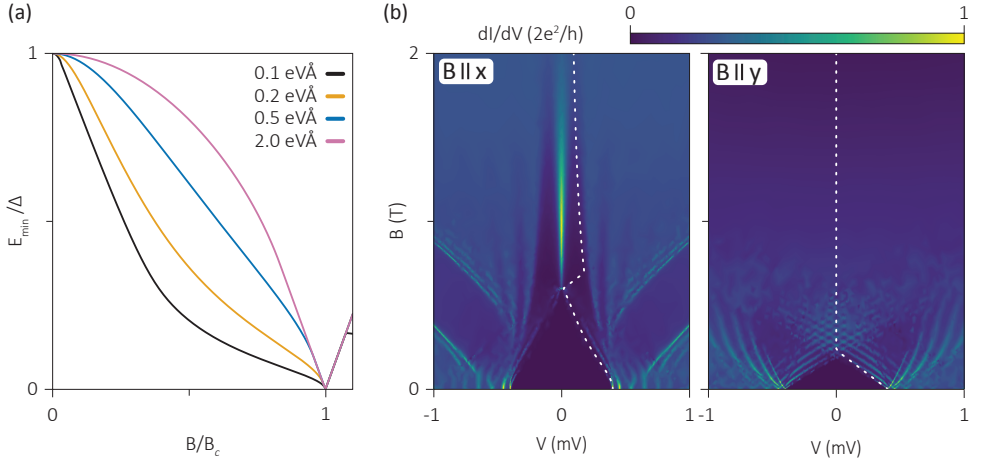


Figure 4.6: Extracting SOI strength from gap closing curvature. (a) Lowest energy state  $E_{\min}$  determining the gap in the one-dimensional model given by Eq. (4.1) as a function of magnetic field,  $B$ , in units of the critical field  $B_c = \sqrt{\Delta^2 + \mu^2}$  for various spin-orbit strengths  $\alpha$ . The curvature of the gap closing is strongly affected by  $\alpha$ . Stronger SOI counteracts the Zeeman effect up to larger  $B/B_c$ , leading initially to a slow gap closing, followed by a sharp gap closing when approaching the critical field, where the lowest energy state is at  $k \approx 0$  for which  $B_{\text{SO}}(k)$  vanishes. The remaining parameters are:  $\Delta(0) = 1$  meV,  $\mu = 2$  meV. (b) Comparison of the numerical simulations on the 3D tight binding model, including the orbital effect (color map), with the 1D model given by Eqs. (4.1) and (4.2) which does not account for the orbital effect (dashed lines). By adjusting the  $g$ -factor used in the Majorana nanowire model from  $g = 50$  to  $65$  to match the gap closing for  $B \parallel B_{\text{SO}}$ , keeping all other parameters the same in both models, we find good agreement for the gap closing for  $B \parallel x$ . We use this same approach to take the orbital effect into account in an effective manner in fits of the experimentally observed gap closing. The remaining parameters used in the simulations shown here are  $\Delta(0) = 0.45$  meV,  $\mu = 0.95$  meV,  $\alpha = 0.2$  eVÅ,  $\Delta V_G = -10$  meV.

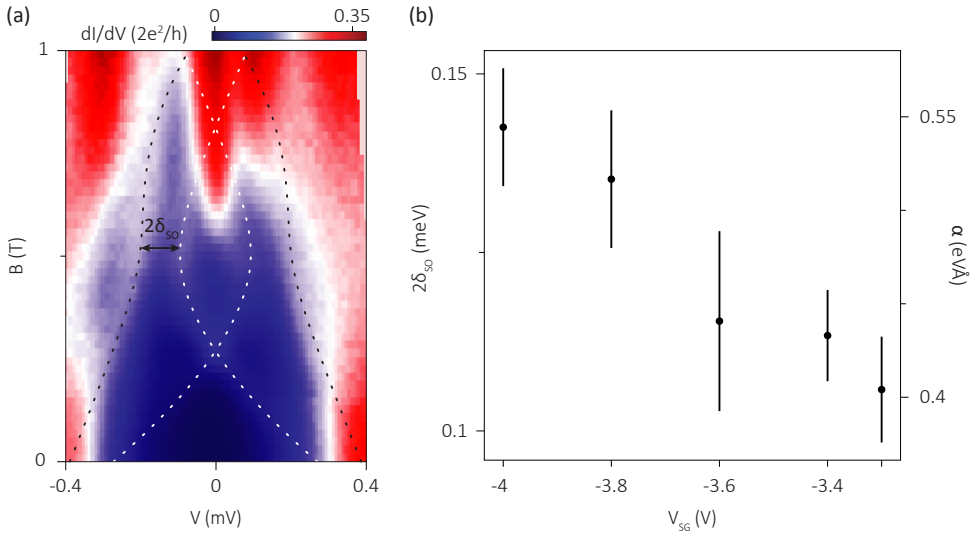


Figure 4.7: Extracting the SOI strength from level repulsion. (a)  $dI/dV$  as a function of  $V$  and  $B$  at  $V_{SG} = -3.3$  V, measured in device E. Two Andreev states come down from the gap edge and exhibit an avoided crossing around  $B = 0.5$  T. The dashed lines indicate fits to the solution of Eq. (4.3). The extracted coupling  $\delta_{SO}$  between the Andreev levels is indicated by the arrow. (b)  $2\delta_{SO}$  as a function of  $V_{SG}$ . The right axis shows the estimation of the SOI strength using  $\alpha = 2\delta_{SO}L/\pi$  for the  $1.2 \mu\text{m}$  long superconducting region. The error bars show the standard deviation in  $\delta_{SO}$  obtained from the fits.

$= \alpha\pi/L$ , where  $L$  is the length of the wire. The extracted  $\delta_{SO}$  is shown in Fig. 4.7(b) for various values of the super gate voltage  $V_{SG}$ . As  $V_{SG}$  becomes more negative, we see an increase in  $\delta_{SO}$ , consistent with an increasing electric field in the nanowire. We can estimate  $\alpha \sim 0.4 - 0.55 \text{ eVÅ}$ . Considering the uncertainty in the relation between  $\alpha$  and  $\delta_{SO}$  and variation in the electrostatic environment of different devices, this magnitude is in line with our estimation based on the gap closing curvature.

## 4.7.4. SUPPLEMENTAL EXPERIMENTAL DATA

## REFERENCES

- [1] A. Y. Kitaev, *Unpaired Majorana fermions in quantum wires*, Phys. Usp. **44**, 131 (2001).
- [2] L. Fu and C. L. Kane, *Superconducting proximity effect and Majorana Fermions at the surface of a topological insulator*, Phys. Rev. Lett. **100**, 096407 (2008).
- [3] C. Nayak, S. H. Simon, A. Stern, M. Freedman, and S. D. Sarma, *Non-Abelian anyons and topological quantum computation*, Rev. Mod. Phys. **80**, 1083 (2008).
- [4] R. M. Lutchyn, J. D. Sau, and S. D. Sarma, *Majorana Fermions and a topological phase transition in semiconductor-superconductor heterostructures*, Phys. Rev. Lett. **105**, 077001 (2010).
- [5] Y. Oreg, G. Refael, and F. von Oppen, *Helical liquids and Majorana bound states in quantum wires*, Phys. Rev. Lett. **105**, 177002 (2010).
- [6] B. Nijholt and A. R. Akhmerov, *Orbital effect of magnetic field on the Majorana phase diagram*, Phys. Rev. B **93**, 235434 (2016).
- [7] V. Mourik, K. Zuo, S. M. Frolov, S. R. Plissard, E. P. A. M. Bakkers, and L. P. Kouwenhoven, *Signatures of Majorana Fermions in hybrid superconductor-semiconductor nanowire devices*, Science **336**, 1003 (2012).
- [8] S. M. Albrecht, A. P. Higginbotham, M. Madsen, F. Kuemmeth, T. S. Jespersen, J. Nygård, P. Krogstrup, and C. M. Marcus, *Exponential protection of zero modes in Majorana islands*, Nature **531**, 206 (2016).
- [9] M. T. Deng, S. Vaitiekėnas, E. B. Hansen, J. Danon, M. Leijnse, K. Flensberg, J. Nygård, P. Krogstrup, and C. M. Marcus, *Majorana bound state in a coupled quantum-dot hybrid-nanowire system*, Science **354**, 1557 (2016).
- [10] Önder Gül, H. Zhang, J. D. S. Bommer, M. W. A. de Moor, D. Car, S. R. Plissard, E. P. A. M. Bakkers, A. Geresdi, K. Watanabe, T. Taniguchi, and L. P. Kouwenhoven, *Ballistic Majorana nanowire devices*, Nat. Nanotechnol. **13**, 192 (2018).
- [11] H. Zhang, C.-X. Liu, S. Gazibegovic, D. Xu, J. A. Logan, G. Wang, N. van Loo, J. D. S. Bommer, M. W. A. de Moor, D. Car, R. L. M. O. het Veld, P. J. van Veldhoven, S. Koelling, M. A. Verheijen, M. Pendharkar, D. J. Pennachio, B. Shojaei, J. S. Lee, C. J. Palmstrøm, E. P. A. M. Bakkers, S. D. Sarma, and L. P. Kouwenhoven, *Quantized Majorana conductance*, Nature **556**, 74 (2018).
- [12] R. M. Lutchyn, E. P. A. M. Bakkers, L. P. Kouwenhoven, P. Krogstrup, C. M. Marcus, and Y. Oreg, *Majorana zero modes in superconductor-semiconductor heterostructures*, Nat. Rev. Mater. **3**, 52 (2018).
- [13] R. Aguado, *Majorana quasiparticles in condensed matter*, Riv. Nuovo Cimento **40**, 523 (2017).

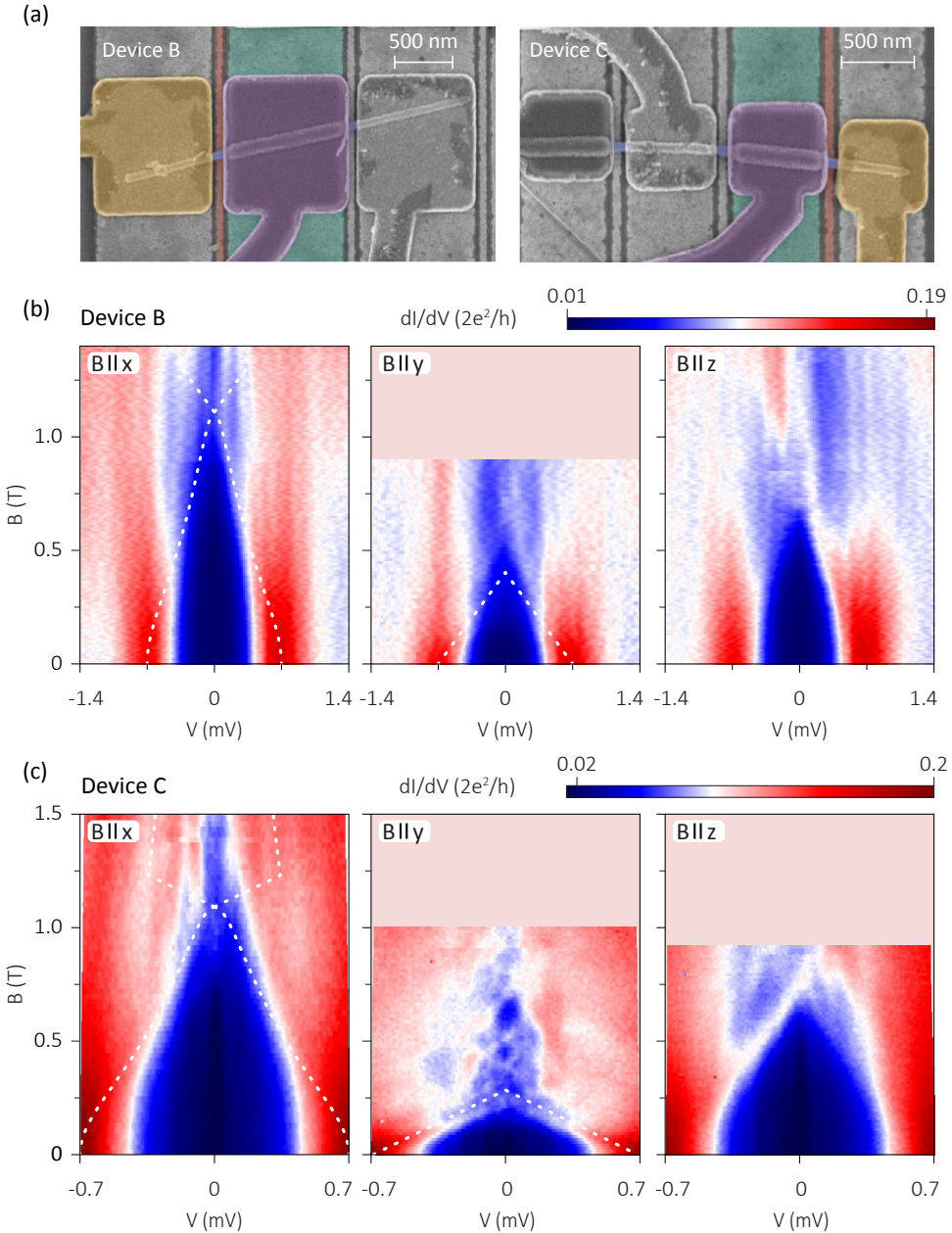


Figure 4.8: Anisotropic gap closing in additional devices. (a) False colored scanning electron micrographs of additional devices B (used in Fig. 4.3) and C, showing anisotropy similar to the device in Fig. 4.1(e). (b,c) Differential conductance,  $dI/dV$ , as a function of the magnetic field,  $B$ , along the  $x$ ,  $y$ , and  $z$ -axes (from left to right). The gap closes at much lower fields along the  $y$ -axis than the  $x$  and  $z$ -axes in all devices fully covered with the superconductor. The white dashed lines indicate fits to the gap closing from which we extract a spin-orbit strength  $\alpha$  of  $0.3 \pm 0.1$  eVÅ [for (b)] and  $0.35 \pm 0.05$  eVÅ [for (c)], with  $g = 60, 85$  and  $\mu = 1.8, 2.7$  meV as the remaining fit parameters for (b), (c) respectively. We note that we do not observe clear reopening of the gap in all devices, which theoretical studies have attributed to the negligible contribution to the tunneling conductance of the states associated with the gap reopening due to their spatial wave function extension into the middle of the wire leading to minimal weight near the tunnel barrier [33, 50–52]. The super gate was set to  $V_{SG} = -1.5$  V,  $-2.6$  V in (b), (c) respectively.

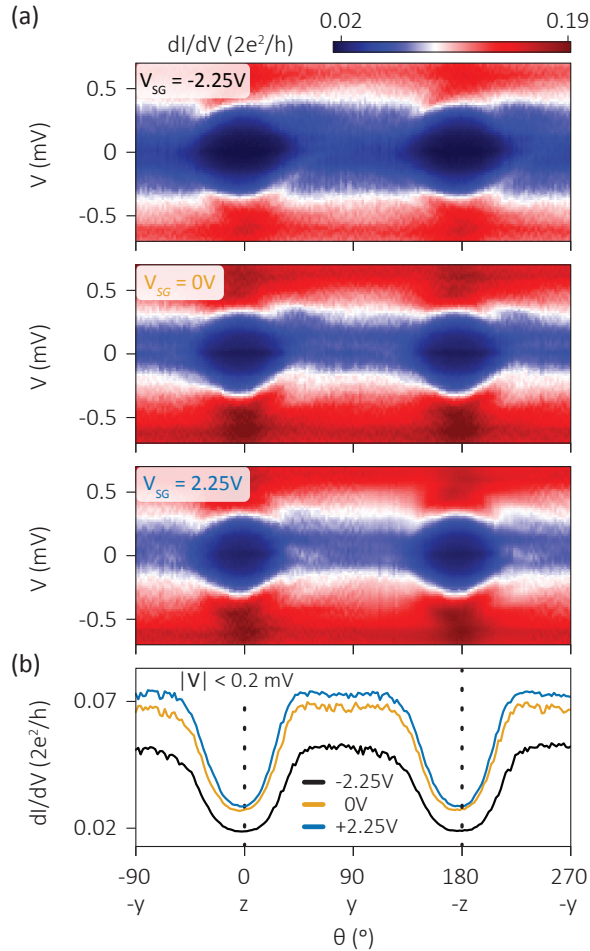


Figure 4.9: Gap dependence on magnetic field orientation in  $zy$ -plane in device A. (a) Differential conductance,  $dI/dV$ , as a function of bias voltage,  $V$ , upon rotation of the magnetic field at 0.25 T over angles  $\Theta$  between  $z$  and  $y$  with different voltages on the super gate  $V_{SG}$  in the three panels. This is the same device as presented in Fig. 4.1(b) Horizontal line cuts of (a) averaged over a bias range  $|V| < 0.2$  mV, showing that the hardest gap is at  $\Theta = 0$ , and increased  $V_{SG}$  suppresses the gap when  $B$  is along  $y$ , the same behaviors observed in device B [Fig. 4.3].

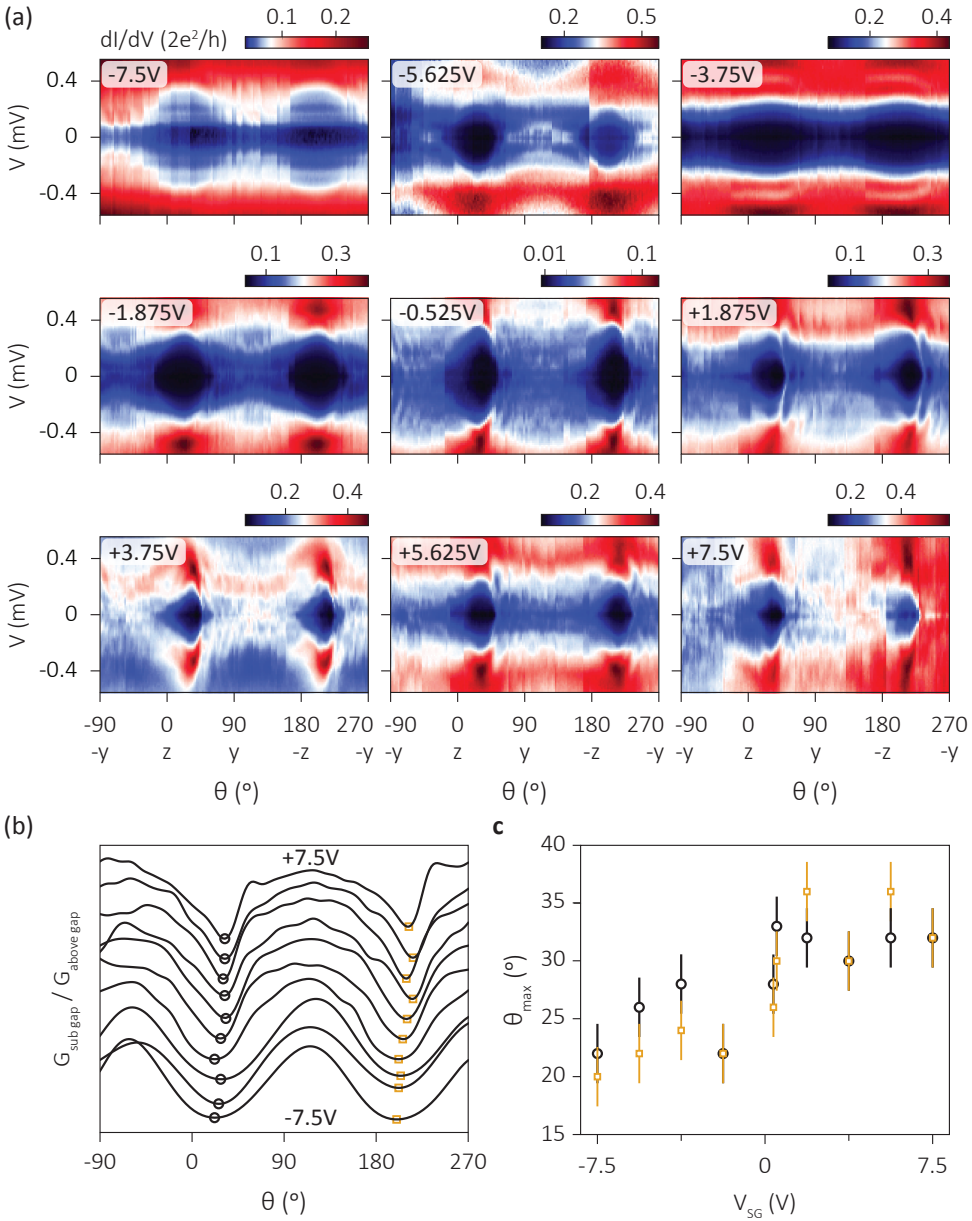


Figure 4.10: Dependence of spin-orbit direction on super gate voltage in device D, which is partially covered by NbTiN. (a) Differential conductance,  $dI/dV$ , as a function of bias voltage,  $V$ , and angle  $\theta$  between  $z$  and  $y$  at various values of  $V_{SG}$  as indicated in the insets. The data is measured at slightly different field magnitudes between 0.1 and 0.2 T for the different  $V_{SG}$  to optimize the anisotropy between  $y$  and  $z$ . The discontinuities in  $dI/dV$  that are visible for some of the scans are likely caused by charge fluctuations in the dielectric environment. (b) The ratio between the sub gap conductance (averaged over  $|V| < 0.2$  V) and the above gap conductance (averaged over  $|V| > 0.4$  V) with  $V_{SG}$  increasing from bottom to top and offset for clarity. The minima of the curves signify the angle at which the gap is hardest,  $\theta_{\text{max}}$ , which shifts to higher angles at increasing  $V_{SG}$ . A low-pass filter is applied along the  $\theta$  direction to suppress the effect of the charge instabilities (this procedure does not affect the minima for the measurements without charge instabilities, such as in Fig. 4.4). (c)  $\theta_{\text{max}}$  as determined from the first (black) and second (yellow) minimum of the curves in (b) as a function of  $V_{SG}$ . The second minima (yellow) signify  $\theta_{\text{max}}$  at negative  $B$  and are subtracted by  $180^\circ$  accordingly.

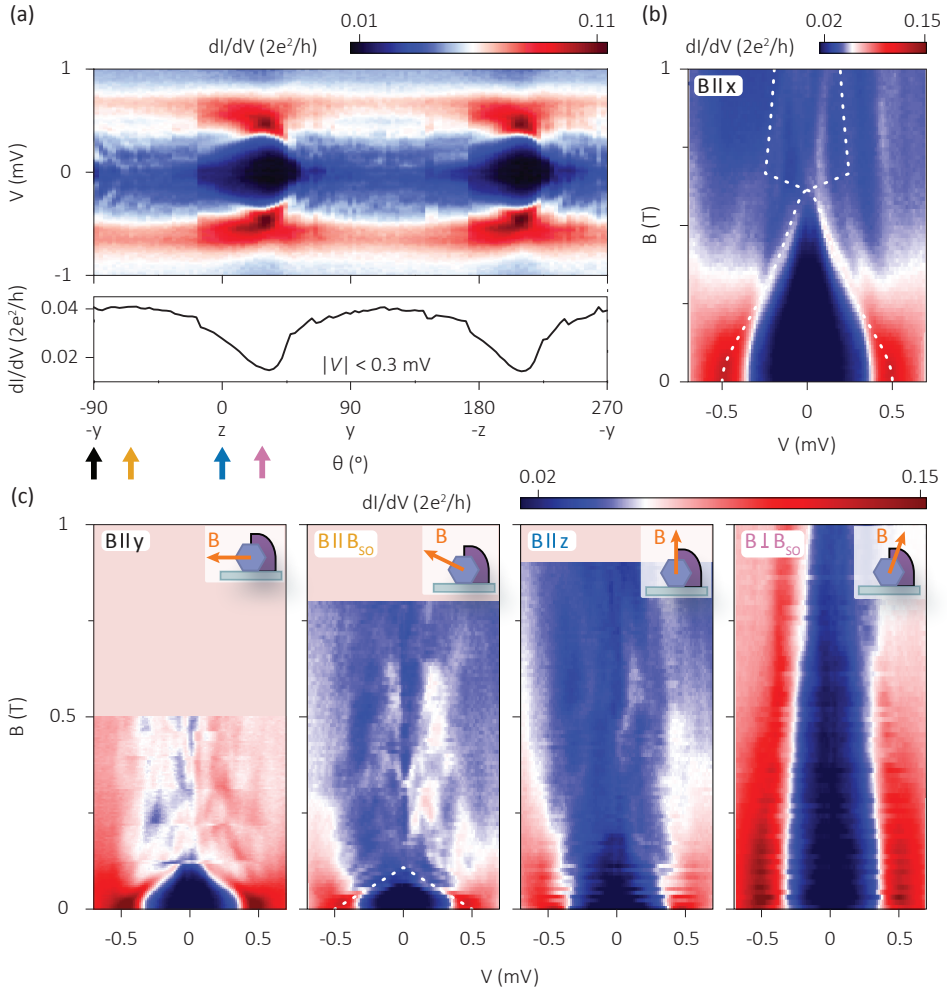


Figure 4.11: Gap dependence on magnetic field orientation in device E, which is partially covered by NbTiN. (a) Differential conductance,  $dI/dV$ , as a function of the angle  $\Theta$  between the  $z$  and  $y$ -axes at  $V_{SG} = 0.525$  V and  $B = 0.1$  T, with a horizontal line cut averaged over a bias range  $|V| < 0.3$  mV in the lower panel. (b)  $dI/dV$  as a function of the magnetic field  $B$  along the nanowire axis, with the white dashed lines showing the fit to the gap closing, resulting in a spin-orbit strength  $\alpha$  of  $0.35 \pm 0.05$  eVÅ (the other fit parameters are  $g = 160$ , see  $B \parallel B_{SO}$  in (c), and  $\mu = 2.8$  meV). (c)  $dI/dV$  as a function of  $B$  along  $y$ ,  $B_{SO}$ ,  $z$  and perpendicular to  $B_{SO}$  from left to right, with the colors in the headers corresponding to the colored arrows in (a). The illustrations in the insets indicate the direction of the magnetic field. Note that due to the changed orientation of  $B_{SO}$ ,  $B$ -sweeps along directions rotated by  $\sim 25^\circ$  from the  $y$ -axis (second panel,  $B \parallel B_{SO}$ ) and the  $z$ -axis (right panel,  $B \perp B_{SO}$ ) now exhibit strong anisotropy, instead of the  $y$  and  $z$ -axes which show strong anisotropy in devices symmetrically covered by NbTiN.

- [14] A. Vuik, D. Eeltink, A. R. Akhmerov, and M. Wimmer, *Effects of the electrostatic environment on the Majorana nanowire devices*, New J. Phys. **18**, 033013 (2016).
- [15] A. E. Antipov, A. Bargerbos, G. W. Winkler, B. Bauer, E. Rossi, and R. M. Lutchyn, *Effects of gate-induced electric fields on semiconductor Majorana nanowires*, Phys. Rev. X **8**, 031041 (2018).
- [16] B. D. Woods, T. D. Stanescu, and S. D. Sarma, *Effective theory approach to the Schrödinger-Poisson problem in semiconductor Majorana devices*, Phys. Rev. B **98**, 035428 (2018).
- [17] A. E. Mikkelsen, P. Kotetes, P. Krogstrup, and K. Flensberg, *Hybridization at superconductor-semiconductor interfaces*, Phys. Rev. X **8**, 031040 (2018).
- [18] C. Fasth, A. Fuhrer, L. Samuelson, V. N. Golovach, and D. Loss, *Direct measurement of the spin-orbit interaction in a two-electron InAs nanowire quantum dot*, Phys. Rev. Lett. **98**, 266801 (2007).
- [19] S. Nadj-Perge, V. S. Pribiag, J. W. G. van den Berg, K. Zuo, S. R. Plissard, E. P. A. M. Bakkers, S. M. Frolov, and L. P. Kouwenhoven, *Spectroscopy of spin-orbit quantum bits in indium antimonide nanowires*, Phys. Rev. Lett. **108**, 166801 (2012).
- [20] M. W. A. de Moor, J. D. S. Bommer, D. Xu, G. W. Winkler, A. E. Antipov, A. Bargerbos, G. Wang, N. van Loo, R. L. M. O. het Veld, S. Gazibegovic, D. Car, J. A. Logan, M. Pendharkar, J. S. Lee, E. P. A. M. Bakkers, C. J. Palmström, R. M. Lutchyn, L. P. Kouwenhoven, and H. Zhang, *Electric field tunable superconductor-semiconductor coupling in Majorana nanowires*, New J. Phys. **20**, 103049 (2018).
- [21] A. E. Hansen, M. T. Björk, C. Fasth, C. Thelander, and L. Samuelson, *Spin relaxation in InAs nanowires studied by tunable weak antilocalization*, Phys. Rev. B **71**, 205328 (2005).
- [22] I. van Weperen, B. Tarasinski, D. Eeltink, V. S. Pribiag, S. R. Plissard, E. P. A. M. Bakkers, L. P. Kouwenhoven, and M. Wimmer, *Spin-orbit interaction in InSb nanowires*, Phys. Rev. B **91**, 201413 (2015).
- [23] J. Kammhuber, M. C. Cassidy, F. Pei, M. P. Nowak, A. Vuik, O. Gül, D. Car, S. R. Plissard, E. P. A. M. Bakkers, M. Wimmer, and L. P. Kouwenhoven, *Conductance through a helical state in an indium antimonide nanowire*, Nat. Commun. **8**, 478 (2017).
- [24] J. Osca, D. Ruiz, and L. Serra, *Effects of tilting the magnetic field in one-dimensional Majorana nanowires*, Phys. Rev. B **89**, 245405 (2014).
- [25] S. Rex and A. Sudbø, *Tilting of the magnetic field in Majorana nanowires: Critical angle and zero-energy differential conductance*, Phys. Rev. B **90**, 115429 (2014).
- [26] D. J. van Woerkom, A. Geresdi, and L. P. Kouwenhoven, *One minute parity lifetime of a NbTiN cooper-pair transistor*, Nat. Phys. **11**, 547 (2015).

- [27] W. Chang, S. M. Albrecht, T. S. Jespersen, F. Kuemmeth, P. Krogstrup, J. Nygård, and C. M. Marcus, *Hard gap in epitaxial semiconductor–superconductor nanowires*, Nat. Nanotechnol. **10**, 232 (2015).
- [28] S. Gazibegovic, D. Car, H. Zhang, S. C. Balk, J. A. Logan, M. W. A. de Moor, M. C. Cassidy, R. Schmits, D. Xu, G. Wang, P. Krogstrup, R. L. M. O. het Veld, K. Zuo, Y. Vos, J. Shen, D. Bouman, B. Shojaei, D. Pennachio, J. S. Lee, P. J. van Veldhoven, S. Koelling, M. A. Verheijen, L. P. Kouwenhoven, C. J. Palmström, and E. P. A. M. Bakkers, *Epitaxy of advanced nanowire quantum devices*, Nature **548**, 434 (2017).
- [29] S. Takei, B. M. Fregoso, H.-Y. Hui, A. M. Lobos, and S. D. Sarma, *Soft superconducting gap in semiconductor Majorana nanowires*, Phys. Rev. Lett. **110**, 186803 (2013).
- [30] C. E. Pryor and M. E. Flatté, *Landé  $g$  factors and orbital momentum quenching in semiconductor quantum dots*, Phys. Rev. Lett. **96**, 026804 (2006).
- [31] F. Qu, J. van Veen, F. K. de Vries, A. J. A. Beukman, M. Wimmer, W. Yi, A. A. Kiselev, B.-M. Nguyen, M. Sokolich, M. J. Manfra, F. Nichele, C. M. Marcus, and L. P. Kouwenhoven, *Quantized conductance and large  $g$ -factor anisotropy in InSb quantum point contacts*, Nano Lett. **16**, 7509 (2016).
- [32] C. W. Groth, M. Wimmer, A. R. Akhmerov, and X. Waintal, *Kwant: a software package for quantum transport*, New J. Phys. **16**, 063065 (2014).
- [33] C.-X. Liu, J. D. Sau, T. D. Stanescu, and S. D. Sarma, *Conductance smearing and anisotropic suppression of induced superconductivity in a Majorana nanowire*, Phys. Rev. B **99**, 024510 (2019).
- [34] B. van Heck, J. I. Väyrynen, and L. I. Glazman, *Zeeman and spin-orbit effects in the Andreev spectra of nanowire junctions*, Phys. Rev. B **96**, 075404 (2017).
- [35] H. Pan, J. D. Sau, T. D. Stanescu, and S. D. Sarma, *Curvature of gap closing features and the extraction of Majorana nanowire parameters*, Phys. Rev. B **99**, 054507 (2019).
- [36] T. D. Stanescu, R. M. Lutchyn, and S. D. Sarma, *Dimensional crossover in spin-orbit-coupled semiconductor nanowires with induced superconducting pairing*, Phys. Rev. B **87**, 094518 (2013).
- [37] T. D. Stanescu, R. M. Lutchyn, and S. D. Sarma, *Majorana fermions in semiconductor nanowires*, Phys. Rev. B **84**, 144522 (2011).
- [38] W. S. Cole, S. D. Sarma, and T. D. Stanescu, *Effects of large induced superconducting gap on semiconductor Majorana nanowires*, Phys. Rev. B **92**, 174511 (2015).
- [39] C. Reeg, D. Loss, and J. Klinovaja, *Metallization of a Rashba wire by a superconducting layer in the strong-proximity regime*, Phys. Rev. B **97**, 165425 (2018).
- [40] H. Zhang, Önder Gül, S. Conesa-Boj, M. P. Nowak, M. Wimmer, K. Zuo, V. Mourik, F. K. de Vries, J. van Veen, M. W. A. de Moor, J. D. S. Bommer, D. J. van Woerkom, D. Car, S. R. Plissard, E. P. Bakkers, M. Quintero-Pérez, M. C. Cassidy, S. Koelling, S. Goswami,

- K. Watanabe, T. Taniguchi, and L. P. Kouwenhoven, *Ballistic superconductivity in semiconductor nanowires*, Nat. Commun. **8**, 16025 (2017).
- [41] D. Car, J. Wang, M. A. Verheijen, E. P. A. M. Bakkers, and S. R. Plissard, *Rationally designed single-crystalline nanowire networks*, Adv. Mater. **26**, 4875 (2014).
- [42] K. Flöhr, M. Liebmann, K. Sladek, H. Y. Günel, R. Frielinghaus, F. Haas, C. Meyer, H. Hardtdegen, T. Schäpers, D. Grützmacher, and M. Morgenstern, *Manipulating InAs nanowires with submicrometer precision*, Rev. Sci. Instrum. **82**, 113705 (2011).
- [43] D. B. Suyatin, C. Thelander, M. T. Björk, I. Maximov, and L. Samuelson, *Sulfur passivation for ohmic contact formation to InAs nanowires*, Nanotechnology **18**, 105307 (2007).
- [44] Önder Gül, H. Zhang, F. K. de Vries, J. van Veen, K. Zuo, V. Mourik, S. Conesa-Boj, M. P. Nowak, D. J. van Woerkom, M. Quintero-Pérez, M. C. Cassidy, A. Geresdi, S. Koelling, D. Car, S. R. Plissard, E. P. A. M. Bakkers, and L. P. Kouwenhoven, *Hard superconducting gap in InSb nanowires*, Nano Lett. **17**, 2690 (2017).
- [45] C.-X. Liu, J. D. Sau, and S. D. Sarma, *Role of dissipation in realistic Majorana nanowires*, Phys. Rev. B **95**, 054502 (2017).
- [46] J. Danon, E. B. Hansen, and K. Flensberg, *Conductance spectroscopy on Majorana wires and the inverse proximity effect*, Phys. Rev. B **96**, 125420 (2017).
- [47] D. R. Hofstadter, *Energy levels and wave functions of bloch electrons in rational and irrational magnetic fields*, Phys. Rev. B **14**, 2239 (1976).
- [48] W. D. Gropp, H. G. Kaper, G. K. Leaf, D. M. Levine, M. Palumbo, and V. M. Vinokur, *Numerical simulation of vortex dynamics in type-II superconductors*, J. Comput. Phys. **123**, 254 (1996).
- [49] Q. Du and X. Wu, *Numerical solution of the three-dimensional Ginzburg–Landau models using artificial boundary*, SIAM J. Numer. Anal. **36**, 1482 (1999).
- [50] E. Prada, P. San-Jose, and R. Aguado, *Transport spectroscopy of NS nanowire junctions with Majorana fermions*, Phys. Rev. B **86**, 180503 (2012).
- [51] F. Pientka, G. Kells, A. Romito, P. W. Brouwer, and F. von Oppen, *Enhanced zero-bias Majorana peak in the differential tunneling conductance of disordered multisubband quantum-wire/superconductor junctions*, Phys. Rev. Lett. **109**, 227006 (2012).
- [52] T. D. Stanescu, S. Tewari, J. D. Sau, and S. D. Sarma, *To close or not to close: The fate of the superconducting gap across the topological quantum phase transition in Majorana-carrying semiconductor nanowires*, Phys. Rev. Lett. **109**, 266402 (2012).



# 5

## ROBUSTNESS OF MAJORANA BOUND STATES IN THE SHORT-JUNCTION LIMIT

---

This chapter has been previously published as Doru Sticlet, Bas Nijholt, and Anton R. Akhmerov, *Robustness of Majorana bound states in the short-junction limit*, Phys. Rev. B **95**, 115421, (2017)

My contributions to this work are developing and performing the numerical simulations of the three-dimensional models and writing the parts of the paper related to them.

## 5.1. INTRODUCTION

The theory of normal conductor-superconductor (NS) hybrid systems distinguishes two limiting cases: long and short junctions. In long junctions, the dwell time  $\tau_{\text{dw}}$  of a quasiparticle inside the normal region is much larger than the time  $\hbar/\Delta$  it spends inside the superconductor (with  $\Delta$  the superconducting gap). In this limit the induced gap inside the semiconductor is equal to  $\hbar/\tau_{\text{dw}}$ , and therefore it varies for different bound states. In the short-junction or strong-coupling limit, the quasiparticles spend most of their time inside the superconductor, while the normal region effectively acts as a delta function scatterer. Then in the presence of time-reversal symmetry, the induced gap is close to  $\Delta$  for every single Andreev bound state. In the short-junction limit Andreev bound states have the most weight in the superconductor, and therefore the conventional approach of integrating out the superconductor and obtaining an effective Hamiltonian of the normal system becomes inefficient due to the strong energy dependence of the effective Hamiltonian.

Systematically studying the short-junction limit is relevant for the creation of Majorana bound states (MBS) [1–5] in semiconductor nanowires [6, 7] partially coated with epitaxially grown aluminum that have high interface quality. These systems were observed to have a well-developed hard induced gap comparable to the gap in the bare Al [8], and subsequently showed zero bias peaks [9] and suppressed splitting of low energy states characteristic to MBS [10]. The theoretical description of the response of strongly coupled zero-dimensional NS junctions to magnetic field was analyzed in Ref. [11], where the authors report a strong suppression of the effective  $g$  factor, potentially leading to the impossibility of inducing a topological phase at magnetic fields below the Clogston limit [12].

Here we extend the analysis of Ref. [11] using the scattering formalism that allows us to capture the nonlinear features of the spectrum, and by considering higher-dimensional systems with translational invariance. The scattering formalism has been routinely applied to short junctions in mesoscopic physics [for review see [13]]. Relevant works to the present study are on two-dimensional electronic gases with spin-orbit interactions [14, 15]. However, in Majorana literature the use of the scattering formalism has been limited [16]. The equivalent of the scattering formalism using the effective Hamiltonian approach amounts to introducing an effective self-energy  $\Sigma(E)$  which has a proper dependence on energy  $E$  [17–19] and then neglecting the energy term in the nonlinear eigenvalue problem  $[H - \Sigma(E)]\psi = E\psi$ , as done in, e. g., Ref. [20].

Our overall findings are favorable for the creation of MBS in Al-based NS systems. Specifically, we find that:

- The critical magnetic field  $B_*$  required to induce a topological phase is independent of the superconducting gap. This is valid also beyond the short-junction limit, as long as penetration of magnetic field into the superconductor is negligible.
- Since  $B_*$  is inversely proportional to the wire cross section, the device design can be used to adjust  $B_*$  within a broad range.
- The localization length  $\xi_M$  of the MBS does not depend on the superconducting gap, and in optimal conditions it is proportional to the spin-orbit length  $l_{\text{SO}}$ .

- Finally, if the interface between the semiconductor and the superconductor has high transparency  $T$ , then  $B_*$  becomes only a slowly varying function of the chemical potential  $\mu$ , as opposed to its usual oscillatory behavior on the scale of the mode spacing in the nanowire [21, 22].

Our analytical calculations fully coincide with the results obtained using a numerical scattering approach to short junctions and exact diagonalization of a discretized tight-binding Hamiltonian. While these conclusions are favorable for the prospect of using weak superconductors for MBS creation, we note that the effects of disorder in the superconductor are not systematically treated here. Disorder has been recently predicted to have a strong detrimental effect on the creation of MBS in systems that are in the short-junction limit [23].

This chapter is organized as follows. Section 5.2 contains a pedagogical review of scattering formalism for the calculation of Andreev spectrum. The following Sec. 5.3 presents scaling arguments supporting our conclusions. In Sec. 5.4 we compute the dispersion relation of a planar NS junction and discuss the typical device parameters. Section 5.5 investigates the Majorana phase diagram and the behavior of the MBS decay length. In Sec. 5.6 we compare the predictions of Sec. 5.5 with numerical diagonalization of finite junctions. Section 5.7 estimates the orbital effect of the magnetic field by computing the Andreev spectrum in a cylindrical geometry in a thin shell limit. In Sec. 5.8 we confirm our findings using a numerically computed Majorana phase diagram of a three-dimensional model. Lastly, section 5.9 sums up our conclusions.

## 5.2. SCATTERING MATRIX FORMALISM AND THE SHORT-JUNCTION LIMIT

This section reviews the scattering approach to calculating the Andreev bound state spectrum and may be skipped by expert readers. We start by considering a general NS junction with  $n$  superconducting terminals [24]. We use the case  $n = 1$  in Secs. 5.4, 5.5, 5.8 and  $n = 2$  in Sec. 5.7.

The levels with  $|E| < \Delta$  are Andreev bound states, i.e., coherent superpositions of electron and hole excitations which occur due to Andreev reflections [25] at the interface between the normal region and the superconducting terminals. The wave function quantization condition on the wave function requires that the total sequence of scattering events results in a phase shift of  $2\pi n$ . For the vector of modes  $\psi$  incoming from the superconductor to the normal region this condition reads:

$$S_A S_N \psi = \psi. \quad (5.1)$$

Here  $S_N$  is the scattering matrix of the normal region, and  $S_A$  the scattering matrix of Andreev reflection processes in the superconducting terminals. The mode vector has electron and hole components  $\psi = (\psi_e, \psi_h)$ .

The Andreev reflection matrix assumes a universal form when the superconductor has  $s$ -wave pairing without any sources of time-reversal symmetry breaking and additionally when the Andreev approximation holds (when the Fermi energy in the superconductor is much larger than  $\Delta$ ). In the literature, the Andreev spectrum is often calculated in

systems where the superconductor Hamiltonian has full spin-rotation invariance (an appropriate approximation for aluminum), making the spin basis a natural choice of basis of  $\psi$ . Yet the universal structure of the Andreev reflection matrix does not change in the presence of spin-orbit coupling in the superconductor. However, in that case it is impossible to choose a spin basis due to lack of spin conservation and it is more appropriate to use a basis where the outgoing modes are time reversed of the incoming modes [26]. Throughout this chapter we work in the latter basis but explain the relation to the more commonly used spin basis for reference at the end of this section. Importantly, we neglect the time-reversal symmetry breaking perturbations in the superconductor, restricting ourselves to magnetic fields much lower than critical.

The scattering matrix of the normal region is block diagonal in the Nambu space:

$$S_N(E, \mathbf{k}) = \begin{pmatrix} S_e(E, \mathbf{k}) & 0 \\ 0 & S_h(E, \mathbf{k}) \end{pmatrix}, \quad (5.2)$$

where  $S_e$  and  $S_h$  are the scattering matrices of electrons and holes. We consider NS junctions with a translational symmetry, and therefore the scattering matrices may depend on the wave vector  $\mathbf{k}$  along the translationally invariant directions. We choose the hole modes  $\psi_h$  as particle-hole partners of the electron modes  $\psi_e$ . In this basis the particle-hole symmetry of the scattering matrix reads:

$$\tau_x S_N^*(E, \mathbf{k}) \tau_x = S_N(-E, -\mathbf{k}), \quad (5.3)$$

Using the block-diagonal structure of  $S_N$  it follows that the normal scattering matrix of holes is the conjugate of the scattering matrix for electrons, at opposite energy and momentum [27]:

$$S_h(E, \mathbf{k}) = S_e^*(-E, -\mathbf{k}). \quad (5.4)$$

In the same basis, the Andreev reflection matrix reads:

$$S_A = \alpha(E)R, \quad R = \begin{pmatrix} 0 & r \\ -r^* & 0 \end{pmatrix}, \quad r = \oplus_j e^{i\phi_j}, \quad (5.5)$$

where the index  $j$  runs over the terminals,  $\phi_j$  is the superconducting phase in lead  $j$ , and  $\alpha(E) = \exp(-i \arccos(E/\Delta))$  [28].

Following Ref. [28], eliminating  $\psi$  from Eq. (5.1), and using an expression for a block matrix determinant one immediately arrives to a determinantal equation for the bound state energies:

$$\det[1 + \alpha^2(E)r^* S_e(E, \mathbf{k})r S_e^*(-E, -\mathbf{k})] = 0. \quad (5.6)$$

The short-junction limit allows us to further simplify the calculation of the Andreev bound state energies when Thouless energy  $E_{\text{Th}} \equiv \hbar/\tau_{\text{dw}} \gg \Delta$ . Thouless energy is the typical energy scale for the matrix elements to change appreciably, therefore in the short-junction limit  $S_N(E, \mathbf{k}) \approx S_N(0, \mathbf{k})$  for any  $E \lesssim \Delta$ . After replacing  $S_e(E)$  with  $S_e(0)$ , the only energy-dependent term remaining in Eq. (5.1) is the coefficient  $\alpha(E)$ . Since the scattering matrices are invertible, Eq. (5.1) reads:

$$RS_N\psi = \alpha^{-1}(E)\psi, \text{ or } S_N^{-1}R^{-1}\psi = \alpha(E)\psi. \quad (5.7)$$

Adding the two equations yields the following energy eigenproblem:

$$\frac{1}{2}[RS_N + S_N^{-1}R^{-1}]\psi = \frac{E}{\Delta}\psi. \quad (5.8)$$

Further squaring this equation and using the unitarity of the scattering matrices  $S_A$  and  $S_N$  we arrive to the eigenproblem expression for the Andreev spectrum:

$$\left\{ \frac{1}{2} - \frac{1}{4} [S_e^\dagger(\mathbf{k})rS_e^T(-\mathbf{k})r^* + \text{H.c.}] \right\} \psi_e = \frac{E^2}{\Delta^2} \psi_e, \quad (5.9)$$

where the energy argument is suppressed, since  $S_e$  is evaluated at  $E = 0$ . If there is only a single superconducting terminal, the Andreev reflection matrix  $r$  reduces to a phase factor, which fully drops out from Eq. (5.9), as required by gauge invariance.

If the spin is conserved, the above derivation is nearly identical in the spin basis. The scattering matrices in the spin basis  $\tilde{S}_e$  and  $\tilde{r}$  are related to the basis of time-reversed modes by a transformation

$$\tilde{S}_e = -i\sigma_y S_e, \quad \tilde{r} = -i\sigma_y \otimes_j e^{i\phi_j}, \quad (5.10)$$

with the Pauli matrices  $\sigma$  spin operators and  $\sigma_0$  an identity matrix. The symmetry condition (5.4), equation (5.6) for the Andreev spectrum, and eigenproblem for the spectrum in short-junction approximation (5.9) are identical in both bases upon replacing  $S_e$  and  $r$  with  $\tilde{S}_e$  and  $\tilde{r}$ .

### 5.3. SCALING ARGUMENTS FOR THE MBS PROPERTIES IN THE SHORT-JUNCTION LIMIT

The superconducting gap enters only as an overall prefactor of the Andreev state energies in Eq. (5.9), while the specific spectrum depends only on the normal state scattering matrix  $S_e$ . This simplification allows us to draw most of our conclusions about MBS properties solely using universal arguments and not by solving a specific model. For instance, since the Majorana phase transition occurs when Eq. (5.9) has a zero-energy solution, the critical field  $B_*$  does not depend on  $\Delta$ . This conclusion also extends beyond the short-junction limit, since the zero energy solutions of Eq. (5.9) always coincide with the zero energy solutions of the Eq. (5.1) and therefore with the full solutions of the Bogoliubov-de-Gennes equation.

Turning to the spatial extent of MBS in the normal region  $\xi_M$ , we observe that it is limited from below by the coherence length  $\xi_S$  in the superconductor. However  $\xi_S$  is often short: For example in aluminum films  $\xi_S \sim 100\text{nm}$  due to disorder effects. If  $\xi_M$  is predominantly set by the properties of induced superconductivity in the normal region,  $\xi_M$  must also be independent of  $\Delta$ , since it is a property of the eigenvectors of Eq. (5.9) at  $E = 0$ .

If the semiconductor has a cross section  $W$ , effective electron mass  $m_n$ , and it is coupled to the superconductor by an interface with transparency  $T$ , then the Thouless energy equals

$$E_{\text{Th}} = TN\delta, \quad \delta \equiv \frac{\hbar^2 \pi^2}{2m_n(2W)^2}, \quad (5.11)$$

where  $N$  is the number of transverse bands occupied in the semiconductor, and  $\delta$  is the typical interband spacing. The denominator of the expression for  $\delta$  contains  $2W$  since it is the total distance traveled by a quasiparticle normal to the interface between two consecutive Andreev reflections. We focus on the experimentally relevant low-density regime when  $N \sim 1$ . In realistic nanowires  $m_n \sim 10^{-2}m_e$ , and  $W \approx 100$  nm, resulting in  $\delta \approx 1$  meV, much larger than the superconducting gap in aluminum  $\Delta_{\text{Al}} \approx 0.2$  meV, which justifies the short-junction approximation for sufficiently transparent contacts  $T \gtrsim 0.1$ .

In order for the spectral gap to close in the normal region—or, in other words, for a topological phase transition to appear—the scattering matrix  $S_e$  must change by  $\mathcal{O}(1)$  since, in the presence of time-reversal symmetry, all the Andreev bound states have the same energy  $E = \Delta$ . For the Zeeman field to cause such a perturbation, the electron spin must precess by a large angle during the propagation inside the scattering region. This results in a condition  $E_Z \tau_{\text{dw}} / \hbar \sim 1$ , or equivalently

$$B_* \sim E_{\text{Th}} / g \mu_B, \quad (5.12)$$

with  $g$  the effective gyromagnetic factor and  $\mu_B$  the Bohr magneton.

The orbital effect of the magnetic field causes an additional time-reversal symmetry breaking perturbation to the normal scattering region. It becomes significant [causes an  $\mathcal{O}(1)$  change of  $S_e$ ] when the flux penetrating the scattering region becomes comparable to the flux quantum  $\Phi_0 = h/e$ . This defines another scale of the magnetic field, characterizing the importance of its orbital effect  $B_{\text{orb}} \sim h/eW^2$ . Comparing  $B_{\text{orb}}$  with  $B_*$  we get

$$\frac{B_{\text{orb}}}{B_*} \sim \frac{g \mu_B m_n}{e \hbar T N}. \quad (5.13)$$

If transparency is high and the number of modes is low, then the relative strength of the orbital and Zeeman effects of the magnetic field is a material parameter dependent on the  $g$  factor and the effective mass. For realistic materials this factor is  $\mathcal{O}(1)$ , which is in line with our results in Secs. 5.7 and 5.8.

Turning to the spatial extent of the MBS  $\xi_M$ , we observe that it must diverge in the topological regime in the absence of spin-orbit coupling. The spectral gap at a finite momentum appears already in the first order perturbation in spin-orbit strength  $\alpha$ , and hence  $\xi_M \sim \alpha^{-1}$ . Finally, in the optimally tuned situation  $N \sim 1$ , and  $B \sim B_*$ , so that  $S_N$  only depends on two energy scales:  $\delta$  and the spin-orbit energy  $E_{\text{SO}} = m_n \alpha^2 / 2 \hbar^2$ . This means that there is only a single length scale inversely proportional to  $\alpha$ , the spin-orbit length  $l_{\text{SO}} = \hbar / m_n \alpha$ , and hence  $\xi_M \sim l_{\text{SO}}$ .

The scattering approach highlights another important property of the Majorana phase diagram, the relation between  $T$  and the oscillatory behavior of  $B_*$ . If  $T \sim 1$ , there is little scattering at the NS interface, and  $\tau_{\text{dw}}$  becomes a smooth function of the chemical potential  $\mu$ . Combining this with Eq. (5.12) we conclude that  $B_*$  must also depend on  $\mu$  in a smooth fashion. In the opposite limit  $T \ll 1$ ,  $E_{\text{Th}}$  reduces on resonance, when  $\mu$  matches the bottom of a subband in the semiconducting region. Away from the resonance, when there are no available states at the selected energy,  $E_{\text{Th}}$  becomes very large. This behavior of Thouless energy results in the appearance of a sharp minimum in  $B_*$  whenever  $\mu$  matches the bottom of a new band in the semiconductor region. In Sec. 5.4 we confirm

the relation between the interface transparency and the oscillatory nature of the Majorana phase boundary.

These findings are different from the predictions of a purely 1D phenomenological model [6, 7] with the Hamiltonian

$$H_{1D} = \left( \frac{p^2}{2m_n} - \mu + \frac{\alpha}{\hbar} \sigma_y p \right) \tau_z + \Delta' \tau_x + E_Z \sigma_z, \quad (5.14)$$

where the induced superconductivity enters as a phenomenological pairing term  $\Delta'$ , and the momentum  $p$  is limited to a direction along the nanowire. The induced gap follows from a perturbation theory in the weak coupling limit between the semiconductor and the superconductor. Therefore the phenomenological model is not directly applicable to the strong coupling regime for highly transparent junctions. The Hamiltonian  $H_{1D}$  undergoes a topological phase transition when  $E_Z^2 = \Delta'^2 + \mu^2$ , and therefore  $B_*$  explicitly depends on  $\Delta'$ . This difference, however, is due to the shortcomings of the effective model, and in reality our conclusions also hold in the weak-coupling/long junction limit. In the long junction limit  $\Delta' \approx E_{Th}$ , immediately leading us to the conclusion that  $B_*$  and  $\xi_M$  are independent of the intrinsic superconducting gap  $\Delta$ . If a long junction is transparent  $T \sim 1$ , then the Fermi momentum drops out of the level quantization condition, hence resulting in the lack of oscillations of  $B_*$  as a function of  $\mu$ . Finally, the rest of our conclusions follow in a similar fashion for the long junctions from the dimensional analysis of Eq. (5.14) after the identification  $\Delta' \sim E_{Th}$ .

## 5.4. MODEL

### 5.4.1. GENERAL SOLUTION

To verify our general arguments, we consider a specific model, a semiconductor nanowire in contact with a large superconductor. We consider the effective superconductor thickness to be infinite, unlike the typical experimental situation where the superconductor thickness is around 10 nm. This limit is nevertheless a reasonable approximation due to the large Fermi surface size mismatch between the superconductor and the semiconductor. A much larger Fermi surface in the superconductor means that most electron trajectories approaching the nanowire from the superconductor side must be reflected back. Full internal reflection in combination with diffuse scattering allows the superconductor to accommodate quasiparticle trajectories much longer than the superconducting coherence length  $\xi_S = \hbar v_{s,F} / \Delta$ , making the superconductor effectively infinite.

We first consider the device geometry shown in Fig. 5.1. The nanowire is oriented along the  $x$  axis, NS interface is at  $y = 0$ , and the outer boundary of the wire is at  $y = W$ . The superconductor occupies the half-space  $y < 0$ . Neglecting the orbital effect of the magnetic field makes the motion in  $z$  direction separable and reduces the problem to a purely two-dimensional geometry, shown in Fig. 5.1(b).

The normal state Hamiltonian of the system is that of a Rashba two-dimensional electron gas coupled to a material with negligible spin-orbit interaction and Zeeman coupling [29]:

$$H = \left[ \mathbf{p} \frac{1}{2m(y)} \mathbf{p} - \mu(y) \right] \sigma_0 + \frac{1}{2\hbar} \{ \alpha(y), \boldsymbol{\sigma} \times \mathbf{p} \} \cdot \hat{\mathbf{z}} + E_Z(y) \sigma_x. \quad (5.15)$$

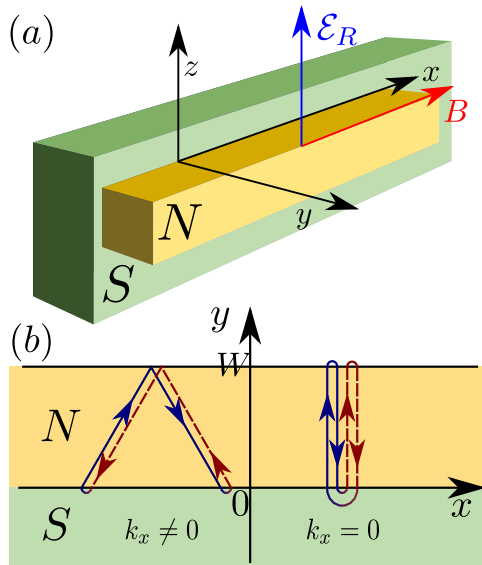


Figure 5.1: (a) Nanowire with width  $W$  oriented along the  $x$  direction and coupled to a bulk superconductor. The magnetic field is parallel to the wire, while the Rashba electric field points along the  $z$  direction. (b) Semiclassical bound state trajectory in the two-dimensional nanowire. Electrons (solid blue) and holes (dashed red) specularly reflect at the boundary with vacuum and undergo Andreev reflection at the interface with the superconductor. Two types of bound states are shown: at finite longitudinal momentum  $k_x$  (left) and vanishing momentum  $k_x = 0$  (right). The induced gap may only close at  $k_x = 0$ .

Here  $\sigma$  are the spin Pauli matrices, and  $\mathbf{p}$  the momentum operator. The chemical potential  $\mu$  and effective mass  $m$  are

$$\mu(y) = \begin{cases} \mu_n, & y \in (0, W) \\ \mu_s, & y < 0 \end{cases}, \quad m(y) = \begin{cases} m_n, & y \in (0, W) \\ m_s, & y < 0 \end{cases}. \quad (5.16)$$

Additionally, we neglect the spin-orbit coupling and the magnetic field effect in the superconductor, therefore restricting the model to  $B \ll B_c$ , with  $B_c$  the critical field of the superconductor:

$$\alpha(y) = \alpha\Theta(y)\Theta(W-y), \quad E_Z = \frac{g\mu_B B}{2}\Theta(y)\Theta(W-y), \quad (5.17)$$

with  $\Theta$  the Heaviside step function and  $\alpha$ , the Rashba spin-orbit coupling strength. The spin-orbit term in Eq. (5.15) is symmetrized using anticommutators to ensure current probability conservation at the interface. The Zeeman energy  $E_Z$  is due to a magnetic field of magnitude  $B$  oriented along the wire direction. The effective electric field generating the Rashba spin-orbit coupling is  $\mathcal{E}_R = 2m_n\alpha/\hbar g\mu_B\hat{z}$ . To compare the short-junction approximation with exact diagonalization results, we use the Bogoliubov-de Gennes (BdG) Hamiltonian:

$$H_{\text{BdG}} = \begin{pmatrix} H(B) & \Delta(y) \\ \Delta(y) & -H(-B) \end{pmatrix}, \quad (5.18)$$

with  $\Delta(y) = \Delta\Theta(-y)$ . The choice of a step-function pairing potential is justified due to a density of states mismatch between the superconductor and semiconductor by more than  $10^6$ , which renders the self-consistency condition on  $\Delta$  unimportant.

To make further analytical progress, we neglect the spin-orbit coupling in the  $y$  direction  $\alpha\sigma_x p_y$ . This is a valid simplification since in semiconductor nanowires the spin-orbit length  $l_{\text{SO}}$  is usually larger than the nanowire width  $W$ . We later verify the validity of this approximation by computing the exact expression for the topological phase boundary and by including the transverse spin-orbit coupling in all the tight-binding simulations.

The wave function  $\psi_n(k_x, y)$  in the nanowire satisfies the boundary condition  $\psi_n(k_x, W) = 0$  and has the general form

$$\psi_n = u_+ c_+ \sin[k_+(W-y)] + u_- c_- \sin[k_-(W-y)], \quad (5.19)$$

with

$$\begin{aligned} u_+ &= \frac{1}{\sqrt{2}} \begin{pmatrix} 1 \\ e^{i\varphi} \end{pmatrix}, & u_- &= \frac{1}{\sqrt{2}} \begin{pmatrix} e^{-i\varphi} \\ -1 \end{pmatrix}, \\ e^{i\varphi} &= \frac{E_Z - i\alpha k_x}{\sqrt{E_Z^2 + \alpha^2 k_x^2}}, \end{aligned} \quad (5.20)$$

and  $c_{\pm}$  unknown amplitudes. The wave function in the superconducting lead has the form

$$\psi_s = \begin{pmatrix} a_{\text{in},\uparrow} e^{iqy} + a_{\text{out},\uparrow} e^{-iqy} \\ a_{\text{in},\downarrow} e^{iqy} - a_{\text{out},\downarrow} e^{-iqy} \end{pmatrix}, \quad (5.21)$$

with  $a_{\text{in}}$  the amplitudes of the incoming modes,  $a_{\text{out}}$  the amplitudes of the outgoing modes, and the relative signs chosen to ensure that the incoming and outgoing modes are time-reversed of each other. Finally, the momenta  $q$  and  $k_{\pm}$  normal to the NS interface are fixed by the dispersion relation at energy  $E$ :

$$\begin{aligned} q &= \left[ \frac{2m_s}{\hbar^2} (E + \mu_s) - k_x^2 \right]^{1/2}, \\ k_{\pm} &= \left[ \frac{2m_n}{\hbar^2} (E + \mu_n \mp \sqrt{E_Z^2 + \alpha^2 k_x^2}) - k_x^2 \right]^{1/2}. \end{aligned} \quad (5.22)$$

We use the wave function continuity at  $y = 0$  as well as the current conservation condition on the wave function derivative normal to the interface, in the  $y$  direction:

$$m_n^{-1} \psi'_n(k_x, 0) = m_s^{-1} \psi'_s(k_x, 0). \quad (5.23)$$

Solving for  $c_{\pm}$  and  $a_{\text{out}}$  for given  $a_{\text{in}}$  we obtain the scattering matrix:

$$S_e = \frac{1}{2} \begin{pmatrix} (r_+ - r_-) e^{i\varphi} & r_+ + r_- \\ -r_+ - r_- & (r_- - r_+) e^{-i\varphi} \end{pmatrix}, \quad (5.24)$$

with the reflection phases of different spin projections given by

$$r_{\pm} = \frac{v_s - i v_{\pm} \cot(k_{\pm} W)}{v_s + i v_{\pm} \cot(k_{\pm} W)}. \quad (5.25)$$

Here we introduced the transverse velocities  $v_s = \hbar q / m_s$  in the superconductor lead and  $v_{\pm} = \hbar k_{\pm} / m_n$  in the nanowire.

The scattering matrix holds generally at energies below the superconducting gap  $|E/\Delta| < 1$ . In the short-junction approximation,  $S_e$  is evaluated at Fermi energy  $E = 0$ . Then the Andreev bound spectrum follows immediately upon solving the eigenvalue problem (5.9):

$$E = \pm \Delta \sqrt{1 - \frac{1}{4} |r_+(k_x) - r_-(k_x)|^2 \cos^2(\varphi)}. \quad (5.26)$$

This dispersion relation admits no zero energy solutions for  $k_x \neq 0$  and  $\alpha \neq 0$ . The parameters values yielding  $E(k_x = 0) = 0$  are the topological phase transitions, and they occur when

$$(r_+ + r_-)|_{k_x=0} = 0. \quad (5.27)$$

In the derivation of the Andreev spectrum (5.26) we neglected the effect of spin-orbit interactions in the  $y$  direction since  $W \ll l_{\text{SO}}$ . For completeness, we analyze the impact of this spin-orbit coupling on the condition for gap closing at  $k_x = 0$ . In the presence of transverse spin-orbit coupling, one needs to take into account the Hamiltonian (5.15) including the  $\alpha \sigma_x p_y$  term. Then the boundary condition at the NS interface needs to be modified in order to ensure the current conservation. Integrating the Schrödinger equation near the interface  $y = 0$  yields:

$$\frac{1}{m(y)} p_y \sigma_0 \psi(y) \Big|_{0^-}^{0^+} + \frac{\alpha}{\hbar} \sigma_x \psi(0) = 0. \quad (5.28)$$

Since at  $k_x = 0$ , the Hamiltonian (5.15) commutes with  $\sigma_x$ , the scattering states in the semiconductor region are also eigenstates of  $\sigma_x$ . Matching the wave functions at the NS interface and solving the scattering problem results in a condition for closing the excitation gap identical to Eq. (5.27), but with the modified scattering phases  $r_{\pm}$  (5.25):

$$k_{\pm} = \left[ \frac{2m_n}{\hbar^2} (E + \mu_n + E_{\text{SO}} \mp E_Z) \right]^{1/2}, \quad E_{\text{SO}} = \frac{m_n \alpha^2}{2\hbar^2}. \quad (5.29)$$

For our parameter choice  $E_{\text{SO}} \approx 40 \mu\text{eV}$ , and is more than two orders of magnitude smaller than  $\delta$ . This confirms that spin-orbit dynamics in  $y$  direction is negligible.

### 5.4.2. TYPICAL PHYSICAL PARAMETERS OF THE HETEROSTRUCTURE

To consider a specific example of the system parameters we take InSb nanowires [30] with effective mass  $m_n = 0.015 m_e$  (here  $m_e$  is the free electron mass), and with spin-orbit length  $l_{\text{SO}} = \hbar^2 / m_n \alpha \approx 250 \text{ nm}$ . The superconductor in the heterojunction is aluminum, with  $m_s \approx m_e$  and chemical potential  $\mu_s = 11.7 \text{ eV}$ . A thin Al film has the bulk superconducting gap  $\Delta = 0.25 \text{ meV}$  and the critical magnetic field  $B_c$  that varies from around 1.5 T to 2 T.

While most of our results scale trivially with  $W$ , we choose  $W = 100 \text{ nm}$  whenever it is necessary to compare the magnetic field or chemical potential scales to the experimental parameters. This results in  $\delta \approx 0.6 \text{ meV} \gg \Delta$ , well within the requirements of the short-junction approximation.

### 5.4.3. MODELING THE NS INTERFACE

The final crucial parameter of the hybrid system is the transparency of the NS interface. In the model Hamiltonian (5.15) the interface properties are set by the velocity ratio  $v_{\pm} / v_s$ , the only way the superconductor Hamiltonian parameters enter the scattering matrix (5.25). We use the  $v_s$  as a free parameter allowing us to study the effect of the interface properties on the topological phase diagram.

While the Fermi energy difference between aluminum and the semiconductor may span several orders of magnitude, the Fermi velocities do not differ so much because of a smaller effective mass in narrow band semiconductors. Specifically, the Fermi velocity in aluminum is  $v_s \sim 2 \times 10^6 \text{ m/s}$ , while  $v_{\pm} \sim 2 \times 10^5 \text{ m/s}$  at a relatively low  $\mu_n = 3 \text{ meV}$ , resulting in  $T \gtrsim 0.4$ . In real systems, the microscopic interface properties such as coupling strength and charge accumulation further influence the interface transparency. In the absence of a Schottky barrier, extra charge density at the interface smoothens the sharp change in velocity between the semiconductor and the superconductor and further enhances the transparency.

Transparency of the NS interface is hard to measure experimentally due to the complicated geometry of the normal metal-nanowire-superconductor samples. The experiments using high  $\Delta$  superconductors such as NbTiN are in a long junction regime allowing us to estimate  $T$  because the induced superconducting gap is  $\approx T\delta$ . On the other hand, tunneling spectroscopy only provides a lower bound on the transparency:  $T \gtrsim \Delta/\delta$  in the short-junction regime.

To explore the impact of interface transparency on the MBS properties we adopt two choices of  $v_s$ : the highly transparent interface corresponding to  $v_s \approx v_{\pm}$  and an interface

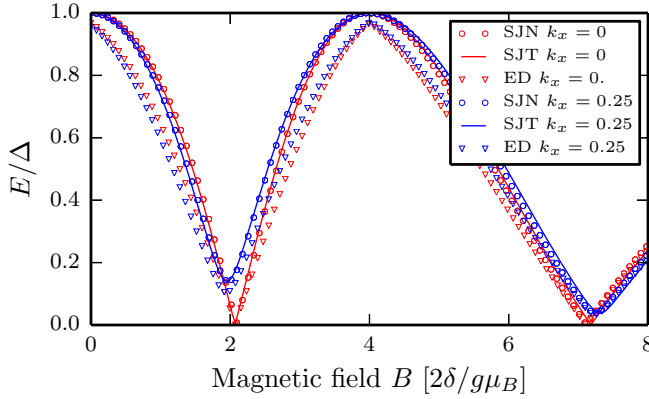


Figure 5.2: Comparison of the Andreev spectra of a transparent NS junction between analytical short-junction predictions (SJK), numerical short-junction results including the spin-orbit interaction in the  $y$  direction (SJK), and exact diagonalization of the BdG Hamiltonian (5.18) (ED). The system parameters are chosen as in Sec. 5.4.2 and 5.4.3. The longitudinal momentum is either  $k_x = 0$  (red), or finite such that the spectrum stays always gapped (blue). Momentum  $k_x$  is in units  $k_F^0 = \sqrt{2m_n\mu_n/\hbar^2}$ , and  $\mu_s = \mu_n = 3\text{ meV}$ .

5

with a finite transparency where we fix the value of  $\mu_s$  to a constant. For convenience we choose an anisotropic mass in the superconductor  $m_{s,y} = m_n$ ,  $m_{s,x} = m_{\parallel} \gg m_n$ , so that  $\mu_s = \mu_n$  results in a perfect transmission at a  $k_x = 0$  and  $B = 0$ . The condition  $m_{\parallel} \gg m_n$  ensures that  $v_s$  only weakly depends on  $k_x$ , as it should due to the Fermi surface in the superconductor being much larger than in the semiconductor. In most calculations we use  $m_{\parallel} = 10 m_n$ , however our conclusions are not sensitive to this choice (see Appendix 5.10 for details).

Adapting the calculations of Sec. 5.4.1 to the case of anisotropic mass and transparent limit yields the same result for the excitation spectrum (5.26), up to replacing the transverse momentum  $q$  in the superconductor with

$$q = \left[ \frac{2m_n}{\hbar^2} \mu_s - \frac{m_n}{m_{\parallel}} k_x^2 \right]^{1/2}. \quad (5.30)$$

#### 5.4.4. COMPARISON WITH TIGHT-BINDING DISPERSION SIMULATIONS

To verify the correctness of the spectrum in the short-junction limit, Eq. (5.26), we compare the analytical expressions with dispersion relations calculated using a Hamiltonian (5.15) discretized on a square lattice with lattice constant  $a = 0.5\text{ nm}$  and simulated using Kwant package [31]. We first numerically obtain the scattering matrix  $S_e(k_x)$  of the normal region and use it as an input to Eq. (5.9) to obtain the dispersion relation of the hybrid system.

A further comparison is provided by modeling the hybrid system using the full BdG Hamiltonian (5.18) and calculating several eigenstates closest to the Fermi level. In this case, the junction remains infinite along the wire, but instead of a superconducting lead,

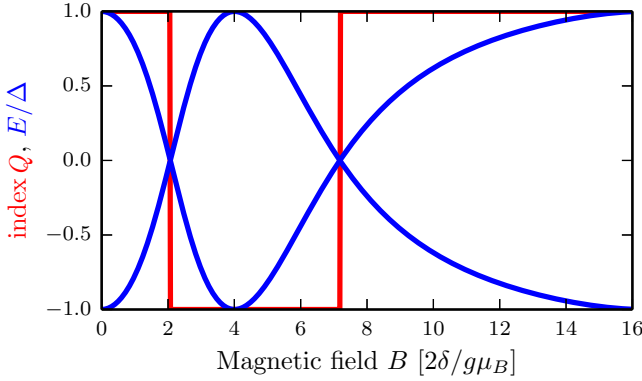


Figure 5.3: The Andreev spectrum and the topological index  $\mathcal{Q}$  (5.31) as a function of magnetic field. Trivial phase has  $\mathcal{Q} = +1$ , topological phase  $\mathcal{Q} = -1$ . The junction is in the transparent regime with  $\mu_s = \mu_n = 3 \text{ meV}$ .

we attach a large superconductor with width  $W_{\text{SC}} \approx 9 \mu\text{m} \gg \xi_S$ .

A comparison between analytics and the two numerical methods at a fixed chemical potential is shown in Fig. 5.2 and shows nearly perfect agreement between different methods. Slight deviations of exact diagonalization results occur near the bulk gap, caused by corrections to the short-junction approximation.

## 5.5. ANALYSIS OF THE TOPOLOGICAL PHASE DIAGRAM

### 5.5.1. PHASES BOUNDARIES AND THE SPECTRAL GAP

Equation (5.27) yields the closing of the spectral gap and the topological transitions in the model. This allows us to define the topological invariant of the Hamiltonian as

$$\mathcal{Q} = \text{sign}[\text{Im}(\sqrt{-r_-^* r_+})]_{k_x=0}, \quad (5.31)$$

where the sign of the square root is fixed by the analytic continuation and chosen such that  $\mathcal{Q} = 1$  in the trivial state. A typical spectrum at  $k_x = 0$  as well as  $\mathcal{Q}$  for a fixed  $\mu$  is shown in Fig. 5.3.

In addition to identifying the topological phase boundaries for each set of parameters  $(B, \mu_n)$  we calculate the spectral gap

$$\Delta_{\text{spec}} = \min_{k_x} |E(k_x)|, \quad (5.32)$$

with  $E(k_x)$  given by Eq. (5.26). The minimization is carried over all  $k_x$  present in the superconductor. In general, the dispersion relation has several local minima, as shown in Fig. 5.4, with the total number of minima approximately equal to the number of transverse modes in the normal region.

The resulting topological phase diagram of a transparent junction (with  $\mu_s = \mu_n$ ) is shown in Fig. 5.5. For typical junction parameters (as described in Sec. 5.4.2)  $g\mu_B B_c \approx 9\delta$ ,

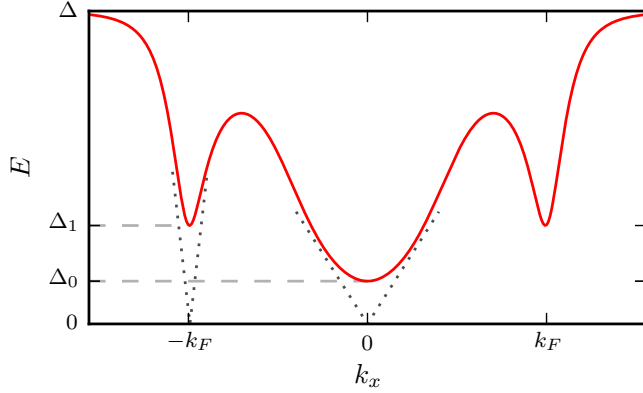


Figure 5.4: A schematic of the dispersion relation of the junction for typical parameters. The dispersion relation near local minima  $\Delta_0$  and  $\Delta_1$  of the Andreev state energy is well approximated with a gapped Dirac dispersion relation, with Dirac cones marked with dashed lines. When the number of available modes in the semiconductor increases, the number of minima at finite momenta grows, but the outermost minimum stays located approximately at  $k_x = k_{n,F}$ .

5

and the phase diagram for higher field values does not apply to such junctions. The minimal value of the critical field in this phase diagram corresponds to  $B_* \approx 0.7T$ . Near the topological phase transitions  $\Delta_{\text{spec}} = \Delta_0$ , the spectral gap at  $k_x = 0$  (see Fig. 5.4), and it varies linearly with the distance  $\varepsilon$  from the phase transition either along the  $\mu$  or  $E_Z$  axis:

$$\Delta_{\text{spec}} = \Delta_0 \sim \Delta \frac{\varepsilon}{\delta}. \quad (5.33)$$

Deep in the topological phase,  $\Delta_{\text{spec}}$  is limited by the gap  $\Delta_1$  at  $k_x \approx k_{n,F}$  (see Fig. 5.4), similar to the phenomenological model of Eq. (5.14). Since  $\Delta_{\text{spec}}$  must vanish linearly with  $\alpha$  in this regime, we get

$$\Delta_{\text{spec}} = \Delta_1 \sim \Delta \sqrt{\frac{E_{\text{SO}}}{\delta}}. \quad (5.34)$$

In both estimates we assumed  $\mu \sim E_Z \sim \delta$ , and  $T \sim 1$ . Comparing Eqs. (5.33) and (5.34) we find the energy scale for the transition between the two behaviors  $\varepsilon_* \sim \sqrt{E_{\text{SO}}\delta}$ .

The most unusual feature of the topological phase diagram in Fig. 5.5 is the smooth behavior of the topological phase boundary, different from the hyperbolic-shaped boundary  $E_Z^2 > \Delta^2 + \mu^2$  of the phenomenological models [6, 7, 22]. This difference appears not due to the short-junction limit—since the magnitude of the gap does not impact the topological phase boundary—but rather because of the high interface transparency. The inset in Fig. 5.5 shows the shape of the topological phase boundary where we have reduced the transparency by fixing  $\mu_s$  at a high value. We find that in this case the phase boundary has a hyperbolic shape predicted by the phenomenological model.

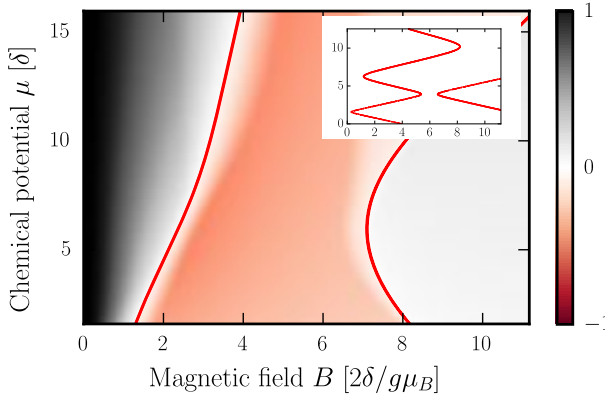


Figure 5.5: The spectral gap times the topological index  $\mathcal{Q}\Delta_{\text{spec}}/\Delta \in (-1, 1)$  as a function of chemical potential  $\mu$  and magnetic field  $B$ . Here we consider a transparent NS interface  $\mu = \mu_s = \mu_n$  and an anisotropic mass in the superconductor  $m_{\parallel} = 10 m_n$ ,  $m_{\perp} = m_n$ . The phase boundaries Eq. (5.27) are given by continuous red lines. The central region of the phase diagram is the topological phase  $\mathcal{Q} = -1$ . The inset shows the phase boundaries in a similar parameter range for a junction with  $\mu_s = 11.7$  eV,  $m_s = 0.015 m_n$  resulting in a low interface transparency.

### 5.5.2. DECAY LENGTH OF MBS

Exact evaluation of the MBS decay length starting from Eq. (5.26) is not possible because the spectrum in the short-junction approximation does not correspond to a local Hamiltonian (the same fact manifests in the complex nonlinear dispersion of the Andreev states). Nevertheless, the decay length is approximated well by assessing the contributions of different local minima of the dispersion relation, as shown in Fig. 5.4. A gapped Dirac cone with velocity  $v$  and gap  $\Delta$  results in a wave function decay length  $\xi = \hbar v / \Delta$  at  $E = 0$ . The size of the MBS  $\xi_M$  is set by the slowest decaying component of the wave function, or the largest  $\xi$ .

Once again, it is instructive to estimate  $\xi$  using scaling arguments in two regimes: near a topological transition and deep in the topological phase. At the phase transition point the slope of the Dirac cone at  $k_x = 0$ ,  $v_0 \propto \alpha$  since without spin-orbit coupling the band touching at  $k_x = 0$  must have a parabolic shape. Since the bulk superconductor gap  $\Delta$  must enter the spectrum only as an overall prefactor, we get

$$\hbar v_0 \sim \frac{\Delta W^2}{l_{\text{SO}}}, \quad \xi_0 = \frac{\hbar v_0}{\Delta_0} \sim \frac{W^2 \delta}{l_{\text{SO}} \varepsilon}. \quad (5.35)$$

The velocity at the outermost Dirac point must not depend on  $\alpha$ , resulting in

$$\hbar v_1 \sim \Delta W, \quad \xi_1 = \frac{\hbar v_1}{\Delta_1} \sim l_{\text{SO}}. \quad (5.36)$$

The two length scales  $\xi_0$  and  $\xi_1$  become equal at  $\varepsilon \sim E_{\text{SO}} \ll \sqrt{E_{\text{SO}} \delta} = \varepsilon_*$ .

We obtain the behavior of  $\xi$  in the tight-binding simulations using Kwant [31] for the same parameters as in Fig. 5.5. In order for the self-energy to become local in the  $x$

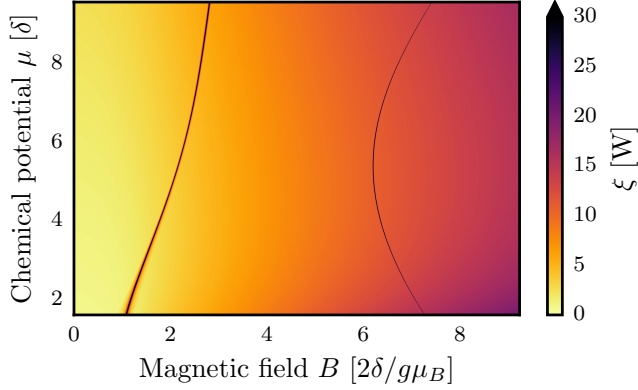


Figure 5.6: The largest decay length of subgap modes in units of wire width  $W$ , as a function of chemical potential  $\mu$  and magnetic field  $B$ . At the topological transitions the decay length rapidly diverges. The junction is in a fully transparent regime with  $\mu_n = \mu_s$  and  $m_{\parallel} = \infty$  in the superconductor.

5

coordinate we neglect the transverse dispersion in the superconductor and set  $m_{\parallel} = \infty$ . We then integrate out the superconductor and add a self-energy to the semiconductor. Finally, similar to Ref. [32] we perform an eigendecomposition of the translation operator in the  $x$  direction at zero energy to obtain the evanescent waves  $\psi \propto e^{-\kappa x}$ , with  $\kappa$  the eigenvalue of the translation operator. The largest decay length is:

$$\xi = \max \text{Re}[\kappa]^{-1}, \quad (5.37)$$

where the maximum is taken over all the eigenvalues. Then in the topological phase  $\xi_M = \xi$ . The results are presented in Fig. 5.6. The divergence in decay lengths seen in Fig. 5.6 corresponds to topological transitions identical to the ones found in Fig. 5.5. Figure 5.6 also confirms that  $\xi_M$  saturates at a distance  $\varepsilon \sim E_{SO}$  away from that phase transition (here  $E_{SO} \approx 40 \mu\text{eV}$ ).

We now refine the scaling arguments of Eqs. (5.35) and (5.36) by using Eq. (5.26). In particular, near the topological transition, the decay length is determined by the spectral gap  $\Delta_0$  and the velocity  $\hbar v_0 = |\partial E / \partial k_x|_{\Delta_0=0, k_x=0}$ :

$$\Delta_0 = \frac{\Delta}{2} |r_+ + r_-|_{k_x=0}, \quad (5.38)$$

with Fermi velocity

$$\hbar v_0 = \frac{\alpha \Delta}{E_Z}. \quad (5.39)$$

Therefore the MBS decay length  $\xi_M$  is inversely proportional to the magnetic field and spin-orbit length near the Majorana phase transitions.

Deep in the topological phase it is more difficult to obtain a closed form approximation for the decay length. Instead, we find the Fermi momentum and the spectral gap by

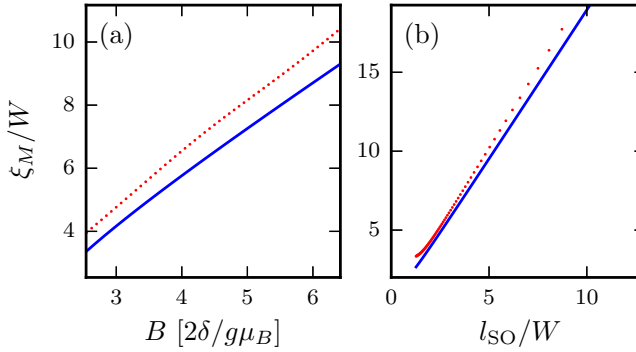


Figure 5.7: Scaling behavior of the MBS decay length  $\xi_M$  deep in the topological phase. Comparison between symbolic calculation of the decay length from the linearization of the energy dispersion (5.26) (blue lines) and the numerical calculation of the slowest decaying mode Eq. (5.37) (red markers). (a) The decay length has a linear dependence with magnetic field  $B$  deep in the topological region,  $\mu = 3$  meV. (b) Linear dependence with spin-orbit length  $l_{SO} = \hbar^2/m\alpha$ . The magnetic field is  $B = 1.5$  T and chemical potential  $\mu = 3$  meV.

performing numerical minimization of the energy dispersion (5.26). The Fermi velocity near  $k_F \neq 0$  follows immediately:

$$\hbar v_1 = \frac{\Delta}{2} \frac{\partial}{\partial k_x} |r_+ + r_-|_{\alpha=0, k_x=k_F}. \quad (5.40)$$

Taking the ratio (5.36), it follows that the MBS decay length does indeed grow linearly with magnetic field and spin-orbit length deep in the topological phase [see Fig. 5.7], in qualitative agreement with the numerical calculation using Eq. (5.37).

Our results for the scaling of  $\xi_M$  with  $B$  and  $l_{SO}$  agree with the predictions of the phenomenological 1D model both near the topological transition or deep in the topological phase (see, e. g., Ref. [33]), but we find no dependence of  $\xi_M$  on  $\Delta$ .

## 5.6. SPECTRUM OF FINITE LENGTH JUNCTIONS

To directly verify the existence of a MBS and the applicability of the short-junction limit to our system, we solve the discretized BdG Hamiltonian of a large rectangular system with a finite superconductor. The system is divided into semiconductor and superconductor regions, both modeled by the BdG Hamiltonian (5.18). The length of the system is  $L = 3 \mu\text{m}$ , sufficiently long to ensure that the overlap between MBS is small. Further, we choose the width of the superconductor sufficiently large  $W_{SC} = 1.4 \mu\text{m} \approx 2 \xi_S$ . The lattice constant in the tight-binding simulation is 10 nm. Finally, the remaining model parameters are chosen according to Sec. 5.4.2 and Sec. 5.4.3. We determine numerically several lowest energy states and compare them with  $\Delta_{\text{spec}}$  calculated in Sec. 5.5, as shown in Fig. 5.8.

We observe that the energy of most subgap states is bounded from below by an energy slightly lower than  $\Delta_{\text{spec}}$ , as expected close to the short-junction regime. At  $B > B_* \approx 1$  T

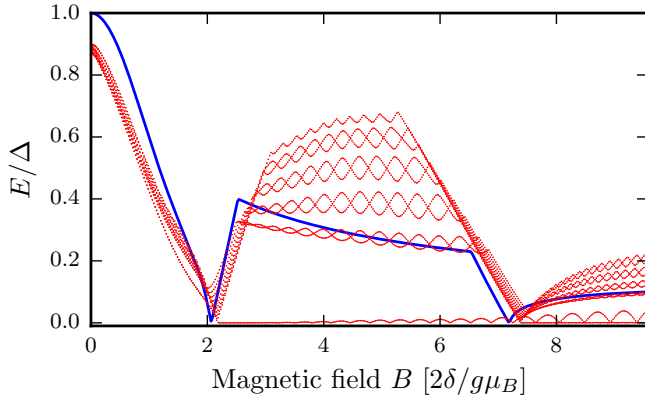


Figure 5.8: Comparison between the predictions of the analytical short-junction approximation and a numerical spectrum of a finite NS junction. Solid line:  $\Delta_{\text{spec}}$  calculated using Eqs. (5.26) and (5.32) as a function of magnetic field. Dotted lines: 10 lowest energy states in a finite size NS junction using the same parameters. The magnetic field is in units of  $2\delta/g\mu_B$ , with level spacing  $\delta$  defined in Eq. (5.11). The junction is in a transparent regime, the superconductor has anisotropic mass  $m_{\parallel} = 10 m_n$ , and the rest of parameters are as specified in Sec. 5.4.2. At a single end of the nanowire, there is only one MBS in the topological phase ( $1 \text{ T} \lesssim B \lesssim 3 \text{ T}$ , for semiconductor width  $W = 100 \text{ nm}$ ) and two in the trivial phase at high field, due to the chiral symmetry.

5

the system enters a topological regime and states with  $E \ll \Delta_{\text{spec}}$  formed by two coupled MBS appear. The coupling of these states decays exponentially with the size of the nanowire  $L$ . Finally after the system undergoes the second gap closing and enters the trivial phase at  $B \approx 3 \text{ T}$  additional low energy states appear due to the presence of chiral symmetry of the Hamiltonian (5.15) [34–36]. We therefore conclude that our calculations fully apply to finite nanowires in the short-junction regime.

Furthermore, we verify in Appendix 5.10.2 using exact diagonalization that the critical field  $B_*$  is indeed independent of the superconducting gap  $\Delta$ . With increasing  $\Delta$  above  $E_{\text{Th}} \approx 1 \text{ meV}$  the system exits the short-junction regime. Nevertheless, the critical magnetic field stays constant, in agreement with the proof of Sec. 5.3.

## 5.7. ORBITAL FIELD EFFECT IN THIN SHELL APPROXIMATION

We now turn to evaluate the consequences of the orbital effect of the magnetic field, known to strongly influence MBS properties [32, 37–39], in the short-junction limit. This effect does not manifest in the model of Sec. 5.4 when magnetic field points in the  $x$  direction. To include the orbital effect we use a thin shell approximation, when the electron wave function in the semiconductor is confined to its surface, similar to the system studied in Ref. [38]. However, unlike Ref. [38] we do not assume a constant induced gap and consider instead the nanowire contacted by a bulk superconductor, as shown in Fig. 5.9. We model the coupling to the superconductor as two infinite planar superconductors on each side of the 2D uncovered wire section. By doing so we neglect the possibility for electrons to tunnel through the superconductor to the other side of the uncovered section, which is justified by the density mismatch between the superconductor and the

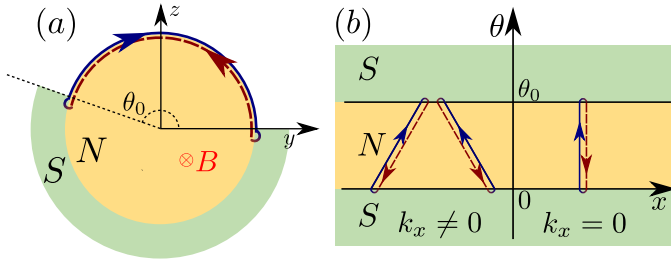


Figure 5.9: (a) A cross section of a NS hybrid junction. The magnetic field is parallel to the wire axis, while the Andreev bound state trajectories are confined to the nanowire surface. (b) The equivalent two-dimensional system defined on the plane  $(x, \theta)$ . Since we neglect the possibility for electrons to tunnel through the superconductor, we consider the superconducting leads at  $\theta < 0$  and  $\theta > \theta_0$  infinite.

semiconductor. The thin shell limit is oversimplified and it overestimates the orbital effect of a magnetic field, however it provides an upper bound on the impact of the orbital effect and remains analytically tractable.

The superconductor covers the wire over an angle  $2\pi - \theta_0$ , while both the wire and the superconductor are translationally invariant in the  $x$  direction. In cylindrical coordinates  $(x, \theta)$  the electron Hamiltonian on the nanowire surface reads:

$$H = \left[ \frac{p_\theta^2 + p_x^2}{2m} - \mu \right] \sigma_0 - \frac{\alpha}{\hbar} p_x \sigma_y + E_Z \sigma_x, \quad (5.41)$$

with  $p_\theta = -i\hbar R^{-1} \partial / \partial \theta$ , and  $R$  the radius of the nanowire. We assume that the magnetic field is fully screened from the superconductor and choose a gauge where the vector potential  $A = 0$  in the uncovered part of the surface, while the two superconducting leads have a phase difference  $\phi = (2e/\hbar)\pi BR^2$ . Compared to the previous sections where the treatment was more general, we assume from the start the transparent junction limit, when Fermi velocities at  $k_x = 0$  are identical in the superconductor and the semiconductor and we also neglect the spin-orbit coupling in the transverse direction, as appropriate for  $l_{SO} \gg R\theta_0$ .

We solve the scattering problem in the basis of conserved spin projections set by Eq. (5.20) corresponding to the basis of incoming and outgoing modes:

$$\mathbf{a}^T = (a_L^+, a_L^-, a_R^+, a_R^-), \quad \mathbf{b}^T = (b_L^+, b_L^-, b_R^+, b_R^-), \quad (5.42)$$

with  $\mathbf{a}$  and  $\mathbf{b}$  the amplitudes of incoming and outgoing modes,  $R$  denoting the modes at  $\theta \leq 0$ ,  $L$  the modes at  $\theta \geq \theta_0$ , and  $\pm$  superscript corresponding to the two conserved spin directions (5.20). For each spin projection the scattering matrix is given by the classic result for transmission through a potential barrier:

$$S_\pm = \begin{pmatrix} r_\pm & t_\pm \\ t_\pm & r_\pm \end{pmatrix}, \quad (5.43)$$

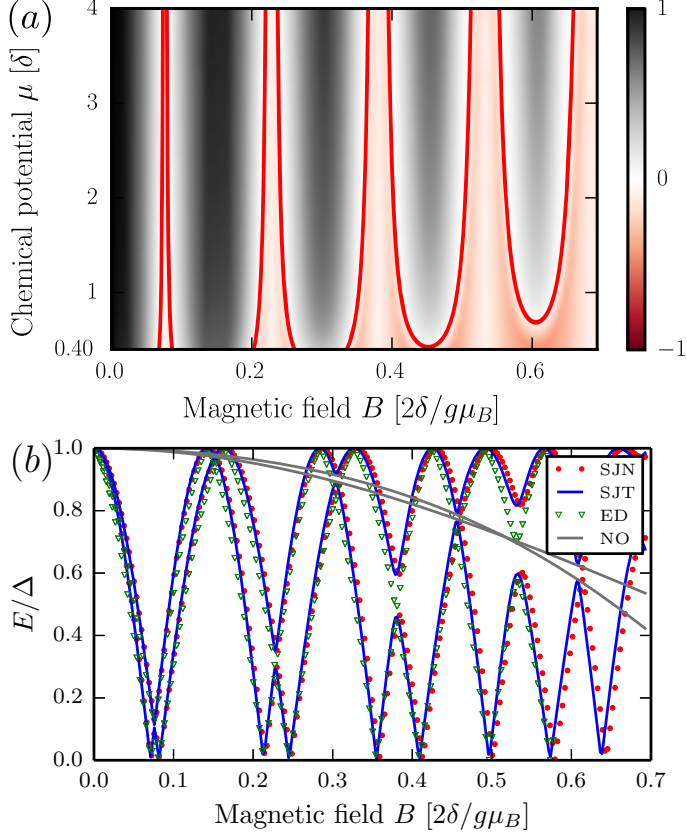


Figure 5.10: (a) Majorana phase diagram  $\mathcal{Q}\Delta_{\text{spec}}$  of a transparent NS junction with  $\mu_s = \mu_n = \mu$ ,  $m_{s,x} = m_{\parallel}$ ,  $m_{s,y} = m$ ,  $m_n = m$ , and  $m_{\parallel} = 10m$ , as a function of chemical potential and magnetic field. The covering angle is  $\theta_0 = 2$  rad, so that the width of the uncovered section  $R\theta_0$  is equal to the wire diameter. (b) An example of Andreev spectrum at  $k_x = 0$ ,  $\mu_n = \mu_s = 3$  meV, and other parameters the same as in (a) in the presence and absence of the orbital effect. Panel (b) additionally presents a comparison between short junction theoretical (SJT), numerical (SJT), and exact diagonalization (ED). The theoretical spectrum without orbital effect (NO) is in gray. The magnetic field is in units of  $2\delta/g\mu_B$  with  $\delta = \hbar^2\pi^2/2mR^2\theta_0^2$ .

with

$$\begin{aligned} r_{\pm} &= \frac{(q^2 - k_{\pm}^2) \sin(k_{\pm}L)}{(q^2 + k_{\pm}^2) \sin(k_{\pm}L) + 2iqk_{\pm} \cos(k_{\pm}L)}, \\ t_{\pm} &= \frac{2iqk_{\pm}}{(q^2 + k_{\pm}^2) \sin(k_{\pm}L) + 2iqk_{\pm} \cos(k_{\pm}L)}, \end{aligned} \quad (5.44)$$

with momenta  $k_{\pm}$  and  $q$  defined by Eq. (5.30). We then transform the scattering matrix to the basis of time-reversed modes (5.21) and calculate the Andreev spectrum using Eq. (5.9) with the phases of superconducting leads equal to  $\phi_R = 0$  and  $\phi_L = \phi$ . We verify again that the dispersion relation obtained this way agrees well with two numerical tight-binding simulations at fixed chemical potential and that the difference also stays small if we include spin-orbit coupling in the transverse direction [see Fig. 5.10(b)]. As before, the spectrum is generically gapped except at  $k_x = 0$ , where topological phase transitions occur.

The resulting Majorana phase diagram is shown in Fig. 5.10(a), and it consists of several narrow topological regions centered around  $\phi_k = (2k + 1)\pi$  with  $k$  integer. At these values of magnetic field, the two superconducting leads have a phase difference of  $\pi$ , thus fully suppressing the induced gap in the transparent limit. The Zeeman field then opens a topological gap resulting in a finite extension of the topological phases around  $\phi_k$ . We conclude that in the thin shell limit, the orbital effect of the magnetic field reduces  $B_*$  by a factor  $\sim 10$  for typical junction parameters (we once again note that the thin shell limit overestimates the orbital effect of the magnetic field). Despite that, it is the Zeeman field responsible for opening the topological gap.

## 5.8. NUMERICAL STUDY OF A THREE-DIMENSIONAL NANOWIRE

To confirm our findings in a model with a more realistic geometry, we numerically calculate the phase diagram of a three-dimensional nanowire in the short-junction limit. The system consists of a semiconductor nanowire infinite in the  $x$  direction and with a square cross section contacted by a bulk superconductor occupying  $y < 0$  half space [see Fig. 5.1(a)].

Due to the large Fermi surface mismatch between the superconductor and the semiconductor we neglect the electron dispersion in the  $x$  and  $z$  directions in the superconductor. Therefore, following Sec. 5.4.2 we set  $m_{s,y} = m_n = 0.015 m_e$  and  $m_{s,x} = m_{s,z} = \infty$ . Since the semiconductor modes with different values of  $k_z$  have different interface transparencies, we cannot ensure a transparent interface for all the modes and instead fix  $\mu_s = 8 \text{ meV}$  while varying  $\mu_n \equiv \mu$ . The remaining system parameters are specified in Sec. 5.4.2.

The model Hamiltonian is a three-dimensional generalization of Eq. (5.15) discretized on a cubic lattice. We include the orbital effect of the magnetic field using Peierls substitution in the gauge  $\mathbf{A} = (0, 0, B y \Theta(y))^T$ . This ensures that the vector potential is constant in the  $x$  direction and that it vanishes at the interface with the superconductor.

We calculate the excitation spectrum using Eq. (5.9) to find  $\Delta_{\text{spec}}$  by minimization over  $k_x$ . The resulting phase diagram of  $\Delta_{\text{spec}}$  is shown in Fig. 5.11. Comparing the top panels of Fig. 5.11 with Fig. 5.5 we observe the two sharp minima of  $B_*(\mu)$ . These correspond to

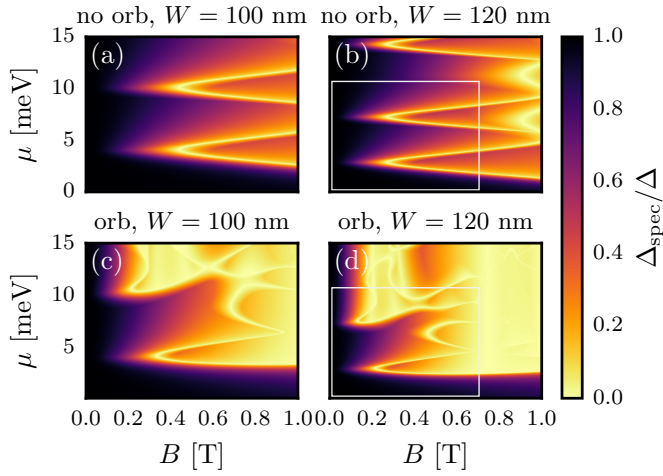


Figure 5.11: Spectral gap  $\Delta_{\text{spec}}/\Delta$  dependence on chemical potential  $\mu$  in the nanowire and magnetic field  $B$  of a square nanowire without (top panels) and with (bottom panels) orbital effect of the magnetic field. Panels (a), (c) show results for wire section  $100 \text{ nm} \times 100 \text{ nm}$ , while (b), (d), for  $120 \text{ nm} \times 120 \text{ nm}$ . The white box in the right panels shows the same parameter range rescaled by a factor  $(100/120)^2$  to highlight the  $W^2$  scaling of the phase diagram.

the appearance of the additional bands with a different value of  $k_z$  and a minimum in the interface transparency.<sup>1</sup>

Similar to our observations from Sec. 5.7, the orbital effect of the magnetic field has a strong effect on the shape of the topological phase boundaries and reduces both  $\Delta_{\text{spec}}$  and  $B_*$  similar to the thin shell simulations. Increasing the cross section of the wire [Fig. 5.11(a), (c), against (b), (d)] confirms that in 3D the critical fields preserve the scaling with  $B_* \sim 1/W^2$  independent of the presence or absence of orbital effects.

## 5.9. CONCLUSIONS AND OUTLOOK

We have studied the impact of a small superconducting gap on the properties of MBS in semiconductor-superconductor junctions. The short-junction formalism, appropriate for this limit, allows us to draw universal conclusions about the MBS properties. Contrary to the intuitive expectations, we show that the reduction of the superconducting gap does not alter the Majorana phase diagram and does not change the size of the MBS. We therefore conclude that in most practical systems the superconducting gap should not be used as an important parameter in optimizing MBS properties.

On the other hand, we find that the transparency of the semiconductor-superconductor boundary has an important and previously overlooked effect on the Majorana phase diagram. An interface with  $T \approx 1$  produces a phase boundary between trivial and topological

<sup>1</sup>The code for the tight-binding simulations of the two-dimensional and three-dimensional junctions is available as the Supplemental Material of [40].

phases which depends weakly on the chemical potential. This is in contrast to  $T \ll 1$ , used in most prior research, that results in the critical magnetic field having an oscillatory dependence on chemical potential with minima corresponding to the opening of a new band.

Orbital effect of magnetic field plays a dual role: It reduces the critical magnetic field as well as the spectral gap in the topological regime. Contrary to the predictions of a phenomenological model that assumes a constant induced gap, we show that relative importance of magnetic field cannot be controlled by the superconducting gap or the diameter of the nanowire.

Our findings suggest that creation of MBS in proximitized two-dimensional electron gases laterally contacted by a superconductor is a promising direction of further research. In these systems the relative strength of the orbital and the Zeeman effect of magnetic field is controlled by an extra tuning parameter: the ratio between the semiconductor thickness and its width. Additionally, the critical magnetic field in such devices could be tuned using a side gate, effectively changing the semiconductor width without altering the superconductor-semiconductor interface transparency.

Another important further direction of research is the interplay between junction transparency and disorder. Since a transparent interface results in a weaker dependence of the critical magnetic field on the chemical potential, it is reasonable to conjecture that the sensitivity of MBS properties to disorder is also reduced in the transparent regime.

## 5.10. APPENDIX

### 5.10.1. INTERFACE TRANSPARENCY IN A TWO-DIMENSIONAL JUNCTION

The validity of the short-junction approximation depends on NS interface transparency  $T$ . In this section, we review the transparency of a sharp interface between two materials with a parabolic dispersion. We provide quantitative arguments for the choice of anisotropic mass in the superconductor in modeling a transparent interface.

We consider a planar NS interface with the boundary located at  $y = 0$ , and both materials occupying a half-plane, and solve the scattering problem as outlined in Sec. 5.4.1. Also following Sec. 5.4.1, we neglect the spin-orbit scattering at the interface, and use the boundary condition (5.23). At a given energy  $E$  there are generally two modes in the semiconductor and two spin-degenerate modes in the superconductor with momenta in the  $y$  direction:  $k_{\pm}$  and  $q$ , respectively:

$$\begin{aligned} k_{\pm} &= \left[ \frac{2m_n}{\hbar^2} (E + \mu_n \mp \sqrt{E_Z^2 + \alpha^2 k_x^2}) - k_x^2 \right]^{1/2}, \\ q &= \left[ \frac{2m_{\perp}}{\hbar^2} (E + \mu_s) - \frac{m_{\perp}}{m_{\parallel}} k_x^2 \right]^{1/2}, \end{aligned} \quad (5.45)$$

where we use the same notation as in Sec. 5.4.1 the superconductor has anisotropic mass  $(m_{\perp}, m_{\parallel})$ .

The transmission probabilities of two spin orientations ( $\pm$ ) follow immediately:

$$T_{\pm} = 4 \left( \sqrt{\frac{v_{\pm}}{v_s}} + \sqrt{\frac{v_s}{v_{\pm}}} \right)^{-2}, \quad (5.46)$$

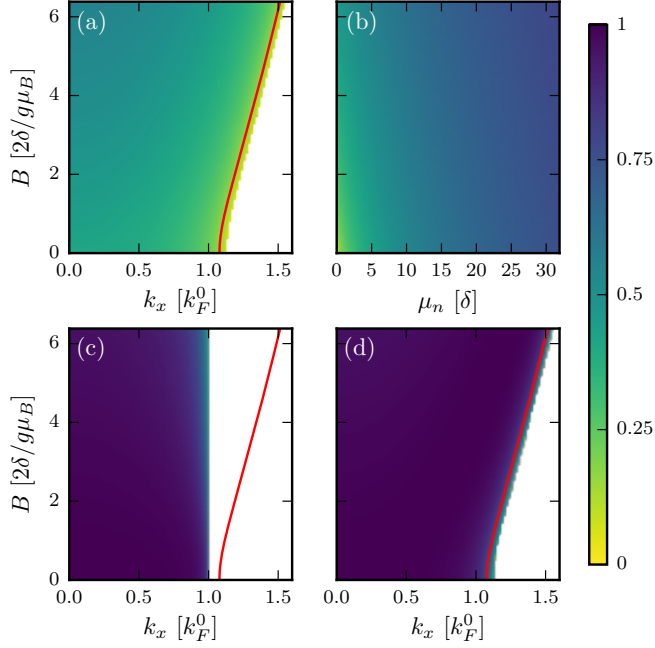


Figure 5.12: Transmission probability of one of the spin polarizations  $T_-$  of an infinite NS junction. (a, c, and d)  $T_-$  as a function of magnetic field  $B$  in units of  $\frac{2\delta}{g\mu_B}$ , with  $\delta$  defined in Eq. (5.11) and parallel momentum  $k_x$  (in units of  $k_F^0 = \sqrt{2m_n\mu_n/\hbar^2}$ ). The momenta  $k_x$  run over the Fermi surface of the semiconductor, which is marked by the red line. (a) Using bare material parameters  $\mu_n = 3 \text{ meV}$ ,  $\mu_s = 11.7 \text{ eV}$ ,  $m_s = m_e$ ,  $m_n = 0.015 m_e$ . (b)  $T_-$  versus  $B$  and  $\mu_n$  at  $k_x = 0$  and the same parameters as in (a). (c)  $T_-$  when the chemical potential and mass are equal in the superconductor and the semiconductor. (d)  $T_-$  for anisotropic mass in the superconductor ( $m_{\parallel}, m$ ),  $m_n \equiv m = 0.015 m_e$ , with  $m_{\parallel} = 10 m$ ,  $\mu_n = \mu_s = 3 \text{ meV}$ . Only evanescent solutions exist in the white regions; transmission  $T_-$  becomes imaginary.

with  $v_s = \hbar q / m_\perp$  and  $v_\pm = \hbar k_\pm / m_n$  the velocities normal to the interface in two materials. Both  $T_+$  and  $T_-$  exhibit similar behavior, except for  $T_+$  vanishing inside the helical gap. In contrast,  $T_-$  is always well defined at  $k_x = 0$  for  $\mu_n > 0$ . For concreteness, we illustrate the dependence of  $T_-$  on the Hamiltonian parameters.

Let us first start with realistic parameters both in the superconductor and the semiconductor. The chemical potential in the nanowire  $\mu_n$  is gate tunable. We choose to fix it at 3 meV, comparable to the level spacing in a nanowire. The rest of the parameters are specified in Sec. 5.4.2. The results are plotted in Fig. 5.12(a), for all momenta in the semiconductor Fermi surface and an experimentally relevant range of magnetic fields. The transparency is mostly around 40% but rapidly vanishes near the Fermi momentum. Modifying the chemical potential in the wire does not appreciably increase the transparency [see Fig. 5.12(b)]. The low transparency is artificial and due to the choice of a sharp change in mass and chemical potential across the interface.

Choosing  $m_\perp = m_\parallel = m_n$  and  $\mu_s = \mu_n$  results in a nearly perfect transmission at all angles, as shown in Fig. 5.12(c). However, this parameter choice is also unphysical since the semiconductor Fermi surface becomes larger than the superconductor one at any finite magnetic field. Then the interface becomes opaque for higher momenta  $k_x$ .

Finally, choosing  $\mu_s = \mu_n$  and an anisotropic mass in the superconductor ( $m_{s,x}, m_{s,y}$ ) =  $(m_\parallel, m_n)$ , with  $m_\parallel \gg m_n$  results in an interface that stays transparent for all  $k_x$  [see Fig. 5.12(d)].

### 5.10.2. INDEPENDENCE OF CRITICAL MAGNETIC FIELD ON THE SUPERCONDUCTING GAP

Here we verify the validity of our conclusions about the scaling of the eigenenergies and the independence of  $B_*$  on  $\Delta$  using exact diagonalization of a finite BdG Hamiltonian for the semiconductor-superconductor heterostructure at different values of the superconducting gap. We use the same setup of a finite heterojunction modeled with the BdG Hamiltonian (5.18) as in Sec. 5.6. We check the behavior of the critical field and the bulk band gap by tracking the energy of the second excited state while varying  $B$  for values of  $\Delta$  ranging from 40  $\mu\text{eV}$  to 3 meV (almost two orders of magnitude). Our results for a heterojunction of size 3000 nm  $\times$  6000 nm with a normal region occupying 3000 nm  $\times$  100 nm are shown in Fig. 5.13.

When  $\Delta \gtrsim E_{\text{Th}} \approx 1$  meV the system transitions to the long junction regime, so that the ratio  $\Delta_{\text{spec}}/\Delta$  continues to decrease, while  $\Delta_{\text{spec}}$  becomes almost independent of  $\Delta$ . In the opposite limit  $\Delta \ll E_{\text{Th}}$ , we observe that  $\Delta_{\text{spec}}/\Delta$  tends to a constant, in agreement with the short-junction limit prediction. The field values  $B_*$  where  $\Delta_{\text{spec}}$  vanishes stay almost constant, with the residual variation due to the effect of a finite system size and lattice constant.

## REFERENCES

- [1] X.-L. Qi and S.-C. Zhang, *Topological insulators and superconductors*, Rev. Mod. Phys. **83**, 1057 (2011).
- [2] M. Leijnse and K. Flensberg, *Introduction to topological superconductivity and Majorana fermions*, Semicond. Sci. Technol. **27**, 124003 (2012).

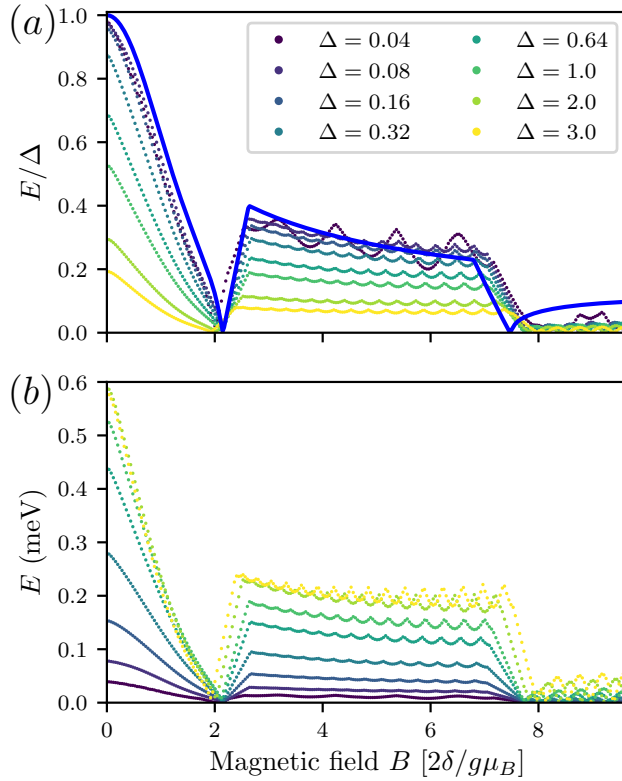


Figure 5.13: The energy of the second excited state of a finite nanowire junction calculated using exact diagonalization. Up to the second topological phase transition it is a good approximation of the induced gap. The eigenenergies are normalized to  $\Delta$  in panel (a) and unnormalized in panel (b). In the long junction regime the induced gap tends to a constant, while in the short-junction regime the ratio  $E/\Delta$  tends to the analytical result derived for the short-junction limit. The legend applies to both panels. The superconducting gaps  $\Delta$  are in meV.

- [3] J. Alicea, *New directions in the pursuit of Majorana fermions in solid state systems*, Rep. Prog. Phys. **75**, 076501 (2012).
- [4] C. Beenakker, *Search for Majorana Fermions in superconductors*, Annu. Rev. Condens. Matter Phys. **4**, 113 (2013).
- [5] S. R. Elliott and M. Franz, *Colloquium: Majorana fermions in nuclear, particle, and solid-state physics*, Rev. Mod. Phys. **87**, 137 (2015).
- [6] R. M. Lutchyn, J. D. Sau, and S. D. Sarma, *Majorana Fermions and a topological phase transition in semiconductor-superconductor heterostructures*, Phys. Rev. Lett. **105**, 077001 (2010).
- [7] Y. Oreg, G. Refael, and F. von Oppen, *Helical liquids and Majorana bound states in quantum wires*, Phys. Rev. Lett. **105**, 177002 (2010).
- [8] W. Chang, S. M. Albrecht, T. S. Jespersen, F. Kuemmeth, P. Krogstrup, J. Nygård, and C. M. Marcus, *Hard gap in epitaxial semiconductor-superconductor nanowires*, Nat. Nanotechnol. **10**, 232 (2015).
- [9] M. T. Deng, S. Vaitiekėnas, E. B. Hansen, J. Danon, M. Leijnse, K. Flensberg, J. Nygård, P. Krogstrup, and C. M. Marcus, *Majorana bound state in a coupled quantum-dot hybrid-nanowire system*, Science **354**, 1557 (2016).
- [10] S. M. Albrecht, A. P. Higginbotham, M. Madsen, F. Kuemmeth, T. S. Jespersen, J. Nygård, P. Krogstrup, and C. M. Marcus, *Exponential protection of zero modes in Majorana islands*, Nature **531**, 206 (2016).
- [11] W. S. Cole, S. D. Sarma, and T. D. Stanescu, *Effects of large induced superconducting gap on semiconductor Majorana nanowires*, Phys. Rev. B **92**, 174511 (2015).
- [12] A. M. Clogston, *Upper limit for the critical field in hard superconductors*, Phys. Rev. Lett. **9**, 266 (1962).
- [13] C. Beenakker, *Andreev billiards*, in *Quantum Dots: a Doorway to Nanoscale Physics* (Springer Berlin Heidelberg, 2005) pp. 131–174.
- [14] E. V. Bezuglyi, A. S. Rozhavsky, I. D. Vagner, and P. Wyder, *Combined effect of Zeeman splitting and spin-orbit interaction on the Josephson current in a superconductor-two-dimensional electron gas-superconductor structure*, Phys. Rev. B **66**, 052508 (2002).
- [15] O. V. Dimitrova and M. V. Feigel'man, *Two-dimensional S-N-S junction with Rashba spin-orbit coupling*, J. Exp. Theor. Phys. **102**, 652 (2006).
- [16] M. Cheng and R. M. Lutchyn, *Josephson current through a superconductor/semiconductor-nanowire/superconductor junction: Effects of strong spin-orbit coupling and Zeeman splitting*, Phys. Rev. B **86**, 134522 (2012).
- [17] J. Liu, A. C. Potter, K. T. Law, and P. A. Lee, *Zero-bias peaks in the tunneling conductance of spin-orbit-coupled superconducting wires with and without Majorana end-states*, Phys. Rev. Lett. **109**, 267002 (2012).

- [18] T. D. Stanescu, R. M. Lutchyn, and S. D. Sarma, *Dimensional crossover in spin-orbit-coupled semiconductor nanowires with induced superconducting pairing*, Phys. Rev. B **87**, 094518 (2013).
- [19] Y. Peng, F. Pientka, L. I. Glazman, and F. von Oppen, *Strong localization of Majorana end states in chains of magnetic adatoms*, Phys. Rev. Lett. **114**, 106801 (2015).
- [20] K. Pöyhönen, A. Westström, and T. Ojanen, *Topological superconductivity in ferromagnetic atom chains beyond the deep-impurity regime*, Phys. Rev. B **93**, 014517 (2016).
- [21] M. Wimmer, A. R. Akhmerov, M. V. Medvedyeva, J. Tworzydło, and C. W. J. Beenakker, *Majorana bound states without vortices in topological superconductors with electrostatic defects*, Phys. Rev. Lett. **105**, 046803 (2010).
- [22] R. M. Lutchyn, T. D. Stanescu, and S. D. Sarma, *Search for Majorana Fermions in multiband semiconducting nanowires*, Phys. Rev. Lett. **106**, 127001 (2011).
- [23] W. S. Cole, J. D. Sau, and S. D. Sarma, *Proximity effect and Majorana bound states in clean semiconductor nanowires coupled to disordered superconductors*, Phys. Rev. B **94**, 140505 (2016).
- [24] B. van Heck, S. Mi, and A. R. Akhmerov, *Single fermion manipulation via superconducting phase differences in multiterminal Josephson junctions*, Phys. Rev. B **90**, 155450 (2014).
- [25] A. F. Andreev, *The thermal conductivity of the intermediate state in superconductors*, J. Exp. Theor. Phys. **46**, 1823 (1964).
- [26] J. H. Bardarson, *A proof of the Kramers degeneracy of transmission eigenvalues from antisymmetry of the scattering matrix*, J. Phys. A: Math. Theor. **41**, 405203 (2008).
- [27] C. Beenakker, *Random-matrix theory of Majorana fermions and topological superconductors*, Rev. Mod. Phys. **87**, 1037 (2015).
- [28] C. W. J. Beenakker, *Universal limit of critical-current fluctuations in mesoscopic Josephson junctions*, Phys. Rev. Lett. **67**, 3836 (1991).
- [29] D. J. BenDaniel and C. B. Duke, *Space-charge effects on electron tunneling*, Phys. Rev. **152**, 683 (1966).
- [30] V. Mourik, K. Zuo, S. M. Frolov, S. R. Plissard, E. P. A. M. Bakkers, and L. P. Kouwenhoven, *Signatures of Majorana Fermions in hybrid superconductor-semiconductor nanowire devices*, Science **336**, 1003 (2012).
- [31] C. W. Groth, M. Wimmer, A. R. Akhmerov, and X. Waintal, *Kwant: a software package for quantum transport*, New J. Phys. **16**, 063065 (2014).
- [32] B. Nijholt and A. R. Akhmerov, *Orbital effect of magnetic field on the Majorana phase diagram*, Phys. Rev. B **93**, 235434 (2016).

- [33] J. Klinovaja and D. Loss, *Composite Majorana fermion wave functions in nanowires*, Phys. Rev. B **86**, 085408 (2012).
- [34] A. P. Schnyder, S. Ryu, A. Furusaki, A. W. W. Ludwig, V. Lebedev, and M. Feigel'man, *Classification of topological insulators and superconductors*, in *AIP Conf. Proc.* (AIP, 2009).
- [35] S. Ryu, A. P. Schnyder, A. Furusaki, and A. W. W. Ludwig, *Topological insulators and superconductors: tenfold way and dimensional hierarchy*, New J. Phys. **12**, 065010 (2010).
- [36] S. Tewari and J. D. Sau, *Topological invariants for spin-orbit coupled superconductor nanowires*, Phys. Rev. Lett. **109**, 150408 (2012).
- [37] J. S. Lim, R. Lopez, and L. Serra, *Emergence of Majorana modes in cylindrical nanowires*, EPL **103**, 37004 (2013).
- [38] J. Osca, R. López, and L. Serra, *Majorana mode stacking, robustness and size effect in cylindrical nanowires*, Eur. Phys. J. B **87**, 84 (2014).
- [39] J. Osca and L. Serra, *Majorana states and magnetic orbital motion in planar hybrid nanowires*, Phys. Rev. B **91**, 235417 (2015).
- [40] D. Sticlet, B. Nijholt, and A. Akhmerov, *Robustness of Majorana bound states in the short-junction limit*, Phys. Rev. B **95**, 115421 (2017).



# 6

## ENHANCED PROXIMITY EFFECT IN ZIGZAG-SHAPED MAJORANA JOSEPHSON JUNCTIONS.

---

This chapter has been previously published as Tom Laeven, Bas Nijholt, Michael Wimmer, and Anton R. Akhmerov, *Enhanced proximity effect in zigzag-shaped Majorana Josephson junctions*, arXiv preprint arXiv:1903.06168, (2019)

My contribution to this work is the writing of the paper, implementing a large fraction of the numerical methods, and performing the numerical simulations.

## 6.1. INTRODUCTION

A hybrid structure containing a semiconductor with strong spin-orbit coupling coupled to a superconductor can become topological upon application of a magnetic field stronger than a critical field  $B_{\text{crit}}$ , with Majorana bound states appearing on its edges [1, 2]. Majorana bound states are a promising candidate to form the basis of a stable platform for topological quantum computing [3–6]. Much of the experimental effort [7–11] currently focuses on creating pairs of Majorana bound states in hybrid normal-superconductor (NS) nanowire structures.

Recently, a modified setup has been proposed [12, 13] relying on a superconductor-normal-superconductor (SNS) junction to lower the critical magnetic field  $B_c$  by introducing a superconducting phase difference  $\phi$ . When both NS interfaces are transparent the SNS junction enters the topological phase at  $\phi = \pi$  at any finite  $B$  field. Two groups [14, 15] have realized this system experimentally, but did not yet observe a hard induced superconducting gap.

An important challenge in creating stable Majoranas is the appearance of a soft gap—a power law decay instead of an exponential decay of the density of states near zero energy. In clean systems a soft gap arises due to the reduction of the induced gap for states with the momentum directed along the junction [16, 17]. From a semiclassical perspective, these momenta correspond to long paths through the semiconductor without interruption by the superconductor, shown in Fig. 6.1(a). These long trajectories have long flight times  $\tau_f \approx L_t / v_F$  (see Fig. 6.1), where  $L_t$  is the trajectory length and  $v_F$  the electron Fermi velocity. Equivalently, the Thouless energy of these trajectories  $E_{\text{Th}} = \hbar / \tau_f$  is small, resulting in a small gap  $E_{\text{gap}} \ll \Delta$ . This problem does not appear when the Fermi surface is small and the zero point motion dominates the transverse velocity, making a low filling of the bands a possible workaround [17, 18]. However, tuning the system to a low chemical potential requires a precise knowledge of the band positions and makes the device more sensitive to disorder or microscopic inhomogeneities. On the other hand, disorder scatters these long trajectories and introduces a cutoff on the scale of the mean free path [19–21] which Ref. [22] proposes to use to improve Majorana properties; however, disorder is impossible to control to a required precision experimentally.

We propose a new experimental setup (see Fig. 6.1(b)) for the creation of Majoranas that eliminates long trajectories and therefore prevents the appearance of a soft gap, while also increasing the topological gap (the smallest gap in the dispersion relation) by more than an order of magnitude, depending on the parameters. The setup consists of a zigzag or snake-like geometry for the semiconductor where long trajectories are not possible due to the geometry.

## 6.2. SETUP

We consider a Josephson junction (Fig. 6.1) consisting of a 2D strip of semiconductor, with superconductors on both sides [12, 13]. (In the App. 6.7.1 we demonstrate that similar physics also occurs in devices with a single superconductor.) We modulate the shape of the normal region to be either zigzag as depicted [Fig. 6.1(b)] or a more smooth sinusoidal-like shape. Similar to the straight system [12], we apply a magnetic field  $B_x$  along the  $x$ -axis. The Bogoliubov-de Gennes Hamiltonians  $H_N$  and  $H_{\text{SC}}$  of the normal

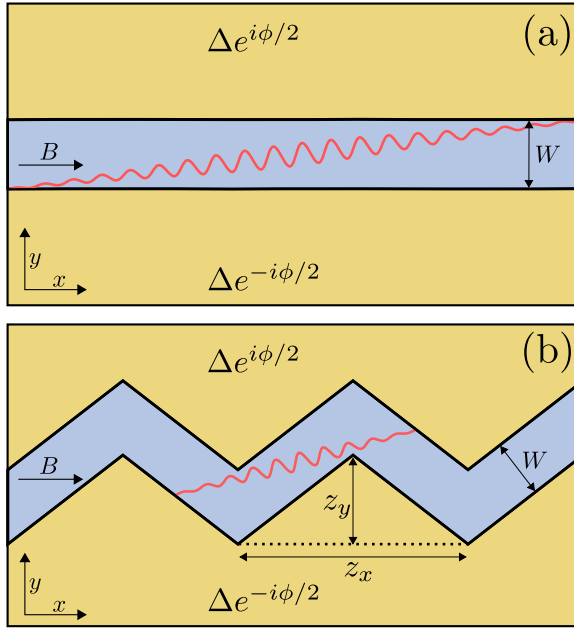


Figure 6.1: The straight (top) and the zigzag (bottom) SNS junction. The zigzag pattern has a peak-to-peak amplitude  $z_y$  and a period  $z_x$ . The yellow areas are superconductors with a phase difference of  $\phi$  between the top and the bottom. The middle area is the semiconductor of width  $W$ . A magnetic field  $B$  pointing in the  $x$ -direction causes a Zeeman splitting in the semiconductor. A trajectory traveling at a grazing angle (red curve) has a very long flight time  $\tau_f$  and a very small induced gap  $E_{\text{gap}} \ll \Delta$ . At the same time, the zigzag geometry limits the length of a trajectory, therefore lowering  $\tau_f$  and increasing  $E_{\text{gap}}$ .

region and the superconducting region are

$$H_N = \left[ \frac{\hbar^2 (k_x^2 + k_y^2)}{2m_{\text{eff}}} - \mu + \alpha (k_y \sigma_x - k_x \sigma_y) \right] \tau_z + E_Z \sigma_x, \quad (6.1a)$$

$$H_{\text{SC}} = \left[ \frac{\hbar^2 (k_x^2 + k_y^2)}{2m_{\text{eff}}} - \mu \right] \tau_z + \Delta \cos \frac{\phi}{2} \tau_x + \Delta \sin \frac{\phi}{2} \tau_y. \quad (6.1b)$$

Here,  $k_x$  and  $k_y$  are the momentum components of the wavevector,  $\mu$  is the chemical potential, and  $m_{\text{eff}}$  is the effective electron mass. The strength of the Rashba spin-orbit coupling is  $\alpha$  and a Zeeman splitting  $E_Z = \frac{1}{2} \mu_B g B_x$ . The superconductor has a coupling strength  $\Delta$ , and the phases of the superconductors are  $\pm \phi/2$ . The Hamiltonian acts on the spinor wave function  $\Psi = (\psi_{e\uparrow}, \psi_{e\downarrow}, \psi_{h\uparrow}, -\psi_{h\downarrow})^T$ , where  $\psi_e, \psi_h$  are its electron and hole components, and  $\psi_{\uparrow}, \psi_{\downarrow}$  are the spin-up and spin-down components. The Pauli matrices  $\sigma_i$  act on the spin degree of freedom and  $\tau_i$  act on the electron-hole degree of freedom. We consider a zigzag pattern with a period  $z_x$ , a peak-to-peak amplitude  $z_y$ , and  $W$  the width of the junction [see Fig. 6.1(b)]. Later we relax this assumption and show that the exact shape is unimportant.

We discretize our continuum Hamiltonian [Eq. (6.1)] on a square grid and implement a tight-binding model using Kwant [23]. To preferentially sample important regions of parameter space, we use the Adaptive package [24]. The entire source code and the resulting raw data are available in Ref. [25].

Unless noted differently, the Hamiltonian parameters are  $\alpha = 20 \text{ meV nm}$ ,  $g = 26$ ,  $m_{\text{eff}} = 0.02 m_e$ ,  $\mu = 10 \text{ meV}$ ,  $B_x = 1 \text{ T}$ ,  $\phi = \pi$ , and  $\Delta = 1 \text{ meV}$ ; and the geometry parameters are  $W = 200 \text{ nm}$ , the period of the zigzag  $z_x = 1300 \text{ nm}$ , the discretization constant  $a = 10 \text{ nm}$ , and the lengths of the superconductors  $L_{\text{SC}} = 300 \text{ nm}$ . Our results only weakly depend on the material parameters.

### 6.3. BAND STRUCTURES

We apply sparse diagonalization to the supercell Hamiltonian at different momenta  $k_x$  to compute the band structure. Because of the large periodicity of the zigzag and the resulting large supercell, the band structure is heavily folded. In Fig. 6.2 we show the resulting band structures of zigzag systems with varying  $z_y$ . The introduction of the zigzag has a striking effect: the bands flatten out and the topological gap increases by more than an order of magnitude.

In the unfolded band structure of a straight system, shown in Fig. 6.2(a), the lowest energy states occur at  $k \approx k_F$ . We interpret the increase of the gap  $E_{\text{gap}}$  shown in Fig. 6.2(b) and (c) as an effect of the zigzag geometry removing these long trajectories traveling at grazing angles. Besides the increased  $E_{\text{gap}}$ , the states from different segments of the zigzag pattern have a negligible overlap and therefore have a vanishing quasiparticle velocity  $v$ . This reduction in velocity strongly reduces the Majorana size, as we discuss in section 6.4. Finally, in a zigzag geometry, every trajectory encounters a superconductor close to normal incidence. Normal incidence has a higher transmission probability for entering the superconductor and therefore a higher Andreev reflection amplitude. This provides another mechanism of the gap enhancement.

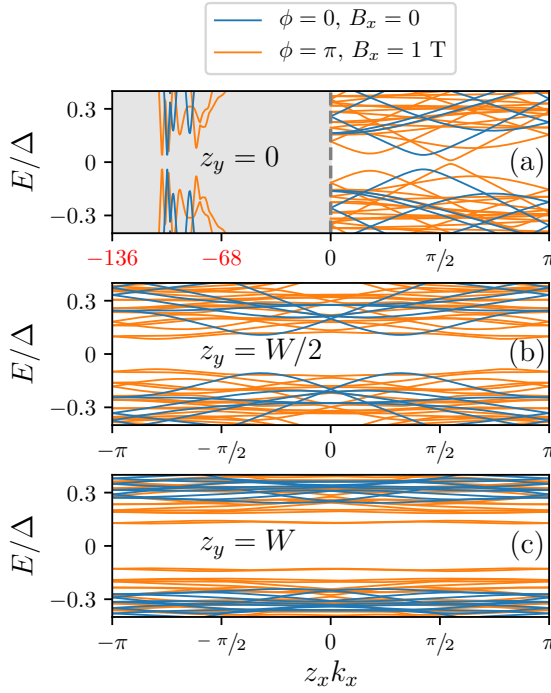


Figure 6.2: Band structures of the system in Fig. 6.1(b) with different zigzag amplitudes. The blue lines correspond to a trivial phase ( $\phi = 0$ ,  $B_x = 0$ ) and the orange lines to a topological phase ( $\phi = \pi$ ,  $B_x = 1$  T). The three subplots are for different amplitudes of the zigzag, with (a) a straight system  $z_y = 0$ , (b)  $z_y = W/2$ , and (c)  $z_y = W$ , where  $W = 200$  nm is the junction width. Subplot (a) has a different  $x$ -scale for  $k_x < 0$  from the other subplots and displays the unfolded band structure. For the right-hand side of (a) ( $k_x > 0$ ), (b), and (c), the folding is the same, such that the velocity  $v = dE/dk$  can be compared visually. Once there are no more straight trajectories inside the junction (when  $z_y = W$ ) the spectrum becomes insensitive to the momentum  $k_x$  and equivalently, the quasiparticle velocity  $v$  decreases. When the zigzag amplitude increases, the band gap  $E_{\text{gap}}$  increases by an order of magnitude. The combination of these ensures a significant decrease of the Majorana size  $\zeta_M \propto v/E_{\text{gap}}$ . The parameter values are listed at the end of Sec. 6.2.

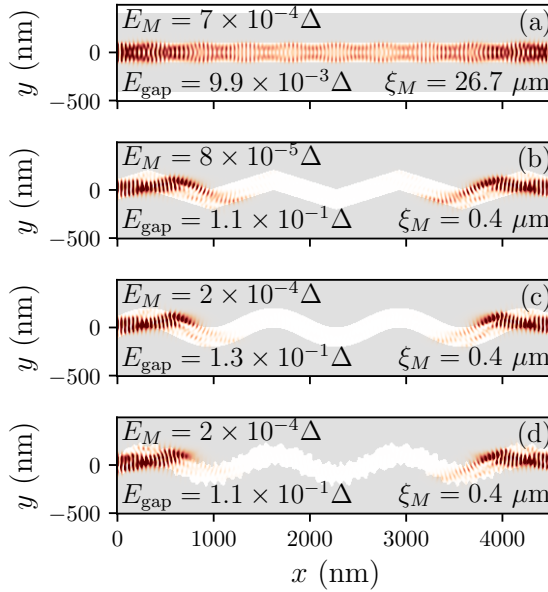


Figure 6.3: Density of Majorana wave functions  $|\psi_M|^2$  for different geometries. With (a) a straight system, (b) a zigzag system, (c) a system where lines parallel to a sinusoid defines the normal region, and (d) similar to (c) but with disordered edges. Inside the figure, we indicate the Majorana length (or coherence length)  $\xi_M$ , the Majorana energy  $E_M$  (the energy of the first excited state), and the topological energy gap  $E_{\text{gap}}$ . We observe that  $\xi_M$  for the straight system is almost two orders of magnitude longer and  $E_{\text{gap}}$  more than an order of magnitude smaller than for the zigzag systems. The robustness of  $E_{\text{gap}}$  and  $\xi_M$  across the zigzag geometries means that the details of the geometry do not matter for the improvements to occur. The length of the system is  $3.5z_x = 4550 \text{ nm}$ , the remaining parameter values are listed at the end of Sec. 6.2.

6

## 6.4. LOCALIZATION LENGTHS AND SHAPE EFFECTS

We model a finite system and compute the Majorana wave function in different geometries: ribbon, zigzag, sine-like parallel curves, and a variant of the latter with disordered edges. By diagonalizing the Hamiltonian, we find the Majorana energy  $E_M$ , and by using the corresponding eigenstate of that lowest energy, we get the wave function. When determining the Majorana size  $\xi_M$  in a zigzag system, we reduce the finite size effects by introducing a particle-hole symmetry breaking potential  $V\sigma_0\tau_0$  on one edge, such that one of the Majorana states is pushed away from zero energy. We then find  $\xi_M$  by fitting an exponential to the density of the single Majorana wave function projected on the  $x$ -axis. In the straight system we use the eigenvalue decomposition of the translation operator at zero energy [18] for performance reasons.

We show the resulting Majorana wave function densities  $|\psi_M|^2$  in different geometries in Fig. 6.3 using the same Hamiltonian parameter values. In the straight system [Fig. 6.3(a)], we see that the decay of the density is long compared to the system size. This is a result of the small topological gap combined with the quasiparticle velocity  $v \approx v_F$

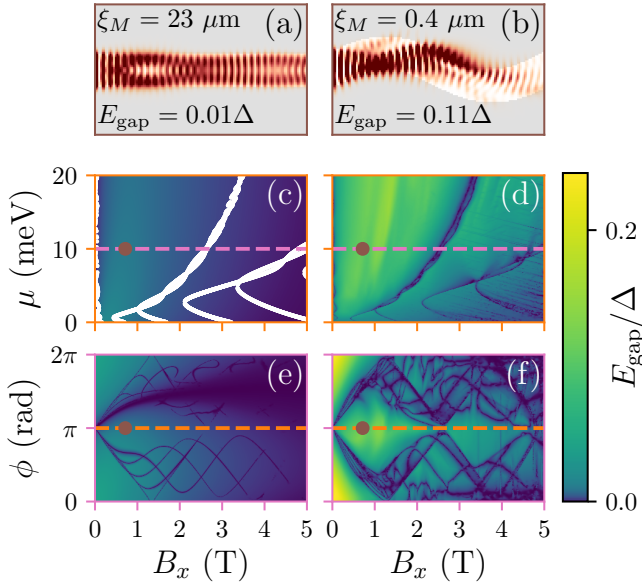


Figure 6.4: A comparison of a straight device (left panels) and a zigzag one (right panels). The top panels show the Majorana wave functions, near the left edge of the system, at the value of  $B_x$  for which  $E_{\text{gap}}$  is maximized in a straight geometry for  $\mu = 10$  meV and  $\phi = \pi$  as well as the values of the gap and the Majorana size. The other panels show gap as a function of  $\mu$  and  $B_x$  at  $\phi = \pi$  (middle panels) and as a function of  $\phi$  and  $B_x$  at  $\mu = 10$  meV (bottom panels). The dashed lines and the dot indicate the parameters used in the other panels. Additionally, in subplot (c) we overlay the phase boundaries. The remaining parameter values are listed at the end of Sec. 6.2, except with  $a = 5$  nm and  $L_{\text{SC}} = 800$  nm.

yielding a large Majorana size

$$\xi_M = \hbar \frac{v}{E_{\text{gap}}}. \quad (6.2)$$

This result follows from an avoided crossing shape of the dispersion relation near the Fermi momentum. Therefore, in straight junctions the wave function extends to the center of the system, resulting in highly overlapping Majoranas and a Majorana coupling  $E_M$  comparable to  $E_{\text{gap}}$ .

We observe that in zigzag systems the Majorana properties improve independent of specific geometric details. All of the zigzag-type geometries have  $\xi_M$  improved by a factor  $\sim 70$  and have the Majorana wave function localized within one segment of the zigzag. Further, the topological gap  $E_{\text{gap}}$  is an order of magnitude higher than in the straight junction, and as mentioned in section 6.3, the quasiparticle velocity  $v$  is more than an order of magnitude lower.

## 6.5. TOPOLOGICAL PHASE DIAGRAM

In Fig. 6.4 we compare the phase diagrams of the straight and the zigzag junction. We plot  $E_{\text{gap}}$  as a function of magnetic field and chemical potential ( $E_{\text{gap}}(B_x, \mu)$ ), and of magnetic field and superconducting phase difference ( $E_{\text{gap}}(B_x, \phi)$ ) for both a straight system [(c) and (e)] and a zigzag system [(d) and (f)]. Additionally, we plot the first 1300 nm (one zigzag period) of the wave functions [(a) and (b)] at the optimal point in parameter space for the straight system. For the straight system, we calculate  $E_{\text{gap}}$  by performing a binary search in  $E$  for the energy at which the propagating modes start to appear [18]. Additionally, in Fig. 6.4(c) we plot the phase boundaries obtained by solving a generalized eigenvalue problem [18]. Due to the large size of the zigzag supercell, we are unable to apply these methods to zigzag geometries. Instead, we calculate  $E_{\text{gap}}$  by finding the absolute minimum of the spectrum  $E_{\text{gap}} = \min |E(k)|$ . By both observing the gap closings and comparing to the topological phase diagram of the straight system, we then infer the topology of the zigzag system and verify this by calculating the Majorana wave function of a finite length zigzag. As a further check, in App. 6.7.2 we also compute  $E_{\text{gap}}$  as function of the angle of magnetic field and observe that the zigzag device protects Majoranas from magnetic field misalignments.

Similar to the findings of Pientka *et al.* [12], we see that the straight geometry has a diamond-shaped topological region in  $(\phi, B_x)$  space. The topological phase diagram of the zigzag system has a qualitatively similar shape but a significantly increased topological gap. The asymmetry of the phase diagram upon replacing  $\phi \rightarrow -\phi$  is consistent with the symmetry of the Hamiltonian, because both inversion and time-reversal change both  $\phi \rightarrow -\phi$  and  $B_x \rightarrow -B_x$ .

## 6.6. DISCUSSION AND CONCLUSIONS

The zigzag geometry increases the topological gap in the high-density regime by more than an order of magnitude, and substantially reduces Majorana size. The improvements occur in a broad range of parameter values, moreover, even using  $B_x$  optimal for the straight system in the high-density regime (Fig. 6.4), the Majorana size  $\xi_M$  and  $E_{\text{gap}}$  are still more than an order of magnitude better for the zigzag system. We expect that the improvement of the device performance will significantly simplify the creation of Majorana devices and the detection of Majorana states. Additionally, it offers a controllable way to remove long trajectories, making it easier to rely on than disorder [22], which has a similar effect.

A soft gap may arise due to mechanisms that do not involve ballistic trajectories: both interface disorder and pair-breaking [26] or temperature and dissipation [27] may create a soft gap. Further, in a multimode junction, the dependence of transmission [28] may produce a subgap conductance similar to that in a device with a soft gap. The zigzag geometry has no impact on these alternative phenomena, and it may therefore serve as a tool to distinguish different mechanisms.

Our work is the first demonstration of the impact of the Majorana device geometry on its performance, and it opens a possible research avenue of finding the optimal geometry. A promising approach to tackle this question would rely on constructing a quasiclassical model of the zigzag devices. Finally, we neglected several important physical effects,

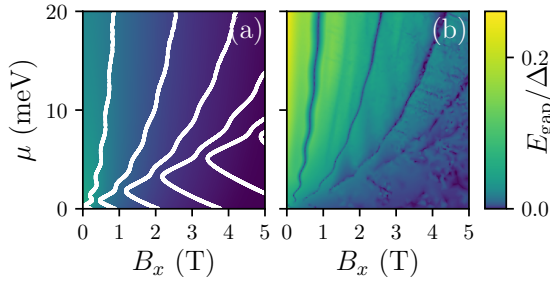


Figure 6.5: Same as Fig. 6.4 (c) and (d) but with one superconductor instead of two. We observe that the zigzag geometry also increases the gap in this case.

such as disorder, electrostatics, the orbital effect of the magnetic field, and the finite thickness of the sample. Although we do not expect these phenomena influence our qualitative findings, a more detailed simulation should provide better guidance to future experiments.

The zigzag geometry is within reach of the standard fabrication techniques as demonstrated by an ongoing experimental project [29]. Further, according to our simulations, the zigzag devices should be robust against the unavoidable variation in the experimental device geometry. We therefore expect, that the new approach to controlling the proximity superconductivity by means of modifying the geometry will become a commonly used technique.

## 6.7. APPENDIX

### 6.7.1. ZIGZAG DEVICE WITH A SINGLE SUPERCONDUCTOR

A zigzag-shaped device with a single superconductor shows a similar enhancement of the superconducting gap as the Josephson junction devices. We demonstrate this by simulating a straight and a zigzag device and computing  $E_{\text{gap}}(B_x, \mu)$  in Fig. 6.5. We observe that the order of magnitude increase of  $E_{\text{gap}}$  also occurs upon the introduction of a zigzag geometry.

### 6.7.2. DIRECTION OF THE MAGNETIC FIELD

Because the zigzag geometry cuts off long trajectories—leaving only short trajectories—this device requires a less precise alignment of the magnetic field. To show this, we perform a simulation of a straight and zigzag device with a rotated field (see Fig. 6.6). We observe that the zigzag device still has a sizeable gap with a  $10^\circ$  misaligned magnetic field, whereas a  $1^\circ$  misalignment makes a straight device gapless.

Strong screening of the magnetic field by the superconductors may distort the magnetic field pattern. To determine whether this effect degrades the device quality, we simulate a device with the magnetic field parallel to the NS interface, shown in Fig. 6.7. We find that the resulting gap is comparable to that of a device with the magnetic field purely in the  $x$ -direction, as shown in Fig. 6.8.

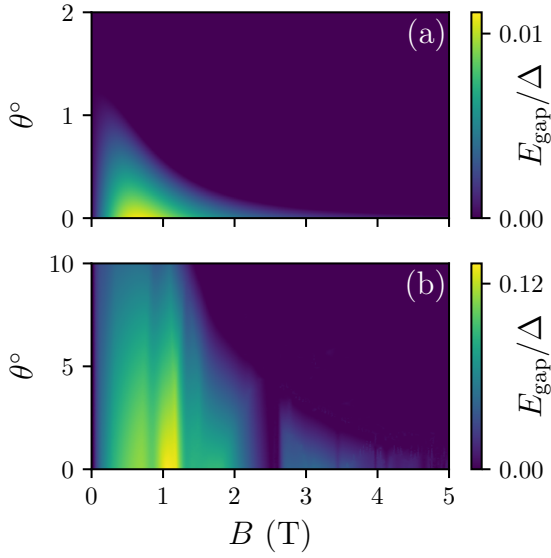


Figure 6.6: The topological gap as a function of the magnetic field magnitude  $B$  and its angle  $\theta = \arctan B_y/B_x$  for a straight device (a) and a zigzag device (b). Note that the colormaps and the  $\theta$ -axes differ between panels: the zigzag-shaped device becomes gapless at  $\theta$  an order of magnitude larger compared to the straight device.

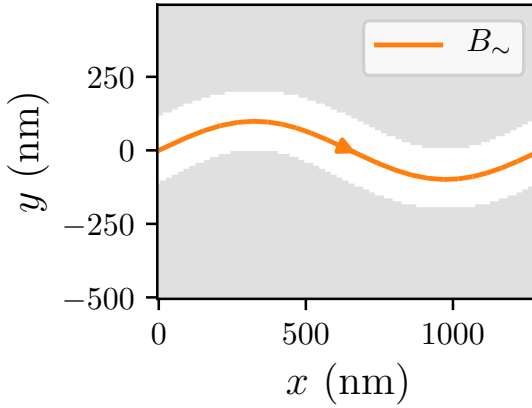


Figure 6.7: The magnetic field pattern emulating strong screening by the superconductors.

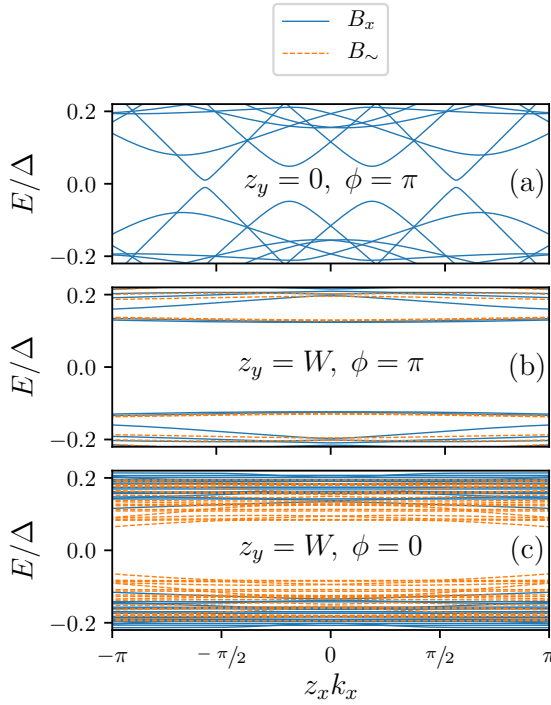


Figure 6.8: Comparison of the zigzag device's band structures with the magnetic field following the shape of the junction (orange) (see Fig. 6.7) and a magnetic field in the  $x$ -direction (blue) for different values of  $z_y$ .

### 6.7.3. INTERFACE TRANSPARENCY VS. PATH LENGTH CUT-OFF

The zigzag geometry both increases the interface transparency (because particles typically hit the superconductor closer to normal incidence) as well as sets an upper limit to the trajectory length. The change in the interface transparency alone is not sufficient to explain the increase of the topological gap. To verify this, we compute the dispersion of a system with  $z_x = z_y = 80 \text{ nm}$  comparable to the Fermi wavelength  $\lambda_F$  and  $W = 400 \text{ nm}$ , so that the angle of the boundaries is sufficiently large, but the boundary modulation is much smaller than the width. We observe that  $E_{\text{gap}}$  becomes  $6.1 \mu\text{eV}$ , a two-fold increase compared to the straight system, not the order of magnitude increase resulting from the cutting off of long trajectories.

## REFERENCES

- [1] R. M. Lutchyn, J. D. Sau, and S. D. Sarma, *Majorana Fermions and a topological phase transition in semiconductor-superconductor heterostructures*, Phys. Rev. Lett. **105**, 077001 (2010).
- [2] Y. Oreg, G. Refael, and F. von Oppen, *Helical liquids and Majorana bound states in quantum wires*, Phys. Rev. Lett. **105**, 177002 (2010).
- [3] J. Alicea, *New directions in the pursuit of Majorana fermions in solid state systems*, Rep. Prog. Phys. **75**, 076501 (2012).
- [4] C. Beenakker, *Search for Majorana Fermions in superconductors*, Annu. Rev. Condens. Matter Phys. **4**, 113 (2013).
- [5] C. Beenakker and L. Kouwenhoven, *A road to reality with topological superconductors*, Nat. Phys. **12**, 618 (2016).
- [6] M. Leijnse and K. Flensberg, *Introduction to topological superconductivity and Majorana fermions*, Semicond. Sci. Technol. **27**, 124003 (2012).
- [7] V. Mourik, K. Zuo, S. M. Frolov, S. R. Plissard, E. P. A. M. Bakkers, and L. P. Kouwenhoven, *Signatures of Majorana Fermions in hybrid superconductor-semiconductor nanowire devices*, Science **336**, 1003 (2012).
- [8] A. Das, Y. Ronen, Y. Most, Y. Oreg, M. Heiblum, and H. Shtrikman, *Zero-bias peaks and splitting in an Al-InAs nanowire topological superconductor as a signature of Majorana fermions*, Nat. Phys. **8**, 887 (2012).
- [9] M. T. Deng, C. L. Yu, G. Y. Huang, M. Larsson, P. Caroff, and H. Q. Xu, *Anomalous zero-bias conductance peak in a Nb-InSb nanowire-Nb hybrid device*, Nano Lett. **12**, 6414 (2012).
- [10] H. O. H. Churchill, V. Fatemi, K. Grove-Rasmussen, M. T. Deng, P. Caroff, H. Q. Xu, and C. M. Marcus, *Superconductor-nanowire devices from tunneling to the multichannel regime: Zero-bias oscillations and magnetoconductance crossover*, Phys. Rev. B **87**, 241401 (2013).

- [11] H. Zhang, C.-X. Liu, S. Gazibegovic, D. Xu, J. A. Logan, G. Wang, N. van Loo, J. D. S. Bommer, M. W. A. de Moor, D. Car, R. L. M. O. het Veld, P. J. van Veldhoven, S. Koelling, M. A. Verheijen, M. Pendharkar, D. J. Pennachio, B. Shojaei, J. S. Lee, C. J. Palmström, E. P. A. M. Bakkers, S. D. Sarma, and L. P. Kouwenhoven, *Quantized Majorana conductance*, *Nature* **556**, 74 (2018).
- [12] F. Pientka, A. Keselman, E. Berg, A. Yacoby, A. Stern, and B. I. Halperin, *Topological superconductivity in a planar Josephson junction*, *Phys. Rev. X* **7**, 021032 (2017).
- [13] M. Hell, M. Leijnse, and K. Flensberg, *Two-dimensional platform for networks of Majorana bound states*, *Phys. Rev. Lett.* **118**, 107701 (2017).
- [14] A. Fornieri, A. M. Whiticar, F. Setiawan, E. Portolés, A. C. C. Drachmann, A. Keselman, S. Gronin, C. Thomas, T. Wang, R. Kallaher, G. C. Gardner, E. Berg, M. J. Manfra, A. Stern, C. M. Marcus, and F. Nichele, *Evidence of topological superconductivity in planar Josephson junctions*, *Nature* **569**, 89 (2019).
- [15] H. Ren, F. Pientka, S. Hart, A. T. Pierce, M. Kosowsky, L. Lunczer, R. Schlereth, B. Scharf, E. M. Hankiewicz, L. W. Molenkamp, B. I. Halperin, and A. Yacoby, *Topological superconductivity in a phase-controlled Josephson junction*, *Nature* **569**, 93 (2019).
- [16] P. de Gennes and D. Saint-James, *Elementary excitations in the vicinity of a normal metal-superconducting metal contact*, *Phys. Lett.* **4**, 151 (1963).
- [17] C. Beenakker, *Andreev billiards*, in *Quantum Dots: a Doorway to Nanoscale Physics* (Springer Berlin Heidelberg, 2005) pp. 131–174.
- [18] B. Nijholt and A. R. Akhmerov, *Orbital effect of magnetic field on the Majorana phase diagram*, *Phys. Rev. B* **93**, 235434 (2016).
- [19] A. A. Golubov and M. Y. Kupriyanov, *Theoretical investigation of Josephson tunnel junctions with spatially inhomogeneous superconducting electrodes*, *J. Low Temp. Phys.* **70**, 83 (1988).
- [20] W. Belzig, C. Bruder, and G. Schön, *Local density of states in a dirty normal metal connected to a superconductor*, *Phys. Rev. B* **54**, 9443 (1996).
- [21] S. Pilgram, W. Belzig, and C. Bruder, *Excitation spectrum of mesoscopic proximity structures*, *Phys. Rev. B* **62**, 12462 (2000).
- [22] A. Haim and A. Stern, *Benefits of weak disorder in one-dimensional topological superconductors*, *Phys. Rev. Lett.* **122**, 126801 (2019).
- [23] C. W. Groth, M. Wimmer, A. R. Akhmerov, and X. Waintal, *Kwant: a software package for quantum transport*, *New J. Phys.* **16**, 063065 (2014).
- [24] B. Nijholt, J. Weston, J. Hoofwijk, and A. Akhmerov, *Adaptive: parallel active learning of mathematical functions*, Zenodo 10.5281/zenodo.1182437.

- [25] T. Laeven, B. Nijholt, A. R. Akhmerov, and M. Wimmer, *Source code and data set for “Enhanced proximity effect in zigzag-shaped Majorana Josephson junctions”*, 10.5281/zenodo.2578027.
- [26] S. Takei, B. M. Fregoso, H.-Y. Hui, A. M. Lobos, and S. D. Sarma, *Soft superconducting gap in semiconductor Majorana nanowires*, Phys. Rev. Lett. **110**, 186803 (2013).
- [27] C.-X. Liu, F. Setiawan, J. D. Sau, and S. D. Sarma, *Phenomenology of the soft gap, zero-bias peak, and zero-mode splitting in ideal Majorana nanowires*, Phys. Rev. B **96**, 054520 (2017).
- [28] T. D. Stanescu, R. M. Lutchyn, and S. D. Sarma, *Soft superconducting gap in semiconductor-based Majorana nanowires*, Phys. Rev. B **90**, 085302 (2014).
- [29] F. K. de Vries, Q. Wang, and S. Goswami, Private communications.

# 7

## ***Adaptive:* PARALLEL ACTIVE LEARNING OF MATHEMATICAL FUNCTIONS**

---

My contribution to this work is developing and implementing a large fraction of the adaptive sampling algorithms and the writing of the text.

## 7.1. INTRODUCTION

In the computational sciences, one often does costly simulations—represented by a function  $f$ —where a certain region in parameter space  $X$  is sampled, mapping to a codomain  $Y$ :  $f: X \rightarrow Y$ . Frequently, the different points in  $X$  can be independently calculated. Even though it is suboptimal, one usually resorts to sampling  $X$  on a homogeneous grid because of its simple implementation.

An alternative, which improves the simulation efficiency, is to choose new potentially interesting points in  $X$ , based on existing data [1–4]. Bayesian optimization works well for high-cost simulations where one needs to find a minimum (or maximum) [5]. However, if the goal of the simulation is to approximate a continuous function using the fewest points, an alternative strategy is to use a greedy algorithm that samples mid-points of intervals with the largest length or curvature [6]. Such a sampling strategy (i.e., in Fig. 7.1) would trivially speedup many simulations. Another advantage of such an algorithm is that it may be parallelized cheaply (i.e. more than one point may be sampled at a time), as we do not need to perform a global computation over all the data (as we would with Bayesian sampling) when determining which points to sample next.

The algorithm visualized in 7.1 consists of the following steps: (1) evaluate the function at the boundaries  $a$  and  $b$ , of the interval of interest, (2) calculate the loss for the interval  $L_{a,b} = \sqrt{(b-a)^2 + (f(b) - f(a))^2}$ , (3) pick a new point  $x_{\text{new}}$  in the centre of the interval with the largest loss,  $(x_i, x_j)$ , (4) calculate  $f(x_{\text{new}})$ , (5) discard the interval  $(x_i, x_j)$  and create two new intervals  $(x_i, x_{\text{new}})$  and  $(x_{\text{new}}, x_j)$ , calculating their losses  $L_{x_i, x_{\text{new}}}$  and  $L_{x_{\text{new}}, x_j}$  (6) repeat from step 3.

7

In this chapter we present a class of algorithms that generalizes the above example. This general class of algorithms is based on using a *priority queue* of subdomains (intervals in 1-D), ordered by a *loss* obtained from a *local loss function* (which depends only on the data local to the subdomain), and greedily selecting points from subdomains at the top of the priority queue. The advantage of these *local* algorithms is that they have a lower computational overhead than algorithms requiring *global* data and updates (e.g. Bayesian sampling), and are therefore more amenable to parallel evaluation of the function of interest.

We provide a reference implementation, the open-source Python package called Adaptive [8], which has previously been used in several scientific publications [9–12]. It has algorithms for  $f: \mathbb{R}^N \rightarrow \mathbb{R}^M$ , where  $N, M \in \mathbb{Z}^+$  but which work best when  $N$  is small; integration in  $\mathbb{R}$ ; and the averaging of stochastic functions. Most of our algorithms allow for a customizable loss function with which one can adapt the sampling algorithm to work optimally for different classes of functions. It integrates with the Jupyter notebook environment as well as popular parallel computation frameworks such as `ipyparallel`, `mpi4py`, and `dask.distributed`. It provides auxiliary functionality such as live-plotting, inspecting the data as the calculation is in progress, and automatically saving and loading of the data.

The raw data and source code that produces all plots in this chapter is available at [13].

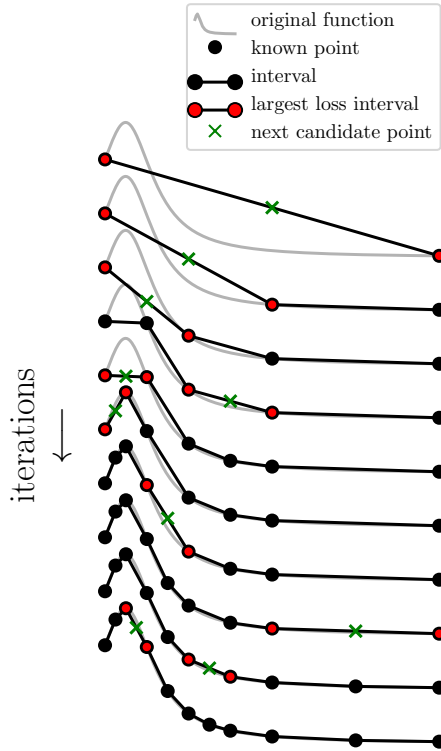


Figure 7.1: Visualization of a 1-D sampling strategy for a black-box function (grey). We start by calculating the two boundary points. Two adjacent existing data points (black)  $\{x_i, y_i\}$  define an interval. Each interval has a loss  $L_{i,i+1}$  associated with it that can be calculated from the points inside the interval  $L_{i,i+1}(x_i, x_{i+1}, y_i, y_{i+1})$  and optionally of  $N$  next nearest neighboring intervals. At each iteration the interval with the largest loss is indicated (red), with its corresponding candidate point (green) picked in the middle of the interval. The loss function in this example is an approximation to the curvature, calculated using the data from an interval and its nearest neighbors.

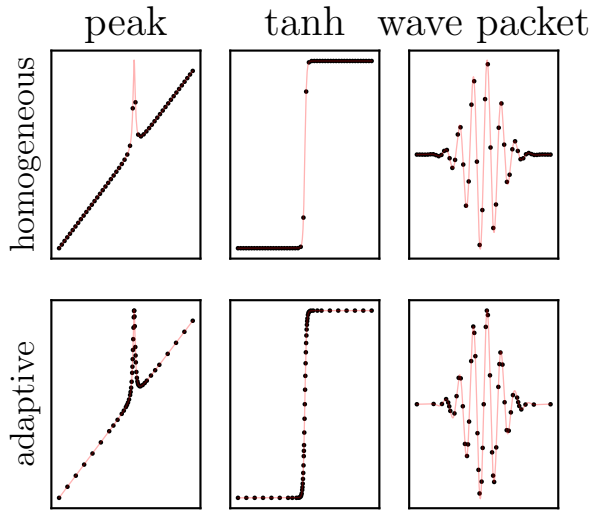


Figure 7.2: Comparison of homogeneous sampling (top) with adaptive sampling (bottom) for different one-dimensional functions (red) where the number of points in each column is identical. We see that when the function has a distinct feature—such as with the peak and tanh—adaptive sampling performs much better. When the features are homogeneously spaced, such as with the wave packet, adaptive sampling is not as effective as in the other cases.

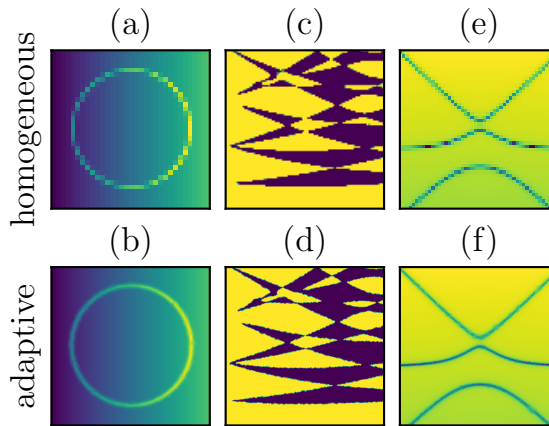


Figure 7.3: Comparison of homogeneous sampling (top) with adaptive sampling (bottom) for different two-dimensional functions where the number of points in each column is identical. On the left is the function  $f(x) = x + a^2 / (a^2 + (x - x_{\text{offset}})^2)$ . In the middle a topological phase diagram from [7], where the function can take the values -1 or 1. On the right, we plot level crossings for a two-level quantum system. In all cases using Adaptive results in a higher fidelity plot.

## 7.2. REVIEW OF ADAPTIVE SAMPLING

Optimal sampling and planning based on data is a mature field with different communities providing their own context, restrictions, and algorithms to solve their problems. To explain the relation of our approach with prior work, we discuss several existing contexts. This is not a systematic review of all these fields, but rather, we aim to identify the important traits and design considerations.

Optimal experiment design (OED) is a field of statistics that minimizes the number of experimental runs needed to estimate specific parameters and, thereby, reduce the cost of experimentation [14]. It works with many degrees of freedom and can consider constraints, for example, when the sample space contains regions that are infeasible for practical reasons. One form of OED is response-adaptive design [15], which concerns the adaptive sampling of designs for statistical experiments. Here, the acquired data (i.e., the observations) are used to estimate the uncertainties of a certain desired parameter. It then suggests further experiments that will optimally reduce these uncertainties. In this step of the calculation Bayesian statistics is frequently used. Bayesian statistics naturally provides tools for answering such questions; however, because it provides closed-form solutions, Markov chain Monte Carlo (MCMC) sampling is the standard tool for determining the most promising samples. In a typical non-adaptive experiment, decisions on which experiments to perform are made in advance.

Plotting a low dimensional function in between bounds requires one to evaluate the function on sufficiently many points such that when we interpolate values in between data points, we get an accurate description of the function values that were not explicitly calculated. In order to minimize the number of function evaluations, one can use adaptive sampling routines. For example, for one-dimensional functions, Mathematica [16] implements a `FunctionInterpolation` class that takes the function,  $x_{\min}$ , and  $x_{\max}$ , and returns an object that samples the function more densely in regions with high curvature; however, details on the algorithm are not published. Subsequently, we can query this object for points in between  $x_{\min}$  and  $x_{\max}$ , and get the interpolated value, or we can use it to plot the function without specifying a grid. Another application for adaptive sampling is numerical integration. It works by estimating the integration error of each interval and then minimizing the sum of these errors greedily. For example, the CQUAD algorithm [17] in the GNU Scientific Library [18] implements a more sophisticated strategy and is a doubly-adaptive general-purpose integration routine which can handle most types of singularities. In general, it requires more function evaluations than the integration routines in QUADPACK [18]; however, it works more often for difficult integrands. It is doubly-adaptive because it can decide to either subdivide intervals into more intervals or refine an interval by using a polynomial approximation of higher degree, requiring more points.

Hydrodynamics [19, 20] and astrophysics [21] use an adaptive refinement of the triangulation mesh on which a partial differential equation is discretized. By providing smaller mesh elements in regions with a higher variation of the solution, they reduce the amount of data and calculation needed at each step of time propagation. The remeshing at each time step happens globally, and this is an expensive operation. Therefore, mesh optimization does not fit our workflow because expensive global updates should be avoided. Computer graphics uses similar adaptive methods where a smooth surface can

represent a surface via a coarser piecewise linear polygon mesh, called a subdivision surface [22]. An example of such a polygonal remeshing method is one where the polygons align with the curvature of the space or field; this is called anisotropic meshing [23].

### 7.3. DESIGN CONSTRAINTS AND THE GENERAL ALGORITHM

The general algorithm that we describe in this chapter works best for low to intermediate cost functions. Determining the next candidate points happens in a single sequential process while the function executions can be in parallel. This means that to benefit from an adaptive sampling algorithm, that the time it takes to suggest a new point  $t_{\text{suggest}}$  must be much smaller than the average function execution time  $t_f$  over the number of parallel workers  $N$ :  $t_f/N \gg t_{\text{suggest}}$ . Functions that are fast to evaluate can be calculated on a dense grid, and functions that are slow to evaluate might benefit from full-scale Bayesian optimization where  $t_{\text{suggest}}$  is large. We are interested in the intermediate case, when one wishes to sample adaptively, but cannot afford the luxury of fitting of all available data at each step. While this may seem restrictive, we assert that a large class of functions is inside the right regime for local adaptive sampling to be beneficial.

Because we aim to keep the suggestion time  $t_{\text{suggest}}$  small, we propose to use the following approach, which operates on a constant-size subset of the data to determine which point to suggest next. We keep track of the subdomains in a priority queue, where each subdomain is assigned a priority called the “loss”. To suggest a new point we remove the subdomain with the largest loss from the priority queue and select a new point  $x_{\text{new}}$  from within it (typically in the centre) This splits the subdomain into several smaller subdomains  $\{S_i\}$  that each contain  $x_{\text{new}}$  on their boundaries. After evaluating the function at  $x_{\text{new}}$  we must then recompute the losses using the new data. We choose to consider loss functions that are “local”, i.e. the loss for a subdomain depends only on the points contained in that subdomain and possibly a (small) finite number of neighboring subdomains. This means that we need only recalculate the losses for subdomains that are “close” to  $x_{\text{new}}$ . Having computed the new losses we must then insert the  $\{S_i\}$  into the priority queue, and also update the priorities of the neighboring subdomains, if their loss was recalculated. After these insertions and updates we are ready to suggest the next point to evaluate. Due to the local nature of this algorithm and the sparsity of space in higher dimensions, we will suffer from the curse of dimensionality. The algorithm, therefore, works best in low dimensional space; typically calculations that can reasonably be plotted, so with 1, 2, or 3 degrees of freedom.

The algorithm described above can be made more precise by the following Python code:

```

1 first_subdomain, = domain.subdomains()
2 for x in domain.points(first_subdomain):
3     data[x] = f(x)
4
5 queue.insert(first_subdomain, priority=loss(domain, first_subdomain,
6     data))
7 while queue.max_priority() < target_loss:
```

```

8  loss, subdomain = queue.pop()
9
10 new_points, new_subdomains = domain.split(subdomain)
11 for x in new_points:
12     data[x] = f(x)
13
14 for subdomain in new_subdomains:
15     queue.insert(subdomain, priority=loss(domain, subdomain, data))
16
17 if loss.n_neighbors > 0:
18     subdomains_to_update = set()
19     for d in new_subdomains:
20         neighbors = domain.neighbors(d, loss.n_neighbors)
21         subdomains_to_update.update(neighbors)
22         subdomains_to_update -= set(new_subdomains)
23     for subdomain in subdomains_to_update:
24         queue.update(subdomain, priority=loss(domain, subdomain, data))

```

where we have used the following definitions:

**f** The function we wish to learn

**queue** A priority queue of unique elements, supporting the following methods: `max_priority()`, to get the priority of the top element; `pop()`, remove and return the top element and its priority; `insert(element, priority)`, insert the given element with the given priority into the queue; `update(element, priority)`, update the priority of the given element, which is already in the queue.

**domain** An object representing the domain of `f` split into subdomains. Supports the following methods: `subdomains()`, returns all the subdomains; `points(subdomain)`, returns all the points contained in the provided subdomain; `split(subdomain)`, splits a subdomain into smaller subdomains, returning the new points and new subdomains produced as a result; `neighbors(subdomain, n_neighbors)`, returns the subdomains neighboring the provided subdomain.

**data** A hashmap storing the points `x` and their values `f(x)`.

`loss(domain, subdomain, data)` The loss function, with `loss.n_neighbors` being the degree of neighboring subdomains that the loss function uses.

An example of such a local loss function for a one-dimensional function is the inter-point distance, i.e. given a subdomain (interval)  $(x_a, x_b)$  with values  $(y_a, y_b)$  the loss is  $\sqrt{(x_a - x_b)^2 + (y_a - y_b)^2}$ . A more complex loss function that also takes the first neighboring intervals into account is one that approximates the second derivative using a Taylor expansion. Figure 7.2 shows a comparison between a result using this loss and a function that is sampled on a grid.

The key data structures in the above algorithm are `queue` and `domain`. The priority queue must support efficiently finding and removing the maximum priority element,

as well as updating the priority of arbitrary elements whose priority is unknown (when updating the loss of neighboring subdomains). Such a datastructure can be achieved with a combination of a hashmap (mapping elements to their priority) and a red–black tree or a skip list [24] that stores (priority, element). This has average complexity of  $\mathcal{O}(\log n)$  for all the required operations. In the reference implementation, we use the SortedContainers Python package [25], which provides an efficient implementation of such a data structure optimized for realistic sizes, rather than asymptotic complexity. The domain object requires efficiently splitting a subdomain and querying the neighbors of a subdomain. For the one-dimensional case this can be achieved by using a red–black tree to keep the points  $x$  in ascending order. In this case both operations have an average complexity of  $\mathcal{O}(\log n)$ . In the reference implementation we again use SortedContainers. We thus see that by using the appropriate data structures the time required to suggest a new point is  $t_{\text{suggest}} \propto \mathcal{O}(\log n)$ . The total time spent on suggesting points when sampling  $N$  points in total is thus  $\mathcal{O}(N \log N)$ .

So far, the description of the general algorithm did not include parallelism. In order to include parallelism we need to allow for points that are “pending”, i.e. whose value has been requested but is not yet known. In the sequential algorithm subdomains only contain points on their boundaries. In the parallel algorithm *pending* points are placed in the interior of subdomains, and the priority of the subdomains in the queue is reduced to take these pending points into account. Later, when a pending point  $x$  is finally evaluated, we *split* the subdomain that contains  $x$  such that it is on the boundary of new, smaller, subdomains. We then calculate the priority of these new subdomains, and insert them into the priority queue, and update the priority of neighboring subdomains if required.

The parallel version of the algorithm can be described by the following Python code:

7

```

1 def priority(domain, subdomain, data):
2     subvolumes = domain.subvolumes(subdomain)
3     max_relative_subvolume = max(subvolumes) / sum(subvolumes)
4     L_0 = loss(domain, subdomain, data)
5     return max_relative_subvolume * L_0
6
7 first_subdomain, = domain.subdomains()
8 for x in domain.points(first_subdomain):
9     data[x] = f(x)
10
11 new_points = domain.insert_points(first_subdomain, executor.ncores)
12 for x in new_points:
13     data[x] = None
14     executor.submit(f, x)
15
16 queue.insert(first_subdomain, priority=priority(domain, subdomain,
17     data))
18
19 while executor.n_outstanding_points > 0:
20     x, y = executor.get_one_result()
21     data[x] = y

```

```

21
22 # Split into smaller subdomains with 'x' at a subdomain boundary
23 # And calculate the losses for these new subdomains
24 old_subdomains, new_subdomains = domain.split_at(x)
25 for subdomain in old_subdomains:
26     queue.remove(old_subdomain)
27 for subdomain in new_subdomains:
28     queue.insert(subdomain, priority(domain, subdomain, data))
29
30 if loss.n_neighbors > 0:
31     subdomains_to_update = set()
32     for d in new_subdomains:
33         neighbors = domain.neighbors(d, loss.n_neighbors)
34         subdomains_to_update.update(neighbors)
35     subdomains_to_update -= set(new_subdomains)
36     for subdomain in subdomains_to_update:
37         queue.update(subdomain, priority(domain, subdomain, data))
38
39 # If it looks like we're done, don't send more work
40 if queue.max_priority() < target_loss:
41     continue
42
43 # Send as many points for evaluation as we have compute cores
44 for _ in range(executor.ncores - executor.n_outstanding_points)
45     loss, subdomain = queue.pop()
46     new_point, = domain.insert_points(subdomain, 1)
47     data[new_point] = None
48     executor.submit(f, new_point)
49     queue.insert(subdomain, priority(domain, subdomain, data))

```

Where we have used identical definitions to the serial case for `f`, `data`, `loss` and the following additional definitions:

**queue** As for the sequential case, but must additionally support: `remove(element)`, remove the provided element from the queue.

**domain** As for the sequential case, but must additionally support:  
`insert_points(subdomain, n)`, insert `n` (pending) points into the given subdomain without splitting the subdomain; `subvolumes(subdomain)`, return the volumes of all the sub-subdomains contained within the given subdomain;  
`split_at(x)`, split the domain at a new (evaluated) point `x`, returning the old subdomains that were removed, and the new subdomains that were added as a result.

**executor** An object that can submit function evaluations to computing resources and retrieve results. Supports the following methods: `submit(f, x)`, schedule the execution of `f(x)` and do not block; `get_one_result()`, block waiting for a single

result, returning the pair  $(x, y)$  as soon as it becomes available; `ncores`, the total number of parallel processing units; `n_outstanding_points`, the number of function evaluations that have been requested and not yet retrieved, incremented by `submit` and decremented by `get_one_result`.

## 7.4. LOSS FUNCTION DESIGN

Not all goals are achieved by using an identical sampling strategy; the specific problem determines the goal. For example, quadrature rules requires a denser sampling of the subdomains where the interpolation error is highest, plotting (or function approximation) requires continuity of the approximation, maximization only cares about finding an optimum, and isoline or isosurface sampling aims to sample regions near a given function value more densely. These different sampling goals each require a loss function tailored to the specific case.

Additionally, it is important to take the class of functions being learned when selecting a loss function into account, even if the specific goal (e.g. continuity of the approximation) remains unchanged. For example, if we wanted a smooth approximation to a function with a singularity, then the interpoint distance loss function would be a poor choice, even if it is generally a good choice for that specified goal. This is because the aforementioned loss function will “lock on” to the singularity, and will fail to sample the function elsewhere once it starts. This is an illustration of the following principle: for optimal sampling performance, loss functions should be tailored to the particular domain of interest.

One strategy for designing loss functions is to take existing loss functions and apply a regularization. For example, to limit the over-sampling of singularities inherent in the distance loss we can set the loss of subdomains that are smaller than a given threshold to zero, which will prevent them from being sampled further.

Another general strategy for designing loss functions is to combine existing loss functions that optimize for particular features, and then combine them together. Typically one weights the different constituent losses to prioritize the different features. For example, combining a loss function that calculates the curvature with a distance loss function will sample regions with high curvature more densely, while ensuring continuity. Another important example is combining a loss function with the volume of the subdomain, which will ensure that the sampling is asymptotically dense everywhere (because large subdomains will have a correspondingly large loss). This is important if there are many distinct and narrow features that all need to be found, and densely sampled in the region around the feature.

## 7.5. EXAMPLES

### 7.5.1. LINE SIMPLIFICATION LOSS

Inspired by a method commonly employed in digital cartography for coastline simplification, Visvalingam’s algorithm, we construct a loss function that does its reverse [26]. Here, at each point (ignoring the boundary points), we compute the effective area associated with its triangle, see Fig. 7.4(b). The loss then becomes the average area of two adjacent triangles. By Taylor expanding  $f$  around  $x$  it can be shown that the area of the triangles relates to the contributions of the second derivative. We can generalize this loss to  $N$

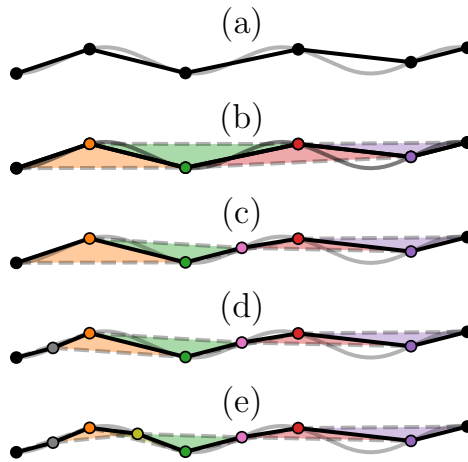


Figure 7.4: Line loss visualization. In this example, we start with 6 points (a) on the function (grey). Ignoring the endpoints, the effective area of each point is determined by its associated triangle (b). The loss of each interval can be computed by taking the average area of the adjacent triangles. Subplots (c), (d), and (e) show the subsequent iterations following (b).

dimensions, where the triangle is replaced by a  $(N + 1)$  dimensional simplex.

In order to compare sampling strategies, we need to define some error. We construct a linear interpolation function  $\tilde{f}$ , which is an approximation of  $f$ . We calculate the error in the  $L^1$ -norm, defined as,

$$\text{Err}_1(\tilde{f}) = \|\tilde{f} - f\|_{L^1} = \int_a^b |\tilde{f}(x) - f(x)| dx.$$

This error approaches zero as the approximation becomes better.

Figure 7.5 shows this error as a function of the number of points  $N$ . Here, we see that for homogeneous sampling to get the same error as sampling with a line loss, a factor  $\approx 1.6 - 20$  times more points are needed, depending on the function.

### 7.5.2. A PARALLELIZABLE ADAPTIVE INTEGRATION ALGORITHM BASED ON CQUAD

In Sec. 7.2 we mentioned the doubly-adaptive integration algorithm CQUAD [17]. This algorithm uses a Clenshaw-Curtis quadrature rules of increasing degree  $d$  in each interval [27]. The error estimate is  $\sqrt{\int (f_0(x) - f_1(x))^2}$ , where  $f_0$  and  $f_1$  are two successive interpolations of the integrand. To reach the desired total error, intervals with the maximum absolute error are improved. Either (1) the degree of the rule is increased or (2) the interval is split if either the function does not appear to be smooth or a rule of maximum degree ( $d = 4$ ) has been reached. All points inside the intervals can be trivially calculated in parallel; however, when there are more resources available than points, Adaptive needs to guess whether an (1) interval's should degree of the rule should be increased or (2) or the

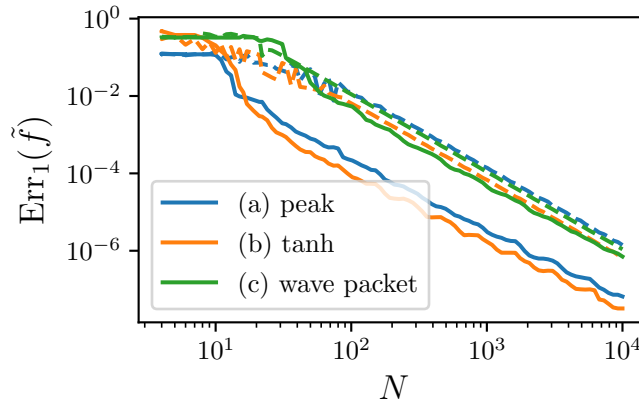


Figure 7.5: The  $L^1$ -norm error as a function of number of points  $N$  for the functions in Fig. 7.2 (a,b,c). The interrupted lines correspond to homogeneous sampling and the solid line to the sampling with the line loss. In all cases adaptive sampling performs better, where the error is a factor 1.6-20 lower for  $N = 10000$ .

interval is split. Here, we choose to always increase until  $d = 4$ , after which the interval is split.

### 7.5.3. ISOLINE AND ISOSURFACE SAMPLING

A judicious choice of loss function allows to sample the function close to an isoline (isosurface in 2D). Specifically, we prioritize subdomains that are bisected by the isoline or isosurface:

```

1 def isoline_loss_function(level, priority):
2     def loss(simplex, values, value_scale):
3         values = np.array(values)
4         which_side = np.sign(level * value_scale - values)
5         crosses_isoline = np.any(np.diff(which_side))
6         return volume(simplex) * (1 + priority * crosses_isoline)
7     return loss

```

See Fig. 7.6 for a comparison with uniform sampling.

## 7.6. IMPLEMENTATION AND BENCHMARKS

We will now introduce Adaptive's API. The object that can suggest points based on existing data is called a *learner*. The learner abstracts the sampling strategy based on a priority queue and local loss functions that we described in Sec. 7.3. We define a learner as follows:

```

1 from adaptive import Learner1D
2
3 def f(x):
4     a = 0.01
5     return x + a**2 / (a**2 + x**2)

```

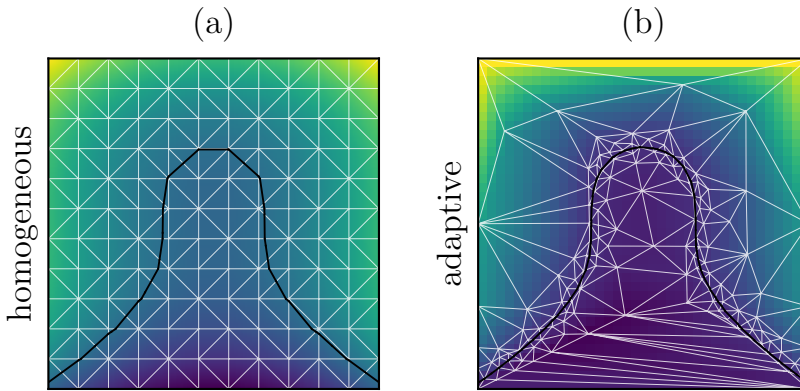


Figure 7.6: Comparison of isoline sampling of  $f(x, y) = x^2 + y^3$  at  $f(x, y) = 0.1$  using homogeneous sampling (left) and adaptive sampling (right) with the same amount of points  $n = 12^2 = 144$ . We plot the function interpolated on a grid (color) with the triangulation on top (white) where the function is sampled on the vertices. The solid line (black) indicates the isoline at  $f(x, y) = 0.1$ . The isoline in the homogeneous case consists of 43 line segments and the adaptive case consists of 94 line segments.

```
6
7 learner = Learner1D(f, bounds=(-1, 1))
```

We provide the function to learn, the domain boundaries, and use a default loss function. We can then *ask* the learner for points:

```
1 points, priorities = learner.ask(4)
```

The learner gives us back the points that we should sample next, as well as the priorities of these points (the loss of the parent subdomains). We can then evaluate some of these points and *tell* the learner about the results:

```
1 data = [learner.function(x) for x in points]
2 learner.tell_many(points, data)
```

To change the loss function we pass a function that takes points and values, like so:

```
1 def distance_loss(xs, ys): # used by default
2     dx = xs[1] - xs[0]
3     dy = ys[1] - ys[0]
4     return np.hypot(dx, dy)
5
6 learner = Learner1D(peak, bounds=(-1, 1),
7     loss_per_interval=distance_loss)
```

If we wanted to create the “volume loss” discussed in Sec. 7.4 we could simply write:

```
1 def uniform_loss(xs, ys):
2     dx = xs[1] - xs[0]
3     return dx
```

```

4
5 learner = Learner1D(peak, bounds=(-1, 1),
    loss_per_interval=uniform_loss)

```

The previous example shows how we can drive the learner manually. For example, to run the learner until the loss is below 0.01 we could do the following:

```

1 def goal(learner):
2     return learner.loss() < 0.01
3
4 while not goal(learner):
5     (x,), _ = learner.ask(1)
6     y = f(x)
7     learner.tell(x, y)

```

This approach allows for the best *adaptive* performance (i.e. fewest number of points to reach the goal) because the learner has maximal information about  $f$  every time we ask it for the next point. However this does not allow to take advantage of multiple cores, which may enable better *walltime* performance (i.e. time to reach the goal). Adaptive abstracts the task of driving the learner and executing  $f$  in parallel to a *Runner*:

```

1 from adaptive import Runner
2 runner = Runner(learner, goal)

```

The above code uses the default parallel execution context, which occupies all the cores on the machine. It is simple to use *ipyparallel* to enable calculations on a cluster:

7

```

1 import ipyparallel
2
3 runner = Runner(learner, goal, executor=ipyparallel.Client())

```

If the above code is run in a Jupyter notebook it will not block. Adaptive takes advantage of the capabilities of the IPython to execute concurrently with the Python kernel. This means that as the calculation is in progress the data is accessible without race conditions via `learner.data`, and can be plotted with `learner.plot()`. Additionally, in a Jupyter notebook environment, we can call `runner.live_info()` to display useful information about the ongoing calculation.

We have also implemented a *LearnerND* with a similar API

```

1 from adaptive import LearnerND
2
3 def ring(xy): # pretend this is a slow function
4     x, y = xy
5     a = 0.2
6     return x + np.exp(-(x**2 + y**2 - 0.75**2)**2/a**4)
7
8 learner = adaptive.LearnerND(ring, bounds=[(-1, 1), (-1, 1)])
9 runner = Runner(learner, goal)

```

Again, it is possible to specify a custom loss function using the `loss_per_simplex` argument.

Frequently, more than one function (learner) needs to run at once, to do this we have implemented the `BalancingLearner`, which does not take a function, but a list of learners. This learner internally asks all child learners for points and will choose the point of the learner that maximizes the loss improvement; it balances the resources over the different learners. We can use it like

```

1 from functools import partial
2 from adaptive import BalancingLearner
3
4 def f(x, pow):
5     return x**pow
6
7 learners = [Learner1D(partial(f, pow=i)), bounds=(-10, 10) for i in
8             range(2, 10)]
9 bal_learner = BalancingLearner(learners)
10 runner = Runner(bal_learner, goal)

```

For more details on how to use Adaptive, we recommend reading the tutorial inside the documentation [28].

## 7.7. POSSIBLE EXTENSIONS

One of the fundamental operations in the adaptive algorithm is selecting a point from within a subdomain. The current implementation uses simplices for subdomains (triangles in 2D, tetrahedrons in 3D), and picks a point either (1) in the center of the simplex or (2) on the longest edge of the simplex. The choice depends on the shape of the simplex; the center is only used if using the longest edge would produce unacceptably thin simplices. A better strategy may be to choose points on the edge of a simplex such that the simplex aligns with the gradient of the function, creating an anisotropic triangulation [29]. This is a similar approach to the anisotropic meshing techniques mentioned in the literature review.

Stochastic processes frequently appear in numerical sciences. Currently, Adaptive has an `AverageLearner` that samples a random variable (modelled as a function that takes no parameters and returns a different value each time it is called) until the mean is known to within a certain standard error. This is advantageous because no predetermined number of samples has to be set before starting the simulation. Extending this learner to be able to deal with stochastic functions in arbitrary dimensions would be a useful addition.

Finally, there is the potential to use Adaptive for experimental control. There are a number of challenges associated with this use case. Firstly, experimental results are typically stochastic (due to noise), and would require sampling the same point in parameter space several times. This aspect is closely associated with sampling stochastic functions discussed in the preceding paragraph. Secondly, in an experiment one typically cannot jump around arbitrary quickly in parameter space. It may be faster to sweep one parameter compared to another; for example, in condensed matter physics experiments,

sweeping magnetic field is much slower than sweeping voltage source frequency. Lastly, some experiments exhibit hysteresis. This means that results may not be reproducible if a different path is taken through parameter space. In such a case one would need to restrict the sampling to only occur along a certain path in parameter space. Incorporating such extensions into Adaptive would require adding a significant amount of extra logic, as learners would need to take into account not only the data available, but the order in which the data was obtained, and the timing statistics at different points in parameter space. Despite these challenges, however, Adaptive can already be used in experiments that are not restricted in these ways.

## REFERENCES

- [1] R. B. Gramacy, H. K. H. Lee, and W. G. Macready, *Parameter space exploration with gaussian process trees*, in *Twenty-first international conference on Machine learning - ICML '04* (ACM Press, 2004).
- [2] L. H. de Figueiredo, *Adaptive sampling of parametric curves*, in *Graphics Gems V* (Elsevier, 1995) pp. 173–178.
- [3] R. M. Castro, *Active learning and adaptive sampling for non-parametric inference*, Ph.D. thesis, Rice University (2008).
- [4] Y. Chen and C. Peng, *Intelligent adaptive sampling guided by gaussian process inference*, *Meas. Sci. Technol.* **28**, 105005 (2017).
- [5] T. Takhtaganov and J. Müller, *Adaptive gaussian process surrogates for Bayesian inference*, arXiv preprint arXiv:1809.10784 (2018).
- [6] S. Wolfram, *Mathematica: Adaptive plotting*, (2011).
- [7] B. Nijholt and A. R. Akhmerov, *Orbital effect of magnetic field on the Majorana phase diagram*, *Phys. Rev. B* **93**, 235434 (2016).
- [8] B. Nijholt, J. Weston, J. Hoofwijk, and A. Akhmerov, *Adaptive: parallel active learning of mathematical functions*, Zenodo 10.5281/zenodo.1182437.
- [9] A. Vuik, B. Nijholt, A. Akhmerov, and M. Wimmer, *Reproducing topological properties with quasi-Majorana states*, *SciPost Phys.* **7**, 061 (2019).
- [10] T. Laeven, B. Nijholt, M. Wimmer, and A. R. Akhmerov, *Enhanced proximity effect in zigzag-shaped Majorana Josephson junctions*, arXiv preprint arXiv:1903.06168 (2019).
- [11] J. D. Bommer, H. Zhang, Önder Gül, B. Nijholt, M. Wimmer, F. N. Rybakov, J. Garaud, D. Rodic, E. Babaev, M. Troyer, D. Car, S. R. Plissard, E. P. Bakkers, K. Watanabe, T. Taniguchi, and L. P. Kouwenhoven, *Spin-orbit protection of induced superconductivity in Majorana nanowires*, *Phys. Rev. Lett.* **122**, 187702 (2019).
- [12] A. Melo, S. Rubbert, and A. Akhmerov, *Supercurrent-induced Majorana bound states in a planar geometry*, *SciPost Phys.* **7**, 039 (2019).

- [13] B. Nijholt, J. Weston, and A. Akhmerov, *Adaptive: parallel active learning of mathematical functions*, <https://github.com/python-adaptive/paper/> (2020).
- [14] A. F. Emery and A. V. Nenarokomov, *Optimal experiment design*, Meas. Sci. Technol. **9**, 864 (1998).
- [15] F. Hu and W. F. Rosenberger, *The Theory of Response-Adaptive Randomization in Clinical Trials* (John Wiley & Sons, Inc., 2006).
- [16] I. Wolfram Research, *Mathematica, version 12.0*, Champaign, IL, 2019.
- [17] P. Gonnet, *Increasing the reliability of adaptive quadrature using explicit interpolants*, ACM Trans. Math. Softw. **37**, 1 (2010).
- [18] M. Galassi, J. Davies, J. Theiler, B. Gough, G. Jungman, P. Alken, M. Booth, and F. Rossi, *GNU scientific library*, No. Release **2** (1996).
- [19] M. Berger and P. Colella, *Local adaptive mesh refinement for shock hydrodynamics*, J. Comput. Phys. **82**, 64 (1989).
- [20] M. J. Berger and J. Olinger, *Adaptive mesh refinement for hyperbolic partial differential equations*, J. Comput. Phys. **53**, 484 (1984).
- [21] R. I. Klein, *Star formation with 3-d adaptive mesh refinement: the collapse and fragmentation of molecular clouds*, J. Comput. Appl. Math **109**, 123 (1999).
- [22] T. DeRose, M. Kass, and T. Truong, *Subdivision surfaces in character animation*, in *Proceedings of the 25th annual conference on Computer graphics and interactive techniques - SIGGRAPH '98* (ACM Press, 1998).
- [23] P. Alliez, D. Cohen-Steiner, O. Devillers, B. Lévy, and M. Desbrun, *Anisotropic polygonal remeshing*, ACM Trans. Graph. **22**, 485 (2003).
- [24] T. H. Cormen, C. E. Leiserson, R. L. Rivest, and C. Stein, *Introduction to Algorithms*, 3rd ed. (The MIT Press, 2009).
- [25] G. Jenks, *Python sorted containers*, <http://www.grantjenks.com/docs/sortedcontainers/> (2019).
- [26] M. Visvalingam and J. D. Whyatt, *The douglas-peucker algorithm for line simplification: Re-evaluation through visualization*, Comput. Graphics Forum **9**, 213 (1990).
- [27] C. W. Clenshaw and A. R. Curtis, *A method for numerical integration on an automatic computer*, Numer. Math. **2**, 197 (1960).
- [28] B. Nijholt, J. Weston, and A. Akhmerov, *Adaptive documentation*, (2018), <https://adaptive.readthedocs.io>.
- [29] N. Dyn, D. Levin, and S. Rippa, *Data dependent triangulations for piecewise linear interpolation*, IMA J. Appl. Math. **10**, 137 (1990).



# CURRICULUM VITÆ

## Bas NIJHOLT

28-12-1990      Born in Rotterdam, the Netherlands.

### EDUCATION

2009–2013      B.Sc. in Applied Physics,  
Delft University of Technology, Delft, the Netherlands

2013–2015      M.Sc. in Applied Physics,  
Delft University of Technology, Delft, the Netherlands

*M.Sc. Thesis:* Orbital effect of magnetic field on the Majorana phase diagram

*Promotor:*    Dr. A. R. Akhmerov

2016–2020      PhD. in Physics  
Delft University of Technology, Delft, the Netherlands

*Thesis:*        Towards realistic numerical simulations of Majorana devices

*Promotor:*    Dr. A. R. Akhmerov

*Copromotor:* Dr. M. T. Wimmer

2020–            Quantum Simulation Engineer  
Microsoft, Station Q, Delft, the Netherlands



# LIST OF PUBLICATIONS

1. **Bas Nijholt** and Anton R. Akhmerov, *Orbital effect of magnetic field on the Majorana phase diagram*, Phys. Rev. B **93**, 235434, (2015)
2. Jakob Kamhuber, Maja C. Cassidy, Hao Zhang, Önder Gül, Fei Pei, Michiel W. A. de Moor, **Bas Nijholt**, Kenji Watanabe, Takashi Taniguchi, Diana Car, Sébastien R. Plissard, Erik P. A. M. Bakkers, and Leo P. Kouwenhoven, *Conductance quantization at zero magnetic field in InSb nanowires*, Nano Lett. **16**, 3482–3486, (2016)
3. Doru Sticlet, **Bas Nijholt**, and Anton R. Akhmerov, *Robustness of Majorana bound states in the short-junction limit*, Phys. Rev. B **95**, 115421, (2017)
4. Daniel R. Burnham, **Bas Nijholt**, Iwijn de Vlaminck, Jinhua Quan, Timur Yusufzai and Cees Dekker, *Annealing helicase HARP closes RPA-stabilized DNA bubbles non-processively*, Nucleic Acids Res. **45**, 4687–4695, (2017)
5. Kun Zuo, Vincent Mourik, Daniel B. Szombati, **Bas Nijholt**, David J. Van Woerkom, Attila Geresdi, Jun Chen, Viacheslav P. Ostroukh, Anton R. Akhmerov, Sebastián R. Plissard, Diana Car, Erik P. A. M. Bakkers, Dmitry I. Pikulin, Leo P. Kouwenhoven, and Sergey M. Frolov, *Supercurrent interference in few-mode nanowire Josephson junctions*, Phys. Rev. Lett. **119**, 187704, (2017)
6. Jouri D. S. Bommer, Hao Zhang, Önder Gül, **Bas Nijholt**, Michael Wimmer, Philipp N. Rybakov, Julien Garaud, Donjan Rodic, Egor Babaev, Matthias Troyer, Diana Car, Sébastien R. Plissard, Erik P. A. M. Bakkers, Kenji Watanabe, Takashi Taniguchi, Leo P. Kouwenhoven, *Spin-orbit protection of induced superconductivity in Majorana nanowires*, Phys. Rev. Lett. **122**, 187702, (2019)
7. Adriaan Vuik, **Bas Nijholt**, Anton R. Akhmerov, and Michael Wimmer, *Reproducing topological properties with quasi-Majorana states*, SciPost Phys. 7, 061, (2019)
8. Tom Laeven, **Bas Nijholt**, Michael Wimmer, and Anton R. Akhmerov, *Enhanced proximity effect in zigzag-shaped Majorana Josephson junctions*, arXiv preprint arXiv:1903.06168
9. **Bas Nijholt**, Joseph Weston, and Anton R. Akhmerov, *Adaptive: parallel active learning of mathematical functions*, manuscript in preparation.
10. **Bas Nijholt**, Georg W. Winkler, Jukka I. Väyrynen, and Roman M. Lutchyn, *Extracting the spin-orbit coupling strength from weak anti-localization measurements using realistic device simulations*, manuscript in preparation.